Experimental and Theoretical Studies of Contaminant Transport Due to Human Movement in a Hospital Corridor

Richard Wood

Submitted in accordance with the requirements for the degree of

Doctor of Philosophy.

The University of Leeds

School of Civil Engineering

August 2015

Intellectual Property and Publication Statements

The candidate confirms that the work is his own, except where work which has formed part of jointly-authored publications has been included. The contribution of the candidate and the other authors work has been explicitly indicated herein. The candidate confirms that appropriate credit has been given within the thesis where reference has been made to the work of others.

The work presented in Chapter 3 of this thesis has appeared in the following publication:

R. Wood, D. J. Borman, C. J. Noakes and A. W. Woods. Contaminant Transport In A Hospital Corridor Using A Water-Bath Model. *Proceedings of Indoor Air 2014*. HP0511.

I was responsible for the designing and carrying out of all experiments, as well as all image analysis and data processing. A. W. Woods was partly responsible for construction of the experimental apparatus, while C. J. Noakes and D. J. Borman contributed in the editing of the manuscript.

Acknowledgements

First and foremost, I would like to thank my supervisors Prof Cath Noakes and Dr Duncan Borman. Their continual support and overall input has not gone unnoticed and without them this endeavour would not have been possible.

Having spent nine months of my studies at the BP Institute, I would like to extend my thanks to all those who helped me during my time there, but in particular Prof Andrew Woods. The relative ease with which the experimental work was executed, was due in no small part to Prof Woods' guidance and suggestions. The implementation of such ideas was provided by: lab technician Andrew Pluck, for all things relating to the construction of the rig; and Health & Safety officer Dudley Simons, for all things relating to lighting and image capture; both of whom I owe thanks to for facilitating the water-bath modelling process.

For their proofreading services, I offer my gratitude to Gemma and Alex.

I wish to say a huge thank you to my family and friends. I owe possibly the biggest thank you to my parents, Glenn and Jane, and brother, Charlie, who have always supported me. To my friends, I thank you for the effort taken to lighten my stress levels during the hardest times and constant asking of the question of "are you *still* here / a student?", the recurrence of which was possibly the biggest motivator of all to finish. To the many office-friends and colleagues I have had the pleasure of working with over the years, thank you for the advice and office banter. I did start to list this last lot by name, but the list grew far too large and I would undoubtedly forget someone, so if you think you might be in this group, you probably are.

Finally, I wish to thank EPSRC for the funding that made this all possible.

Abstract

This thesis considers numerical, physical and theoretical modelling approaches to investigate the influence of a person's wake on the dispersion of an airborne pathogen in a hospital corridor and the implications this has in terms of infection risk. The various physical and computational modelling approaches were conducted using geometries corresponding to a 1:15 reduction in length-scale, when compared to the full-scale, and then interpreted in the context of a full-scale scenario in a hospital corridor.

The movement of people in a corridor was approximated using a translating circular cylinder. A physical water-bath model was used to investigate contaminant transport using food-dye in a channel with different sized cylinders and translation frequencies. Dye concentrations were quantified through a calibration method dependent upon changes in light-intensity, leading to accurate tracking of the dye and allowing the amount of dye in different regions of the water-bath to be calculated over time. The centre of mass of the dye cloud was found to be dependent upon the square root of the translation frequency, amplitude, cylinder diameter and elapsed time. Based on the hypothesis that the dispersal of the dye could be described by a turbulent diffusion process, a theoretical model was constructed to predict the evolution of the dye concentration using a Gaussian function, which agrees well with experimental data for a broad range of cylinder diameters and translation properties.

Two and three-dimensional computational fluid dynamics (CFD) models were developed to investigate the transport of a passive scalar due to a translating cylinder in a channel, their geometries and boundary conditions bearing close resemblance to the water-bath. Seven turbulence models were tested to determine the most suitable, using the water-bath data for validation. The shear-stress transport (SST) model was found to offer solutions in closest agreement with experimental results and theoretical predictions, as well as offering up to a 70 % reduction in computation time compared to SAS, DES and LES turbulence models. The commonly used $k-\epsilon$ model was found to be inappropriate for modelling the flows encountered here.

The numerical and theoretical models were used to investigate a number of scenarios in a corridor at the full-scale where an infectious contaminant is released. This includes a unidirectional flow applied along the corridor, where it was shown that the wake of the cylinder was still able to transport contaminant 'upstream' against the direction of the flow. This implies that a walking person may be able to transport an airborne contaminant in their wake even in the presence of ventilation. Infection risks were calculated for a person making a single pass and multiple passes of the corridor based on the amount of contaminant inhaled and published data on the infectiousness of different pathogens. Results showed that the theoretical model developed here led to each individual breath having its own infection risk based on temporal and spatial differences, whereas a model assuming a well-mixed contaminant distribution did not.

Results demonstrate that a person's wake is likely to influence the spread of an airborne contaminant in a hospital corridor, even if ventilated within current recommended guidelines. This highlights that a person's risk of infection, in the presence of airborne pathogens, is partly determined by any human traffic passing through the space before them and not solely on any ventilation within the space, as is often assumed in airborne infection models. Furthermore, the experimental work has provided strong validation data for the CFD models and allowed for the construction of uncomplicated yet powerful theoretical models. It has been shown that, when appropriate modelling assumptions are taken, confidence can be had in CFD predictions of contaminant transport involving complex flow behaviour, such as eddy shedding, within a built environment. The study also confirms that poor selection of 'default' modelling assumptions, for example use of the $k - \epsilon$ turbulence model, will provide very poor predictions, highlighting need for careful selection of each aspect of a model.

Contents

List of Figures

List of Tables

Nomenclature

The following symbols, and associated dimensions are used throughout, unless otherwise stated. All dimensions are given in metres (m), millimetres (mm), grams (g), kilograms (kg), hours (hrs), minutes (min), seconds (s) and degrees Celsius (°C), unless stated otherwise.

Symbol	**Term**	**Unit**
∇	$\mathbf{i}\frac{\partial}{\partial x} + \mathbf{j}\frac{\partial}{\partial y} + \mathbf{k}\frac{\partial}{\partial z}$	Dimensionless
Δ	Small variable change (e.g. Δt, Δx)	Dimensionless
A	Amplitude	m
A_r	Area	m^2
ACH	Air changes per hour	Dimensionless
C	Dye concentration	g $litre^{-1}$
C_D	Drag coefficient	Dimensionsless
C_L	Lift coefficient	Dimensionsless
C_{pb}	Base pressure coefficient	Dimensionsless
d	Diameter	mm or m
D	Molecular/Mass Diffusivity	m^2 s^{-1}
D_t	Turbulent Diffusivity	m^2 s^{-1}
f	Vortex shedding frequency	s^{-1}
F_D	Drag force	kg m s^{-2}
F_L	Lift force	kg m s^{-2}
g	Acceleration due to gravity	m s^{-2}
I	Number of infectors	Dimensionless
k	Turbulent kinetic energy	kg m^2 s^{-2}
L	Light Intensity	non-dimensional
m	Mass	g or kg

M_i	i'th Moment of a distribution	m^i *[variable units]*
p	Pressure	Pascals (Pa)
p_{br}	Pulmonary breathing rate	$\mathrm{m}^3\ \mathrm{min}^{-1}$
Pe	Peclet number	Dimensionless
Q	Volumetric flow rate	$\mathrm{m}^3\ \mathrm{s}^{-1}$ or $\mathrm{m}^3\ \mathrm{min}^{-1}$
r	Radius	mm or m
Re	Reynolds number	Dimensionless
S	Number of susceptibles	Dimensionless
Sc	Schmidt number	Dimensionless
St	Strouhal number	Dimensionless
t	Time	hrs, min & s
T	Temperature	°C
$\mathbf{U} = (U_x, U_y, U_z)$	Velocity	$\mathrm{m\ s}^{-1}$
V	Volume	m^3
(x, y, z)	Cartesian coordinates	Dimensionless
$\bar{X}$	Distribution centre of mass	mm or m
y^+	y plus	Dimensionless
Γ	Scalar Diffusion Coefficient	$\mathrm{m}^2\ \mathrm{s}^{-1}$
ϵ	Turbulent dissipation	$\mathrm{m}^2\ \mathrm{s}^{-3}$
λ_{ci}	Swirling strength	s^{-1}
μ	Dynamic viscosity	$\mathrm{kg\ m}^{-1}\ \mathrm{s}^{-1}$
ρ	Density	$\mathrm{kg\ m}^{-3}$
ϕ	Scalar quantity	Dimensionless
ω	Frequency	s^{-1}

The following notations and subscripts are used throughout, unless stated otherwise:

Symbol	**Term**
$\bar{w}$	Mean of w
w_i	Value of w with x coordinate x_i
$w_{i,j}$	Value of w with coordinates (x_i, y_j)

w^0	Initial value of a variable w at time = 0
w_f	w relates to full-scale
w_m	w relates to model-scale

Abbreviation	**Term**
ASHRAE	American Society of Heating, Refrigeration, and Air Conditioning Engineers
CDC	Centers for Disease Control
CFD	Computational Fluid Dynamics
CI	Confidence Interval
DES	Detached Eddy Simulation
GRE	Glycopeptide Resistant Enterococcal
HCAI	Healthcare Acquired Infection
HVAC	Heating, Ventilation and Air-Conditioning
LES	Large Eddy Simulation
MRSA	Meticillin Resistant Staphylococcus Aureus
MSSA	Meticillin Sensitive Staphylococcus Aureus
NHS	National Health Service
NS	Navier Stokes
SARS	Severe Acute Respiratory Syndrome
SAS	Scale Adaptive Simulation
SSI	Surgical Site Infection
SST	Shear Stress Transport
TB	Tuberculosis
WHO	World Health Organization

Chapter 1

Introduction

Contents

Airborne infection is well recognised as an important disease transmission route, however the role of human movement in dispersing airborne microorganisms is not well understood. This thesis considers the transport of airborne pathogens due to human walking in the context of a hospital corridor, using a variety of modelling techniques. This first chapter outlines the importance of the subject area, the key gaps in knowledge, sets out the aims and objectives of the study, and describes the structure of the work that follows.

1.1 Overview

Healthcare associated infections (HCAIs) cost lives, and so understanding their transmission and how they can be controlled is of great importance. Estimates suggest that there are more than 100,000 HCAIs contracted in NHS hospitals per year, leading to approximately 5,000 deaths and acting as a potential contributor in a further 15,000 (National Audit Office, 2000). As if this mortality rate was not reason enough to motivate a desire to reduce HCAI cases, the projected cost of these infections in the UK is in the region of £1 billion, annually (National Audit Office, 2000). Reducing the number of HCAI cases, and consequently protecting the well-being of the population and the economy, is obviously a worthwhile cause.

To achieve this reduction it is necessary to first understand the underlying causes behind the transmission of these infections, including the manner in which the microorganisms causing the infection are being spread. The majority of HCAIs are thought to be disseminated via contact transmission (Beggs, 2003), but, as outlined in Section 1.2, the dispersion of pathogens through the air also plays a key role. In these cases, research has shown that the design of the environment, and ventilation, is a key factor in transmission and control (Li et al., 2007).

Due to the risks involved, working with real microorganisms, and the challenges of conducting experiments in working healthcare environments, understanding of disease transmission mechanisms is often derived from models, both numerical (Edge et al., 2005; Brohus et al., 2006; Choi and Edwards, 2008, 2012) and experimental (Tang et al., 2005; Poussou, 2008; Yan et al., 2009; Tang et al., 2013). However, much of the current research into airborne disease transmission in healthcare environments focusses on clinical and patient rooms such as wards, operating theatres and isolation rooms (Tang et al., 2005; Noakes and Sleigh, 2009; Richmond-Bryant, 2009; Zoon et al., 2011; Gilkeson et al., 2013). As yet, very little attention has been paid to the corridors that connect the more occupied spaces of most buildings, including hospitals. Since the corridor space is used for transporting both the healthy and sick alike, the dearth of literature focussing on this area is surprising. In an effort to rectify this, it is the aim of the current research to quantify the contribution of human movement on the transport of a contaminant in a hospital corridor using a combination of numerical, experimental and theoretical modelling approaches.

1.2 Healthcare Associated Infections

The interest in reducing the number of HCAIs may seem relatively recent, but the application of good hygiene practices can be traced back as far as 500 BC in India, Egypt, Palestine and Greece (Selwyn, 1991). However, over the centuries these standards declined and as recently as the 19th century, hospital standards were considered to be inferior to those almost 2,500 years ago (Selwyn, 1991). It was not until the latter half of the 19th century that pioneers Florence Nightingale and John Simpson urged reform in hospital hygiene practices (Wilson, 2006), forming the basis of cleaner and safer hospitals which we are still building upon today.

Moving forward a little over 100 years, 1998 saw the UK's Department of Health commission research into hygiene best practice for reducing the number of HCAIs in NHS hospitals. The original findings of the research resulted in the *EPIC Guidelines for Preventing Healthcare Associated Infections* (Department of Health, 2001). These guidelines have since been revised (Department of Health, 2014), and include recommended hygiene practices for aspects such as hospital cleanliness, hand-washing and catheter maintenance.

Over the same 100 year period it was also acknowledged that buildings play a role in the spread of infection. Florence Nightingale (1863) was one of the first to recognise this and was one of the early pioneers in hospital ward design. Later in the 20th century this was built upon by research from Whyte et al. (1983) and Lidwell et al. (1983) who linked operating theatre ventilation to infection risk. Research of this kind, linking building ventilation with infection risk, prompted the publication of documents such as HTM 03-01, issued by Department of Health (2007) (there are others), which set out guidelines to minimise this risk.

In order to determine whether these guidelines and good hygiene practices were performing as intended, mandatory surveillance of cases of Staphylococcus aureus, including the meticillin resistant strain MRSA, was introduced in April 2001 in all National Health Service (NHS) hospitals. This surveillance scheme has since been expanded to include glycopeptide-resistant enterococcal (GRE) bacteraemia, Clostridium difficile (C. diff.) associated disease, surgical site infections (SSIs), meticillin-sensitive Staphylococcus aureus (MSSA) and Escherichia coli (E. Coli) (Health Protection Agency, 2008). Through

regular reports, annual at best, figures that show the number of these HCAIs contracted in NHS hospitals are released publicly (see Table 1.1).

	No. of cases			
	MRSA	MSSA	C. diff.	E. Coli
2011/2012	1,116	8,767	18,022	24,071*
2012/2013	924	8,812	14,694	32,309
2013/2014	862	9,290	13,361	34,275

Table 1.1: Figures from Public Health England (2014a) showing number of cases of HCAIs in NHS hospitals over the past 3 years. * Figures obtained from July 2011 to March 2012. Extrapolating this value leads to a yearly estimate of 32,095 cases.

In the latest version of the report (Public Health England, 2014a), although the number of reported cases of MRSA and C. Diff was in decline, the number of reported cases of E. Coli and MSSA had risen. In order to further increase these rates of decline, more action needs to be taken; there were still 14,255 deaths attributed to MRSA between 2008-2012 (Office for National Statistics, 2013). A naive view might be that even one HCAI is too many, however it needs to be stated that not all HCAIs are preventable (Health Protection Agency, 2011) and so the aim of vastly reducing, rather than eliminating, HCAIs is a more realistic goal. It should also be noted that communicable disease transmission remains a concern in some areas of a hospital. Diseases such as Tuberculosis (TB), influenza, chickenpox and measles have all been associated with hospital outbreaks, as discussed in section 1.3.

1.2.1 HCAI Modes of Transmission

Infections may be transmitted from a host (the infected) to a recipient (the susceptible) in a number of ways (Centers for Disease Control, 2007):

Direct contact

Physical contact between a susceptible and infected person. The most likely direct route is via contact with healthcare workers or visitors. For healthcare workers there is usually an obvious need to make contact with the patient to give care through any number of procedures, whereas a visitor could pass an infection through a kiss, hug or handshake. Direct transmission is generally considered to be the most common route of HCAIs (Beggs et al., 2006).

Indirect contact

A third party object, such as a door knob, kitchen work surface, light switch, piece of machinery, etc., is used as a depository that the susceptible makes contact with after the infected has already done so. In a hospital environment this route is a major concern with medical equipment and instruments. The period of time for which a given pathogen remains infectious may vary, but human norovirus has been found to capable of surviving on a surface up to seven days after deposition (Weber et al., 2010).

Droplet

Small droplets, often considered to be those with diameters $> 5\,\mu$m, such as those produced in a cough, sneeze, enunciation of certain consonants or medical procedure. These can contain a significant amount of infectious material that a susceptible person can come into contact with. It is usually understood that droplets will settle out to the ground or deposit on surfaces as they are too large to succumb to evaporation before they land (Xie et al., 2007). As such, droplet transmission is often considered a form of contact transmission. However, the idea that a droplet possessing a diameter greater than $5\,\mu$m is guaranteed to settle to the ground, and vice versa, is somewhat misleading, as is discussed in section 2.1.1.

Airborne

Small particles, with diameters $< 5\,\mu$m, containing infectious droplet nuclei (the remains of an evaporated droplet) that remain in the air for a significant period of time are inhaled. This creates a direct transmission route where a susceptible person develops a disease through this inhalation. Whereas the larger droplets operate under ballistic conditions, smaller droplets can evaporate in a very short time-scale, $\sim O(10^{-2})$ s, reducing to the nucleus of the droplets that can still contain infectious microorganisms. These much smaller particles are capable of being transported on air currents over very large distances $\sim O(10^{2})$ m (Bourouiba et al., 2014), meaning they can be inhaled at a significant distance from the source. The same caveat as outlined for the previous description on droplets applies here; particles with diameters smaller than $5\,\mu$m are still able to settle out of the air given a long enough period of time, just as those larger are able to stay suspended.

Vectorborne

Organisms that are capable of carrying and transmitting diseases, such as mosquitoes, ticks, flies and rats. Although most of western civilisation may not be able to identify with the presence of these organisms in and around a healthcare environment, in developing nations, organisms carrying deadly infections such as malaria, yellow fever and dengue, are not uncommon. Vectorborne diseases accounts for 17 % of all infectious diseases, leading to over 1 million deaths per year. Over 2.5 billion people are currently considered 'at risk' of contracting dengue alone (World Health Organization, 2014).

Food/Water-borne

Ingestion of food or water that is already infected with harmful microorganisms. Some of the infections more commonly associated foodborne disease include Salmonella, E. Coli and Campylobacter. The Centers for Disease Control (2014) estimates that as many as 48 million Americans contract illnesses via the foodborne route per year, leading to approximately 3,000 deaths. Contaminated drinking water poses an even greater risk to human health. Worldwide, it is estimated that some 1.8 billion people use a water-source that is contaminated with faecal matter (Bain et al., 2014) and that 502,000 diarrhoea deaths were linked to contaminated drinking water in 2012 (Prüss-Ustün et al., 2014).

Bloodborne

Introducing harmful organisms through the blood or other bodily fluids. Bloodborne diseases include strains of hepatitis, the human immunodeficiency virus (HIV), acquired immune deficiency syndrome (AIDS) and a multitude of sexually-transmitted infections/diseases (STI/STDs). These infections can be passed from person to person through a number of mechanisms, including: needlesticks, blood transfusions, bites, sex, or contact between an infected fluid and a mucous membrane (Centers for Disease Control, 1988).

The focus of this work is on the airborne transmission route, which is estimated to account for as much as 20% of HCAIs (Brachman, 1970). While concern over airborne HCAIs has been around for 40 years, a more recent event sparked a renewed interest in airborne transmission. In 2003-2004, the deaths of 8,096 people, across at least 29 countries, were attributed to an outbreak of a new disease: severe acute respiratory syndrome (SARS)

(World Health Organisation, 2015). Although difficult to quantify, it has been estimated that the outbreak of this disease cost the global economy as much as US$ 40-54 billion (National Research Council, 2004). Following the outbreak, much research was conducted into the mechanisms responsible for the ease with which the disease spread (Riley et al., 2003; Lipsitch et al., 2003; Gopalakrishna et al., 2004; Qian et al., 2009). Studies were able to link the ventilation of buildings with the spread of SARS by showing that the patterns of infection were related to airflows in hospital wards (Wong et al., 2004; Li et al., 2005; Yu et al., 2005) and high-rise apartments (Li et al., 2004). Research into understanding underlying principles, mechanisms and consequences of airborne disease transmission has increased ever since.

Although the case for airborne transmission is not definitive for many pathogens, there is some evidence that suggests that it may have played a role. Research has showed that a health worker contracted chickenpox from a patient despite having never made contact with them nor set foot in their room (Tang et al., 2005), and that a measles outbreak in a paediatric practice occurred with only one secondary case making contact with the initial host (Bloch et al., 1985). Further, authors of this latter study performed airflow pattern studies, confirming that an aerosol released from the host patient's location was able to be distributed around the building through ventilation alone.

1.3 Airborne Transmission and Control

In addition to SARS, airborne transmission is recognised as a probable infection mechanism for a number of respiratory infections such as chickenpox, measles, influenza and tuberculosis (Gustafson et al., 1982; Remington et al., 1985; CDC, 2005; Blachere et al., 2009). There is also increasing evidence that some HCAIs can be transmitted via an airborne route (Kowalski and Bahnfleth, 1998; Eames et al., 2009). With hospitals bringing together patients with infectious diseases and those who are most vulnerable to infection, it is not surprising that there is considerable interest in strategies to prevent transmission, both in research and in engineering guidance.

1.3.1 Ventilation in Healthcare Buildings

Transportation of pathogens via the airborne route is heavily influenced by the dynamics of the airflow in which the pathogens are carried. Airflows are affected by many

factors making their assessment difficult and challenging, especially as a complete list of influencing factors may not always be known or quantifiable for any given airflow. In healthcare buildings, the heating, ventilation and air-conditioning (HVAC) system contributes to the airflow within internal spaces. The HVAC system as a whole often incorporates both mechanical ventilation, such as air-conditioning units and fans, and, in the UK, natural ventilation, such as open windows and doors.

The role of ventilation in buildings is to remove the stale and polluted air within the building space and replace it with 'fresher' outdoor air. This is of the utmost importance for healthcare buildings as ventilation is used as the primary tool for diluting and removing pollutants, including airborne pathogens, as well as helping to maintain thermal comfort for the patients inside (World Health Organisation, 2009). The overall ventilation of a space is dependent upon the pressure and temperature differences in the air. These differences lead to movements within the air space, which if considered over a particular volume give rise to the value of a flow rate.

Ventilation guidelines published by the UK (Department of Health, 2007) and USA (ASHRAE, 2013) provide recommended values for the number of air changes per hour (ACH) for a given space. It is then up to the management within a healthcare facility to design and maintain the HVAC system to achieve these ACH values. The UK Department of Health (2007) also proposes validation methods that, if carried out correctly, can determine whether certain healthcare spaces are ventilated within the recommended guidelines.

This process involves quantifying and estimating flow rates within the space concerned and of the HVAC system supporting it. However, this is not straightforward as the ambient pressure and temperature can vary considerably, giving rise to complex flow features within the space, such as recirculation regions, within which air is 'trapped' and not so easily removed. Even if the maximum and minimum pressures and temperatures are taken into account and a space is ventilated in accordance with the relevant guidelines, a key factor missing when considering the airflow patterns within the space is the effect of transient movements. Any airflow patterns will be affected by the presence of people in the space and by their subsequent motion.

The degree to which these movements will contribute to the disturbance and mixing of the

airspace clearly depends on the type of motion considered. If we consider a room in a ward as an example, the upper-body motion of a bedridden patient is not going to impact on overall air movement as much as one or more nurses making the bed. Similarly, a person walking along a corridor will not generate as much air movement as a group of people pushing a bed along the same corridor. These examples serve to demonstrate the range of motions which might occur at any one time and highlight the challenge of capturing all of these movements within a single model.

1.3.2 Modelling Airborne Pathogen Transmission

When conducting research into airborne disease transmission, modelling methods are often employed to avoid the obvious risks of working with real pathogens and the complexities of working with live cultures. Models can be broadly divided into two categories: transient models that take time dependence into account, and those that don't, thus obtaining information on time-averaged (steady state) data.

A large proportion of past studies, particularly those using numerical computational fluid dynamics (CFD) models, have been conducted under steady state conditions (Chow and Yang, 2005; Chow et al., 2006; Beggs et al., 2008; Loomans et al., 2008). This kind of modelling can give an understanding of ventilation design and average performance, and by using a scalar species or particle tracer can be used to explore dispersion of infectious airborne particles. However, it does not take into account the potential for transient effects or movements of any kind to contribute to airborne contaminant dispersal, and as a result such models may over or underestimate infection risk.

The advancements in CFD techniques, paired with ever increasing computing power, has meant that interest in indoor air flow research is now moving from steady-state studies to transient studies. The current research continues this trend by looking at how human movements can affect contaminant transport and, in particular, how these movements may affect airborne disease transmission in a hospital corridor.

Numerical modelling is not the only modelling approach that has seen technological advances start to push the balance in favour of transient studies. Studies using physical models have reaped the benefits of digital photography and increased data storage over the past 10 years. The method of quantifying the dye concentration used in this study is

based on the original work of Cendedese and Dalziel (1998), who used images obtained from a video camera recording on tape at a resolution of 512×512 pixels. Although the techniques applied here still require rigorous attention to detail through calibration (explained in Chapter 3) the use of a digital camera and memory card with gigabytes of storage space together with automated image analysis routines make this a more feasible process compared to the original method.

1.4 Contaminant Transport in Human Wakes

From a fluid mechanics perspective, the human form can be considered as a bluff body. Although limb movement complicates things a little, a walking human is essentially a non-aerodynamic, flat fronted shape passing through a fluid. This means that like all other bluff bodies, once moving beyond a certain speed an unsteady wake is produced. This is shown by Settles (2006) in Figure 1.1. Although the wake produced will depend on the shape of the body, it is characterised by a low pressure region 'behind' the body (where the body is assumed to be travelling 'forward'), separated flow and, if moving fast enough, vortex shedding (Poussou and Plesniak, 2012). The shed vortices carry large (relative to the ambient) quantities of vorticity, causing spiralling motions within the wake, entraining the surrounding fluid and enhancing mixing (Cohen and Director, 1975). Therefore, should a walking person pass through a contaminated region of air, their ensuing wake will mix

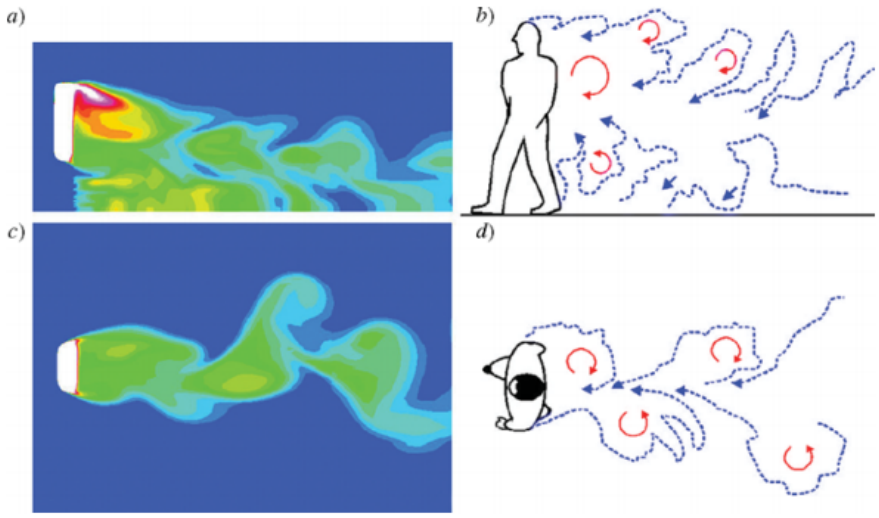

Figure 1.1: Images (b) and (d) show qualitative sketches of wake motions found during full-scale experiments, using smoke as a visualising agent, while images (a) and (c) show the numerical counterparts. The wake entrainment processes are clearly visible in both approaches (Settles, 2006).

this air adding to its dispersion.

1.4.1 Contaminant Transport Modelling

Capturing properties relating to the human wake is difficult. Visualisation of the wake at full-scale with a human subject appears only to have been done by Craven (2014). Two techniques were used to produce the images, Schlieren imaging, and a combination of lasers and smoke. The former can be complicated and expensive to set up, while the latter necessitates the use of lasers which can pose a safety challenge when working with human subjects. Because of this, many studies employ modelling methods instead, usually taking one of three forms:

Full-scale experimental

Full-scale studies typically employ human mannequins and a tracer gas such as nitrous oxide (N_2O) (Mattsson et al., 1997; Bjorn and Nielsen, 2002; Kalliomäki et al., 2014). Doing so lessens the risk of using human subjects while still capturing the human form, albeit at the cost of losing the ability for a walking motion (see Figure 1.2a); experiments are also more consistent and repeatable. Sulfur hexafluoride (SF_6) has also been used as a tracer gas when humans have been used (Rydock and Eian, 2004).

Full-scale numerical

Studies involving CFD modelling vary in the degree to which they aim to model a human, from the simple bluff body (Mazumdar et al., 2011), to a simple body comprised of limbs and torso (Edge et al., 2005), through to the almost lifelike models employed by Choi and Edwards (2008).

Small-scale water-bath models

Water-bath models usually draw on the analogy between humans and simple bluff bodies, so circular and square cylinders are often used in place of an anatomically correct scaled model. Previous studies have used moving cylinders to investigate contaminant transport in airline cabins (Poussou et al., 2010; Mazumdar et al., 2011). However, Tang et al. (2013) managed to obtain a toy/figurine that fit the scaling of their geometry, allowing a close representation of a human shape at the

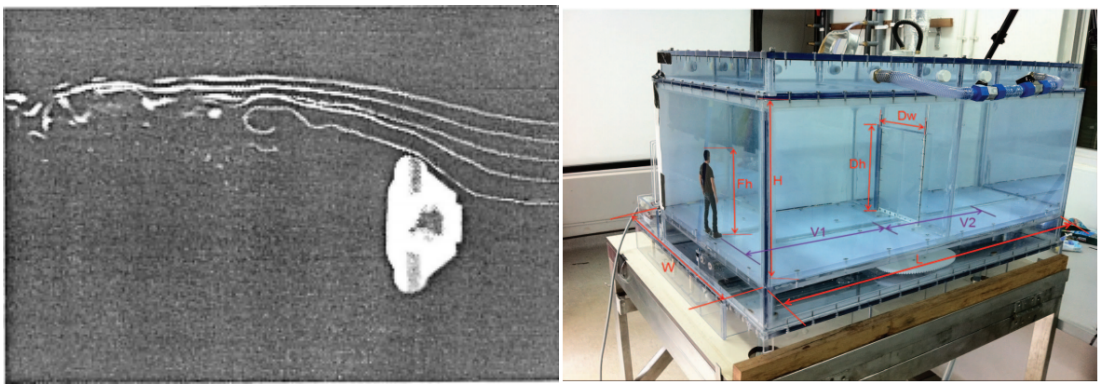

(a) (b)

Figure 1.2: Examples of modelling approaches used to investigate contaminant transport in human wakes: (a) full-sized mannequin (Mattsson et al., 1997); (b) scaled water-bath (Tang et al., 2013).

model-scale (see Figure 1.2b). Their study considered flows in an isolation room and is discussed further in Section 2.3.1.

1.5 Aims and Objectives

The main aim of this research is to quantify the effect of a traversing body on the dispersion of an airborne contaminant in an indoor environment. The study is carried out in the context of human motion in a corridor and the findings from the research are used to predict the impact on infection risk that moving bodies would have in a typical hospital corridor environment.

The research detailed in this thesis applies experimental, theoretical and numerical techniques to address this aim through the following objectives:

1) Identify and understand the existing knowledge on processes involved in contaminant transportation in indoor air flows and mechanisms for airborne infection, with a particular focus on :

i Airborne pathogens, their transmission, and current forms of mitigation,

ii The potential for contaminant transport in human wakes,

iii Ventilation guidelines and strategies for various healthcare environments,

iv Infection risk models,

v Oscillatory flows around circular cylinders.

2) Through water-bath experiments, quantify how a neutrally buoyant contaminant is transported by a cylinder regularly translating back and forth. The specific goals here are to:

i Develop and verify suitable techniques to allow quantification of dye concentrations captured in photographic images.

ii Through the use of these methods, calculate the quantity of dye transported over a given time frame, for different translation properties (e.g. amplitude, frequency).

iii Establish underlying analytical relationships capable of describing the behaviour found in the experiments, that may be used to predict contaminant transport for other fluids, length-scales and time-scales.

3) Develop transient, computational models whose outputs can be compared with experimental and analytical work, to establish whether CFD simulation is a viable approach for evaluating contaminant transport, due to human movement. The sub objectives here are to:

i Establish suitable methods to conduct moving body simulations that are comparable to experimental studies.

ii Determine the most suitable CFD model parameters for contaminant transport predictions, by investigating parameters such as the transport variables in a turbulence model.

4) Use numerical and analytical models to explore potential for infection in hospital corridors at full scale. The methods to do this will involve:

i Using the previously constructed CFD and theoretical models to make informed predictions on the rate of contaminant transport possible at the full-scale.

ii Applying risk models, similar to those found in the literature, to quantify the likelihood of infection, using the findings from the models.

1.6 Structure of this Thesis

Chapter 2: Airborne Pathogens in Healthcare Buildings

In this chapter, a literature review detailing current approaches aimed at minimising the spread of airborne pathogens in healthcare buildings is presented, followed by a review of the ventilation strategies put in place to do this in healthcare buildings. It is highlighted that these current ventilation strategies are well described for critical care environments, such as operating theatres and isolation rooms, but the guidance is not as explicit for general purpose corridors. This is identified as a key driving force behind the necessity of this research.

Chapter 3: Water-Bath Modelling

This chapter details the water-bath modelling approach used in the study. Background and theory relating to the water-bath modelling approach are outlined first, including a review of previous studies. Specifics relating to the water-bath modelling carried out in this study are then presented. This includes: physical dimensions of the model; the image analysis method used; the types of quantifiable data that are obtained; and the theoretical models derived from data. Predictions made from the theoretical models are presented in Chapter 7.

Chapter 4: Computational Fluid Dynamics Modelling Methods

This chapter reviews the application of CFD modelling to infection risk flows and documents the relevant theory behind the numerical work in this study. Specifics relating to the CFD models actually created are presented in Chapters 5 and 6. The governing equations, the methods of solving them, and parameters relevant to the studies are described. The chapter concludes with details on the solution process and the errors associated it.

Chapter 5: 2D CFD Modelling of Water-Bath Experiments

This chapter sets out the details of the CFD modelling in two-dimensions. This covers approaches applied to each simulation, including meshing and boundary conditions. Simulations that employ a static geometry and cylinder are presented first, followed by results from simulations using a moving body.

Chapter 6: 3D CFD Modelling

In this chapter, the two-dimensional models presented previously are adapted to develop three-dimensional models. The chapter progresses in a similar manner to Chapter 5; the geometry and mesh are presented first, then simulations using a stationary model are discussed, before finally moving onto the results of a model that contain a translating cylinder.

Chapter 7: Modelling Infection Risk

This chapter demonstrates how the theoretical and numerical models developed in Chapters 3 and 6 may be applied at full-scale. Infection risk calculations are put forward based on theoretical model predictions for a number of scenarios involving an airborne contaminant in a hospital corridor. Various arrangements are considered that investigate infection risk based on changing: the number of occupants, occupant breathing properties, ventilation rates, and initial contaminant location.

Chapter 8: Conclusions and Further Work

The thesis concludes by bringing together the conclusions from each aspect of the study to draw overall findings. These are related to the original research aims and used to consider the implications of the research and highlight where further study would be beneficial.

Chapter 2

Airborne Pathogens in Healthcare Buildings

Contents

This chapter presents some of the most prominent studies related to airborne particles and the pathogens that may be carried on or within them. The chapter first reviews studies which examine airborne particles and pathogens that may be carried on them, and considers some of the ways these particles may be created. These potentially pathogen-laden particles are able to be transported through the air and so the importance of and possible means of their mitigation is discussed. Finally, the modelling methods used to aid in reducing the infection risk due to the inhalation of airborne pathogens are reviewed.

2.1 Airborne Particles (Aerosols)

The air we breathe plays host to a large number of particles, both man made and naturally occurring. While we may not always be able to see them, there are many different types and sources of these particles coming in a range of different sizes. Fine, sub-micron particles may take on transport properties like those of a passive tracer, due to their small masses having an insignificant impact on the surrounding air (Gao and Niu, 2007). The main threat to human health that these tiny particles pose is through inhalation, as they are able to follow the trajectory of the air into the respiratory system. Once inhaled, sub-micron particles are capable of reaching the alveoli within the lungs, whereas those of a larger diameter typically settle out much sooner in the oropharynx and tracheobronchial zone (Newman, 1985). Typical deposition patterns can be seen in Figure 2.1a, the locations of which are shown in Figure 2.1b.

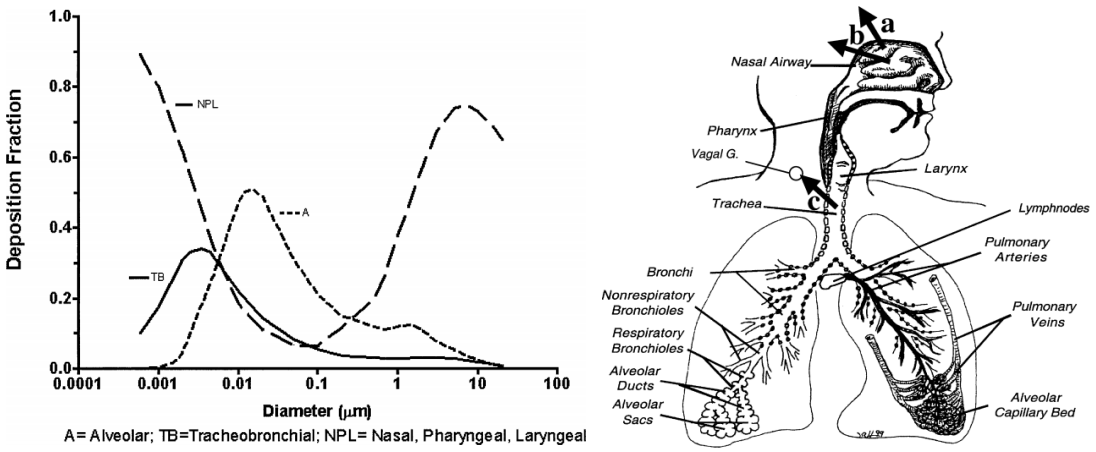

(a) (b)

Figure 2.1: (a) Particle deposition in the respiratory system by particle diameter, (Oberdörster et al., 2004). (b) Human respiratory system, (Oberdörster et al., 2004).

The alveoli are responsible for transferring oxygen from the inhaled air to the blood, via a thin membrane that exists between the alveoli and blood vessels. Unfortunately, this membrane is also the route which pathogens can take in to the blood stream, where they are able to travel around the body and spread infection (Lambrecht, 2006). The body's reaction to the inhalation of an airborne particle depends on what the particle is. The main defence mechanism to any foreign matter within the lungs is through the production of alveolar macrophages, a type of white blood cell that aims to encapsulate and eliminate any foreign material, thus rendering any possible threat to the body harmless (Gordon and Read, 2002; Rubins, 2003). This approach is carried out for the majority of encounters

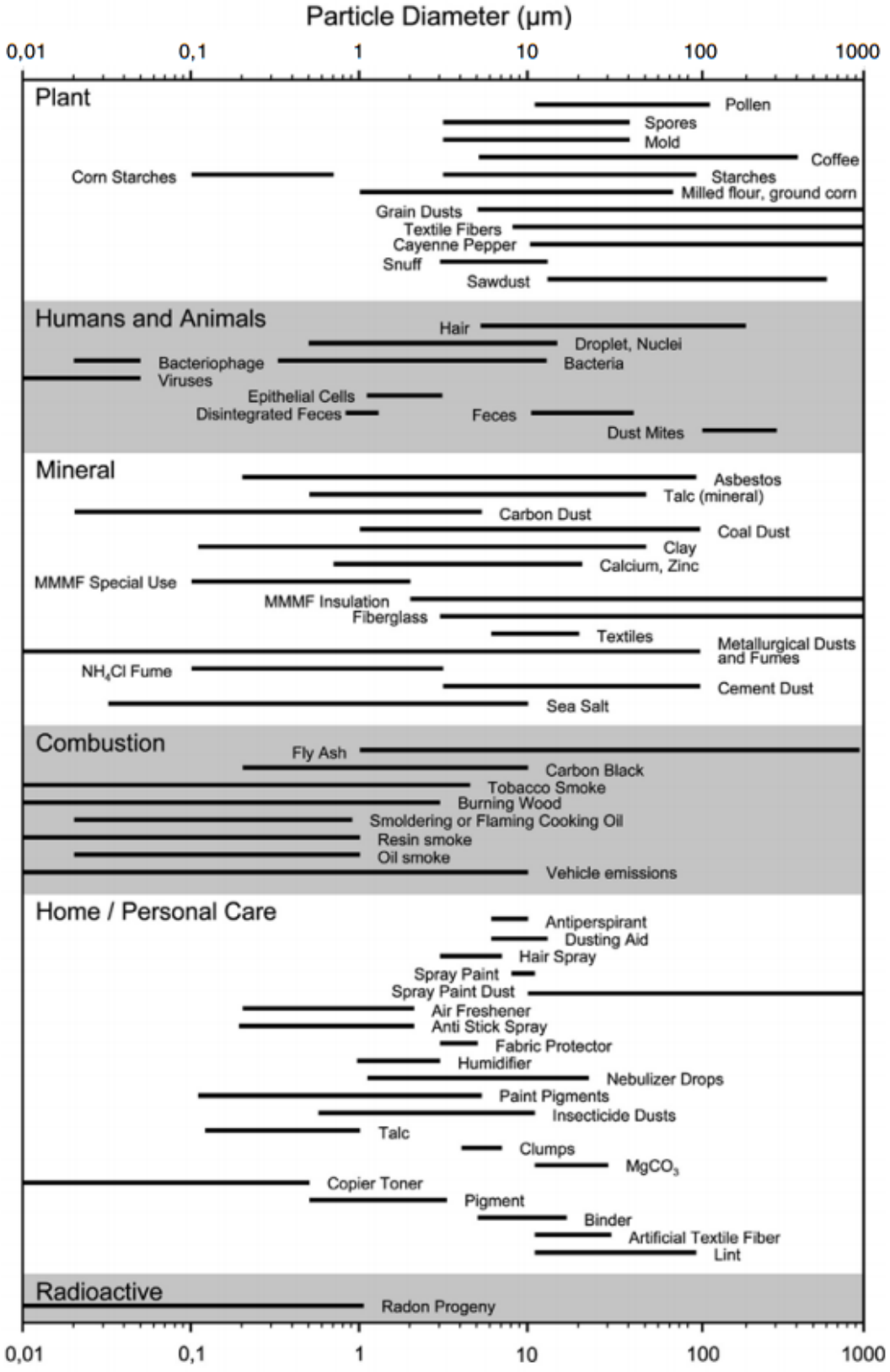

Figure 2.2: Particle size chart of common airborne particles (Morawska and Salthammer, 2003).

between the macrophages and airborne particles and goes unnoticed (Sibille and Reynolds, 1990). However, the response to a more serious threat such as *Mycobacterium tuberculosis* for example, the bacteria that causes tuberculosis (TB), is the formation of lesions or granulomas on the walls of the lungs that contain a combination of the alveolar macrophages, the infection and a host of other cells (Gammack et al., 2004). It is the particles that carry other biological entities (bioaerosols) capable of endangering human health that make the study of airborne particles important. Of particular interest here are the particles capable of carrying viruses, bacteriophages and bacteria. Microbes of such a small size, $d \sim O(1)$ μm, are able to be transported on some of the particles and fungi listed in Figure 2.2, such as dust, hair, spores, or within liquid aerosols.

2.1.1 Bioaerosols

Microbial life has been around for millions of years. For most of this time, sunlight exposure and temperature extremes kept their airborne survival rates in check and most disease transmission is likely to have taken place via the direct route (Kowalski and Bahnfleth, 1998). Indeed, sunlight within the UV-B range is still considered to be nature's strongest defence against microbes (Deller et al., 2006). Once man started seeking shelter and living indoors, the more habitable temperatures for man unfortunately suited the microbe population too and airborne survivability increased (Kowalski and Bahnfleth, 1998).

The vehicle upon which pathogens travel is clearly important in understanding airborne pathogen transmission. Figure 2.2 not only shows the sizes of typical microorganisms associated with airborne transmission, but also provides a (non-exhaustive) list of possible vehicles. One of the more common vehicles for the dissemination of these pathogens is via bioaerosols created from an infected host during coughing, sneezing or talking. Bioaerosols formed in this way are termed 'respiratory droplets'.

Respiratory droplets are formed in the respiratory tract by the interaction of exhaled air from the lungs with liquid on the tract surface walls. The initial size of the droplet appears to be determined by an atomization process, dependent upon the pressure and velocity of the exhaled air, although the details of the process are not well understood (Morawska, 2006). The size and spread of the kinds of droplets created during a cough or sneeze was first photographed by Jennison (1942). The size distribution of the droplets typically released during a respiratory event was first studied by Duguid (1946), although

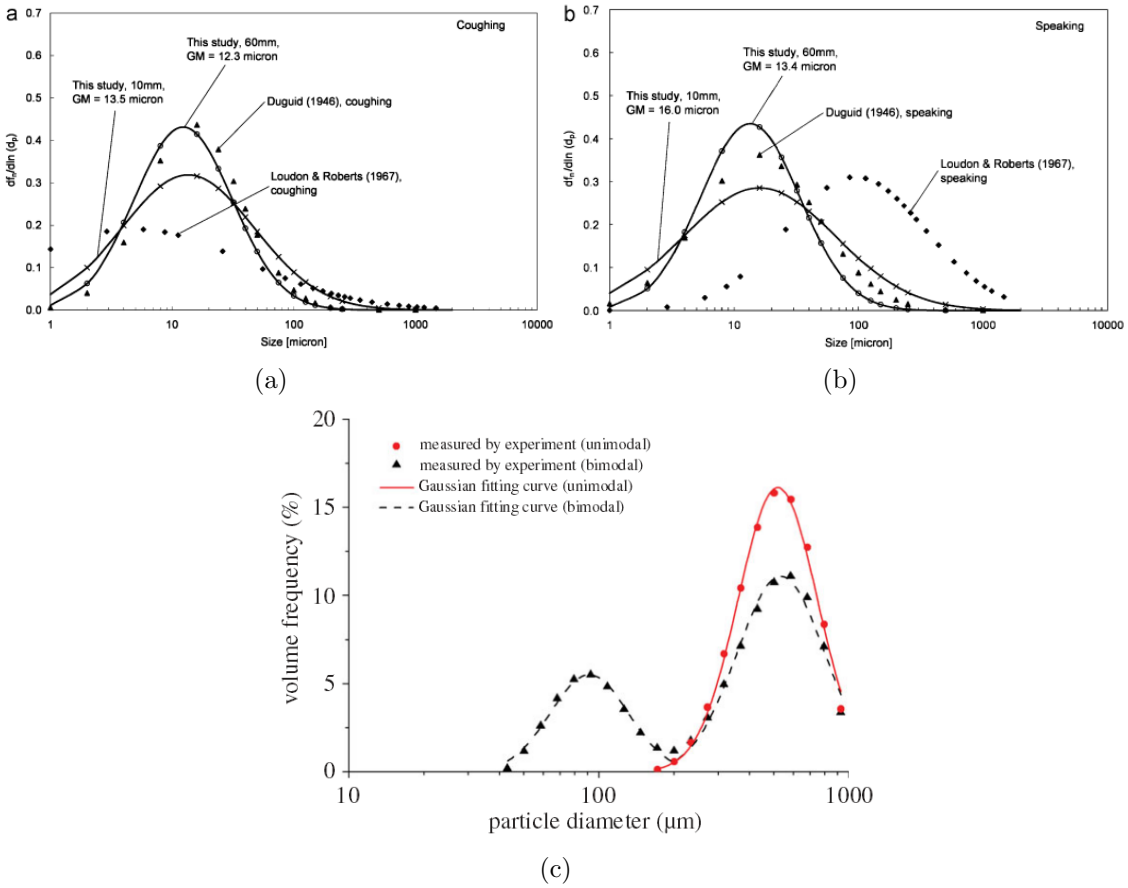

Figure 2.3: Size distribution of droplets emitted during tests on (a) coughing, (b) speaking, (Chao et al., 2009), and (c) sneezing, (Han et al., 2013).

this only shows those of a size visible to the eye. Chao et al. (2009) undertook a study on the size distribution of expelled droplets during coughing and talking. Their findings showing that droplets seem to be normally distributed around a peak droplet frequency for droplets of diameter $\sim O(10)\mu$m (see Figures 2.3a,b). Han et al. (2013) carried out a similar study investigating the size distribution of droplets emitted during sneezing, observing both unimodal and bimodal distributions, though both appearing to show a peak droplet frequency for droplets $\approx 500\mu$m (see Figure 2.3c). Those studies listed here are by no means an exhaustive list of studies relating to droplet creation, exhalation and deposition, the full range of which is beyond the scope of this study.

Droplet transmission is generally stated as being applicable for particles of diameter $> 5\ \mu$m; anything smaller is usually considered to be transmitted via the airborne route. However, this sizing definition has been disputed and alternative size ranges have been suggested (Tang et al., 2006). It has even been shown that it is possible for droplets of diameters up to 50 μm to remain in the air, where they may be drawn into ventilation

systems or inhaled (Bourouiba et al., 2014), although such particles may not reach deeper parts of the lungs. The distinction between droplet and airborne transmission is made even less clear by the varying distance to which droplet transmission is considered capable of infecting. The often quoted infective range associated with droplets of 3 feet (≈ 0.91 m) is subject to variation depending on the forces associated with the expelling of the droplet and environmental factors. The CDC say the 3-foot distance associated with droplet transmission is merely an example of a *"short distance from a patient"* and that droplet transmission may reach as far as 6-10 feet from the source (Centers for Disease Control, 2007). This is evidenced by Xie et al. (2007) who found that droplets of diameter 60-100 μm were able to be transported more than 6 m away from their source when formed and expelled during a sneeze.

Respiratory droplets are made largely of water but may also include assorted types of cells, electrolytes and pathogens, depending on where the droplet content originates (World Health Organisation, 2009). These droplets are subject to the chemical processes associated with all states of matter, but evaporation is of particular significance to their size and subsequent transport. For example, if we consider droplets released from a height of 2 m, smaller droplets ($O(10^{-6})$ m and smaller) will lose enough mass through evaporation such that they may be carried by airflows, whereas larger droplets ($O(10^{-5})$ m and larger) will reach the ground before evaporation takes effect (see Figure 2.4). The importance of evaporation on respiratory droplets was first brought to our attention by Wells (1934), who coined the term "*droplet nuclei*" for the microorganisms that form an infectious respiratory droplet once most of the water had evaporated. Wells was able to correctly identify that other authors' studies using agar plates to capture droplets only a few feet from the source were not telling the whole story, going on to state that a lack of evidence of the droplet nuclei does not "*prove their absence*" (Wells, 1934).

The size of a droplet nucleus is dependent on many factors, such as air humidity, air density and velocity of the exhaled droplet, but is generally assumed to have a diameter < 5 μm (Centers for Disease Control, 2007). Stokes' law states that for a small spherical object settling in a viscous fluid, at sufficiently small enough Reynolds number (see Section 2.3.1.1):

$$F_d = 3\pi\mu dU \tag{2.1}$$

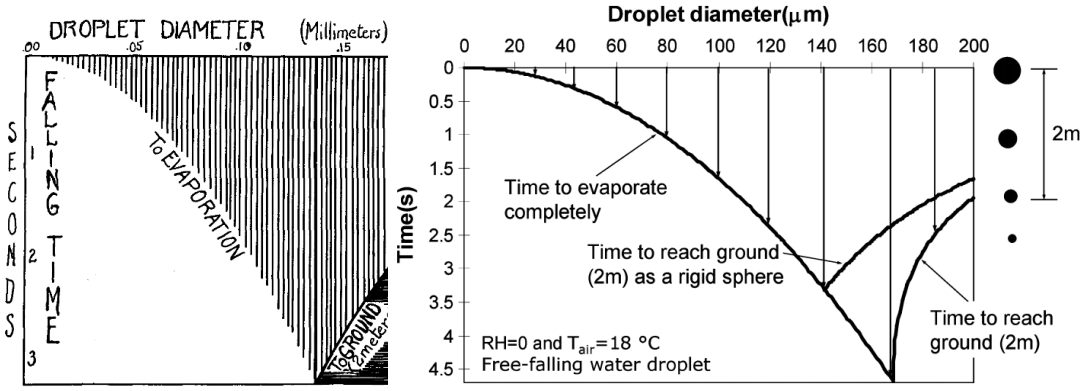

(a) (b)

Figure 2.4: Evaporation falling curves, relating droplet diameter, falling time and distance travelled. (a) Original by Wells (1934), and (b) recreated by Xie et al. (2007).

where F_d is the drag force, μ the fluid viscosity, d the diameter of the sphere and U the flow velocity (Bachelor, 1967). By balancing opposing forces when the particle is at terminal velocity, this yields a settling velocity of:

$$U_s = \frac{(\rho_p - \rho_f)gd^2}{18\mu} \tag{2.2}$$

A quick application of Stokes' law for a spherical water particle of diameter 1 μm falling under gravity in still air yields a settling velocity $U_s = 3.5 \times 10^{-5}$ m s^{-1} (Seinfeld and Pandis, 1998). The time-scale involved for settling a distance 1 m is thus 3.5×10^5 s or ≈ 4 days. Clearly the settling velocity of particles of this order magnitude is negligible over any time-scale which may be under consideration when dealing with airborne transmission. This goes to show why the airflow in which these small particles are residing is very important in determining their transport and final resting place as the influence of gravity on them is all but irrelevant.

Performing the same calculations for slightly larger particles highlights a potential flaw in the 5 μm classification of whether a bioaerosol is considered to be a droplet or airborne particle. Another application of Stokes' law shows that a particle of diameter 10 μm yields a settling velocity of $U_s = 3.06 \times 10^{-3}$ m s^{-1} (Seinfeld and Pandis, 1998), taking 3.06×10^3 s, or ≈ 51 mins, to settle a vertical distance of 1 m. However, this value is obtained through calculations that assume the air is still, though still subject to Brownian motion. It is easily conceivable that in the presence of sufficient buoyant forces that droplets of this size (and larger) may remain suspended in the air for much longer than the settling velocities indicate. The human thermal plume alone is capable of generating air velocities of up to

0.24 m s^{-1} above the body (Craven and Settles, 2006). Convection currents and airflow patterns created by building ventilation provide a further means of keeping these particles in the air for longer periods of time than a simple Stokes' law calculation may indicate.

A further complication to the transit of these particles is that the location in which they land may not be their final resting place. They are capable of being resuspended by motions that disturb the airflow such that any adhesion forces acting on the particle (van der Waals, capillary or electrostatic) are overcome by hydrodynamic effects such as lift, drag, bombardment or vibration (Qian et al., 2009). Particle and surface materials are known to have a significant impact on the size of these forces (Buttner et al., 2002). Studies have shown how particle resuspension can increase contaminant concentrations in the breathing zone from movement of clothing (Bohne and Cohen, 1985; Mcdonagh and Byrne, 2014) and walking (Luoma and Batterman, 2001; Qian and Ferro, 2008).

2.1.2 Detecting Airborne Pathogens

Sampling airborne pathogens in-situ is a difficult task. Although current methods are available to count the number of particles passing through a given space, and to detect some chemical pollutants in real time, biological analysis of their content must be done having subsequently captured air samples. Detection of pathogens is usually done by either culturing the sampled microorganisms in a laboratory or by using molecular techniques such as polymerase chain reaction (PCR) sequencing (Tang et al., 2011b). Hence, determining whether or not a captured droplet or particle contains a pathogen is only possible once removed from the air space it initially resided in, changing the environment of the droplet and potentially affecting the population and survivability of any pathogen in it. In a *very* loose comparison with the uncertainty principle of Heisenberg (1927), it is possible to monitor the population and position of airborne particles, *or* their content; currently it is not possible to know both at the same time. Impaction of the droplets with the sampling surface can have an effect on the pathogen survival (Stewart et al., 1995) and the measuring devices themselves are capable of causing a bias through the airflows they create at the inlets (Després et al., 2012). This all creates a certain level of ambiguity over whether a captured and analysed sample is a true representation of the air space under investigation. It is therefore unsurprising that classifying a pathogen as being airborne or not, and whether it is capable of infecting via the airborne route, is subject to some debate. Some favour the notion many pathogens are likely to be capable

of this form of transmission, possibly including all pathogens that are able to colonise in the respiratory tract (Tang et al., 2006; Kowalski and Bahnfleth, 1998), while others consider only a handful of pathogens to be airborne, (Centers for Disease Control, 2007) including only those which have been shown to be airborne through studies rather than conjecture. Acknowledging influenza as an airborne pathogen, which has been the subject of much study, is still controversial (Blachere et al., 2009). It has even been postulated that MRSA, which is usually associated with contact transmission, is capable of airborne transmission (Shiomori et al., 2001).

One pathogen that seems to be well accepted as being capable of being transmitted via the airborne route is tuberculosis (TB). The idea of TB being airborne stems back to the research of Wells and Lurie (1941). This was ultimately confirmed by Riley et al. (1959) who passed air from a TB ward on to caged guinea pigs. By taking care when setting up the experiments, the only logical explanation of how the guinea pigs tested positive for TB was by concluding that it was being disseminated through airborne transmission. A similar experiment was carried out by Escombe et al. (2007), which was also able to relate infections in guinea pigs back to specific patients.

In 2003, 1.3 million deaths worldwide were attributed to TB (Global Burden of Disease, 2013) and the number of cases in the UK has not declined over the past 10 years (see Figure 2.5). Although the number of cases contracted through airborne transmission is not discernible from the total, these figures highlight the prevalence and seriousness of airborne pathogens to date.

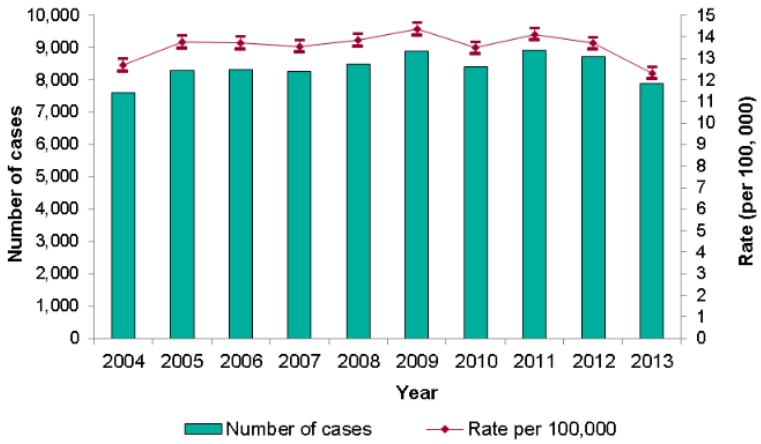

Figure 2.5: Occurrences of TB in the UK for the past 10 years. (Public Health England, 2014).

2.2 Mitigating Airborne Infection

As already mentioned, the air is rife with microbial life that we can not see. Because of this, we can never be totally certain what we are breathing in at any one moment. In the context of health-care buildings, where the chance of encountering a source of pathogens and the consequences are greater than most other indoor spaces, the risk of breathing in potentially harmful organisms is ever present. Mitigating this risk of infection via the airborne route is therefore difficult as it is not always easy to visualise the impact that a measure is having.

2.2.1 Management and Human Control

To keep employees and employers safe at work, a hierarchy exists for putting in to place health and safety control measures (NIOSH, 2015). The full five-tier hierarchy is applicable to all work environments, however a three-tier version of this hierarchy of controls exists when considering the spread of TB in a hospital (CDC, 2005) and could just as easily be applied to other diseases.:

1. Administrative controls,
2. Environmental controls,
3. Use of personal protective equipment (PPE),

It could be said that the simplest way of mitigating the infection of such pathogens is to stop them entering the human body by way of blocking the route of entry: the respiratory system. This can be achieved by wearing a mask, acting as a filter for droplets above a certain size. The wearing of masks is typically practised once the risk of airborne, or droplet, infection has been identified as likely to increase, i.e. a potential source of infection has been identified, making the act of mask wearing retroactive (Centers for Disease Control, 2007). This was most evident during the SARS outbreak of 2003-2004, where the wearing of masks in Hong Kong and surrounding East Asia was widespread once the threat of airborne infection was identified (NewScientist, 2003). However, even surgical masks were not designed to offer protection against aerosols (Health And Safety Executive, 2008) and their effectiveness against aerosolised influenza has been called into question (Department Of Health, 2014).

Current guidance recommends that healthcare workers wear a surgical face mask when assessing/caring for those with respiratory infections and located within 1 m (3 ft) of the patient (Health Protection Agency, 2012). However, when dealing with patients who have highly infectious diseases that can be disseminated by airborne transmission, such as measles, TB or SARS, the more protective N95 respirators are recommended (Coia et al., 2011). In addition to the recommendations that health care workers wear masks or respirators as part of their PPE, it has also been suggested that the spread of respiratory infection may be reduced by the fitting of masks to patients (World Health Organization, 2009; Tang et al., 2011a; Health Protection Agency, 2012). However, wearing PPE is last in the hierarchy of control measures (see CDC hierarchy above) and so other means of infection mitigation need to be considered. This typically means administrative controls, such as the recommendation of guidelines and policies (see Section 2.2.2.1), and environmental controls, such as the implementation of ventilation or ultraviolet germicidal irradiation devices (see Section 2.2.3).

2.2.2 Ventilation

It has been estimated that people in developed countries spend approximately 90 % of their time indoors (U. S. Environmental Protection Agency, 1989). The air inside a building is not as easily replenished when compared to the outdoors, nor is it subject to the defence provided by the sunlight's UV rays. Instead, the building's ventilation is used to keep the air of sufficient quality. No matter whether mitigation measures are used, the transit of an airborne pathogen is ultimately determined by the flow of the air in which it resides due to its small mass. In the case of healthcare buildings, the airflow rate is determined by the ventilation, with the flow pattern controlled by this and heat and momentum sources. By extracting contaminated air and replenishing it with clean supply air, a ventilated system aims to remove the offending pathogens (Centers for Disease Control, 2007). While the most obvious way to maximise the removal efficiency of a ventilation system is to instigate a large flow-rate, thus diluting any contaminant quickly, taking into account practicality and thermal comfort means there is some compromise.

Li et al. (2007) provide a comprehensive review of the role that ventilation plays in the built environment; their findings based upon 40 studies ranging from 1960 to 2005. In particular, the studies that were investigated looked at ventilation in schools, offices and hospitals. Ten of these studies were able to find a link between the ventilation and transmission

of the airborne infection concerned. However, while it was concluded that there was sufficient evidence to determine this link, there was insufficient evidence to recommend any guidance for ventilation rates, or ventilation systems, to minimise the spread of an airborne infection. However, the study of Menzies et al. (2000) suggest that air flow rates below 2 air changes per hour (ACH) could lead to an increased risk of TB infection.

2.2.2.1 Healthcare Building Ventilation Guidelines

Health-care building ventilation guidelines are defined differently throughout the world. In the UK, the guidelines that such buildings should follow is outlined in the document 'Health Technical Memorandum 03-01: Specialised ventilation for healthcare premises' (HTM 03-01), issued by the Department of Health (2007). In the USA, the equivalent document 'Standard 170-2013 - Ventilation of Health Care Facilities' published by the American Society for Heating, Refrigerating and Air Conditioning Engineers (ASHRAE) is used. In Germany and Switzerland, the corresponding regulations can be found in DIN 1964 part 4, issued by Deutsches Institut für Normung (German Institute for Standardisation) and SWKI 99 3, issued by Schweizerischer Verein von Gebäudetechnik Ingenieuren (the Swiss Association of Building Engineers), respectively. There are many more similar documents for other countries, however, due to the ease with which it is possible to understand and extract the necessary information, the guidelines set out in HTM 03-01 shall be used for reference and comparison in this study.

Specialist care facilities require specialist ventilation strategies due to the higher risk of contamination. Operating theatres and isolation rooms fall into this category. When in an operating theatre, a patient's immune system is at higher risk of being compromised due to the enhanced exposure to the atmosphere at the surgical site. Should an airborne pathogen be present, its entry into the body is made much easier if the skin has been broken (Centers for Disease Control, 2007). To reduce the likelihood of this occurring, operating theatres are subject to high ventilation rates and are held at positive pressure, relative to the surrounding building environment. HTM 03-01 specifies that operating theatres be held at a pressure of 25 Pa above ambient and are subject to 25 ACH.

Negative-pressure isolation rooms are typically used to house patients that have contracted a highly contagious infection, such as tuberculosis. The ventilation is used to ensure that the air is replenished through flows directed into the room rather than out, thus ensuring

any contaminant within the room cannot spread further. The contaminated air is only able to leave the room via designated exhaust vents. HTM 03-01 specifies that negative-pressure isolation rooms be held at a maximum of -5 Pa, relative to adjacent airways, and circulate a minimum of 10 ACH.

The filters used in the HVAC systems are another line of defence against any airborne threat. The filters used in isolation rooms inlets are grade 4 (G4) standard. This means that they are capable of stopping at least 90% of "*test dust*". Although no quantitative properties about the test dust are mentioned, it is stated that the dust is large enough to settle out in the air distribution system. This indicates that such filters are not likely to remove any of the finer particles still capable of transporting pathogens. Inputting filters of a coarse grade, relative to the size of any pathogen, is understandable as the most likely source of airborne particles is from the occupant of the room and not the ventilation system. However, this generalisation may not always hold, as was shown by Li et al. (2007).

Operating theatres use F7 or, in the case of ultra-clean suites, H10 filters. F7 filters are designed to filter at least 80% of "*fine staining particles*" which are claimed to be of comparable size to bacteria, while H10 filters are claimed to remove at least 85 % of sub-micron particles. Filters of this standard are necessary to reduce the likelihood of infection due to the weakened immune systems of those under procedure. There were still over 8,000 readmissions due to surgical-infections between April 2009 and March 2014 (Public Health England, 2014b). Filters of H10 standard or greater are known as high-efficiency particle air (HEPA) filters and are used sparingly due to their cost.

According to HTM 03-01, the recommended ventilation to be imposed in a general ward consists of no less than 6 ACH, at atmospheric pressure, between 18-28°C. Although not specifically stated, it is assumed henceforth that corridors come under this general ward heading when considering ventilation, as there is no explicit guidance for general use corridors. They also recommend the use of the G4 filter as found in negative-pressure isolation rooms. However, wards can also be naturally ventilated in UK hospitals (Department of Health, 2007), in which case filters are not used. The standard set out by ASHRAE (2013) does specify guidelines for corridors and recommends an even lower air flow rate of just 2 ACH.

2.2.3 Other Environmental Controls

Ultraviolet germicidal irradiation (UVGI) devices aim to mitigate the risk by passing contaminated air through light of a particular wavelength, (200-320 nm) corrupting the pathogen's DNA and inhibiting their ability to reproduce or killing them entirely (Kowalski, 2009). The devices are typically placed somewhere within the heating ventilation and air conditioning (HVAC) system or on the inner walls of a building. Although manufacturers of UVGI devices often claim a reduction in pathogen concentration greater than 99%, the actual amount is subject to many factors: UV irradiation intensity of the device, the susceptibility of the pathogen to the dose of radiation received, air velocity and air humidity, to name a few. Consequently, while UVGI devices may kill close to 100% of pathogens that pass through the radiated region, ensuring that all contaminated air within a space passes sufficiently close to the radiative lamps for eradication is difficult.

In the past, it had been suggested that air ionisation may also help reduce airborne disease transmission (Kerr et al., 2006). Preliminary findings looked promising, however the results from more recent studies relating air ionisation to an infection reduction were put in doubt as it was later found that the antibacterial mechanism was likely to the exposure to large concentrations of ozone, as opposed to the ionisation process itself (Fletcher et al., 2007).

2.3 Airborne Infection Modelling

Although it is possible to sample infectious microorganisms from the air, this poses a significant challenge (as indicated in Chapter 1) and therefore proxy methods employing tracers, scale models or numerical techniques are usually applied to evaluate the potential for airborne infection.

2.3.1 Experimental Methods

A number of past studies have carried out experimental modelling at full-scale. Modelling at full-scale is likely to result in air being used as the working fluid and so visualisation becomes an issue. Therefore, visualising at full scale often involves the use of a tracer gas. Grimsrud (1980) points out some of the ideal properties that a tracer gas should have:

- Be easily obtainable/cheap,
- Be detectable even at low concentrations,
- Not be allergenic, noxious or flammable,
- Be approximately neutrally buoyant in air,
- Not be easily adsorbed,
- Not be present in a typical air space sample.

Two gases which meet most of these criteria, and have been used in tracer gas studies, are sulfur hexafluoride (SF_6) and nitrous oxide (N_2O).

Gustafson et al. (1982) used SF_6 to perform airflow studies in a hospital ward that had experienced an outbreak of varicella (chickenpox). The airflow studies revealed that the isolation rooms adjacent to the corridor central to the outbreak were held at a positive pressure, relative to the corridor. Working off the assumption that these isolation rooms were held at negative pressure, an immunocompromised patient with varicella, the source patient, was held inside one of these positively pressured rooms which is believed to have led to the outbreak.

A combination of both SF_6 and N_2O was used by Kalliomäki et al. (2014) to determine the airflow across a doorway, for both sliding and hinged doors. Two rooms, connected by a door, were each filled with one of the tracer gases, so that the airflow could be determined in both directions. Tests were then performed opening the door, sometimes with a mannequin passing through the doorway to simulate a person walking through. Analysed gas samples revealed that the transit of a body through the doorway is significant and that the sliding door yielded a smaller transfer of gas through the doorway than the hinged door.

A release of CO_2 (via balloons) was also used by Gilkeson et al. (2013) to show how effective natural ventilation is at reducing the airborne infection risk in a hospital environment. Although CO_2 is not so ideal as a tracer gas, as it is already present in the air and exhaled by people breathing, it is an easy gas to work with and sensors are readily available and inexpensive.

2.3.1.1 Reduced Length Scale Modelling

As air is largely invisible, to the naked eye, many flow patterns that arise within it often go unnoticed. It is often much easier to study a similar flow using a liquid instead, within which it is much easier to visualise the flow. The studies of Reynolds (1883) and Stokes (1851) resulted in a relationship that characterised flow properties for flows involving similar geometries only with different fluids. Here, the term similar is taken to mean the geometries have the same shape and implies that all lengths and angles of the geometries obey the same scaling relationship. This relationship we know as the Reynolds number, Re:

$$Re = \frac{\rho U L}{\mu} \tag{2.3}$$

where ρ is the fluid density, μ the fluid viscosity, U a relevant velocity and L a characteristic length-scale. With this relation realised, it opens up the idea that information relating to the movement of air around a person can be obtained by considering flows of different fluids around geometries that bear resemblance to a human.

If performing a full-scale study is not feasible, small-scale models are often used instead. As this means the length-scales are reduced, the Re is used to ensure that small-scale models are comparable to their full-scale counterpart. This, in turn, usually means a change in fluid is necessary, which typically means using water or saline (more is discussed on this changing of fluid and length scales in Section 3.2.2). These so-called water-bath models are relatively underused for studies involving airborne infection, possibly due to the difficulty in quantifying the concentration of a liquid tracer in all but the simplest of geometries, despite the modelling techniques being around since the 1980s (Linden and Simpson, 1985).

Of those studies that have taken advantage of the water-bath modelling approach, when concerning airborne infection, the most common scenario under investigation is the transport of a contaminant in an aircraft. Poussou (2008), Poussou et al. (2010) and Mazumdar et al. (2011) all used a water-bath to investigate the transport of an airborne contaminant due to a human body moving down the centre of an aircraft cabin. The images taken from the water-bath model experiments were used to validate a CFD model, though virtually no information is given as to how the dye concentrations were calculated

from the images. Nevertheless, the water-bath experiments show that a human body has the potential to carry an airborne contaminant the length of an aircraft cabin.

Much like the full-scale work of Kalliomäki et al. (2014), water-bath models were used by Tang et al. (2005), Eames et al. (2009) and Tang et al. (2013) to investigate the airflows caused by opening a door. Tang et al. (2005) and Eames et al. (2009) used two rooms filled with water, connected by a doorway, with one room having food dye added to it. The door was opened into the room with the food dye then closed a short time later. Images taken during the experiments show that the door motions were capable of expelling a significant volume of the dye solution into the fresh water room. This resulted in the possible explanation of how a healthcare worker was able to contract varicella despite never setting foot in the room of an infected patient.

Tang et al. (2013) used a water-bath set up that was a 1:10 scale model of that used by Kalliomäki et al. (2014), complete with a figurine as opposed to a mannequin. However, in this smaller-scale study, food dye was used to determine the likely airborne infection transport due to a combination of door opening motions and human movement through a doorway. The results were found to be similar to those of the full-scale study, i.e. the sliding-door disturbed the air less than the hinged door and the motion of the figurine increased the fluid exchange, and subsequent contaminant transport, between the two rooms.

2.3.2 Numerical Methods

Experimental techniques can be costly in both time and resources. Numerical methods, including zonal models and CFD, can offer a relatively cheap alternative for modelling the dispersal of airborne pathogens and hence infection risk. Zonal models operate on the assumption that an airspace can be divided into smaller regions, or zones, within which flow properties and pollutant concentrations are assumed to be well-mixed. Typically, these zones are not empircally derived and so simple shapes, such as rectangles or cuboids, are assumed to ease calculations (Song et al., 2008). Zonal models give an idea of bulk, or macroscopic, airflows within an airspace and are particularly useful when applied to multi-connected spaces. Although they are relatively easy to implement once ventilation rates are known, they are not able to capture the intricacies associated with turbulent airflow, such as regions of recirculation or buoyancy. Nevertheless, their

predictive capabilities remain useful in large spaces. They have been shown to offer a good comparison to CFD predictions (Noakes et al., 2004) and also that models assuming a well-mixed airspace could be under-predicting infection risk (Nicas, 1996; Noakes and Sleigh, 2009).

CFD is a much more advanced numerical method (detailed in Chapter 4.1), that is capable of predicting finer details associated with the flow and is used as a modelling tool across a whole range of research areas, including modelling airborne infection risk. The capabilities of CFD models have increased as computational resources become more readily available. Early CFD studies relating to airborne infection typically used relatively simple geometries and were modelled as a steady-state problem, bypassing any complex transient phenomena (Chow and Yang, 2005; Chow et al., 2006; Beggs et al., 2008). Increased computer power has allowed for more complex geometries and models to be created. Likewise, steady-state simulations have since made way for transient simulations. The resulting time-dependent flows offer more detail across every aspect of a model and can take advantage of motions that a steady-state simulation cannot (Choi and Edwards, 2008; Mazumdar et al., 2011; Wang and Chow, 2011).

The tracer gases and food dye, used as proxies for an airborne contaminant during experimental modelling methods, clearly need to be modelled differently in CFD models. A cloud of an airborne contaminant is made up of a number of discrete particles and bioaerosols, and they may be modelled as such using what is known as the Lagrangian approach. This method involves tracking the (x, y, z) coordinates of each particle so that they may be individually tracked, and has been used to model the trajectories of particles originating from the human respiratory tract (Zhu et al., 2005; Gupta et al., 2011). At large enough numbers of particles, the entire population may also be modelled as a continuum, in what is known as the Eulerian approach (Crowe et al., 1996). The Eulerian approach does not track the individual components of a contaminant release, but typically monitors values of a scalar, or species, representative of contaminant concentrations. The Eulerian approach also has a place in the context of airborne infection, as the particle releases usually considered are quite large and may be modelled as a continuum (Lai and Cheng, 2007; Choi and Edwards, 2008).

2.3.3 Infection Risk

Studies investigating the transport of a particular pathogen, or infection, are typically concerned only with location. That is, the focus of the study is to find out how and where a pathogen may spread to. Interpreting this information into a likelihood of contamination, or a quantifiable risk, is not trivial and depends on many factors.

To gain some understanding of disease outbreaks, mathematical models can be built which use existing data to look at the likelihood of the spread of an infection given certain parameters and information, such as that gained from experiments or numerical models. The parameters required to populate such a model vary from model to model but usually involve quantifying the infectiousness of the disease and some time-based variable, resulting in the probability that the disease is passed on to another person.

2.3.3.1 Epidemic Models

Possibly the first combined mathematical and epidemiological model constructed to predict disease outbreaks was proposed by Kermack and McKendrick (1927). The model comprises two ordinary differential equations (ODEs), combining susceptible, infected and removed populations, together with two model constants. Despite being a rather simple model, it has been successfully fitted to data sets from past epidemics (Brauer, 2005).

Around the same time as the Kermack-McKendrick model was created, the Reed-Frost epidemic model was being developed by Wade Hampton Frost and Lowell Reed at Johns Hopkins University (Fine, 1977). The Reed-Frost Epidemic Model, though unpublished by its creators, has been around since the 1920s and is discussed/used by many authors and medical schools in the USA, showing good agreement with past epidemic data (Abbey, 1952; Fine, 1977; Schenzle, 1982). The model is made up of the two equations:

$$C_{t+1} = S_t(1 - q^{C_t}) \tag{2.4}$$

$$S_{t+1} = S_t - C_{t+1} \tag{2.5}$$

where C_t is the number of cases at time t, $1 - q^{C_t}$ the probability that an individual will become infected (one of the C_t) and S_t is the number of susceptible cases.

These models, or ones based on similar principles, have been applied to a variety of

scenarios, ranging from the chances of catching a cold in a small household (Heasman and Reid, 1961) to the chances of surviving a zombie apocalypse (Munz et al., 2009). Although the latter may seem far-fetched, the findings have applications to infections that can remain dormant.

Susceptible-Exposed-Infector-Removed Model

The Kermack and McKendrick and Reed-Frost epidemic models only take into account the total number of people susceptible to a disease, S, and the number that are infected, C (or I). Susceptible-Exposed-Infector-Removed (SEIR) models improve on this approach by including two extra stages in the infection cycle.

The first additional stage, E (exposed), takes into account those people that have been exposed to the disease but are not showing signs of infection and are not infectious themselves. The exposure stage occurs between the susceptible and infector stages in the SEIR cycle. The second additional stage, R (removed), accounts for people that have been taken out of consideration either because they are immune to the disease or have died from it. The removed stage occurs after the infectious stage. The SEIR model is most easily applied to outbreaks of contact diseases (Stehle et al., 2011; Shah and Gupta, 2013) though has been considered in the context of airborne disease outbreaks (Noakes et al., 2012).

2.3.3.2 Airborne Infection Models

The previous models all assume face-to-face or contact transmission, i.e. there is some parameter that takes into account the chance of encountering an infected person. This is not necessarily the case if one considers an airborne infection or respiratory disease. Infectious bioaerosols and other particles may remain in the air long after the infectious

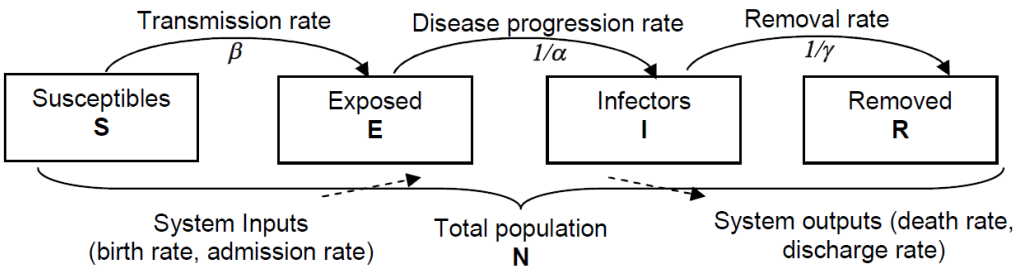

Figure 2.6: Schematic of the SEIR modelling approach as shown by Noakes et al. (2012).

host is no longer around. This means that quantifying the risk of infection through airborne transmission requires a different modelling approach than the epidemiological models in the preceding section. There are two different approaches used to model the risk of infection due to an airborne pathogen: dose-response curves and the Wells-Riley model.

Dose-Response

Dose-response curves, as the title suggests, relate the response of a system to given dose values. In the context of airborne transmission, this typically results in a relationship that may be used to model the chance of infection based on an exposure to a pathogen-laden air sample (see Figure 2.7).

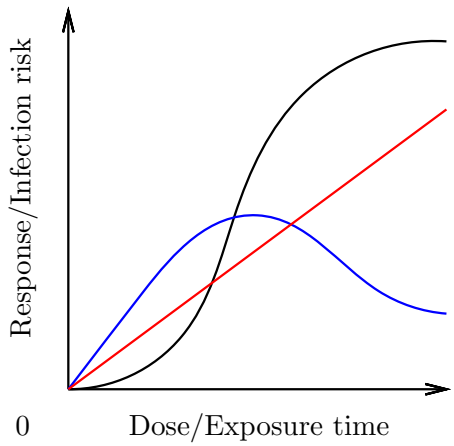

Figure 2.7: Examples of possible trends found in dose response curves. Note that the 'dose' and 'response' labels are generic terms for the axes labels but may be redefined to be more suitable to the model at hand, as is shown here.

One of the main difficulties with the dose-response approach is obtaining data for the the dose-response curve for a particular disease. Obtaining dose-response data from human studies is very difficult to obtain, and controversial, as this typically requires human testing. The alternatives are: to use data from experiments with animals; obtain relevant data once a disease outbreak has been realised; or estimate the relationship based on assumptions.

The dose-response approach appears to have been initiated by Haas (1983). This study evaluated the effectiveness of four approaches to fitting a series of data relating to waterborne infection. The approach has since been used to quantify infection risk for a variety of diseases, including respiratory infections and airborne infections. Nicas (1996)

used a dose-response model to provide a way of estimating the incidence of TB in a population. It was assumed that the risk of infection (response), R, obeyed:

$$R = 1 - e^{-D} \tag{2.6}$$

where D is the number of infectious doses inhaled. The infectious dose inhaled, D, was also modelled and assumed to be dependent on various factors affecting the air space. Sze-To et al. (2008) modelled the infection risk of a virus in an indoor space using an approach similar to that of Nicas (1996), assuming the probability of infection obeys a relationship similar to equation 2.6.

The relationship seen in equation 2.6 is based on theory and not observation. Armstrong and Haas (2007) tested the fit of six dose-response curve relationships to a set of data relating the spread of Legionnaires' disease in a guinea pig population. The authors reason that particle deposition patterns in the pulmonary regions of guinea pigs and humans are similar, hence the model parameters are likely to be comparable. The exponential (equation 2.6) and β-Poisson based models were found to perform the best.

Wells-Riley Model

The Wells-Riley model appears to be the most common approach for quantifying infection risk when considering airborne transmission, having been used in numerous studies. Some of the more important examples are commented upon, here.

The original model is based on the equation:

$$P = \frac{C}{S} = 1 - e^{\left(-\frac{Iqpt}{Q}\right)} \tag{2.7}$$

where I is the number of infectors, p the pulmonary breathing rate (m^3 min^{-1}), t time (min), Q the room ventilation rate (m^3 min^{-1}) and q a unit termed 'quanta'. One quantum is defined to be the number of pathogen-laden airborne particles necessary to infect 1 - 1/e (63.2%) of susceptible persons. Despite being developed by Riley et al. (1978), the model applies the findings of Wells (1955), hence the name.

Values for the quanta, q, are usually obtained by back-calculating, using values from previous outbreaks once they have ended. The inclusion of room ventilation rates in equation 2.7 means that, more often than not, the room ventilation flow rates relating to

a disease outbreak are also obtained after the outbreak has ended, not guaranteeing that the flow rates at the time of the outbreak are the same as those measured. An exception to this is the work of Escombe et al. (2007), who passed air from a TB ward on to guinea pigs, measuring the ventilation rates over 505 days, allowing calculations of q with suitable ventilation flow rates.

In the form presented in equation 2.7, the Wells-Riley model is only applicable for steady-state flows, unable to account for time-dependent features. Further, the model assumes the air space is uniformly mixed, a state that is difficult to achieve in reality (Nazaroff et al., 1998). Rudnick and Milton (2003) built upon the original version of the model to correct for the steady state and well mixed assumptions.

The Wells-Riley model bears a strong resemblance to the dose-response models that assume an exponential model, like that seen in equation 2.6. The main difference being that the factors affecting the infectious particles are implicit for the Wells-Riley model, being accounted for by q. The two approaches are compared by Sze-To and Chao (2010), who concluded that both are useful in understanding disease transmission mechanisms.

2.3.4 Human Movement

This study focuses on the impact human movement has on the transport of an airborne contaminant in a hospital corridor and the ensuing infection risk this could pose to a person located in it. The water-bath experiments and CFD simulations to follow (Chapters 3, 5 and 6) model the impact a human has whilst walking along a corridor rather than implementing a realistic walking motion. The validity of this modelling approach is now considered based on the findings of previous studies.

The only way to truly capture human motion is to use a human that is moving. To avoid potential issues relating to ethics, health and safety and cost, human subjects are not often used and are modelled instead. That being said, some studies still opt for the realism approach by using human subjects (Rydock and Eian, 2004; Craven, 2014; Mcdonagh and Byrne, 2014), although the majority use some type of model.

To recreate human motion can be a complex task, for both experimental and CFD models. In the context of CFD models, even the smallest movements require either the use of complex techniques such as dynamic meshing or the immersed boundary method (IBM)

(see Chapter 4.1). Before either of these approaches is employed, the movement needs to be first characterised into a mathematical form, which, again, is not trivial. To avoid these approaches, previous studies have been known to model the effects of simple motions, rather than implement the motion itself, by adding a momentum source (Brohus et al., 2006).

Arguably the most common motion considered in the context of airborne infection is that of a walking human. Various mathematical models have been put forward that claim to capture the basic walking motion (Mochon and McMahon, 1979; Boulic et al., 1990; Garcia et al., 1998). However, implementing these models into a CFD model is not trivial and to date has only been performed by a handful of studies (Choi and Edwards, 2008, 2012). Instead, most studies consider a body in translation through a space and do not consider the walking motion itself, both numerical (Poussou et al., 2010; Mazumdar et al., 2011) and experimental (Poussou, 2008; Tang et al., 2013; Kalliomäki et al., 2014). Modelling in this way means that although effects relating to individual limb motion may be lost, features relating to the bulk flow due to the body remain.

2.3.4.1 The Human Wake

The human form can be thought of as a bluff body. The flow around a bluff body is characterised by flow separation, the subsequent wake this separation produces and the associated pressure drag caused (Roshko, 1955). At large enough velocities, this flow separation leads to a process known as vortex shedding, whereby the vorticity generated at the boundary of the body is transferred into the wake, leaving a trail of eddies or vortices (regions of high local vorticity). The interaction between this wake and a contaminant in it establishes the interest in human wakes, in the context of airborne pathogen transport. Very few studies are explicitly concerned with properties relating to the wake of a person. Nevertheless, many studies are implicitly concerned due to the link just highlighted between the wake and contaminant transport.

Approaches to capturing flows related to the human wake have varied. As is the case for capturing human motion, the only way to capture the wake of a human is to use a human subject; no amount of modelling can make up for this. Due to the aforementioned issues that can arise when using human subjects, the majority of studies use models instead. The models used in previous studies to represent a human body differ significantly, some aiming

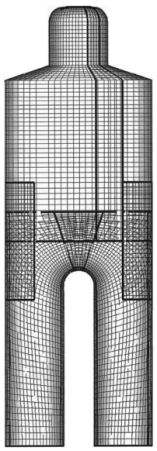

Figure 2.8: Geometry used for investigating flows around a human by Edge et al. (2005).

to capture the complexities associated with the head and limbs (Choi and Edwards, 2008, 2012; Tang et al., 2013) while others opt for a more simplistic and 'smoother' geometry offered by that of a mannequin (Bjorn and Nielsen, 2002) or similar (see Figure 2.8) (Edge et al., 2005). These smoother, featureless geometries have been shown to still produce wakes in agreement with those of a human subject (Settles, 2006).

Simplifying a body like that seen in Figure 2.8 even further, i.e. removing the 'legs' and 'head', could result in something akin to a cylinder. Cylinders have been used as geometries representative of a human in many studies. Most of these studies used cylinders as they are working with small-scale water-baths, where it can often be difficult to find/construct a shape that closely resembles a human body (Poussou, 2008) (Poussou et al., 2010) (Mazumdar et al., 2011), though the assumption of a cylindrical body has also been used to simplify calculations when quantifying contaminant concentrations entering the human wake (Kim and Flynn, 1991). Despite the lack of features offered by the cylinder, it has been shown that the wake generated by flow around a human mannequin is qualitatively similar to that around a circular cylinder (Mattsson et al., 1997). The current study follows the modelling approach of these latter studies and uses a circular cylinder to represent a human body in both the water-bath model and CFD simulations.

2.3.4.2 Flows Around Circular Cylinders

The flow around a circular cylinder is a widely studied problem in fluid mechanics. The juxtaposition of such a simple geometry with the complex flow phenomena it is capable of producing, such as the aforementioned vortex shedding, has captured the interest of

mathematicians, physicists and engineers for many years. The vortex shedding is caused by an instability in shear layers 'shed' from the cylinder that first occurs at $Re = 47$ (Dai and Jazar, 2012). For increasing Re these shear layers roll up and form vortices (eddies), deposited out into the wake behind the cylinder (Williamson and Roshko, 1988; Turner et al., 1993) (see Figure 2.9a). Wakes around cylinders that consist of these vortices are known to enhance mixing and overall mass transport (Cohen and Director, 1975).

Since the vortices shed from a cylinder mix the surrounding fluid, the frequency with which they are shed is clearly important. Vortex shedding is characterised by the Strouhal number, St:

$$St = \frac{fL}{U} \tag{2.8}$$

where f is the frequency with which the vortices are being shed, L a relevant length-scale to the geometry (taken as the diameter for a cylinder) and U is the fluid velocity (Strouhal, 1878). Values calculated using equation 2.8 are often used to validate CFD models that investigate flows around cylinders (Breuer, 1998; Braza et al., 2006; Kanaris et al., 2011). This method of validating a CFD model against St values has also been used in airborne infection studies as a preliminary check that a CFD model is capable of predicting correct eddy shedding properties, before proceeding with the model of interest (Choi and Edwards, 2008). Figure 2.9b shows how St varies with Re for flows around a circular cylinder.

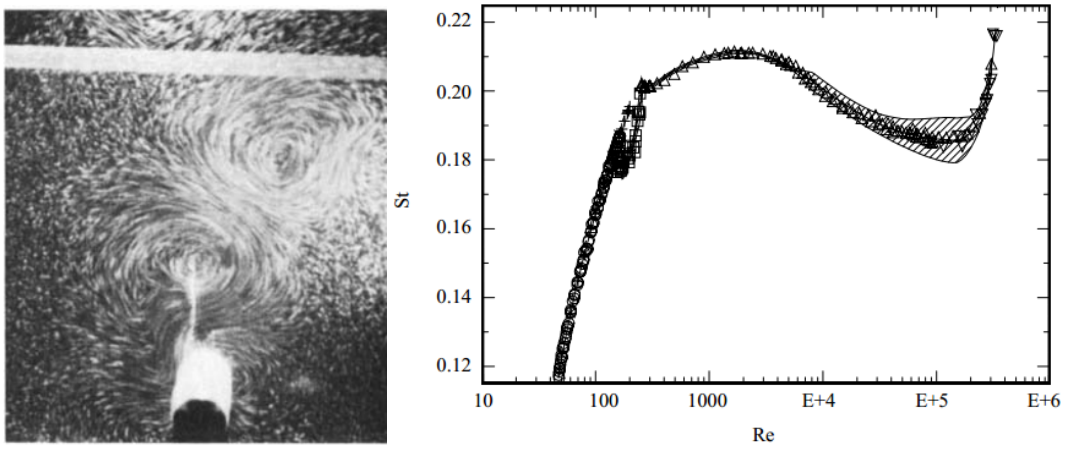

(a) (b)

Figure 2.9: (a) Vortices in the wake of a cylinder visualised by adding particles to the fluid surface as visualised by Williamson (1984); (b) St for various values of Re for flows around a circular cylinder (Norberg, 2003).

In the experiments and CFD simulations to follow, the movement of the simulated person is provided by a mechanical apparatus, for the water-bath experiments, and an algorithm, for the CFD. To simulate either a constant and regular stream of people walking along a corridor or a single person pacing up and down a corridor, a cylinder is translated back and forth along the length of the water-bath and CFD geometry[1]. While the flow around stationary cylinders has been well studied, the flow around a translating cylinder has received relatively little attention. Studies using translating cylinders have drawn analogies with flows around seamounts (mountains that are entirely subaquatic) (Gostiaux and Dauxois, 2007) and off shore constructions (Chakrabarti, 1987; Yeung and Vaidhyanathan, 1993). To date, there are no studies that have used a translating cylinder to represent a stream of human traffic.

Translatory, or oscillatory, flows can be characterised by the Keulegan-Carpenter (KC) number, which relates the relative importance of drag to inertial forces:

$$KC = \frac{U}{\omega d} \tag{2.9}$$

where U is the flow velocity amplitude, ω the translation, or oscillation, frequency and d the diameter of the cylinder. Studies concerned with the flow around offshore structures usually investigate values of $KC < 45$ (Mackwood and Bearman, 1997), though have been known to study up to $KC = 60$ (Williamson, 1984). Although the experiments and simulations conducted in this study are carried out at $20 < KC < 100$, and hence are conducted at KC numbers comparable to those in the literature, the influence the translation has on a scalar (dye) at these KC and Re values is so far unstudied. Studies have been conducted that investigate the influence of an oscillating cylinder on the mixing of a scalar (heat), but have been carried out at much lower values of Re and KC values than those considered here (Celik and Beskok, 2009; Mahfouz and Badr, 2002).

2.4 Summary

Here, a brief summary of each section in this chapter is presented and the relevance of that section to the current work is highlighted.

[1]The frequency of these translations is calculated such that once Re values are matched, and time-scaling principles are applied, the cylinder's speed is comparable to that of a person walking ($O(1)$ m s^{-1}).

2.1 Airborne Particles (Aerosols)

The literature shows that pathogens are capable of being transported on very small particles. The bioaerosols generated during respiration are particularly hazardous as they may evaporate down to sizes that keep them suspended in the air where they may be inhaled, contributing to airborne pathogen transport. There are already methods put in place within the healthcare system that aim to minimise the inhalation of such particles. The current study, while not particularly concerned with the final destination of such droplets, aims to build upon the research that looks at their transport. In the context of hospital corridors, this has yet to be done.

2.2 Mitigating Airborne Infection

Until airborne infections are completely eradicated, mitigation remains the best defence against them. A hierarchy of control currently in place for minimising the spread of airborne infections such as TB identifies that environmental controls, including ventilation, are to be prioritised over the wearing of PPE, such as masks.

The air quality of hospitals around the world is maintained by HVAC systems comprising both mechanical and natural ventilation methods. The guidelines for these systems is set out by a relevant authority. Some of these guidelines are detailed for critical-care facilities but are less thorough and specific for the communal areas, including corridors. The current research aims to see what effect the ventilation guidelines that are assumed to cover general use corridors are likely to have on the transport of airborne pathogens, once the airflows are disturbed by human movements. To the author's knowledge, research of this nature has not been carried out before.

2.3 Airborne Infection Modelling

To avoid unnecessary risk, studies investigating airborne infection often use models. These models are often created to a reduced-scale. To ensure predictions from reduced-scale models are relevant to the full-scale, through the matching of non-dimensional parameters, water is often used as the working fluid in so-called water-bath models. To date, studies using water-bath modelling to investigate airborne infection risk are qualitative, rather than quantitative, and therefore applying the method quantitatively in this study is novel.

Studies have already been carried out that investigate the flows created by humans as they

move. This has been done both numerically and experimentally at full and reduced-scale, using both human subjects and models. Of those studies that chose to use a model, a variety of bluff body shapes have been used to represent a person, ranging from a simple rectangular or circular cylinder to an almost lifelike recreation of the human form. The link between the wake of a simple bluff body and a human has been established previously and so the choice of a circular cylinder to represent a person in the current work appears valid.

The flow around a circular cylinder is a very popular choice for investigation in the field of fluid mechanics. Since a circular cylinder is used for the models in this study, characteristics relating to the flow around a cylinder may be used as validation for the CFD simulations, where many of these properties are easily calculable.

Vortices are shed from circular cylinders, in a flow, for all but very low Re values ($Re < 47$). These vortices are known to enhance mixing and increase mass transport in the ensuing wake. If a cylinder is considered to be translating in an otherwise quiescent fluid, the flow properties appear to be characterised by the Keulegan-Carpenter (KC) number. Values of $KC < 45$ are typically studied as they have relevance to structures and topographies in the ocean. The experiments in this study yield $20 < KC < 100$, hence some of the studies could be comparable to values of KC obtained in other studies. However, studies relating to scalar mixing and transport due to a translating cylinder have been carried out at Re and KC values much lower than those considered here. As such, to the author's knowledge the mixing of a scalar due to a translating cylinder at values of KC and Re considered here have not been studied together, making the experimental and numerical work to follow unique.

Chapter 3

Water-Bath Modelling

Contents

This chapter first describes the water-bath modelling approach in general, highlighting the important aspects that must be considered for results to be relatable to the full scale. Next, the methodology implemented during the experimental phase of the research is described, specific properties relating to the physical model are given. The image analysis techniques used are very important in this stage of the research and are discussed in detail. Finally, the results and model relationships obtained from the image analysis and experimental work are presented and discussed. This chapter focusses only on the water-bath experiments, together with a model based on the results, and not on their implications, which are discussed later in Chapter 7.

3.1 Introduction

The detailed behaviour of airflows occurring in buildings are typically difficult to visualise and measure at full-scale. Because of this, researchers often resort to modelling. One experimental approach that can be used is water-bath modelling. This involves using a scaled-down physical model and replacing the air in the model with water such that the flows behaviours are comparable.

One of the main advantages of water-bath modelling, when compared to full scale modelling, is the ease by which the flows can be visualised (and potentially measured). If the walls of such a model are made to be transparent, features of the fluid flow may be visually captured externally from any desired point of view. Various types of visualisation aids can be used to observe the desired flow features, such as fluorescein, food dye or small, neutrally-buoyant particles. For this reason, the tanks used for water bath-modelling are often made of perspex or glass.

The water-bath approach, applied to indoor air, appears to have first been employed by Linden and Simpson (1985), where the air-flows in and out of open doors and windows were investigated. Since then, it has been used to great effect when modelling other natural ventilation flows (Hunt and Linden, 1999; Gladstone and Woods, 2001; Thatcher et al., 2004). It has also been used to model flows initiated by door openings (Tang et al., 2005, 2013) and human movements (Poussou, 2008). Although the models cannot always be validated against their full scale counterparts, they show physically realistic phenomena. Furthermore, studies have shown good agreement with computational fluid dynamics (CFD) models (Finlayson et al., 2004; Poussou, 2008; Mazumdar et al., 2011).

In terms of contaminant transport, water-bath models have been used to qualitatively analyse airborne contaminant transport in a number of different scenarios. Tang et al. (2005); Eames et al. (2009) and Tang et al. (2013) all investigated door opening motions into a room, through water-bath experiments, with the latter also simulating a person walking through the door. Studies have also been conducted that investigated the impact of the human wake on the transport of a contaminant in an aircraft cabin (Poussou, 2008; Mazumdar et al., 2011).

3.1.1 Principles of Water-Bath Modelling

The water-bath modelling technique is based on the principle of dynamic similarity between the model and full-scale. By ensuring comparable dimensionless parameters such as Reynolds number, Re, Peclet number, Pe, and Schmidt number, Sc, dynamic similarity between the model and full scale can be achieved.

3.1.1.1 Non-Dimensional Parameters

The Reynolds number, Re, (named after fluid dynamicist Osborne Reynolds *[1842 - 1912]*) is a dimensionless parameter often used to characterise fluid flows and is the ratio of the inertial to viscous forces, within a fluid flow. It was previously defined in equation 2.3 and is often used as a guide to characterise whether a particular flow is turbulent or laminar, although values of Re alone do not fully determine this[1].

Despite the name, the initial discovery that arranging the variables in the form shown in equation 2.3 was enough to be able to characterise flows of similar geometry and boundary conditions was made by Sir George Stokes (1851). (The parameter gained its current name, however, due to the extensive work performed by Reynolds (1883)). This means that for a particular set of geometry and boundary conditions, changes in values of U, L, ρ and μ can be taken account of by a relationship dependent on equation (2.3) (Bachelor, 1967).

Other relevant dimensionless parameters include the Peclet and Schmidt numbers, defined as:

$$Pe = \frac{UL}{D} \qquad \text{and} \qquad Sc = \frac{\mu}{\rho D}, \text{ respectively,}$$

where D is the (mass) diffusivity. The Peclet number can be thought of as the ratio between advection and diffusion, and the the Schmidt number as the ratio between momentum diffusivity and mass diffusivity.

The necessity of matching Pe and Sc here is due to their involvement in diffusion, and hence importance in models where contaminant transport is considered. It is necessary that any diffusion effects of a dye, or other tracer, used in the water-bath model are comparable with those of the full scale contaminant particles in air. By matching these

[1]The geometry itself and surface roughness also play a part in determining whether the flow is laminar or turbulent

dimensionless parameters, dynamic similarity between model and full scale is ensured.

In the experiments carried out in this study, all modelling is carried out under, nominally, isothermal conditions. No additional heat source is implemented to the water or equipment and the effects of heat are not considered. For works where thermal conditions are modelled or considered, additional non-dimensional parameters such as Prandtl number, Pr, Grashof number, Gr and Nusselt number Nu also need to be considered. However, it has been suggested that studies using water-bath models that consider thermal effects will come into difficulties when taking thermal effects into account, through the matching of these additional non-dimensional parameters (Chen, 2009).

3.1.2 Impact of Length and Time Scales

As has already been mentioned, water-bath modelling involves operating at a different length-scale to the full-scale. This change in length-scale has a knock-on effect when it comes to time scales and must be taken account of.

This is highlighted in considering a human, of shoulder width 0.5 m, walking at 1 m s^{-1} down a corridor. At full scale, assuming the corridor is filled with air at 20°C, this yields $Re_f \approx 33,000$, where $_f$ is used to denote reference to the full-scale; $_m$ is used to denote values relating to the model (fluid viscosities and densities throughout have been calculated from Lide (2001), unless otherwise stated). If they are to walk the length of a 15 m corridor, this clearly takes 15 s to complete. If we now consider a 1:15 scale water-bath model, with a comparable shoulder width of ≈ 0.033 m, it is necessary to find a value for the velocity to give $Re_m \approx 33,000$, for dynamic similarity to occur. This yields a velocity of $U_m \approx 1$ m s^{-1}. The 1:15 model is 1 m long, meaning the person would cover the corridor's length in 1 s. This is ≈ 15 times faster than the full-scale equivalent, meaning in this case, 1 s at the model-scale needs to be interpreted as 15 s at the full-scale.

Although full-scale data is not available for comparison to show the validity of these scaling principles, they are covered in depth by Thatcher et al. (2004) and have been used to good effect by Hathway et al. (2014) and Mazumdar et al. (2011). However, a comparison between the data obtained from CFD simulations at identical Re, but different length-scales, is provided later in Section 7.1.1.

3.2 Methodology

The water-bath modelling was undertaken at the BP Institute (BPI), Cambridge, a research centre that specialises in all manner of fluid flow phenomena. The model was constructed specifically for this research by the technical staff at the institute and comprises a perspex, open-topped channel with a circular cylinder located inside the cavity. The design of the rig was developed by author, supervisors and technical staff of BPI. The cylinder is capable of being traversed the length of the tank by motorised apparatus (a linear actuator). The walls of the model represent those of a corridor and the translating cylinder that of a person moving inside it. The regular nature of the translation means that the model is representative of either a person walking up and down the corridor multiple times, typical of perhaps a patient or visitor nervously pacing up and down whilst waiting for information, or of a number of people walking up and down a corridor where it is assumed that at the end of each pass of the water-bath one 'person' leaves the corridor space as another enters it coming the opposite way. Although this is an idealised model (e.g. a circular cylinder is not anatomically correct and the regular frequency of movement may not be strictly adhered to in a real situation), by taking into account changes in length and time scale, (see Section 3.1.2), the model aims to give some insight into the mixing and transport processes involved in a full scale corridor experiencing frequent human traffic.

3.2.1 Materials and Equipment

The water-bath itself is made of 10 mm thick polymethyl methacrylate (Perspex) sheeting, the main body of which forms a cavity 98 mm wide, 1110 mm long and 200 mm tall. This corridor section of the water-bath leads to a cuboid-shaped section at either end, henceforth termed the 'end-tanks', which are approximately 250mm in all directions (see Figure 3.1). The end-tanks were put into place to suppress the influence of the ends of the corridor, extending the region of interest within the water-bath.

A layer of foam-rubber, approximately 1 mm thick, provides a water-proof seal between the corridor section of the water-bath and the end-tanks. On all other adjoining surfaces the pieces of acrylic are glued together. Prior to experimental work beginning, checks were performed to make sure that the tank was watertight. A spirit level was used to make sure the tank was horizontal.

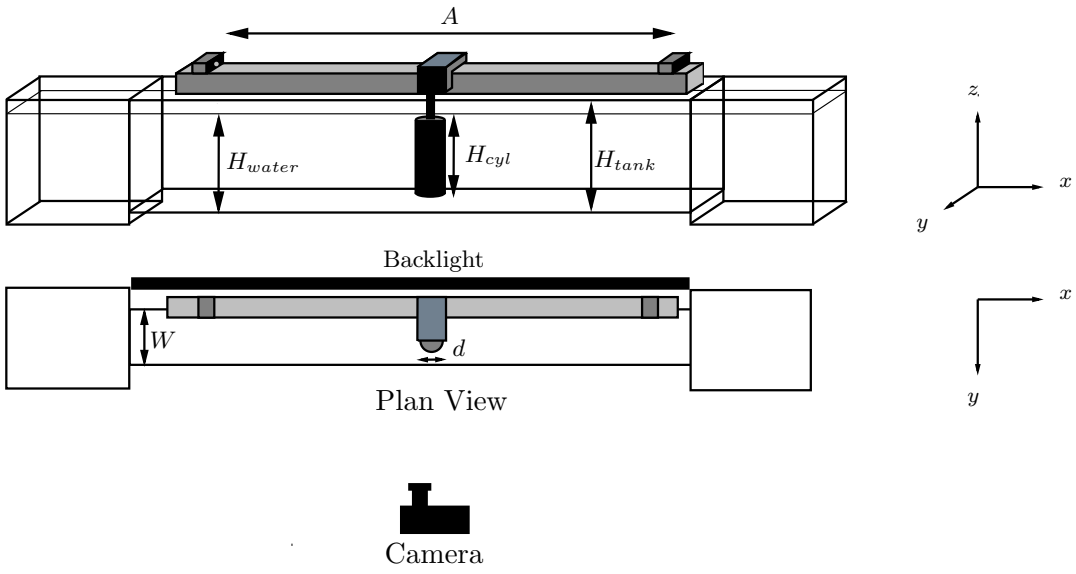

Figure 3.1: Experimental setup, not to scale. A cylinder of height H_{cyl} and diameter d is made to oscillate at a frequency ω and amplitude A in a tank H_{tank} high and W wide, filled with water to a height H_{water}. For all experiments: H_{cyl}=110 mm, H_{tank}=200 mm, H_{water} = 136 mm. and W = 98 mm. The two end-tanks are used to remove any end effects of the corridor and are not included in the analysis.

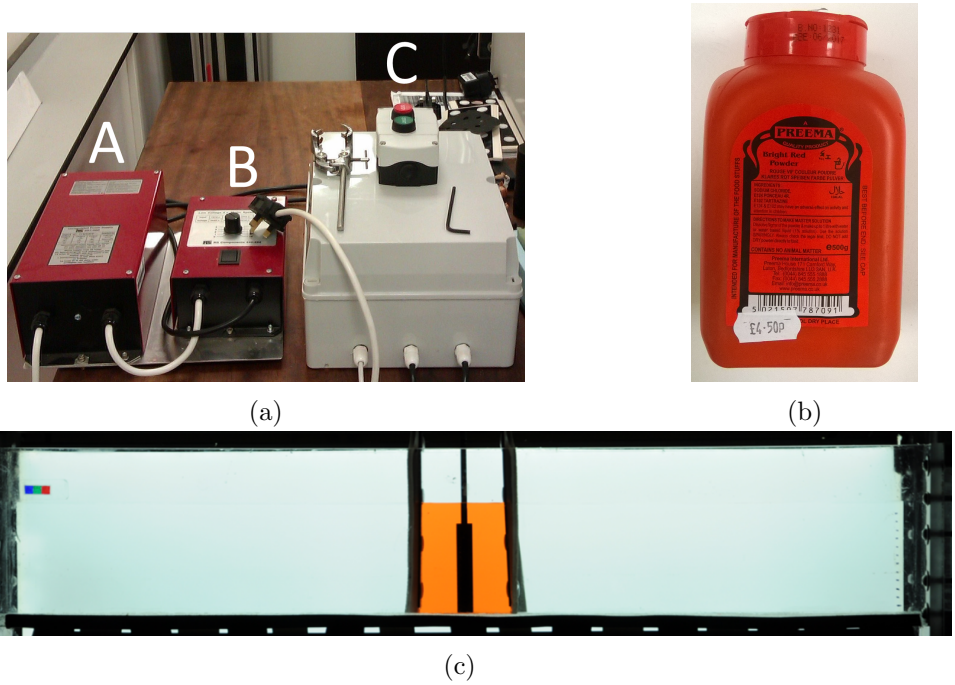

Figure 3.2: (a) View from behind the tank. Boxes 'A' and 'B' determine the voltage passed to the motor. The potentiometer control can be seen on top of box 'B'. Box 'C' houses the motor for the linear actuator and is controlled by the feed from the potentiometer; (b) PREEMA food dye used for all experiments; (c) View of the water-bath, as seen from the camera, at the start of a typical experiment.

A linear actuator sits atop the water-bath and is bolted to two plates of acrylic for stability. A potentiometer feeds into the motor of the actuator so that the velocity can be altered, from zero up to a maximum of 0.3 m s^{-1} (see Figure 3.2a). The voltage output from the potentiometer is determined by the rotational position of a dial, but the actual voltage output is not observed or measured. Instead, the numerical values indicated by the affixed dial are used to assign approximate velocities to the actuator (e.g. a reading of $4 \approx 100$ mm s^{-1}). The actual velocities imposed on the cylinder are not determined until the results are analysed (so that they can be measured precisely).

A plastic housing, connected to the cylinder, is attached to a metal plate whose motion is determined by the actuator. The steel arm that protrudes from this housing has been manufactured to have an aerofoil-like cross-section, so as to impose the minimum influence on the resulting fluid flow. As the velocities used in this study are small, it is assumed that the actuator arm is sufficiently stiff to absorb the small acceleration without stressing or bending the metal arm. Consequently the cylinder is assumed to be travelling with constant velocity from time $t = 0$.

Experiments were conducted using seven cylinders, made of black PVC. All are 110 mm tall and possess diameters of 10, 15, 20, 25, 33.5, 40 and 50 mm. With the cylinder attached, there is ≈ 1 mm clearance between the bottom of the cylinder and the floor of the tank. The tank is filled with water so that $H_{water} = 136$ mm for all calibration images and experiments.

A region of the water-bath is initially isolated between two 'lock-gates', 100 mm apart and surrounding the initial position of the cylinder. Approximately 50 ml of water is extracted from this region, mixed with a powdered food-dye (see Figure 3.2b), poured back into this isolated region and well mixed (see Figure 3.2c). The lock-gates are made of a foam rubber, held rigid with a PVC sheet and plastic rivets. A thin layer of silicon grease is applied to the edges of the foam rubber to make the interface between the lock-gates and tank watertight. Additionally, the grease facilitates the removal of the lock-gates at the start of each experiment, helping to reduce unwanted disturbances of the surrounding fluid. Due to the very nature of the no-slip condition, fluid always adheres to the sides of the lock-gates which inevitably disturbs the dye region. This disturbance is deemed not to impose much on the overall dispersal of the dye as the momentum imparted from the cylinder quickly dominates the flow. As results will later show, repeat readings were

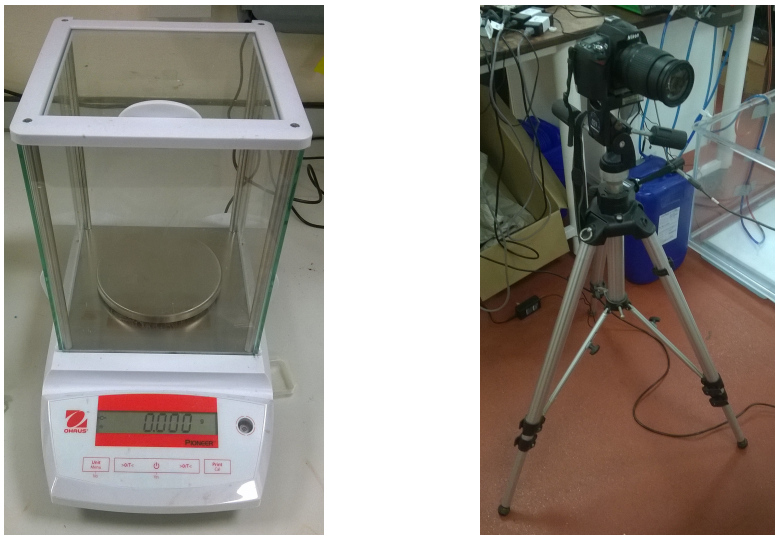

(a) (b)

Figure 3.3: (a) Mass-balance used for measuring the dye; (b) Camera and tripod set up opposite the water-bath.

shown to be consistent, proving further that the slight variability in initial conditions is of little consequence to the overall mixing.

The red, powdered, food-dye used acts as both a contaminant and a visualising agent, and was measured using a mass balance accurate to within 5×10^{-4} g (see Figure 3.3a). Due to its availability, the food-dye used was of the type typically found on supermarket shelves. The same dye has been used in water-bath experiments where quantitative analysis of its concentration was necessary (van Sommeren et al., 2012), giving confidence that the dye is suitable for use here. Once dissolved, the aqueous food-dye solution has a density greater than water, potentially giving rise to a gravity current. To avoid this, the concentration of dye used, ≈ 0.04 g L^{-1}, was found to have a negligible density difference compared to water. This made the dye solution act like a passive tracer, a feature that is important when comparing experimental results to CFD results later.

Approximately 3 m from the water-bath, a Nikon D90 digital single-lens reflex (DSLR) camera with a 18-105 mm zoom was set-up on a tripod (see Figure 3.3b). The D90 is a consumer grade DSLR and outputs compressed images in JPEG format. Due to available resources, greater specification cameras were not used. The camera was aligned horizontally and the bottom of the lens aligned with the floor of the water-bath. All automatic image-enhancing techniques were disabled to give as much control over the light properties of each photographic image as possible. The camera-controlling software

DIY photobits 5.2 was used to remotely operate the camera, and capture the photographs, via a USB connection to a laptop. The images were shot in a resolution of 4,288 x 2,848 pixels ($\approx$ 12.2 megapixels), the highest resolution the camera is capable of operating at.

Each pixel of an image is comprised of a red, green and blue (RGB) component that, when combined, give a colour in the visible light spectrum (Poynton, 2003). The individual RGB components take on values between 0-255. A pixel's RGB component values are denoted as if they were a three-coordinate system (R,G,B). If a single integer takes up the same value in each of the three components, a shade of grey on the standard 256-greyscale is obtained, where $(255, 255, 255)$ indicates white and $(0, 0, 0)$ indicates black. Since every pixel possesses a value for each of the three components, one can imagine an image constructed of only one of these light component values, ranging between 0-255. This image can then be viewed as a 256-greyscale intensity map, where each pixel's value is repeated in the other two light channels. Quantitative data about the dye concentration gradients can then be obtained from these intensity maps, as described in Section 3.2.3.

Since the analysis procedure is dependent upon quantifying changes in light intensity, it is important that the light properties of the room were made as consistent and repeatable as is practicable. To do this, the fitted lights were switched off in the room for all procedures. The only light source present was a bank of white LEDs, mounted behind a sheet of semi-opaque acrylic, placed behind the tank to provide constant illumination. The acrylic acted as a diffuser to help make the light emitted from the LEDs more uniform. This lighting arrangement is henceforth referred to as the 'backlight'.

It can be seen in the upper left of Figure 3.2c (reproduced in Figure 3.4) that there is

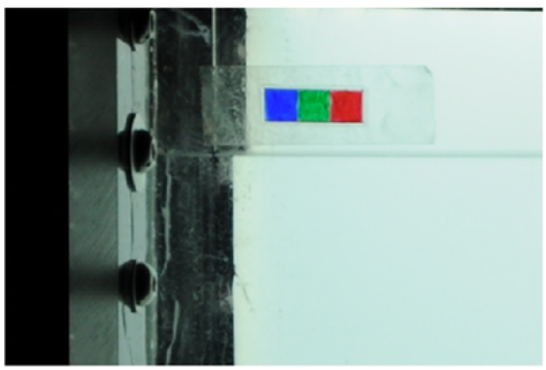

Figure 3.4: Coloured piece of film used as a reference point for RGB values for every exposure. Note that the film is placed above the water-line, so any variations detected in the RGB values are caused by variations in the light emitted from the backlight, not variations due to water quality.

a small piece of coloured film attached to the outside of the water-bath. This piece of initially transparent film was coloured red, green and blue to create a control for the RGB properties of each exposure. The film was placed above the water line so that the light passing through the film did not vary between experiments and was consistent for every exposure. This was necessary as it was found on rare occasions that the backlight experienced a surge in power, resulting in slightly different optical properties. During image analysis, this coloured film was monitored and those images identified as being taken at a time that the backlight was experiencing this surge were discounted.

3.2.2 Model Scaling and Relevant Parameters

The water-bath was constructed to a 1:15 length scale. Once up-scaled, this gives the modelled corridor dimensions $\approx$ 1.5 m $\times$ 2 m $\times$ 15 m, the 'people' a height of 1.65 m, and widths 0.15 to 0.75 m. To relate the scale model experiments to the full scale flow behaviour, dynamic similarity principles are applied, i.e. the reduction in length scale is partnered with an increase in fluid viscosity for the model. By using water as the working fluid, it is now shown that the relevant non-dimensional parameters confirm that the water-bath model operates at suitable conditions.

At full-scale, a Reynolds number of $Re \approx 34,400$ can be calculated for someone walking in a corridor, based on a shoulder width of 0.5 m and walking speed of 1 m s^{-1}. The experimental set up is constrained by both the dimensions of the tank and the length of the actuator, allowing for a maximum $Re \approx 17,000$ based on corresponding dimensions. Although the condition of dynamic similarity is not strictly fulfilled, flows around a circular cylinder between $Re \approx 1,000$ and $Re \approx 40,000$ are classified in the same subcritical flow regime, when the boundary layer is not fully turbulent, and the flow features are shown to be similar (Zdravkovich, 1997). Further, Thatcher et al. (2004) suggest that the water-bath modelling technique is still capable of giving relevant data at full scale, even with a substantial difference between Reynolds numbers. Nevertheless, ensuring a small difference between the two Reynolds numbers means that it is more likely that the flow features of the full-scale are captured at the model-scale, and vice-versa.

Appropriate values of Sc and Pe at full and model scale enable the diffusive properties of the dye in water to be related to the diffusion of small particulates in air. For the scale model, $Sc_m \sim O(10^3)$ based on the molecular diffusion of the dye used in this study

(van Sommeren et al., 2012). For airborne pathogens, typically we are concerned with the particles of diameter $O(1)$ μm, which yields a Schmidt number for the full scale, $Sc_f \sim O(10^5)$ (Seinfeld, 1986). Although there is a difference in magnitude, both Schmidt numbers $\gg 1$ indicating that in both cases flows are dominated by momentum diffusivity, or viscosity.

When looking at Peclet numbers, $Pe_m \sim O(10^6) - O(10^7)$ and $Pe_f \sim O(10^5)$. Both model and full scale flows are dominated by advection as indicated by the large Peclet numbers. Although the model scale results in a larger Pe, it is clear that both flows are dominated by advection and diffusion plays a very small role in the overall contaminant transport.

3.2.3 Quantification Through Image Analysis

3.2.3.1 Calibration

Prior to experimental work beginning, a relationship between the dye concentration and light intensity as seen by the camera was determined. Although the relationship between a material and the light attenuating through it can be characterised by the Beer-Lambert law (Splinter and Hooper, 2006), here an empirical approach based on the theory given by Cenedese and Dalziel (1998) was used, where the concentration is assumed to be line-of-sight averaged, i.e. constant along a particular light ray. This means that dye concentration variations across the tank are not detected. Tests were initially performed where images were also captured from above the tank to obtain information on these variations, but ripples on the water's surface and light refraction made any quantification from this point of view not possible using the current approach.

The technique itself is not new but an important modification was implemented in its use here. Authors using this method of analysis have previously applied one of two methods. Either it is assumed the light distribution is homogeneous and so one relationship is applied for the entire domain (Rummel et al., 2002), or, it is accepted that the light source used is inhomogeneous and so a cell-based spatial filter is applied, resulting in a series of relationships dependent upon where in the tank the analysis is being performed (van Sommeren et al., 2012). Here, upon examination of the intensity map for the backlight on its own, it was clear that the lighting provided was not uniform (see Figure 3.5a). It was found that the 'bottom' corners of the backlight were considerably darker than the

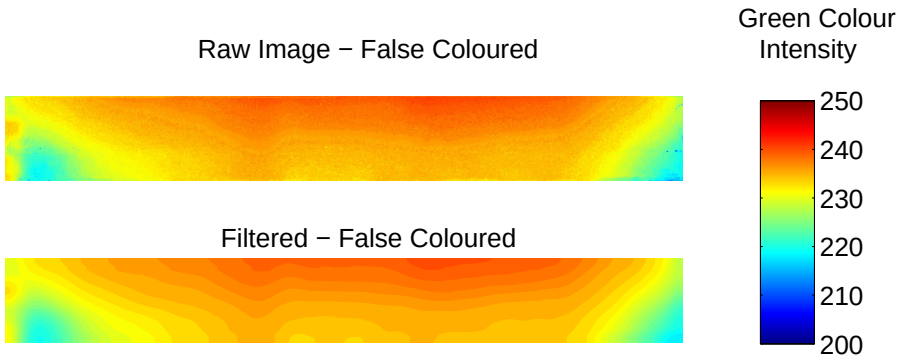

(a)

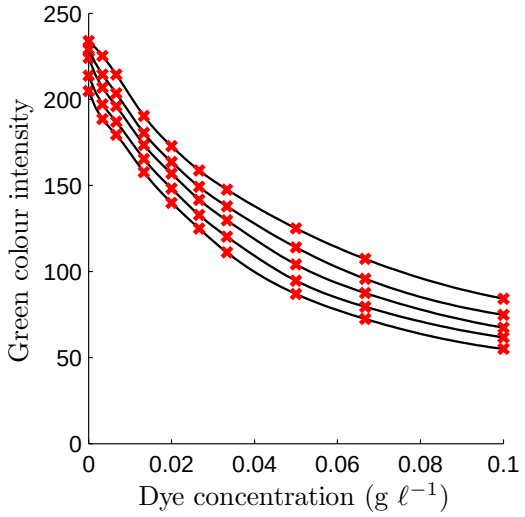

(b)

Figure 3.5: (a) A false coloured image of only water in the tank and the corresponding transformation into individual contour regions once the spatial filter is applied; (b) Typical series of calibration curves. Note that the number of curves shown has been reduced for clarity. For any given set of experiments, the corresponding calibration curves contain $\approx 20 - 25$ different relationships.

top, by as much as 25 shades of grey, $\approx 10\%$. To get around this, a slightly different take on the cell-based spatial filtering process was applied.

The Gaussian low-pass spatial filter was used to remove any noise, which resulted in clearly defined, albeit non-uniform, contour regions. The filter applies a weighting function to all pixels within a radius of influence, r_{inf}, using:

$$G(x,y) = \frac{1}{2\pi\sigma^2} e^{-\frac{(x^2+y^2)}{2\sigma^2}} \tag{3.1}$$

where σ is the standard deviation of the two-dimensional Gaussian distribution G. A distribution is calculated for each pixel which results in a series of concentric circles, so that the pixels closest to the point of application were weighted more than those further away. The default values mentioned in the MATLAB help files are $r_{inf} = 1$ and $\sigma = 0.5$, i.e. only a pixel's neighbour has any influence on the filtered value. Using these default values had virtually no effect on the images here and provided minimal noise cancelling, resulting in disjoint contour regions. Trial and error resulted in values of $r_{inf} = 50$ and $\sigma = 70$ producing a noise-free image that had consistently well-defined contour regions. The resulting filtered image is shown in Figure 3.5a.

Once the images were divided up into contour regions, each region was then assigned its own calibration curve, so that as the dye passed between the brightly and (relatively) dimly lit areas, the concentrations were calculated relative to their position in the water-bath. The calibration curves were created by incrementally adding 2 g of dye to the water-bath, mixing, and a photo taken after each addition. A total of 10 images were used per calibration: images were taken at [0, 0.1, 0.2, 0.3, 0.4, 0.5, 0.75, 1.0 1.5 2.0 g]. The curves were created by interpolating a cubic spline onto this data set. The result is a series of curves, similar to those shown in Figure 3.5b, capable of quantifying the dye concentrations from the experimental images as the dye is transported to different areas of the water-bath. While differences in the x and z directions were taken into account, the relationship between the dye concentration and light intensity was assumed to be uniform in the y direction, as data was only acquired from one camera.

3.2.3.2 Experiments

The images were digitally analysed using custom-built algorithms written using MATLAB. Each image was cropped down to size so that only the water, backlight, cylinder and dye remained in view. This meant that the only region of the image that had pixels possessing low red light-component values was the cylinder. The light radiating from the backlight, passing through the clear water and red dye was depicted by pixels with large red components. This meant that it was possible to accurately determine where the cylinder was located in each image. This was important as a certain proportion of the dye was hidden from view by the cylinder, in each image. In knowing which pixels represented the cylinder, they could either be cropped out of the image entirely or replaced with an

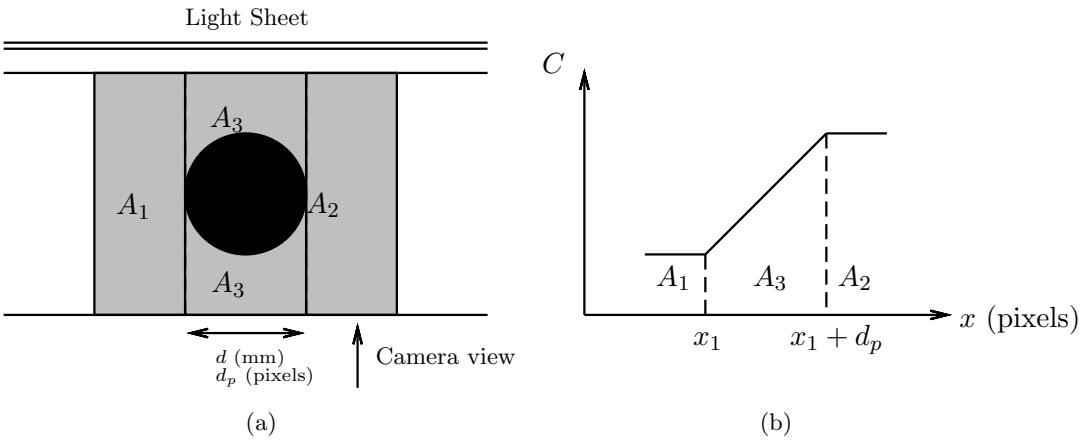

Figure 3.6: (a) Tank as seen from above once the cylinder is in place. Dye to the left and right (from the point of view of the camera) of the cylinder, A_1 and A_2 respectively, is used to estimate the dye occulded by the cylinder, A_3; (b) Sketch of a typical concentration profile estimated for the dye occluded by the cylinder in A_3.

approximation of the dye that they occluded.

Two methods of replacing the cylinder were tested. In the first case, the cylinder was replaced with the average dye concentration as found in the entire image. While this was suitable once the dye was close to being uniformly spread, up until this point this method underestimated the amount of dye in each image. An alternative approach was then adopted, which took the dye values of the pixels along the edge of the cylinder and propagated them through the cylinder's thickness, for each image (see Figure 3.6a). Assuming the cylinder spans d_p pixels of the image in the x direction (assumed to be the direction of translation), the dye concentration, C, was estimated to vary across A_3 linearly as:

$$C(A_3) = C(A_1) + \frac{x}{d_p}\left(C(A_2) - C(A_1)\right), \tag{3.2}$$

for $x = 1 : d_p$, resulting in a dye concentration profile similar to that shown in Figure 3.6b. This yielded a similar result to that obtained from the first approach when the dye was uniformly mixed, but also resulted in a more accurate calculation of the occluded dye for all time. This method was selected for all subsequent analysis.

The extent to which the dye has spread is determined by using the blue light component of the images. The light absorption properties of the dye are such that it absorbs blue light a lot more easily than green or red (see Figure 3.7). Looking at a standard greyscale image (see Figure 3.7a), it is not always clear where the boundary of the dye region is. By examining an intensity map of the blue light component (see Figure 3.7d), the difference

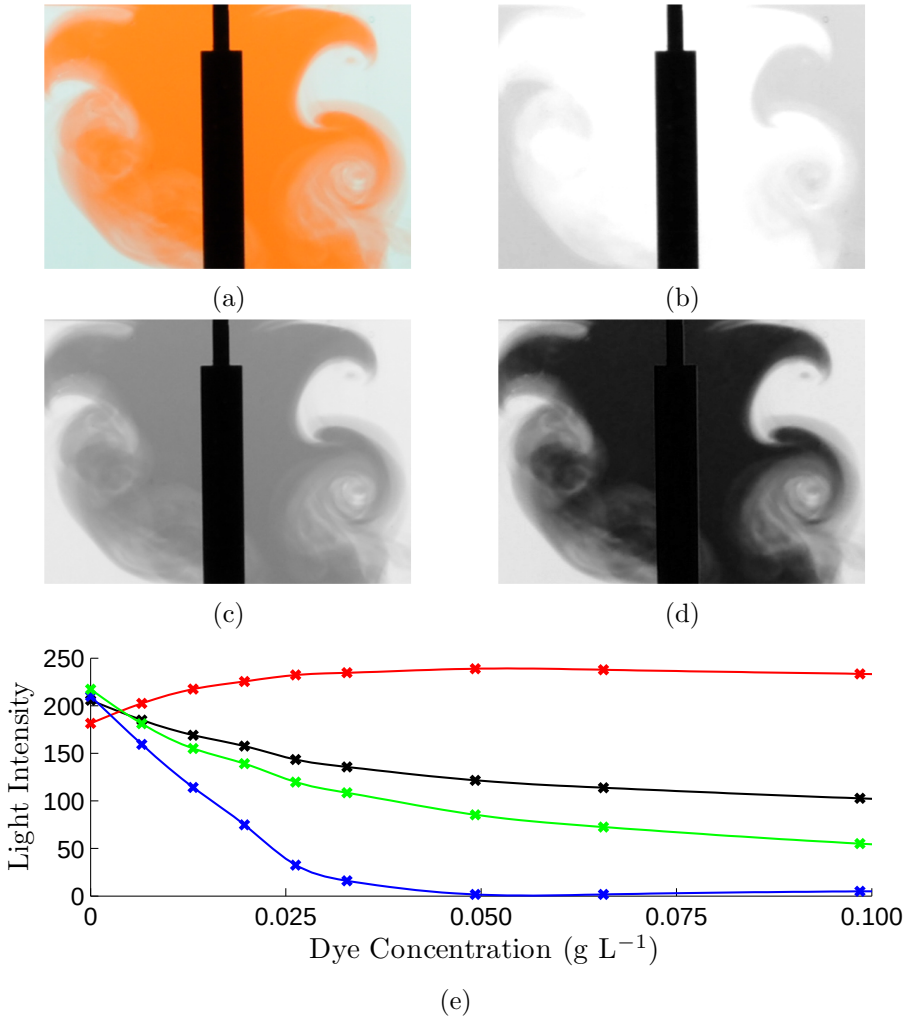

Figure 3.7: (a) Original RGB image; (b) Red component only; (c) Green component only; (d) Blue component only. Darker shades indicate lower light-intensity values. (e) Light intensity response to changing dye concentration. Relationships coloured by light colour, black corresponding to images converted to greyscale using MATLAB's rgb2gray function.

between regions of dye and water becomes clear.

In order to determine dye concentrations, the green component of the pixels is used. As can be seen in Figure 3.7e, neither the red or blue components offer a suitable empirical relationship over the range of dye concentrations under consideration. However, the blue light component is the most sensitive to changes in dye concentration, making it easier to distinguish water from dye based on its value. In light of this, a pixel's blue light component is used to assess whether it contains any dye, but the corresponding green light component is then used in the calibration process to determine its concentration.

3.3 Results and Discussion

3.3.1 Calculation of Mass Conservation

Before the first series of experiments were undertaken, the accuracy of the previously outlined analysis procedure was tested. The equipment was set up as it would be for the experiments, except the cylinder was removed. Doing this meant the cylinder was no longer occluding any dye and the camera could capture all the dye in the water-bath. The dye was placed between the lock-gates and mixed, the lock-gates were removed and the movement of the dye was determined only by the initial momentum imparted from the lock-gate removal and, to a much lesser extent, molecular diffusion. This meant that the dye predominantly stayed in the initial position and fully in view of the central section of the water-bath, allowing the total amount of dye in the tank to be calculated, with confidence, over a period of time.

The principle of mass conservation means that the total amount of dye in the water-bath does not change with time. As such, for the image analysis procedure to be meaningful, it is desirable that the calculated mass of dye in the water-bath is also conserved. The total calculated mass of dye in an image, m, was obtained by using the calibration curves to

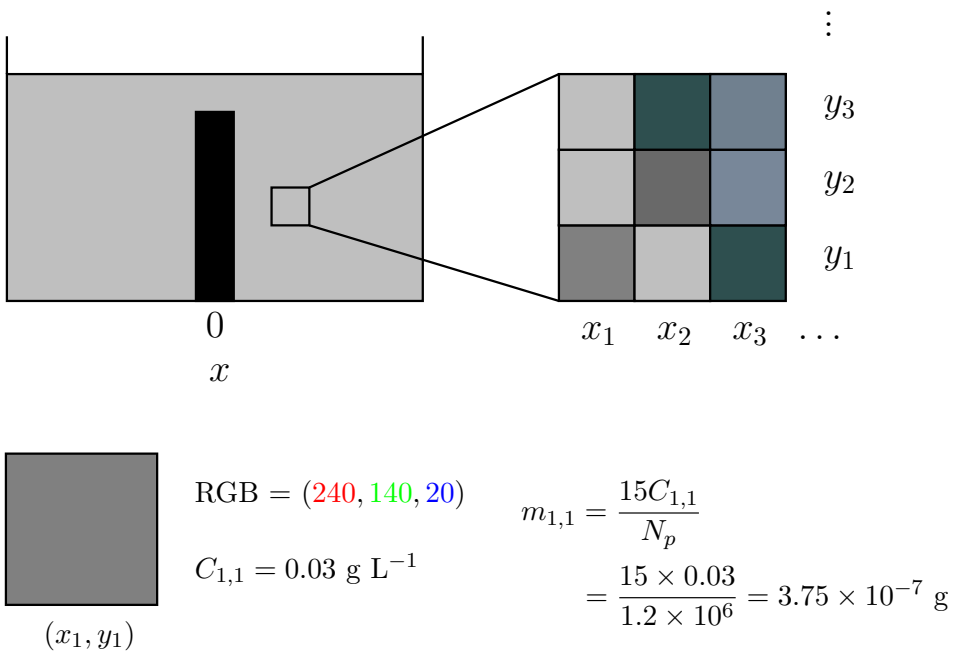

Figure 3.8: Sketch of a small selection of pixels of a greyscale image. Allocating the pixels cooridnates (x_i, y_j), as shown, allows for calculation of the mass of dye, $m_{i,j}$, in each pixel of each image. Example procedure shown for one pixel, (x_1, y_1).

calculate the amount of dye represented by each pixel, $m_{i,j}$ (for x_i and y_j), and summing them. The dye concentrations obtained from the calibration curves are used to calculate a mass for each pixel, and subsequently the entire image, using:

$$m_{i,j} = \frac{15\, C_{i,j}}{N_p} \tag{3.3}$$

$$m = \sum_i \sum_j m_{i,j} \tag{3.4}$$

where $C_{i,j}$ is the dye concentration calculated for the pixel with coordinates (x_i, y_j) and N_p is the number of pixels in the image. The factor 15 was introduced to equation 3.3 as the calibration curves relate light intensity to concentration in grams per litre (g L^{-1}) and the corridor section of the water-bath held 15 L of water, thus giving the right hand side of equations 3.3 in grams. This is then divided by the number of pixels in the image ($N_p \approx 1.2 \times 10^6$) to give a calculated mass of dye in each pixel. All values of $m_{i,j}$ are then summed to give the total mass of dye, m, as shown in equation 3.4. An example for the calculation of the mass of dye in one pixel is shown in Figure 3.8. This procedure was repeated for every pixel and automated using a script written in MATLAB (see Appendix A).

Over a period of 2 minutes the calculated amount of dye in the tank, m, decreased by only 6 % from the initial value, m^0 (see Figure 3.9)[2]. The values for m are also subject to small fluctuations, possibly due to a combination of lighting conditions and the dye mixing so that the concentration is not constant along a light ray in some places. Once

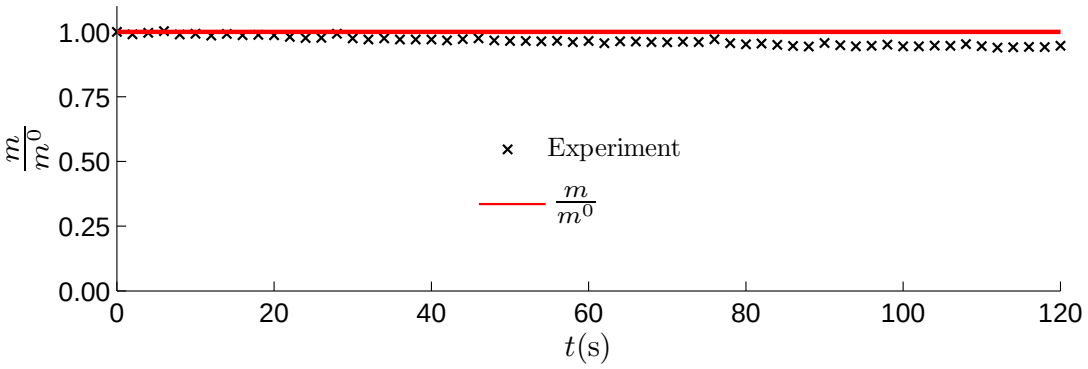

Figure 3.9: Total amount of calculated dye in the tank, m, normalised by the mass calculated from the first image after the lock gates are removed, m^0, over a two minute sequence of images.

[2]Here, the convention of superscripts referring to time and subscripts referring to spatial parameters is adopted. A popular approach in fluid dynamics textbooks.

the cylinder was replaced for the experiments, the size of these fluctuations understandably increased, as equation 3.2 was used to estimate the dye concentration hidden from view. The largest fluctuations from the mean correspond to the largest cylinder diameters, due to the increase in the size of the region blocked by the cylinder and hence mass calculated by equation 3.2.

Each experiment, with a cylinder, was run until the dye in the tank appeared uniformly mixed. However, the images were only analysed on the proportion of the recorded data where the dye was contained in the 1 m corridor section of the tank, 0.5 m either side of the cylinder's initial location. As the cylinder translated back and forth in the tank, a proportion of the dye was eventually transported from the corridor region into the two end-tanks. The camera was set up to only capture images of the dye in the central section of the water-bath and as such, the loss of dye resulted in an error in the calculation of the mass of dye, which compromised the accuracy of the analysis. It is therefore important to identify the point in an experiment where this is significant and hence quantitative analysis can no longer be performed.

To compare the point at which the quantitative analysis is no longer appropriate, the non-dimensional parameter ωt is introduced, which corresponds to the number of completed traverses of the tank (see Figure 3.10). From here on, the moment at which a significant mass of dye has left the corridor is denoted as ωt^*. Each combination of

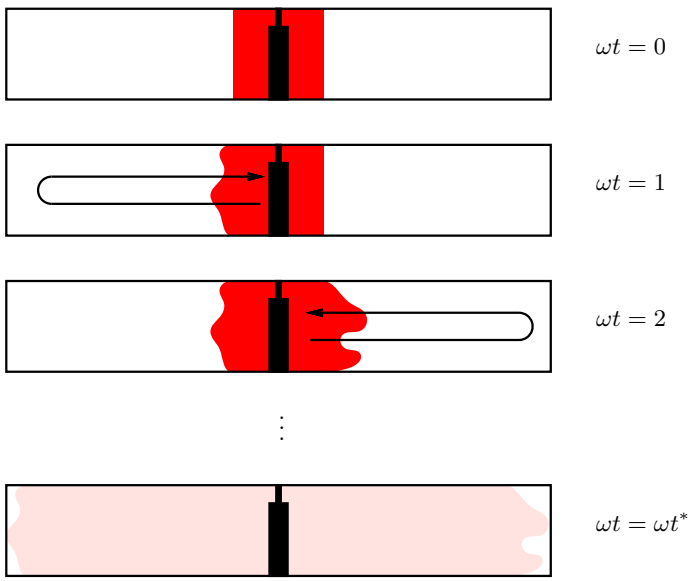

Figure 3.10: Sketch depicting how ωt relates to each experiment and visualisation of the point ωt^*.

cylinder diameter, d and translation frequency, ω has its own value of ωt^*. Values of ωt^* are obtained by analysing the values of the dye concentration at the ends of the central section of the water-bath. The value of ωt^* relating to a specific experiment is defined to be the moment at which the concentration at one end of the water bath reaches 2% of the initial concentration. The method by which the dye concentration is calculated from the experimental images is explained later in Section 3.3.2.

The value of 2% was chosen as it coincides with the value expected when judged by eye when looking at the experimental images and comparing with the calculated mass plots seen in Figure 3.11 and 3.12. Attempts were made to define ωt^* in a more rigorous manner by defining it to be the point at which a certain percentage of dye had left the observable section of the water-bath. However, due to small fluctuations in the calculated value of m, this led to calculated values of ωt^* not in agreement with the analysed images, which showed that the dye had clearly not reached the ends of the tanks. Because of this, ωt^* should be taken as more of a guide, rather than the precise moment at which the dye begins to leave the central section of the water-bath. Values of ωt^* are given in Table 3.1.

Figures 3.11 and 3.12 show the normalised mass of dye in the tank for all cylinder diameters plotted against ωt, as calculated for all the experiments, where the mass is normalised by $\bar{m}$, the mean value of m for $0 \leq \omega t \leq \omega t^*$. Most the experiments show an initial period of dye conservation up to a particular value of ωt that is comparable to the value of ωt^* given in Table 3.1, dependent on d. After this point the normalised mass of dye steadily drops as the dye migrates to the end tanks. The most notable exception to this is seen in Figure 3.11b, for the $d = 15$ mm experiments, where the calculated mass is in decline well before the calculated values of ωt^* are reached. It was found that the calibration curves relating to the experiments performed for this cylinder size were noisier and less consistent than the others. This could have led to the concentrations calculated throughout the tank being inconsistent or inaccurate, possibly as a result of human error during calibration.

d (m)	ω (s^{-1})	ωt^*	d (m)	ω (s^{-1})	ωt^*
0.010	0.143	>44.2 †	0.0335	0.132	6.3
0.010	0.200	>66.7 †	0.0335	0.205	7.1
0.010	0.231	>76.2 †	0.0335	0.231	7.1
0.010	0.258	>83.1 †	0.0335	0.260	8.1
0.010	0.287	87.8	0.0335	0.294	9.2
0.015	0.139	>41.9 †	0.040	0.071	6.9
0.015	0.194	46.3	0.040	0.107	6.5
0.015	0.227	36.3	0.040	0.137	7.0
0.015	0.265	41.6	0.040	0.192	6.0
0.015	0.295	45.8	0.040	0.228	7.7
0.020	0.054	12.8	0.050	0.139	3.5
0.020	0.139	14.1	0.050	0.201	4.7
0.020	0.200	18.3	0.050	0.226	4.4
0.020	0.237	14.9			
0.020	0.252	11.0			
0.025	0.139	12.8			
0.025	0.192	12.0			
0.025	0.222	13.5			
0.025	0.241	14.4			
0.025	0.290	10.0			

Table 3.1: Values of ωt^* for all experimental cases. † Denotes those experiments for which the 2% concentration was not reached having analysed all available experimental data

The calculated mass of dye, m, is subject to fluctuations, probably due to a combination of the estimated dye concentration provided by equation 3.2 and the small fluctuations in light intensity due to the backlight. If the analysis method worked perfectly, the mass-conservation plots shown in Figures 3.11 and 3.12 would depict a horizontal line at $m/\bar{m} = 1$ for $0 \leq \omega t \leq \omega t^*$, then a negative gradient thereafter. Most of the experiments show trends that represent this ideal scenario, although the data is subject to small fluctuations.

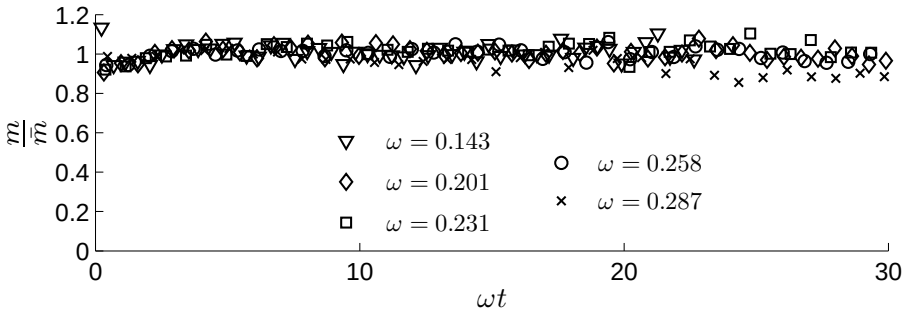

(a) $d = 10$ mm

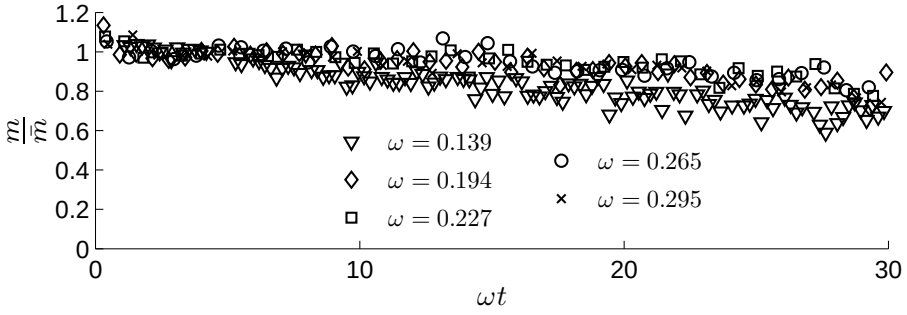

(b) $d = 15$ mm

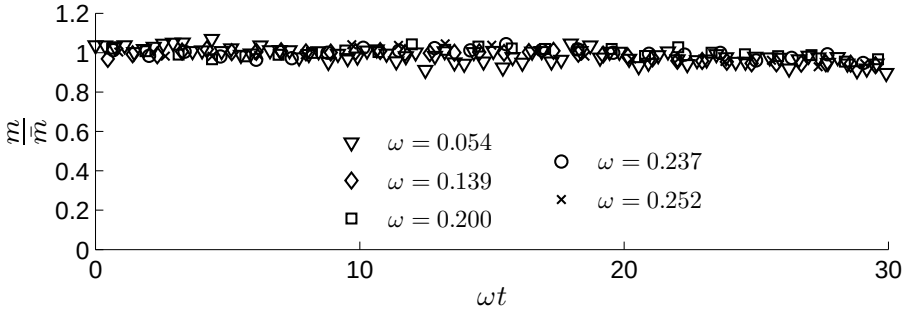

(c) $d = 20$ mm

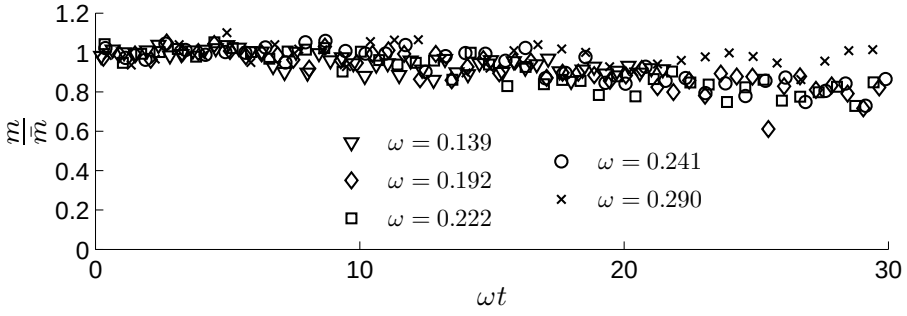

(d) $d = 25$ mm

Figure 3.11: Mass of dye in the tank, m, normalised by $\bar{m}$, the mean amount of visible dye in the tank for $0 \leq \omega t \leq \omega t^*$ in each experiment, plotted against non-dimensional parameter ωt for: (a) $d = 10$ mm; (b) $d = 15$ mm; (c) $d = 20$ mm; (d) $d = 25$ mm;

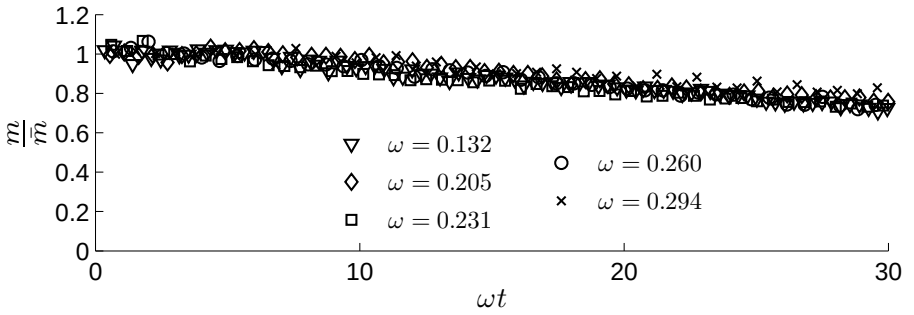

(a) $d = 33.5$ mm

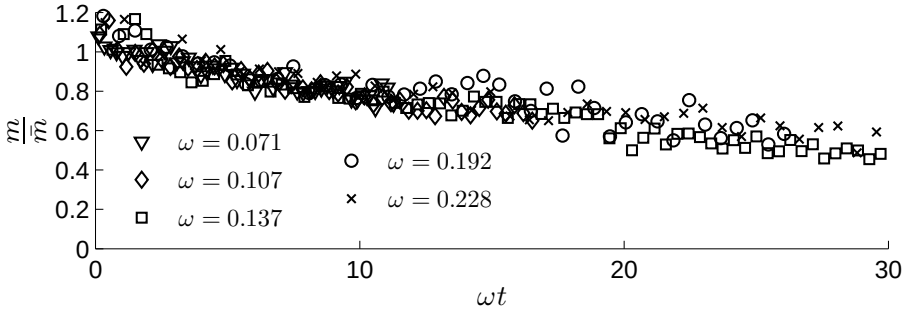

(b) $d = 40$ mm

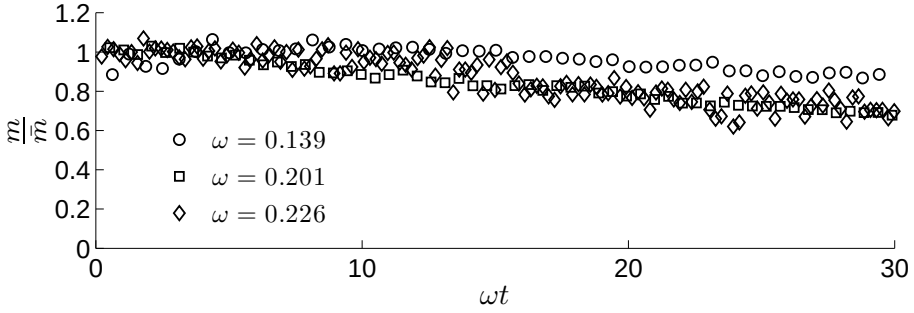

(c) $d = 50$ mm

Figure 3.12: Mass of dye in the tank, m, normalised by $\bar{m}$, the mean amount of visible dye in the tank for $0 \leq \omega t \leq \omega t^*$ in each experiment, plotted against non-dimensional parameter ωt for: (a) $d = 33.5$ mm; (b) $d = 40$ mm; (c) $d = 50$ mm.

3.3.2 Quantifying Dye Transport

The mixing induced by the translation of the cylinder over time is shown qualitatively in Figure 3.13, for $d = 20$ mm and $\omega = 0.139$ s^{-1}. This shows a typical set of images before any image analysis (Figure 3.13a) and the false colour dye contours that are produced after image analysis has been performed (Figure 3.13b). Focussing on the original images, the dye can be seen to be getting mixed with each successive image. However, the boundary between what is water and what is dye is not clear for all but the first image ($\omega t = 0$). The analysed images reveal a clearer picture of the dye transport than the originals. Using a series of 'look-up tables' created from the calibration curves, dye concentrations are

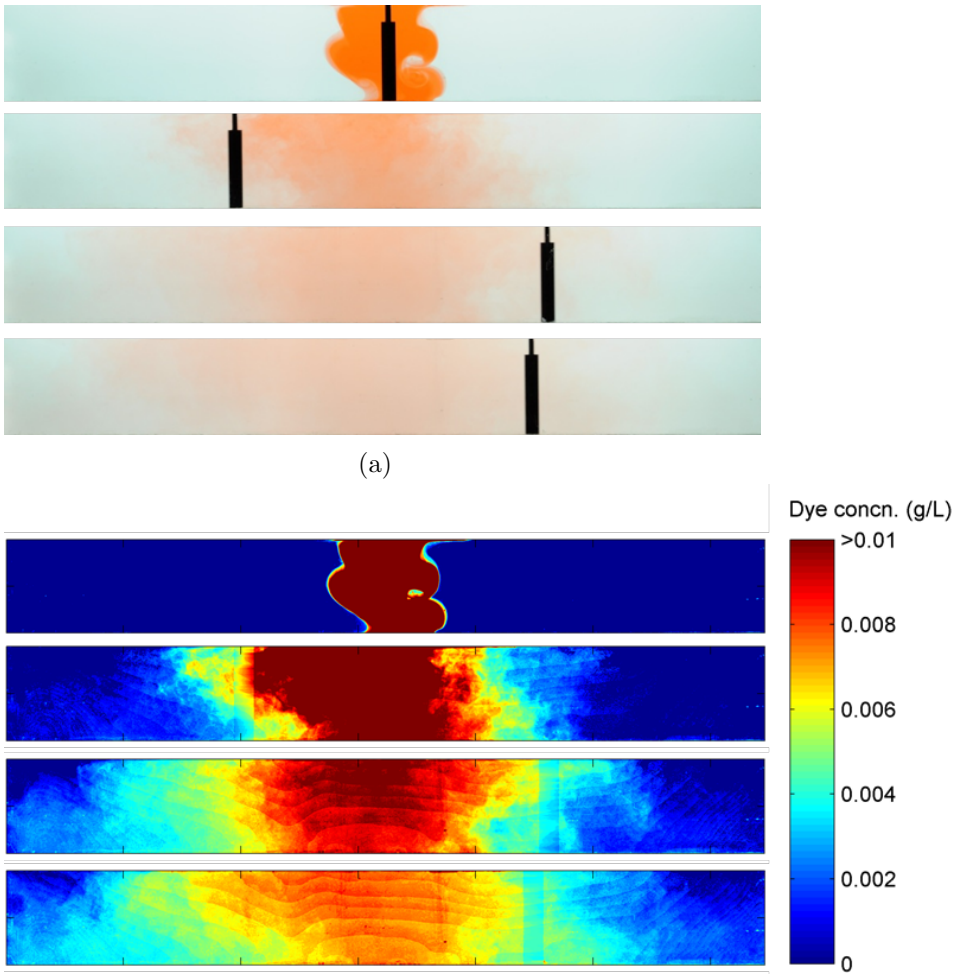

(a)

(b)

Figure 3.13: Example images depicting the cylinder induced contaminant mixing over time. Here, $d = 20$ mm and $\omega = 0.139$ s^{-1} (a) Time series of original images. (b) False colour dye concentration contours. Images are at $\omega t = \{0, 5.2, 10.8, 15.9\}$, the final image being just after the calculated value of $\omega t^* = 14.1$

.

obtained from the light intensities. The images in Figure 3.13b show quantitative data for dye concentrations below 0.01 g L^{-1}. In the first three images there are regions of saturation, indicated by the solid dark red areas, which are off the scale. The scale has been chosen this way to highlight the boundary between dye and water at either end of the image.

Images like those produced in Figure 3.13 give a visual representation of the dye concentrations throughout the tank, but are only able to give qualitative information regarding the transport of the dye within the water-bath. To determine quantitative behaviour, further analysis is required. The calculated concentrations of dye per pixel, $C_{i,j}$, can be used to determine an average dye concentration along a particular 'column'

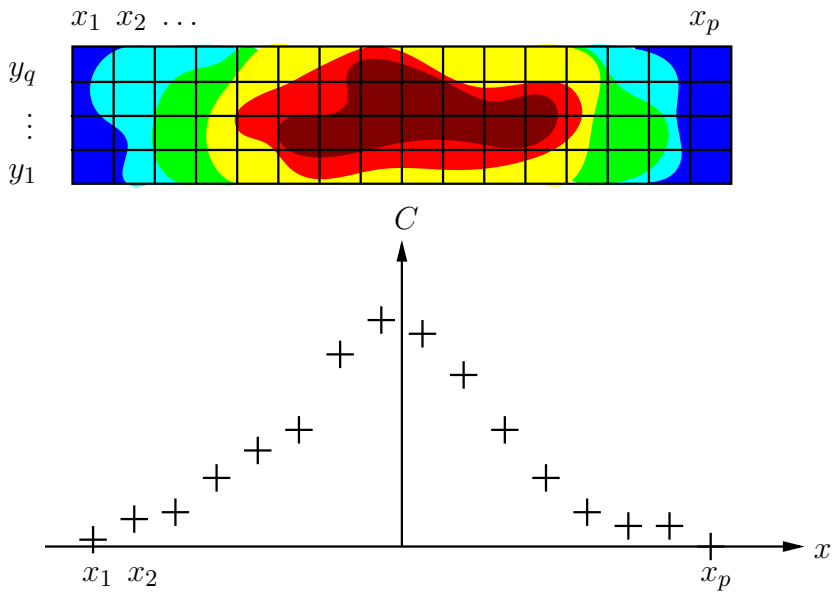

Figure 3.14: Example of a dye contour image and the profile it may produce when averaging the concentration in the y direction.

of pixels, C_i (pixels with $x = x_i$), giving a one-dimensional dye profile along the length of the water-bath:

$$C_i = \frac{1}{q} \sum_{j=1}^{q} C_{i,j} \tag{3.5}$$

where the image is assumed to be made up by pixels with coordinates taken from $(x_1, \cdots, x_p)$ and $(y_1, \cdots, y_q)$ (see Figure 3.14). As these profiles can be calculated at different timesteps, the progression of the dye over time can be carefully tracked.

Figure 3.15 shows how the normalised and y-averaged dye concentration varies along the length of the water-bath for various d and ω combinations as the number of traverses, ωt, increases. Comparisons between values of ωt for different experiments is not possible, as the times at which the photos were captured is not consistent. The values shown are chosen to highlight the changes in the dye concentration profile over time for a particular experiment, up to the calculated value of ωt^*. The concentrations are normalised by C^0, the peak concentration in the first image after the lock-gates were removed, so that each series of concentration profiles is on a $[0, 1]$ scale, hence the profile plots obtained at ωt^* correspond to the moment when the normalised concentration has reached 0.02 at one end of the water-bath.

For these plots, x is defined as the distance coordinate running the length of the water-bath

and its origin is located at the centre of the cylinder in its initial position. At $\omega t = 0$, the dye is in its starting location just after the lock-gates have been removed. The slight depression at the peak of the curve is where the cylinder occludes the dye, as has already been discussed. The linear relationship used to estimate the dye in this region, as outlined in equation 3.2, is clearly visible in this same region. As ωt increases, the dye remains at its highest concentration nearest its initial location, for most cases. For some of the cases where $d = 33.5, 40$ or 50 mm (not shown) there is a slight shift in the location of the dye cloud, so that the resulting distribution is centred around a non-zero value of x (see Figures 3.15e and 3.15f). This is to be expected as the larger cylinders impart a larger momentum to the contents of the water-bath.

Plots for successive values of ωt show the dye spreading out from the location of largest concentration as a series of flattening bell curves, getting more dilute as x tends to the ends of the tank. Although only six d and ω combinations have been used to show the changes in C over time, with all demonstrating the flattening and widening of the distribution over time, all experiments showed a similar trend.

Although the concentration profiles cannot be compared at specific ωt values, what can be seen in Figure 3.15 and the data in Table 3.1 is that the value of ωt^* decreases with increasing cylinder size, implying that the larger cylinders are mixing the dye at a faster rate. This potential relationship between the rate of mixing and cylinder size is now explored by building a model that aims to capture the concentration profiles found for all the experiments.

3.4 Theoretical Model for Dye Distribution

The dye concentration profiles shown in Figure 3.15 all show similar behaviour. In an attempt to predict these profiles with a theoretical model, first it is useful to consider a more general model as a starting point. Consider a concentration distribution, $C(x, t)$, diffusing in one dimension in an unbounded domain with initial mass, m:

$$m = \int_{-\infty}^{\infty} C(x, 0)\, dx. \tag{3.6}$$

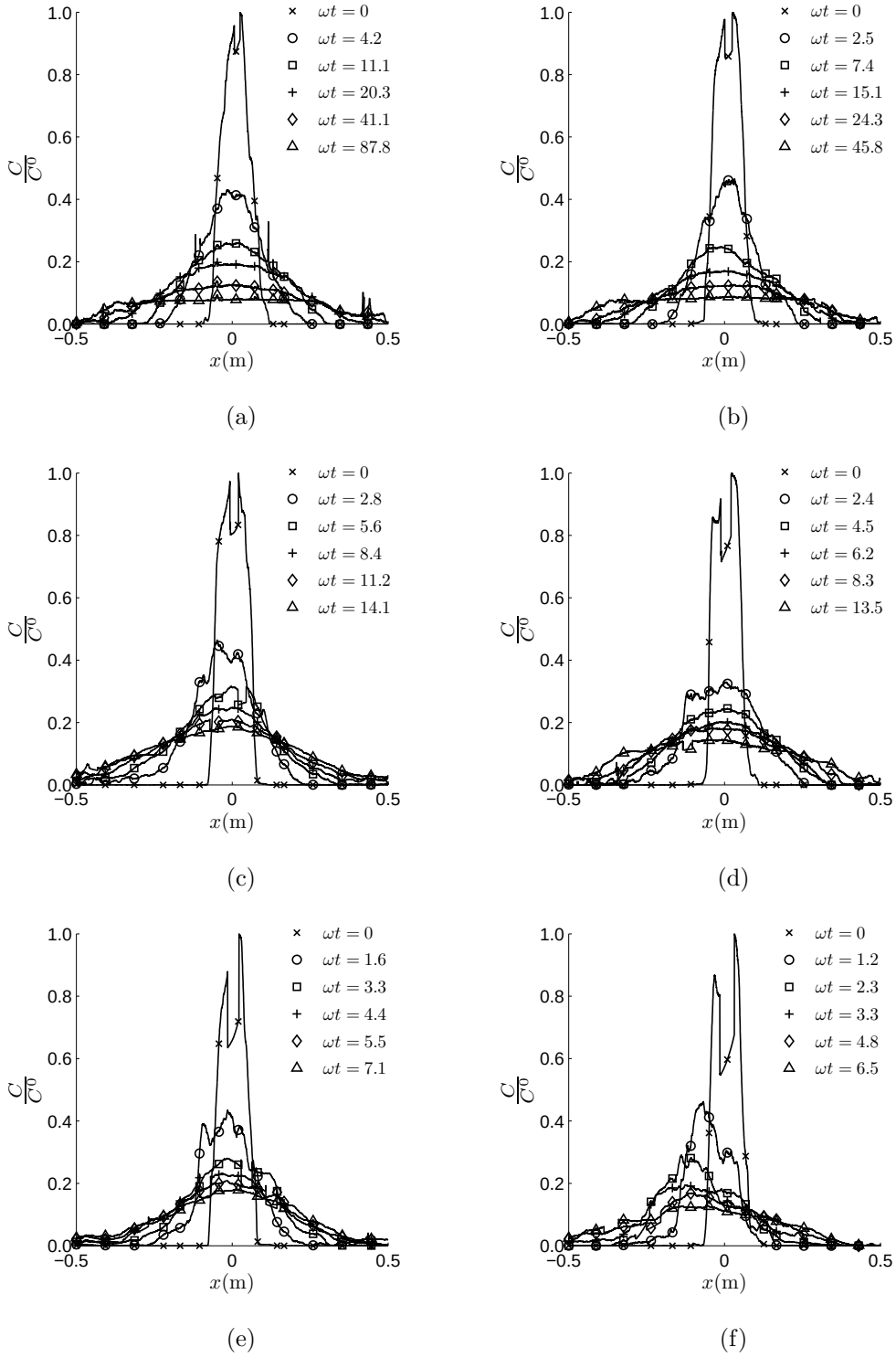

Figure 3.15: Profiles of dye concentration, C, normalised by peak initial concentration, C^0, for: (a) $d = 10$ mm, $\omega = 0.287$ s^{-1}; (b) $d = 15$ mm, $\omega = 0.194$ s^{-1}; (c) $d = 20$ mm, $\omega = 0.139$ s^{-1}; (d) $d = 25$ mm, $\omega = 0.222$ s^{-1}; (e) $d = 33$ mm, $\omega = 0.205$ s^{-1}; (f) $d = 40$ mm, $\omega = 0.107$ s^{-1}.

Applying the principle of mass conservation, it is necessarily true that for all times t:

$$m = \int_{-\infty}^{\infty} C(x,t)\,dx = M_0, \tag{3.7}$$

where M_0 is the zeroth moment of the distribution C. The corresponding first and second moments of the distribution can be calculated as follows:

$$M_1 = \int_{-\infty}^{\infty} xC(x,t)\,dx, \tag{3.8}$$

$$M_2 = \int_{-\infty}^{\infty} x^2C(x,t)\,dx. \tag{3.9}$$

The mean, μ, and variance, σ^2, of the distribution can be calculated from these moments as:

$$\mu = \frac{M_1}{M_0}, \tag{3.10}$$

$$\sigma^2 = \frac{M_2}{M_0} - \mu^2, \tag{3.11}$$

(see Fischer et al. (1979)). With the mean and variance of the distribution calculated as above, it can be shown that the distribution diffuses according to a Gaussian distribution of the form:

$$C(x,t) = \frac{m}{\sqrt{4\pi Dt}} e^{\left(-\frac{(x-\mu)^2}{4Dt}\right)} \tag{3.12}$$

with diffusion coefficient D (Bachelor, 1967; Fischer et al., 1979). Assuming the initial release is at the origin, integration of equation 3.12 allows the mean and variance to be identified as $\mu = 0$ and $\sigma^2 = 2Dt$, respectively.

Although this theory was developed for molecular diffusion of a concentration C in a quiescent fluid, it is postulated that it may be applied for the experiments presented here, where D now takes on the role of a turbulent diffusion coefficient, D_t. Therefore, it is proposed that C may be modelled by the function:

$$C(x,t) = \frac{m}{\sqrt{4\pi D_t' \,\omega t}} e^{\left(-\frac{x^2}{4D_t' \,\omega t}\right)}, \tag{3.13}$$

where $D_t = D_t' \,\omega$. This substitution is introduced as it has already been shown that there is a likely dependence on ωt when characterising the dye transport and mixing (see Figures 3.11 and 3.12). Hence, D_t is likely to be a function of ω. As there are no constraints stated on Re for the original formulation of equation 3.12 by Fischer et al. (1979), it is postulated that equation 3.13 is applicable for all Re in this study.

Assuming experimental values of C obey the relationship proposed in equation 3.13, by fitting a similar function to the experimental data, values for D_t', and hence D_t, can be obtained. To do this, the various concentration profiles are plotted on rescaled x and C axes and then a function is fitted which allows a value of D_t' to be obtained. To motivate this approach, first consider a normal distribution, $f(x)$, with mean $\mu = 0$ and variance σ^2:

$$f(x) = \frac{1}{\sqrt{2\pi\sigma^2}} e^{-\left(\frac{x}{\sqrt{2\sigma^2}}\right)^2}. \tag{3.14}$$

Now consider a second distribution, $g(x)$:

$$g(x) = \frac{1}{\sqrt{2\pi}} e^{-\left(\frac{x^2}{2}\right)}. \tag{3.15}$$

If g were to be plotted against x, it would clearly yield just a single profile over any range of x values, as the remaining parameters are constant. Therefore, consider the rearrangement of equation 3.14:

$$\sigma f = \frac{1}{\sqrt{2\pi}} e^{-\left(\frac{y^2}{2}\right)} \qquad \text{where} \qquad y = \frac{x}{\sigma}. \tag{3.16}$$

Comparing equations 3.15 and 3.16, it is clear that if σf were to be plotted against x/σ, the plots would overlay one another, for any values of σ, over the same range of x values. Applying this same rearranging approach to equation 3.13 :

$$C\sqrt{\omega t} = \frac{m}{\sqrt{4\pi D_t'}} e^{\left(-\left(\frac{x}{\sqrt{\omega t}}\right)^2 \frac{1}{4D_t'}\right)}, \tag{3.17}$$

and defining a parameter, y,

$$y = \frac{x}{\sqrt{\omega t}} \tag{3.18}$$

so that:

$$C\sqrt{\omega t} = \frac{m}{\sqrt{4\pi D_t'}} e^{\left(-\frac{y^2}{4D_t'}\right)}, \tag{3.19}$$

it can be seen that equation 3.19 is in the same form as equation 3.16, assuming D_t' is constant, which means that plotting $C\sqrt{\omega t}$ against $x/\sqrt{\omega t}$ ought to show a collapse of the C profiles for the experimental data, if the model is indeed correct (see Figure 3.16). The same would be true for a rescaling of any combination that contained $\sqrt{t}$, the only

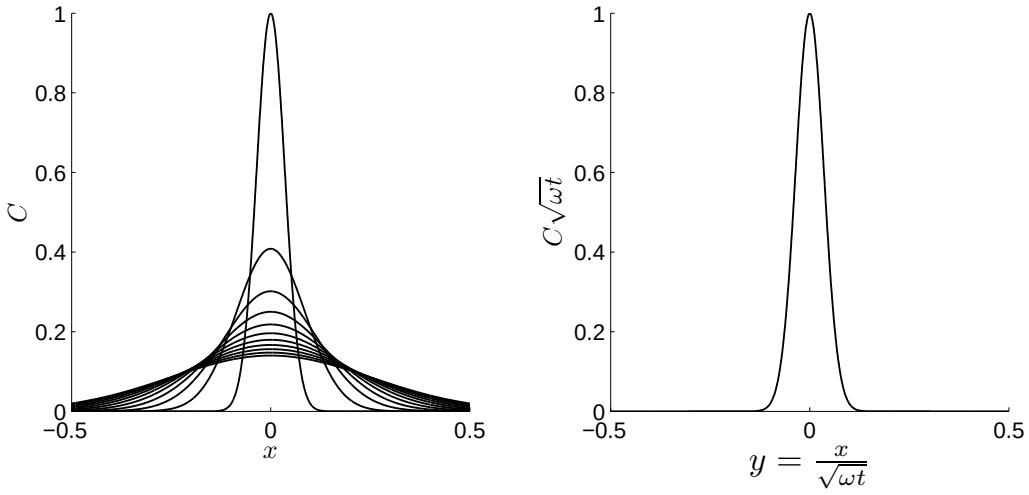

(a) (b)

Figure 3.16: Theoretical plots of C, calculated using equation 3.13 for $-0.5 \leq x \leq 0.5$, $m = 0.05$, $D'_t = 0.0025$, $\omega = 1$ and $t = [1 : 5 : 51]$; (b) Same data with x-axis scaled by $1/\sqrt{\omega t}$ and C-axis scaled by $\sqrt{\omega t}$.

.

parameter that changes in values and hence alters the shape of the C profiles, but $\sqrt{\omega t}$ is chosen as it bears a particular relevance to the data here, it being one traverse of the water-bath.

To obtain values of D'_t, a function of the form:

$$F(x) = \frac{K_1}{\sqrt{4\pi K_2}} e^{\left(-\frac{(x+K_3)^2}{4K_2}\right)}, \tag{3.20}$$

is fitted, using a least squares approach, to the dye concentration profile data rescaled by $\sqrt{\omega t}$, where K_1, K_2 and K_3 are constants to be determined. Comparing equations 3.19 and 3.20, it is clear that, once fitted, values of K_1 will correspond to values of m and values of K_2 will correspond to values of D'_t. Despite the assumption that $\mu = 0$, including the constant K_3 allows the values of K_1 and K_2 to still be appropriately determined when the peak concentration no longer lies at $x \approx 0$ (as was seen in Figure 3.15f when there was a shift in the dye cloud location).

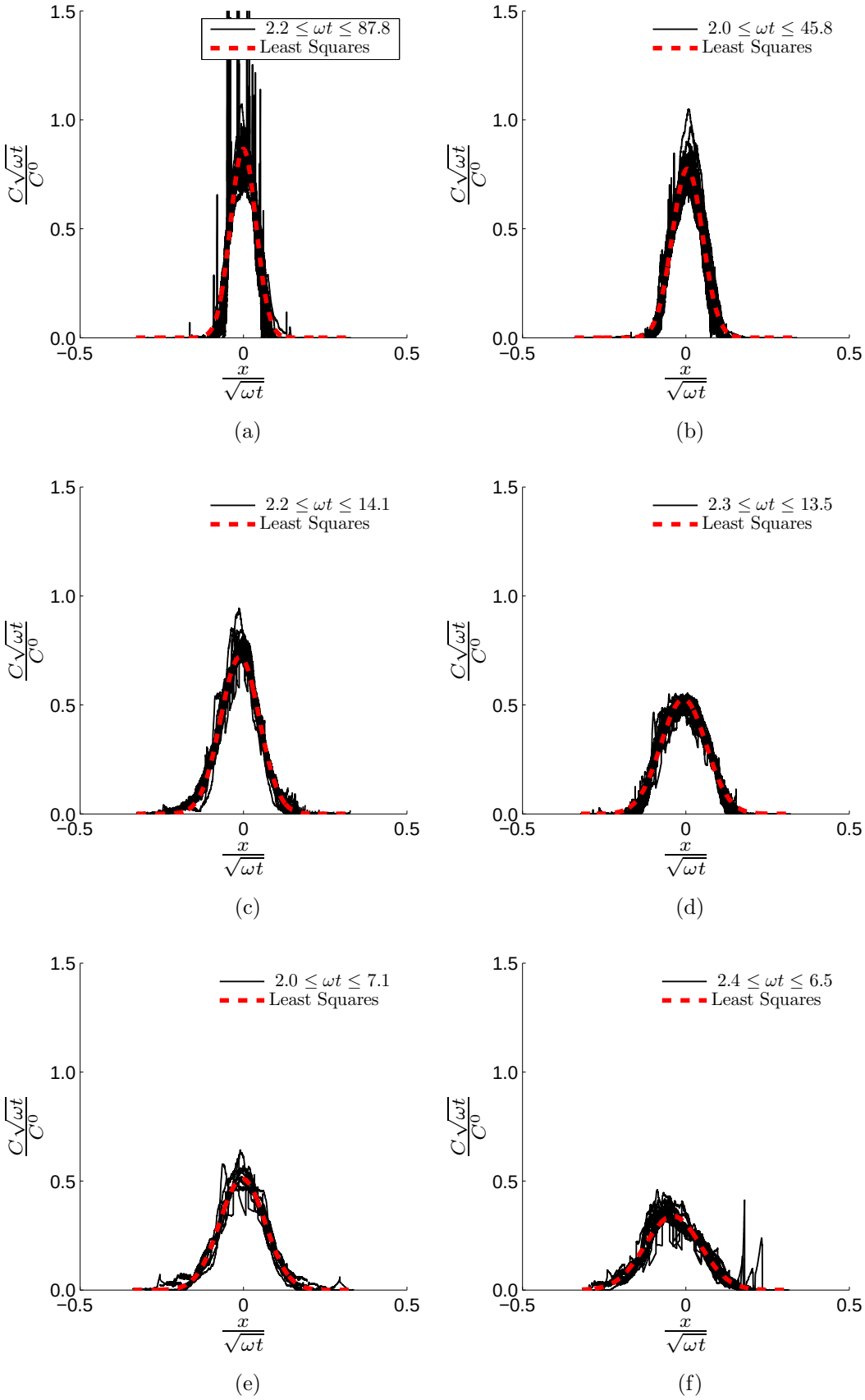

Figure 3.17: Profiles of dye concentration, C, normalised by peak initial concentration, C^0, for $\approx 2 \leq \omega t \leq \omega t^*$ and experimental parameters: (a) $d = 10$ mm, $\omega = 0.287$ s^{-1}; (b) $d = 15$ mm, $\omega = 0.194$ s^{-1}; (c) $d = 20$ mm, $\omega = 0.139$ s^{-1}; (d) $d = 25$ mm, $\omega = 0.222$ s^{-1}; (e) $d = 33$ mm, $\omega = 0.205$ s^{-1}; (f) $d = 40$ mm, $\omega = 0.107$ s^{-1}.

Equation 3.20 is fitted for $\approx 2 \leq \omega t \leq \omega t^*$. By looking at values in this range, the analysis starts after the cylinder has travelled to both ends of the water-bath, reducing any bias associated with the initial direction of travel, and ends before a significant amount of dye has entered the end-tanks. Figure 3.17 shows how the data in Figure 3.15 appears under this transformation for the specified ωt range. In all cases this shows a good collapse of the data, showing that equation 3.13 is indeed a suitable model for the prediction of the dye concentration in the x-direction, however, the dependence of D_t' on the available experimental parameters still needs to be determined. The spiky nature of Figure 3.17a is down to some of the images having a breaking wave near the arm holding the cylinders, which is interpreted as a region of large local dye concentration. The majority of these regions are cropped out but some pixels remain, leaving small 'pockets' of high concentration. As there is only a small number of pixels at this concentration, they do not have a significant impact on the calculated mass of dye.

The values of K_2 obtained from equation 3.20 correspond to values for $D_t^{'}$ and are used as such, allowing a measurement of D_t to be made for all experimental cases (see Figure 3.19a). To determine what comprises $D_t^{'}$, and hence D, dimensional analysis principles may be applied. Diffusion coefficients necessarily have dimensions of *[Length]* ^{2} *[Time]* $^{-1}$. If it is assumed that D has a dependence on ω, then $D_t^{'}$ has units of *[Length]* ^{2}. The most obvious length to assume dependence on is the cylinder diameter, d, as the plots in Figure 3.17 show a change in peak for different sized cylinders. At first it was assumed that $D_t \sim d^2$, but this relationship did not yield consistent results. Instead, it is proposed that the second length-scale contributing to D_t is the amplitude of translation A, so that:

$$D_t = D_t^{'}\,\omega = f(dA\,\omega), \tag{3.21}$$

for some function f. Starting with the most simplest of functions, if f is assumed to be a constant, η say, then:

$$\eta = \frac{D_t}{dA\omega}. \tag{3.22}$$

To see that the proposed definition of η is suitable, Figure 3.18 shows how the value of η described in equation 3.22 is relatively consistent for all Re, albeit with a reasonable degree of scatter. It is now assumed that η is approximately constant over the range of experiments.

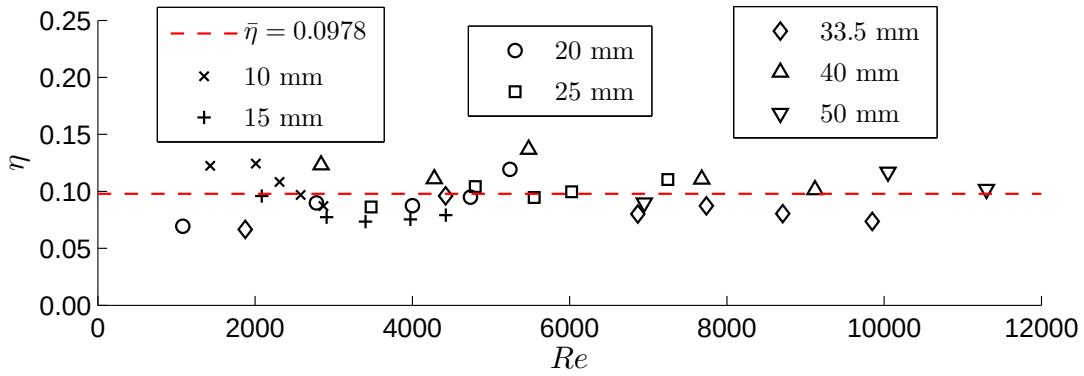

Figure 3.18: η plotted against Re for all experiments and cylinder diameters. The mean $\bar{\eta} = 0.0978$ is used for all subsequent calculations.

Based on a line of best fit $\eta = 0.0978 \pm 0.0407$, suggesting that f can be considered a constant for the range of Re considered, where the Reynolds number is calculated using:

$$Re = \frac{\rho U L}{\mu} = \frac{\rho A \omega d}{\mu}. \tag{3.23}$$

It can be seen in equation 3.23 that the cylinder diameter is chosen as a relevant length-scale and the velocity scale is chosen to be $A\omega$.

Despite the relatively large range for error in the value of η, 42%, it will now be shown how the mean value of $\bar{\eta} = 0.0978$ is able to yield good predictions for D_t.

Equations 3.21 and 3.22, together with $\eta = 0.0978$ combine to give:

$$D_t = 0.0978 d A \omega. \tag{3.24}$$

Equation 3.24 can be used to make predictions of D_t which, in turn, allows predictions of the dye concentration, C.

Figure 3.19 shows how the model predictions compare with the measured values of D_t, where the least squares fitted, linear function takes on values $y = 0.991x + (4 \times 10^{-5})$ with $R^2 = 0.908$. Values of 1 for both the gradient of the least-squares fitted function and the value of R^2 would be the result of a model perfectly replicating the observed values of D_t. Therefore, values of above 0.9 for both these variables is an indicator that equation 3.24 is able to consistently predict suitable values of D_t.

Two of the most obvious outliers correspond with readings taken at $\omega \approx 0.29$ s^{-1} for the $d = 25$ and $d = 33.5$ mm cases (highlighted in the blue circles). One possible explanation

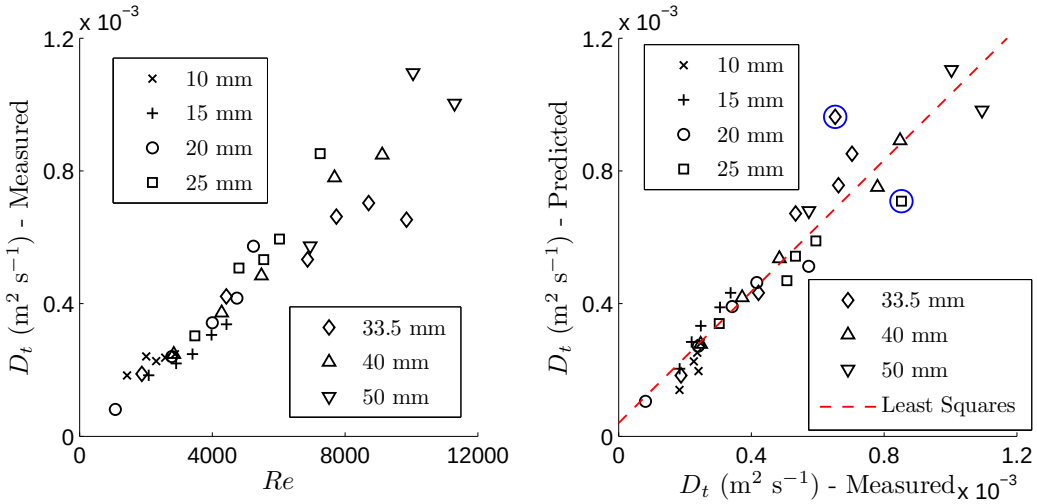

(a) (b)

Figure 3.19: (a) D_t obtained using values of K_2 and plotted against Re. Legend indicates cylinder diameter d; (b) Predicted values of D_t (using equation 3.24) against measured D_t values obtained using values of K_2. Linear function with equation $y = 0.991x + (4 \times 10^{-5})$ is least squares fitted to all data with $R^2 = 0.908$. Potential outliers highlighted with a blue circle.

for these slightly erroneous readings is the increased disturbance at the water level during the experiments, resulting in the occasional misinterpretation of the fluid behind the arm holding the cylinder (as was seen in the 'spiky' dye concentration plot in Figure 3.17a). Although these readings do reside some distance from the model predictions, they are not omitted and still included in the subsequent analysis. However, if these two readings were to be omitted, a stronger correlation is recognised with $R^2 = 0.948$. Further, if the line $y = x$ is fitted to the data, this still results in positively correlated data with $R^2 = 0.890$, suggesting that a constant value for η is in agreement with the values of D_t obtained.

The resulting model concentration profile predictions are shown for two cases in Figure 3.20. Figures 3.20a and 3.20b show how the predicted values of D_t are capable of producing C profiles in excellent agreement with the experimental data (here, $d = 15$ mm, $\omega = 0.139$ s^{-1}). The predicted peak concentration is in agreement with the obtained value and the shape of the profiles is matched throughout. Figures 3.20c and 3.20d show the predictions made for one of the cases where the calculated D_t value could be considered an outlier ($d = 25$ mm, $\omega = 0.290$ s^{-1}). Despite this, the model still shows reasonable agreement with the experimental data for the small time series shown. There is a slight over prediction in the peak concentrations, but there is still substantial agreement between predicted and actual dye profiles towards the ends of the tank (at $x = \pm 0.5$ m).

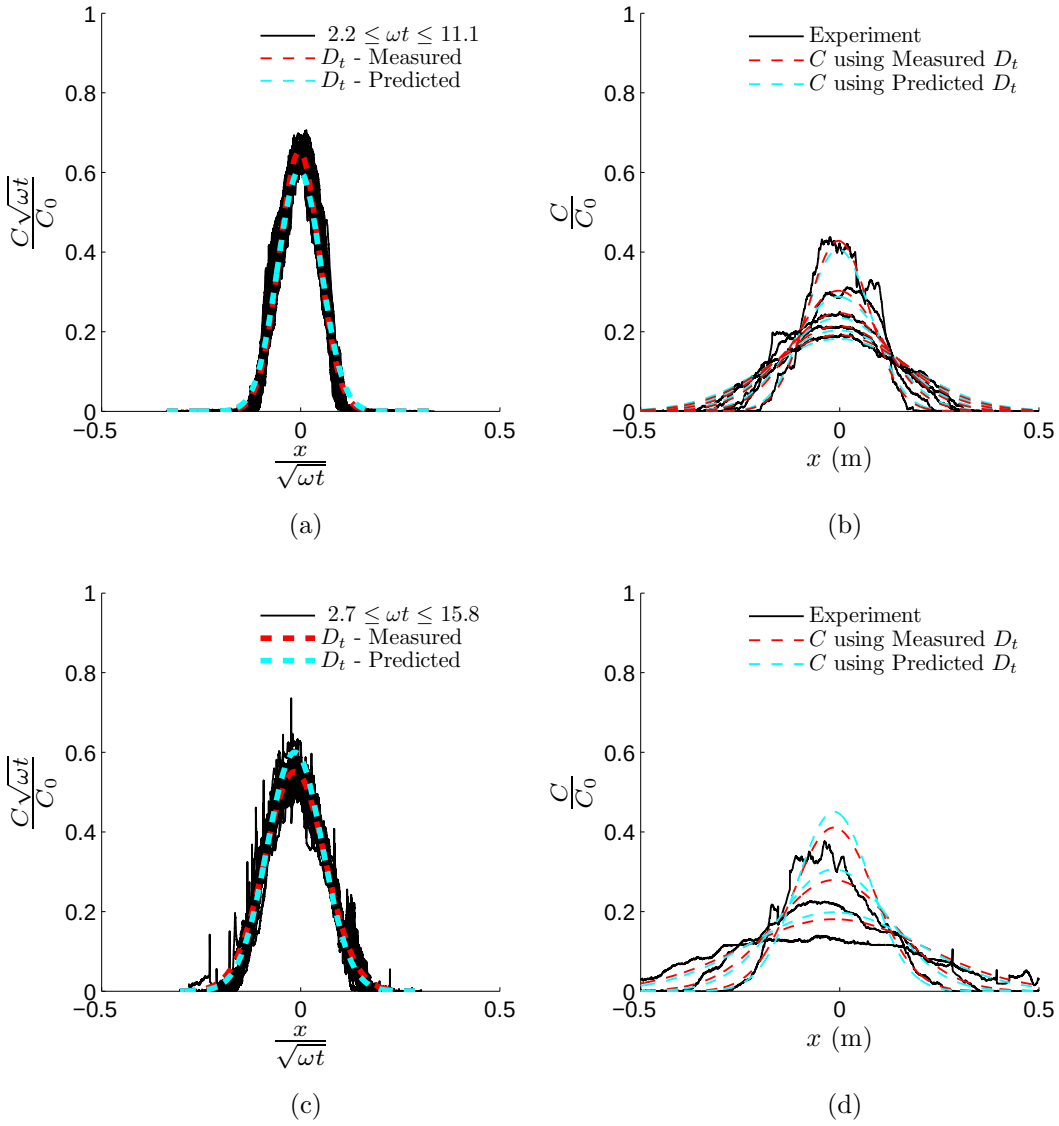

Figure 3.20: Comparison between dye concentration profiles (experiment) and equation 3.20, where D_t is obtained by least-squares (measured) and equation 3.24 (predicted) for: (a)-(b) $d = 15$ mm, $\omega = 0.139$ s^{-1}; (c)-(d) $d = 25$ mm, $\omega = 0.290$ s^{-1}.

3.4.1 Centre of Mass

To compare the model predictions with the experimental data via the concentration profiles of each experiment over any significant period of time is difficult to clearly present. It is more convenient to compare a property that takes on just one value per timestep. Here, the centre of mass, or first moment, of the distribution, $\bar{X}$, is used as a metric.

Using the same coordinate system as defined previously in Section 3.3.1 and shown in Figure 3.8, if $m_{i,j}$ is the calculated mass of dye at pixel coordinates (x_i, y_j), which includes all the dye along an imagined extrusion through the tank at these coordinates, then the

centre of mass of the dye cloud, $\bar{X}$, is:

$$\bar{X} = \frac{\sum_i x_i m_i}{\sum_i m_i} \tag{3.25}$$

where m_i is the sum of the dye masses that have x-coordinate x_i in any given image. For example, considering just the nine pixels highlighted in Figure 3.8:

$$m_1 = (m(x_1, y_1) + m(x_1, y_2) + m(x_1, y_3)) \tag{3.26}$$

$$m_2 = (m(x_2, y_1) + m(x_2, y_2) + m(x_2, y_3)) \tag{3.27}$$

$$m_3 = (m(x_3, y_1) + m(x_3, y_2) + m(x_3, y_3)). \tag{3.28}$$

If m^* is the total mass of dye of these nine pixels, then the centre of mass of dye of these same pixels is:

$$\bar{X} = \frac{x_1 m_1 + x_2 m_2 + x_3 m_3}{m^*}. \tag{3.29}$$

This principle is expanded to all pixels of each experimental image.

Using the same coordinate system as defined previously, with the origin at the cylinder's initial location, $\bar{X}$ can be tracked to the left and right hand sides of the water-bath. To remove any bias from the initial movement of the cylinder, from here on $\bar{X}$ shall refer to the average of the left and right values.

An example of how $\bar{X}$ corresponds to the dye concentration profiles is shown in Figure 3.21. For this one case, where $d = 0.02$ m and $\omega = 0.054$ s^{-1}, $\bar{X}$ is seen to increase as the dye profiles 'flatten', indicating that the dye is spreading along the water-bath in both Figures 3.21a and 3.21b. The relationship between Figures 3.21a and 3.21b is shown in Figure 3.21c for six time values. Only half of the profiles are shown, as $\bar{X}$ corresponds to the average of both sides of the tank and the value of $\bar{X}$ corresponding to each profile is marked using the same colour. The distance between successive values of $\bar{X}$ is clearly decreasing as the dye gets mixed more and more towards homogeneity. Once uniformly mixed, $\bar{X} = 0.25$ m, necessarily equalling the midpoint of half the water-bath length, as long as $x = 0$ is defined to be in the middle (which it is).

To compare model predictions with the values of $\bar{X}$ obtained from equation 3.25, it is first necessary to calculate the zeroth and first moments (see equations 3.7 and 3.8) of

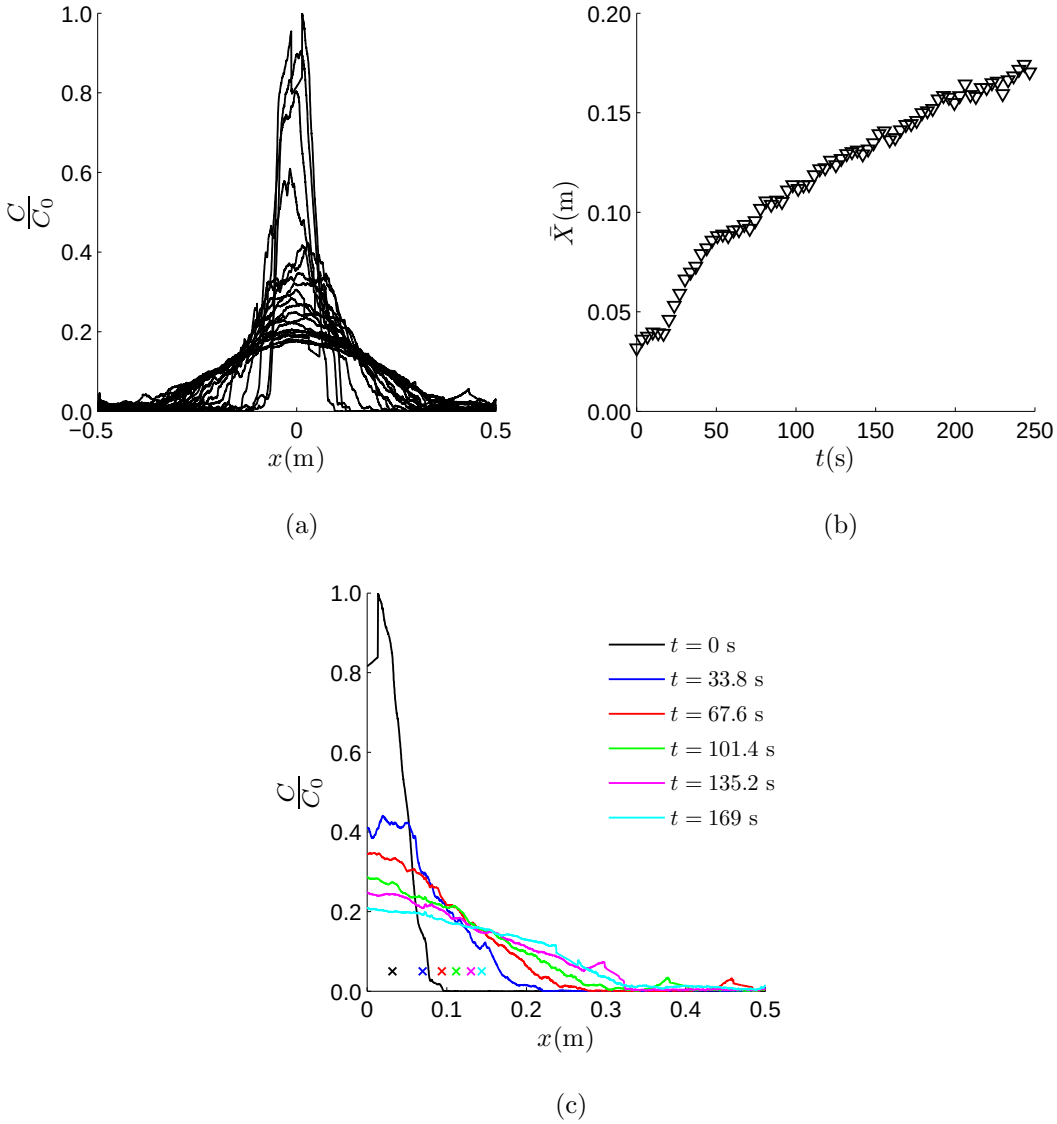

Figure 3.21: Dye concentration data for $d = 0.02$ m and $\omega = 0.054$ s^{-1} over 250 s. (a) C profiles, normalised by initial concentration C_0, readings are spaced 13.52 s apart; (b) $\bar{X}$ over time, readings are spaced 3.38 s apart; (c) Selection of seven concentration profiles with $\bar{X}$ indicated in the corresponding colour. Note that $\bar{X}$ only corresponds to the centre of mass in the x direction, the height of these points on the plot is of no relevance.

the distribution predicted by the model. The value of $\bar{X}$ obtained is an average of left and right values, therefore the centre of mass is calculated on half of the distribution C, implying that $\mu = M_1/M_0$ is no longer necessarily zero.

Zeroth moment

The zeroth moment, for half the distribution, is defined as:

$$M_0 = \int_0^\infty C(x,t)\,dx. \tag{3.30}$$

Using the definition of C from equation 3.12, with $\mu = 0$ and D relabelled to D_t, this yields:

$$M_0 = \frac{m}{\sqrt{4\pi D_t t}} \int_0^\infty e^{\left(-\frac{x^2}{4D_t t}\right)} dx. \tag{3.31}$$

Acknowledging that this Gaussian distribution is symmetrical about $x = \mu = 0$:

$$M_0 = \frac{1}{2}\left(\frac{m}{\sqrt{4\pi D_t t}} \int_{-\infty}^\infty e^{\left(-\frac{x^2}{4D_t t}\right)} dx \right), \tag{3.32}$$

which after substitution becomes:

$$M_0 = \frac{m\sqrt{4D_t t}}{2\sqrt{4\pi D_t t}} \int_{-\infty}^\infty e^{-z^2}\, dz \qquad \text{where } z = \frac{x}{\sqrt{4D_t t}}. \tag{3.33}$$

Knowing that

$$\int_{-\infty}^\infty e^{-z^2}\, dz = \sqrt{\pi}, \tag{3.34}$$

equation 3.33 yields

$$M_0 = \frac{m}{2}. \tag{3.35}$$

First moment

Similarly, the first moment is defined as:

$$M_1 = \int_0^\infty xC(x,t)\, dx, \tag{3.36}$$

$$= \frac{m}{\sqrt{4\pi D_t t}} \int_0^\infty xe^{\left(-\frac{x^2}{4D_t t}\right)} dx, \tag{3.37}$$

$$= \frac{2D_t t m}{\sqrt{4\pi D_t t}} \int_{-\infty}^0 e^z\, dz \qquad \text{where } z = \frac{-x^2}{4D_t t}. \tag{3.38}$$

$$\tag{3.39}$$

Knowing that

$$\int_{-\infty}^0 e^z\, dz = 1, \tag{3.40}$$

equation 3.38 yields

$$= \frac{m\sqrt{D_t t}}{\sqrt{\pi}}. \tag{3.41}$$

This means that the centre of mass of one half of the distribution C is:

$$\bar{X}_c = \mu = \frac{M_1}{M_0} = \sqrt{\frac{4D_t t}{\pi}} = \sqrt{\frac{4\eta dA\omega t}{\pi}}. \tag{3.42}$$

The relationship proposed in equation 3.42 is able to describe the rate at which the dye is transported over time, but it does not take into account the slight differences in initial conditions of each experiment. This theoretical model predicts that initially $\bar{X}_c = 0$, whereas in reality this is not the case due to width of the initially isolated region between the lock gates not being zero. Further, the localised flow effects that occur as the lock-gate is lifted create some uncertainty in the initial conditions of each experiment. This uncertainty is represented by a variable X_0 as follows:

$$\bar{X}_c = \sqrt{\frac{4\eta dA\omega t}{\pi}} + X_0 \tag{3.43}$$

X_0 is calculated on a case-by-case basis, using a least-squares approach, with values for each case given in Table 3.2. There appears to be no underlying relationship between the values of X_0, which is expected as the variable is simply a way of characterising the slight time offset due to the nature of the experiments.

The resulting model predictions for $\bar{X}_c$ are plotted against experimental data for $\bar{X}$ for all seven cylinder diameters in Figures 3.22 and 3.23. The agreement between model predictions and experimental data is, in general, very good for all cylinder sizes. For the five smallest cylinders ($d = 10, 15, 20, 25$ and 33.5 mm) the agreement is consistently strong, with the model predictions capturing the progression of $\bar{X}$ well. For the two largest cylinders ($d = 40$ and 50 mm) the agreement appears less strong, as the experimental data is subject to larger fluctuations. As previously postulated, the larger cylinders are more likely to incorporate more error in calculations relating to dye location, as a larger proportion is estimated when using equation 3.2. This is most apparent in the readings of $d = 40$ mm and $\omega = 0.071$ s^{-1}, and $d = 50$ mm and $\omega = 0.139$ s^{-1}, where the model predictions are seen to deviate from the $\bar{X}$ values in an almost oscillatory manner. Despite the increase in uncertainty regarding the dye concentration occluded by the cylinder for

d (m)	U (m s^{-1})	ω (s^{-1})	Re	X_0
0.010	0.143	0.143	1,430	0.0197
0.010	0.200	0.201	2,010	0.0152
0.010	0.231	0.231	2,310	0.0042
0.010	0.258	0.258	2,580	-0.0069
0.010	0.287	0.287	2,970	-0.0163
0.015	0.139	0.139	2,085	-0.0016
0.015	0.194	0.194	2,910	-0.0076
0.015	0.227	0.227	3,405	-0.0108
0.015	0.265	0.265	3,975	-0.0097
0.015	0.295	0.295	4,425	-0.0136
0.020	0.054	0.054	1,086	-0.0044
0.020	0.139	0.139	2,770	0.0064
0.020	0.200	0.200	4,000	-0.0042
0.020	0.237	0.237	4,746	-0.0003
0.020	0.252	0.252	5,040	0.0148
0.025	0.139	0.139	3,475	0.0014
0.025	0.192	0.192	4,800	0.0125
0.025	0.222	0.222	5,550	0.0046
0.025	0.241	0.241	6,025	0.0051
0.025	0.290	0.290	7,250	0.0170
0.0335	0.132	0.132	4,405	0.0143
0.0335	0.205	0.205	6,878	-0.0012
0.0335	0.231	0.231	7,735	-0.0003
0.0335	0.260	0.260	8,723	0.0037
0.0335	0.294	0.294	9,812	-0.0014
0.040	0.071	0.071	2,840	0.0051
0.040	0.107	0.107	4,280	0.0224
0.040	0.137	0.137	5,480	0.0082
0.040	0.192	0.192	7,680	-0.0086
0.040	0.228	0.228	9,120	0.0082
0.050	0.139	0.139	6,950	0.0270
0.050	0.201	0.201	10,035	0.0079
0.050	0.226	0.226	11,320	0.0138

Table 3.2: Experimental values of d and ω, with corresponding values for Re and X_0.

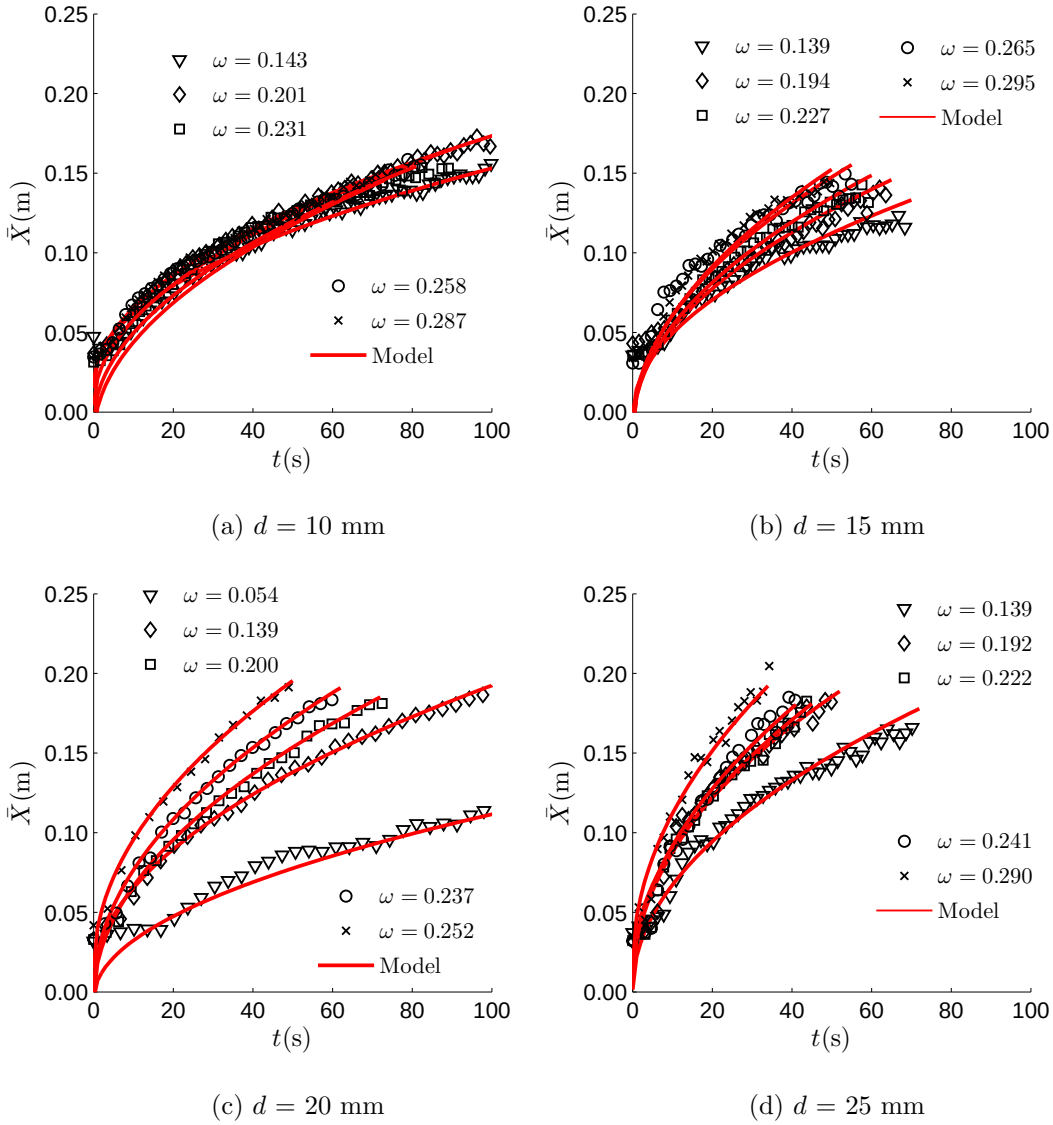

(a) $d = 10$ mm

(b) $d = 15$ mm

(c) $d = 20$ mm

(d) $d = 25$ mm

Figure 3.22: Plots of experimental and theoretical values for the centre of mass of the dye distribution, $\bar{X}$, for: (a) $d = 10$ mm; (b) $d = 15$ mm; (c) $d = 20$ mm; (d) $d = 25$ mm

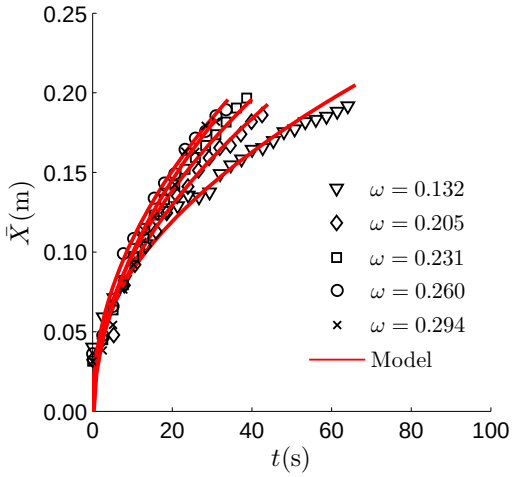

(a) $d = 33.5$ mm

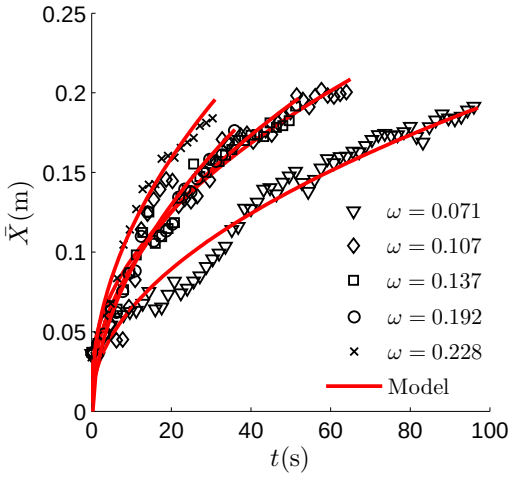

(b) $d = 40$ mm

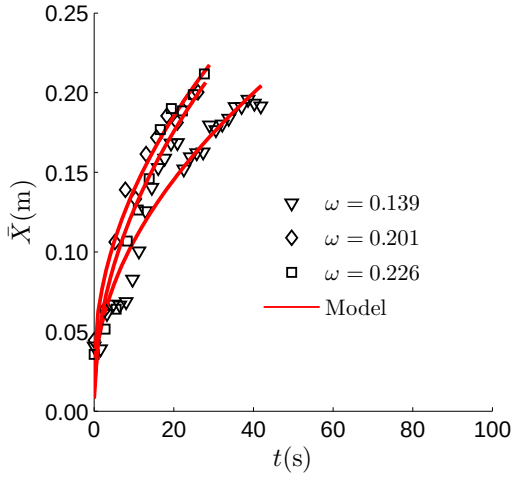

(c) $d = 50$ mm

Figure 3.23: Plots of experimental and theoretical values for the centre of mass of the dye distribution, $\bar{X}$, for: (a) $d = 33.5$ mm; (b) $d = 40$ mm; (c) $d = 50$ mm.

these larger values of d, the agreement between experiment and equation 3.43 is still good.

Although for a full-scale case it may be difficult to determine an appropriate value for X_0, equation 3.43 is capable of predicting the rate at which the dye mixes for all the Re tested, so can potentially be used for predicting any untested d and ω combinations.

3.4.1.1 Varying Amplitude

So far, all the results have been obtained with the cylinder making a full traverse of the tank, $A = 1$ m. As such, it is not certain that the A dependency proposed in equation 3.24 is correct. To test this dependence, a series of experiments were conducted where the

amplitude of cylinder motion was varied. Keeping d and U fixed, A and ω were varied as outlined in Table 3.3.

d (m)	U (m s^{-1})	A (m)	ω (s^{-1})
0.0335	0.056	1.0	0.056
0.0335	0.056	0.7	0.080
0.0335	0.056	0.5	0.112
0.0335	0.056	0.3	0.187
0.0335	0.056	0.2	0.280
0.0335	0.056	0.1	0.560

Table 3.3: A and ω combinations tested in series of experiments investigating the relationship between D_t and A.

As in previous experiments, the data was analysed to determine the evolution of the concentration profiles with time. This series of experiments revealed a bifurcation in the way that the transport and mixing occurred, as indicated by the shape of the dye profiles. Although the larger amplitudes still revealed dye concentrations that appear to be closely related to a Gaussian distribution (see Figures 3.24a - 3.24c), the shorter amplitudes tested showed a bimodal distribution (see Figures 3.24d - 3.24f), which equation 3.13 clearly does not produce.

The three largest amplitudes tested (A = 1.0, 0.7 and 0.5 m) all show behaviour in agreement with the majority of the experimental results for fixed A = 1 m, that is, the distribution appears Gaussian and the rescaling with $\sqrt{\omega t}$ shows a good collapse of the concentration profiles. The fit for the case where A = 0.5 m is the weakest of the three, but the shape of the profile is still Gaussian.

For the smallest three amplitudes (A = 0.3, 0.2 and 0.1 m) the Gaussian distribution is no longer clear and a bimodal behaviour appears. The double peaks of a bimodal distribution are clearly present for the A = 0.2 and 0.1 m solutions, but are less pronounced for the A = 0.3 m solution. Therefore, it is proposed that the relationship proposed in equation 3.24 is indeed valid for varying A, d and ω, but subject to a minimum value of A. It is suggested this value is around $A \approx 0.3 - 0.5$ m, however this is not fully determined here and requires further experimentation.

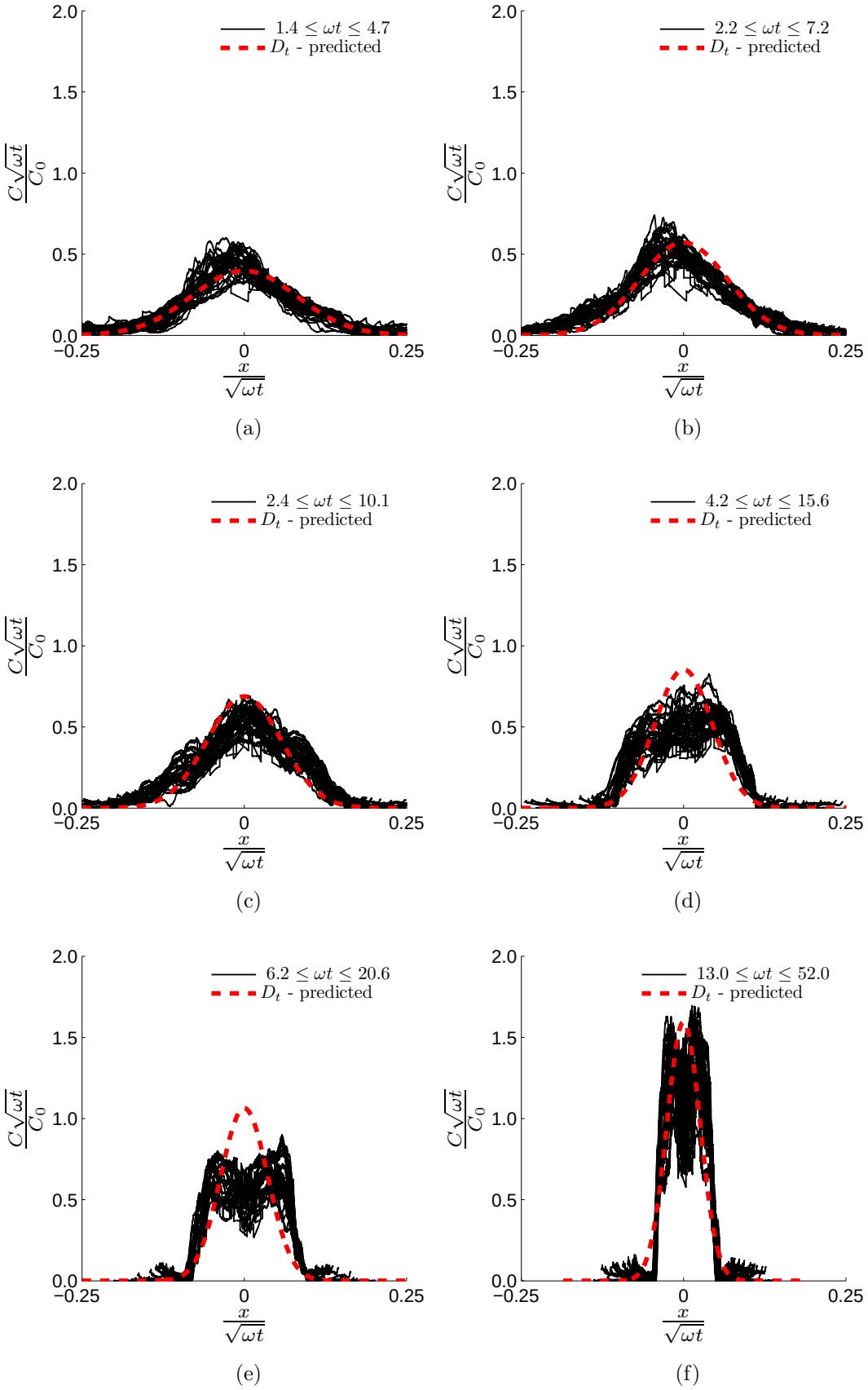

Figure 3.24: Comparison between dye experimental and predicted concentration profiles, normalised by initial concentration C_0, where D_t is obtained by equation 3.24 for d = 33.5 mm and: (a) A = 1.0 m and ω = 0.056 s^{-1}; (b) A = 0.7 m and ω = 0.080 s^{-1}; (c) A = 0.5 m and ω = 0.112 s^{-1}; (d) A = 0.3 m and ω = 0.187 s^{-1}; (e) A = 0.2 m and ω = 0.280 s^{-1}; (f) A = 0.1 m and ω = 0.560 s^{-1}.

3.4.2 Quantifying Error

3.4.2.1 Photograph timing

A SONY, 8GB, class 4, SD card was used in the Nikon D90 camera for all experiments. The class 4 indicates that the card can receive data at 4 MB s^{-1} (SD Association, 2015). The photographs captured were approximately 2 MB in size, suggesting that the photographs ought to be able to be captured every 0.5 s. However, the speed at which the camera was able to output the images could not match this speed, resulting in a longer time between exposures.

The timestamps associated with each photograph were only accurate to the nearest minute. Because of this, the time between exposures, Δt, was estimated based on the number of photographs taken over the entire experiment, the time of which was observed. These estimates yielded timesteps of $\Delta t = 1.5 - 3.5$ seconds, the size of Δt increasing as the memory card became more full. Clearing the memory card after every experiment would have guaranteed that Δt remained as small as possible, however once the calibration procedure was performed the camera could not be touched/disturbed, for fear of disturbing the camera's position and removing the ability to quantify dye concentrations in the water-bath.

Digital cameras have a 'buffer' that enables them to store a finite number of images in the camera's in built memory. The images are held in the buffer, awaiting image processing, and then written to the memory card. The maximum allowable number of images stored in this buffer is dependent upon the size of the image and the size of the buffer. The frequency with which photographs are taken affects how quickly the buffer fills up. When the memory card had a substantial amount of data on it[3], the speed with which the images were passed from the buffer to the memory card slowed, altering the regularity exposures and constant value of Δt. The amount by which Δt changed was hard to gauge, as it was not measured, but it is estimated to change the value of Δt by up to ≈ 0.5 s. These variations have the potential to alter the values of D_t obtained in Chapter 3, although a quick example will show that allowing for slight variation in values of Δt would not significantly alter the findings presented in this chapter.

A Monte Carlo simulation was performed to obtain 1,000 sets of $(t, \bar{X})$ data over 100

[3]The actual value is hard to judge, but estimated to be around 4 GB of data.

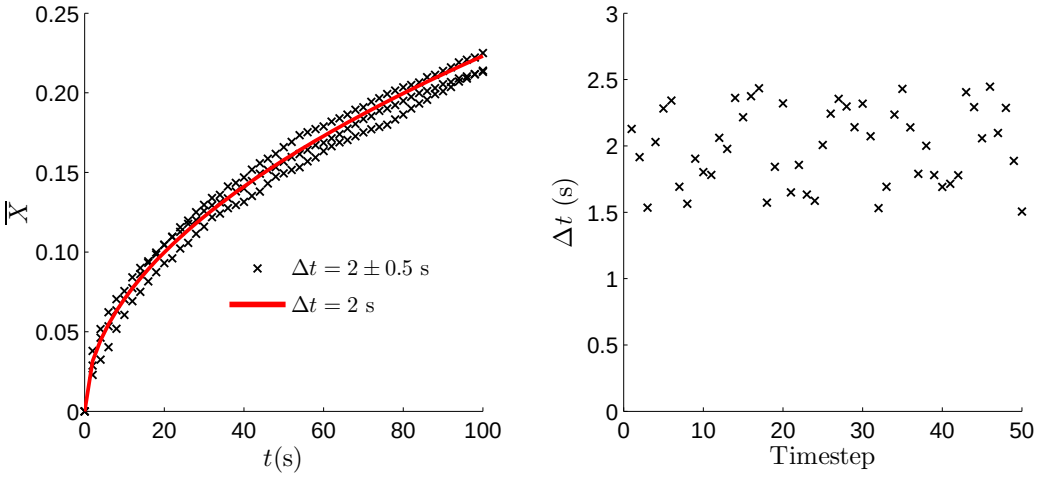

(a) (b)

Figure 3.25: (a) Example of three possible distributions of $\bar{X}$ for random samples of Δt, with a mean of 2 s, when $d = 20$ mm and $\omega = 0.200$ s^{-1}; (b) Typical distribution of Δt from one simulation.

seconds, using equation 3.42, allowing Δt to vary by up to ± 0.5 s (see Figure 3.25). Values of D_t were then calculated from each of these 1,000 data sets, using a least-squares approach. The maximum and minimum of these possible D_t values were then used as error bars to the values previously calculated by equation 3.24 (see Figure 3.26). Repeating this process for all experimental cases showed that the maximum and minimum values of D_t were within $\pm 8\%$. Since the values of D_t directly influence the value of η (see equation 3.22), the impact of the camera buffer on the overall result can be estimated.

The Monte Carlo simulations reveal that an uncertainty in the value of Δt by 0.5 s could only change the value of the constant η by up to 8%. If calculations of equation 3.43 using a value of t_1 yield a particular value of $\bar{X}$, allowing the value of η to vary by $\pm 8\%$, but

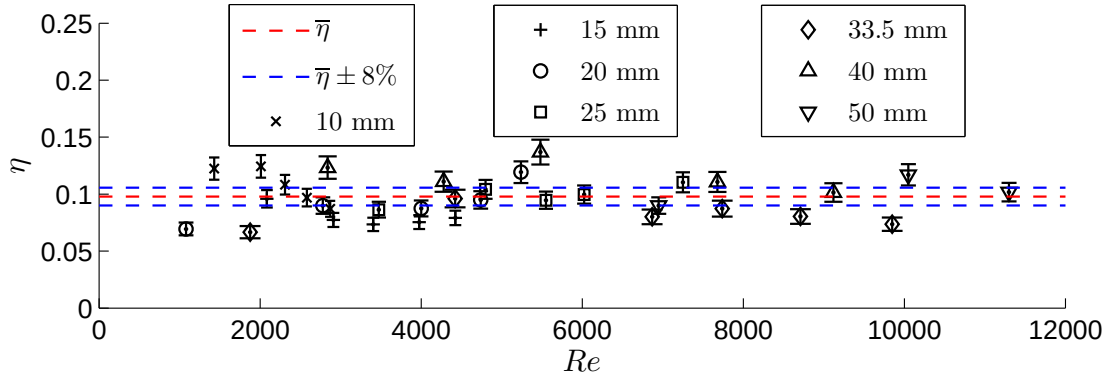

Figure 3.26: Plots of D_t and η for all data, with error-bars estimated

considering the same value of $\bar{X}$ means that:

$$\bar{X} = \sqrt{\frac{4\eta dA\omega t_1}{\pi}} = \sqrt{\frac{4(1 \pm 0.08)\eta dA\omega t_2}{\pi}}, \tag{3.44}$$

$$\implies t_2 = \frac{t_1}{1 \pm 0.08}, \tag{3.45}$$

$$t_2 = 1.087\ t_1(+8.7\%) \quad \text{or} \quad 0.926\ t_1(-7.4\%). \tag{3.46}$$

This means that there could be a change in the predicted rate of spread of a contaminant of up to 8.7%. In all likelihood the error associated with the slight variation in the value of Δt will be smaller than this, as the distribution of Δt values was not as extreme as that seen in Figure 3.25b. The 'click' of the camera, associated with an exposure, sounded consistent for the vast majority of cases, however, estimating a more probable distribution of Δt is difficult as the only source of data on the timing is the author's ear.

3.4.2.2 Calculating Dye Concentration

The calibration curves were constructed using the mean light intensity values, μ, within given contour regions across ten calibration images. The light distribution values obtained within each contour region were normally distributed (see Figure 3.27). By using the variance, σ, of these samples, a tolerance of error for the dye values may be calculated.

A confidence interval of $\pm 2\sigma$ is applied to the mean of each sample, covering $\approx 95\%$ of the distribution, the upper and lower limits of which are then used to calculate alternative calibration curves for a given set of data, to calculate the error associated with calculations of $\bar{X}_c$ (see Figure 3.27c). Values of σ range from 0.38 - 3.04, depending on contour region and amount of dye in the image, with σ values increasing with dye concentration. As there is a value of σ associated with each contour region and each experimental image, there are $\approx 200 - 250$ values of σ per set of calibration data. Since all the calibration curves followed a very similar trend, the values of σ calculated for one data set are assumed to be representative of the corresponding values for all other sets of calibration data. Therefore, only one set of calibration data is considered here, with two experimental cases used as examples to highlight the error associated with the calculated dye concentrations.

Figure 3.28 shows the differences between calculated values of $\bar{X}_c$ when the dye concentrations are populated using values of $\mu + 2\sigma$ and $\mu - 2\sigma$, the values previously

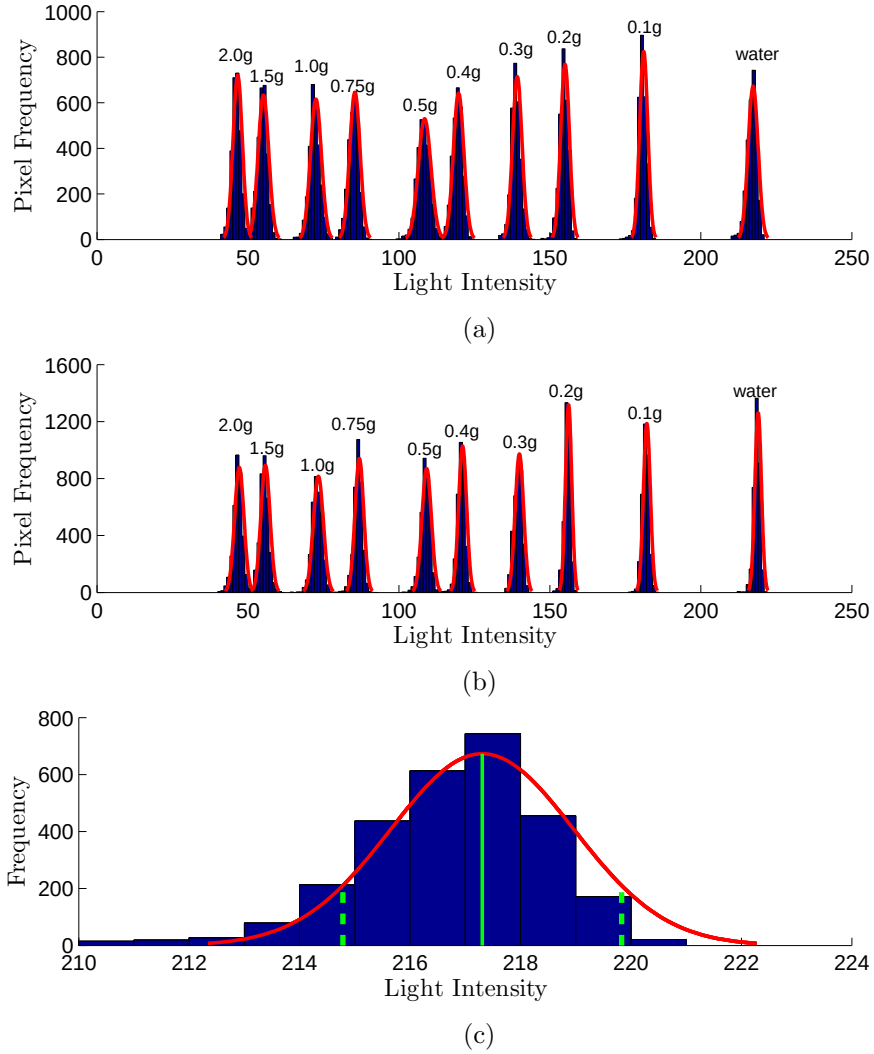

Figure 3.27: (a)-(b) Histograms of light intensity values per pixel for two contour regions, of which there are typically 20-25 per set of calibration curves, across all ten calibration images for one set of data. Text labels correspond to the amount of dye in the water-bath. (c) Typical distribution of just one sample for the image with only water in the tank. Values of μ and 2σ are indicated by solid and dashed green lines, respectively.

documented in Section 3.4.1 lying in between the two sets of data. The likely percentage errors incurred by the calibration curve values can be calculated using the two sets of $\bar{X}_c$ data. Looking at the last data points in Figure 3.28a, for $d = 20$ mm and $\omega = 0.200$ s^{-1}, the value of $\bar{X}$ was found to change by $+2.5\%$ when using the curves corresponding to $\mu + 2\sigma$, and -3.0% when using the curves corresponding to $\mu - 2\sigma$. Figure 3.28b shows changes of $+2.5\%$ and -2.9% to the $\bar{X}$ data for $d = 20$ mm and $\omega = 0.237$ s^{-1}. These small changes show that the error associated with the calibration curve approach is small, assuming all the calibration curves follow a similar distribution to that seen in Figure 3.27.

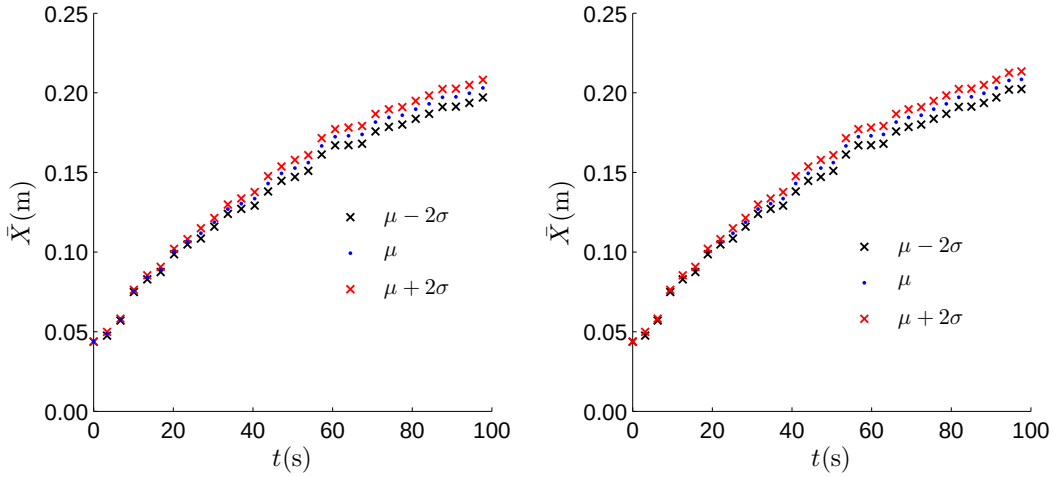

Figure 3.28: Plots of $\bar{X}_c$ using the calibration curves based on the mean value of each contour region, μ, and values calculated using $\mu \pm 2\sigma$ for experimental cases (a) $d = 20$ mm and $\omega = 0.200$ s^{-1}; (b) $d = 20$ mm and $\omega = 0.237$ s^{-1}.

3.4.2.3 Repeatability

Each water-bath experiment was only performed once. To ensure that this one reading was representative of the flow expected for a given d and ω, repeat readings were taken of one d and ω combination, with $d = 20$mm and $\omega = 0.200$ s^{-1}. As the sample size is small, $n = 3$, a 95 % confidence interval (CI) is calculated using t-distribution data. A value of 4.303 is used for the critical value to calculate the upper and lower limits of the CI, based on 2 degrees of freedom. Figure 3.29 shows that the repeatability of the experiments is high, implying that one reading is likely to be representative of the expected flow for a given d and ω.

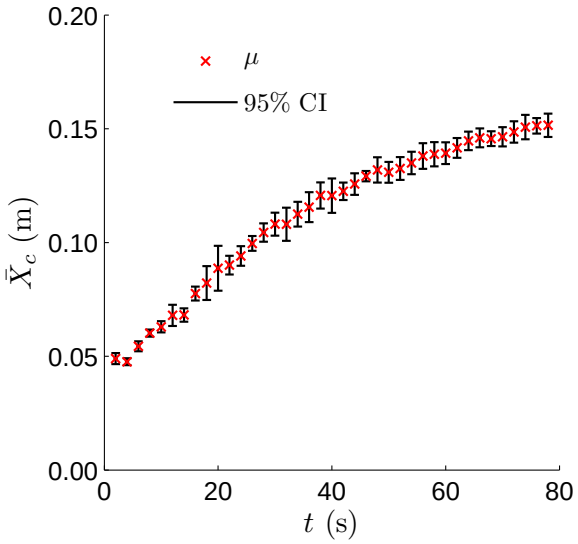

Figure 3.29: $\bar{X}_c$ data for three repeat readings of $d = 33.5$ mm and $\omega = 0.057$ s^{-1}, presented as a mean of the three readings, μ , and a 95% CI.

3.5 Summary

Water-bath experiments were carried out to quantify the mixing induced by a translating cylinder in a channel. The results demonstrate that it is possible to obtain quantitative information relating to the mixing and transport of a food dye in a water-bath by measuring differences in light intensity in a series of photographic images. It was postulated that the observed contaminant transport could be attributed to a turbulent diffusion process over the amplitude of translation, and a model was put forward that represented this. The proposed model showed good agreement with the experimental data once the dependence on suitable model parameters was understood.

The model proposed for the evolution of the dye distribution, equation 3.13, is based on observed experimental behaviour and describes the concentration profile of the dye in time and space. Model predictions of C show good agreement with dye profiles calculated from the experimental data for the cases presented. Results show that the mixing, quantified by a turbulent diffusion coefficient D_t, is proportional to the square root of the translation frequency, ω, amplitude of translation, A, cylinder diameter, d, and elapsed time, t. Since it was impractical to compare equation 3.13 with the dye profile at every timestep for each case, the centre of mass of dye cloud, $\bar{X}$ was compared to the centre of mass of the predicted distribution, $\bar{X}_c$. Again, the model shows good overall agreement with the

experimental data.

For all experimental cases, it was assumed that the lock gates were removed at an initial time $t_0 = 0$. However if this initial condition is applied to equation 3.13, the concentration distribution C starts as an infinitely long spike, which is clearly unphysical. Because of this, equation 3.13 only provides a good representation of the dye profiles after an initial time of, typically, $\omega t \approx 1 - 2$.

The water-bath model and translating cylinder are used as a proxy, to represent the movement of people up and down a corridor. The experiments conducted here, and the theoretical models developed, show that a translating cylinder can mix up a contaminant in a channel very quickly. This has implications for the infection risk of people walking in a contaminated corridor, which shall be discussed later in Chapter 7.

Chapter 4

Computational Fluid Dynamics Modelling Methods

Contents

This chapter covers the necessary background for the CFD simulation chapters that follow. The types of equations solved during simulations performed as part of this study, as well as the means by which they are solved, are presented.

4.1 Introduction

Numerical modelling involves solving discretised equations that describe a physical problem. Here, that means solving differential equations that are capable of predicting certain aspects of fluid flow. This particular branch of numerical modelling is known as computational fluid dynamics (CFD).

Equations that are related to fluid flow are solved in a discretised domain, subject to boundary conditions specific to the problem. The equations solved in the majority of CFD models are: the Navier-Stokes (NS) conservation equations, which describe the transport of momentum; the energy equation, that describes the transport of heat; and the continuity equation, that describes mass transport. Despite existing since the 19th century, analytical solutions are only known to exist for a handful of very simple problems (Darrigol, 2002). Finding existence and uniqueness of a general analytical solution still remains as one of the unsolved millennium problems (for which there is a substantial cash prize!) (Clay Mathematics Institute, 2000). This forces us to look elsewhere when seeking a general solution to the NS equations and numerical modelling is often seen as the answer.

When using the finite volume method (see Section 4.5), before obtaining a numerical solution, the initially continuous domain is split up into a number of discrete control volumes (CVs). The NS equations are then solved within each CV according to the corresponding boundary conditions. To obtain a numerical solution, the terms in the integral equations are discretised into a system of algebraic equations by using approximations, such as Taylor expansions.

Due to the non-linearity of the NS equations this system of equations is typically solved iteratively. As the iterative procedure progresses, the calculated solution gets closer to the exact solution of the system of equations. The difference between these two solutions is known as the *residual* and is often used to determine whether the solution is deemed to have *converged*, i.e. the calculated solutions are within some specified tolerance of the exact solutions of the system of equations.

An important point to note is that the converged solution does not necessarily bear any resemblance to the solution of the real physical problem being modelled. The difference

between the modelled and real solutions is known as the *'Modelling Error'* and is one of two main types of error, broadly speaking, that are introduced into the solutions obtained from a CFD simulation, the other being *Numerical Error*. Both of these sources of error are explained in more detail in Section 4.6.

4.2 CFD Software

In general, to numerically solve the NS, continuity and energy equations, computer software is employed. This is done using either an in-house developed code (usually for very specific works) or a commercial package. Both of these approaches have benefits and drawbacks and so the choice of software used is problem dependent.

In-house codes have the advantage that they can be written to include only those variables, equations, models, etc., that are required. Codes written in compiled programming languages, such as Fortran or C, also typically offer considerably faster run times when compared to those written in interpreted codes, such as Python or MATLAB (Visser et al., 2015). The major disadvantage of the in-house codes is that the development of the code itself is much slower due to the required increase in programming time.

The alternative to developing a specific CFD code is to use a commercially available CFD package, offering a lot more flexibility in terms of application, though usually at the cost of customisation and run-time. The lack of customisation can lead to a 'black box' scenario, where the user can never truly know what the code is doing. Some CFD packages side step this problem by making the software completely open source, such as OpenFOAM (2011). Others allow additions to the software through small sections of code written in Fortran, such as CFX (ANSYS, Inc., 2012a), or C/C++, such as Fluent (ANSYS, Inc., 2012b) or STAR-CCM+ (CD-adapco, 2004). There are other commercial CFD packages available, though far too many to list here (a comprehensive list is provided by cfd-online (2015)).

The three packages available for use on the high performance computing (HPC) facilities used are: CFX, Fluent and OpenFOAM. For this study, one of the main features that the CFD code has to offer is the ability to deal with a moving object in a stationary domain. All three of those just listed can deal with movement within the domain, however due to the author's prior knowledge and expertise with CFX and Fluent, tests were carried out

to determine which of these two solvers was most appropriate. It was found that a much tighter control over the mesh movement could be obtained more readily using CFX and so this solver was chosen for the main body of the work. The rest of this chapter outlays the formulations for equations and models as solved by CFX. (Comparable equations are solved by other codes/solvers).

4.3 Governing Equations

This section outlines the equations that are solved in the CVs. The models developed in this study are assumed to be isothermal, hence the energy equation is not required; the flow is determined by the NS and continuity equations. Here outlines the general procedure and algebraic manipulation that takes the partial differential equations (PDEs) of the NS and continuity equations to those used in the numerical model.

The NS equations for a compressible fluid, in conservative form, can be written as:

$$\rho\left(\underbrace{\frac{\partial U_i}{\partial t}}_{\text{Time dependence}} + \underbrace{U_j\frac{\partial U_i}{\partial x_j}}_{\text{Advection}}\right) = \underbrace{\frac{\partial p}{\partial x_i}}_{\text{Pressure}} + \underbrace{\frac{\partial \tau_{ij}}{\partial x_j}}_{\text{Viscosity}} + \underbrace{\rho F_i}_{\text{Body forces}}, \tag{4.1}$$

where $\mathbf{U} = (U_x, U_y, U_z)$ is the fluid velocity, ρ the fluid density, p the fluid pressure, $\mathbf{F}$ any body forces acting on the fluid (typically, $\mathbf{F} = (0, 0, g)$, where g is the acceleration due to gravity) and $\tau =$ the viscous stress tensor:

$$\tau_{ij} = \mu\left(\frac{\partial U_i}{\partial x_j} + \frac{\partial U_j}{\partial x_i} - \frac{2}{3}\delta_{ij}\frac{\partial U_k}{\partial x_k}\right) \tag{4.2}$$

where δ_{ij} is the Kronecker-delta function.

The Einstein summation convention is used throughout, where it is understood that repeated indices of i, j, k are summed over the three spatial dimensions x, y, z.

The continuity equation, also in conservative form, may be written:

$$\frac{\partial \rho}{\partial t} + \frac{\partial}{\partial x_i}(\rho U_i) = 0. \tag{4.3}$$

These equations can be simplified if the fluid is assumed to be incompressible. Although all fluids are actually compressible, the degree to which they can be compressed is often

so small that, under certain conditions, we may assume them incompressible; water can usually be treated this way. The incompressibility assumption is generally taken to be applicable for air flows satisfying $M < 0.3$ (Nguyen and Wereley, 2006), a criteria which is met for all flows in this study. For incompressible steady-state flows:

$$\nabla \cdot \mathbf{U} \equiv \frac{\partial U_i}{\partial x_i} = 0. \tag{4.4}$$

The derivation of this is given in most fluid dynamics texts, such as Bachelor (1967). Under the incompressible flow assumption the last two terms in equation (4.2), for the definition of τ, are necessarily zero, so that the incompressible NS equations read:

$$\rho \left(\frac{\partial U_i}{\partial t} + U_j \frac{\partial U_i}{\partial x_j} \right) = -\frac{\partial p}{\partial x_i} + \mu \left(\frac{\partial^2 U_i}{\partial x_j \partial x_j} \right) + \rho F_i. \tag{4.5}$$

4.4 Turbulence Modelling

The incompressible NS equations (equation 4.5), together with the continuity equation (equation 4.3), are capable of describing a large range of fluid flows. However, a problem arises when trying to obtain a solution to the NS equations for a turbulent flow. By their nature, turbulent flows exhibit fluctuations in properties associated with the flow. These, seemingly random, fluctuations can occur on all manner of length and time scales. This means that the equations would need to be solved on suitably small length and time scales to capture the prediction of all fluctuations. The length and time scales needed for this to happen are so small that the computing power needed to solve the large number of equations far exceeds that available for most users; this method of choosing to solve the NS equations for all scales of the flow is known as *Direct Numerical Simulation* (DNS) and is currently used in a small number of problem specific studies. This means that for most turbulent flows additional modelling is seen as the answer, instead of resolving all length scales of the flow. Typically, this is done in one of two ways: either model all length scales of the flow, or resolve the largest scales in the flow and model all those below some threshold. Various models capable of doing this are outlined in the following sections.

4.4.1 The Reynolds-Averaged Navier-Stokes (RANS) Equations

The RANS approach considers all flow properties as being made up of a mean value and a fluctuating part. For the velocity this means:

$$U_i = \bar{U}_i + U_i^{'}, \tag{4.6}$$

where $\bar{U}_i$ denotes the mean velocity, over some time t:

$$\bar{U}_i = \frac{1}{t}\int_t U\, dt, \tag{4.7}$$

and $U_i^{'}$ the fluctuating component. Here, t is a time scale that is suitably large enough so that $\bar{U^{'}}_i = 0$.

Substituting equation 4.6 into equations 4.3 and 4.5 yields:

$$\frac{\partial}{\partial x_i}\left(\rho(\bar{U}_i + U_i^{'})\right) = 0, \tag{4.8}$$

$$\rho\left(\frac{\partial(\bar{U}_i + U_i^{'})}{\partial t} + (\bar{U}_j + U_j^{'})\frac{\partial(\bar{U}_i + U_i^{'})}{\partial x_j}\right) = -\frac{\partial(\bar{p} + p^{'})}{\partial x_i} + \mu\left(\frac{\partial^2\left(\bar{U}_i + U_i^{'}\right)}{\partial x_j \partial x_j}\right) + (\bar{F}_i + F_i^{'}). \tag{4.9}$$

Since it is assumed that the flow is incompressible, it is further assumed that $\rho = \bar{\rho}$ and $\mu = \bar{\mu}$ are constant for all t (and thus the time derivatives of them are zero).

By noticing that

$$\frac{\partial\left((\bar{U}_i + U_i^{'})(\bar{U}_j + U_j^{'})\right)}{\partial x_j} = (\bar{U}_j + U_j^{'})\frac{\partial(\bar{U}_i + U_i^{'})}{\partial x_j}, \tag{4.10}$$

for incompressible flows, equation 4.10 may be substituted in to equation 4.9 to arrive at a different form of the NS equations. The non-linear advection term now gives rise to a new series of terms of the form $\rho\overline{U_i^{'}U_j^{'}}$, known as *Reynolds stresses*. After this substitution and ensemble-averaging the resulting equation, the general form of the incompressible Reynolds-Averaged Navier Stokes (RANS) equations result:

$$\frac{\partial}{\partial x_i}\left(\rho \bar{U}_i\right) = 0, \tag{4.11}$$

$$\rho\left(\frac{\partial \bar{U}_i}{\partial t} + \frac{\partial(\bar{U}_i\bar{U}_j)}{\partial x_j}\right) = -\frac{\partial \bar{p}}{\partial x_i} + \mu\left(\frac{\partial^2 \bar{U}_i}{\partial x_j \partial x_j}\right) - \rho\frac{\partial \overline{U_i' U_j'}}{\partial x_j} + \bar{F}_i, \tag{4.12}$$

where the following ensemble averaging identities have been used:

$$\bar{\bar{A}} = \bar{A} \qquad \overline{A+B} = \bar{A} + \bar{B} \qquad \overline{A\bar{B}} = \bar{A}\bar{B}. \tag{4.13}$$

It is particularly noteworthy that the time-average of any fluctuating property is necessarily zero, however the Reynold-stresses remain as the average of the product of two fluctuations is not subject to this rule.

Acknowledging the properties seen in equation 4.13, and looking at the potential values of $\rho\overline{U_i' U_j'}$, it can be seen that there are six unknown Reynolds-stresses, across the three momentum equations. Combine these six unknowns with the already unknown U_x, U_y, U_z and p, and there are a total of 10 unknown variables with only four equations to solve. This leads to a closure-problem, i.e. there are not enough equations to obtain a unique solution for all the variables concerned. This is where RANS turbulence models come in: by modelling certain aspects of equations 4.12 the number of variables is reduced so that the system is closed, and hence solvable.

4.4.2 Zero-Equation Models

The simplest models are the zero-equation models. These models are so called as they aim to take account of turbulence using only the variables already being solved for, i.e. U_x, U_y, U_z, p and any associated gradients, with no additional PDEs introduced. These models make use of the Boussinesq hypothesis (Boussinesq, 1887), which makes the assumption that the Reynolds stresses can be calculated from the velocity gradients and a so called 'eddy viscosity', μ_t. Whereas molecular viscosity is a well defined concept and property of the fluid, the eddy viscosity was introduced by Boussinesq to try describe the transport of turbulent momentum. It was postulated that:

$$-\rho\overline{U_i U_j} = 2\mu_t S_{ij} - \frac{2}{3}k\rho\delta_{ij} \tag{4.14}$$

where

$$S_{ij} = \frac{1}{2}\left(\frac{\partial \bar{U}_i}{\partial x_j} + \frac{\partial \bar{U}_j}{\partial x_i}\right) \tag{4.15}$$

is the rate-of-strain tensor, and k is the turbulent kinetic energy (TKE):

$$k = \frac{1}{2}\left(\overline{U_i' U_i'}\right) = \frac{1}{2}\left(\bar{U}_x'^{\,2} + \bar{U}_y'^{\,2} + \bar{U}_z'^{\,2}\right). \tag{4.16}$$

This means the $-\rho\overline{U_i U_j}$ term in the momentum equation (4.12) can now be replaced with (4.14). However, while this approach models the Reynolds stresses, two more unknown variables are introduced, k and μ_t. The eddy viscosity term itself can also be modelled, using Prandtl's mixing theory (Prandtl, 1925), which expresses μ_t in terms of characteristic velocity and length scales in the flow:

$$\mu_t = \rho \hat{L} \hat{U}. \tag{4.17}$$

The length-scale $\hat{L}$ is usually chosen to coincide with a geometry length-scale, such as a diameter or height. The characteristic velocity $\hat{U}$ is assumed to depend upon the mean velocity gradient:

$$\hat{U} = \hat{L}\left|\frac{dU}{dy}\right|, \tag{4.18}$$

where, here, it is assumed that y is the coordinate perpendicular to the flow, if a simple uni-directional flow in the x direction is considered.

The second unknown, k, is a scalar quantity and may be absorbed into the pressure term so that a modified pressure is solved for:

$$p' = p + \frac{2}{3}\rho k. \tag{4.19}$$

Once a length-scale is determined, the system of RANS equations is closed; all variables can be calculated by solving equations (4.11), (4.12), (4.14) and (4.17). There are a lot of assumptions made when using this zero-equation model approach, a consequence of which is the model is unable to capture many complex fluid flows. Nevertheless, it is still capable of giving meaningful results for simple shear flows.

4.4.3 One-Equation Models

One-equation models, are seen as an improvement upon the zero-equation models for many flows, but they are more computationally intensive due to the extra equation they solve. This is an important point to note as this is the trade off that is always made in CFD. While an increase in the number of equations solved will often lead to an increase in the accuracy of the results, the computation time needs to be taken into consideration to see whether the more 'advanced' models are worth the improvements in results.

The weakness of the zero-equation approach is that the turbulent mixing is assumed to solely depend upon one length-scale, the so called mixing-length. As already mentioned, for the zero-equation model the length-scale chosen is often one that corresponds to the largest length-scales of the geometry concerned, typically a relevant diameter or height, and not of the flow itself. As such there is no consideration of the change in size or intensity of the turbulent eddies throughout the flow. The one-equation models aim to address this by introducing a transport equation for k.

For the zero-equation model, the turbulent eddy viscosity was estimated using a characteristic length-scale, $\hat{L}$, and a characteristic velocity, $\hat{U}$, dependent on the mean velocity gradient. Despite helping found the theory, Ludwig Prandtl *[1875-1953]* realised that this was an over simplification of turbulence, and that the equations being introduced to close the RANS equations needed to depend on properties of the flow itself, and not the geometry. Kolmogorov (1942) and Prandtl (1945) independently came up with the idea of introducing k as the relevant velocity scale, as it is a measure of the intensity of the eddies (vortices) and associated turbulence. Since it was understood that turbulence is a function of space and time, it made sense to define suitable PDEs instead of assuming the constant length and velocity-scales, as was done previously. Thus, k, the turbulent kinetic energy, was introduced to the RANS equations by using it as the base for $\hat{U}$ when defining μ_t:

$$\hat{U} = C_\mu \sqrt{k} \tag{4.20}$$

$$\implies \qquad \mu_t = C_\mu \rho \hat{L} \sqrt{k} \tag{4.21}$$

for empirical constant C_μ.

In acknowledging that k varies in time and space, a further transport equation needs to

be solved for it. This, in turn, introduces more unknowns which need to be modelled for any one-equation turbulence models:

$$\underbrace{\frac{\partial(\rho k)}{\partial t}}_{\text{Time dependence}} + \underbrace{\frac{\partial(\rho \bar{U}_j k)}{\partial x_j}}_{\text{Advection}} = \underbrace{\frac{\partial}{\partial x_j}\left(\left(\mu + \frac{\mu_t}{\sigma_k}\right)\frac{\partial k}{\partial x_j}\right)}_{\text{Viscosity}} + \underbrace{2\mu_t S_{ij}\frac{\partial \bar{U}_i}{\partial x_j}}_{\text{Production}} + \underbrace{P_{kb}}_{\text{Buoyancy}} - \underbrace{\rho\epsilon}_{\text{Dissipation}} \tag{4.22}$$

where ϵ is the turbulent dissipation rate, characterising the transfer of k into heat, σ_k is the turbulent Prandtl number taken to be ≈ 1 (Launder and Spalding, 1972) and P_{kb} represents any buoyancy forces acting on k. The buoyancy term is mentioned only for completeness and is not actually used for simulations in this study, though it is comprised of known terms.

This leads to three additional unknowns, μ_t, k and ϵ, with only one new additional equation, (4.22). As a means of modelling one of these terms, Taylor (1935) stated that the dissipation rate ϵ may be described in the following way:

$$\epsilon = C_\mu \frac{(U')^3}{\hat{L}} = C_\mu \frac{k^{\frac{3}{2}}}{\hat{L}} \tag{4.23}$$

for empirical constant $C_\mu = 0.09$ (Wilcox, 2006).

This means that once a length-scale has been prescribed, giving μ_t a value, the closure problem is resolved for this one-equation approach. An additional term has been introduced, k, but the transport equation describing it (4.22) contains known terms $C_\mu, \sigma_k, \rho, \hat{L}, \mu, \mu_t$. This means that the five unknowns $\bar{U}_x, \bar{U}_y, \bar{U}_z, p$ and k can be obtained with the five equations (4.11), (4.12) and (4.22), where it is understood that (4.12) comprises three equations.

4.4.4 Two-Equation Models

Two-equation models are based on the idea that since the length-scales that drive the turbulent eddies change throughout the flow, using one value of $\hat{L}$ is insufficient and so the length-scales are calculated from a second additional transport equation.

$k - \epsilon$ Model

The most commonly used two-equation model, including applications for indoor air modelling, is the $k - \epsilon$ model (Wilcox and Alber, 1972), so called because the second

additional equation included is for the transport of ϵ. By inserting equation (4.23) into (4.21), the explicit dependence of the length-scale $\hat{L}$ can be removed so that the turbulence is described only in terms of k and ϵ:

$$\mu_t = C_\mu \rho \frac{k^2}{\epsilon} \tag{4.24}$$

with corresponding transport equation:

$$\underbrace{\frac{\partial(\rho\epsilon)}{\partial t}}_{\text{Time dependence}} + \underbrace{\frac{\partial(\rho\bar{U}_j\epsilon)}{\partial x_j}}_{\text{Advection}} = \underbrace{\frac{\partial}{\partial x_j}\left(\left(\mu + \frac{\mu_t}{\sigma_\epsilon}\right)\frac{\partial \epsilon}{\partial x_j}\right)}_{\text{Viscosity}} + \underbrace{\frac{\epsilon}{k} C_{1\epsilon}\left(\mu_t S_{ij}\frac{\partial \bar{U}_i}{\partial x_j}\right)}_{\text{Production}} + \frac{\epsilon}{k}\left(\underbrace{C_{1\epsilon}P_{\epsilon b}}_{\text{Buoyancy}} - \underbrace{C_{2\epsilon}\rho\epsilon}_{\text{Dissipation}}\right) \tag{4.25}$$

where $C_{1\epsilon}, C_{2\epsilon}$ and $C_{3\epsilon}$ are empirical constants. As before, the buoyancy term is not considered in this study but is included for completeness and made up of known quantities. The values most commonly used are those suggested by Launder and Spalding (1974):

$$C_\mu = 0.09,\ C_{1\,\epsilon} = 1.44,\ C_{2\,\epsilon} = 1.92,\ \sigma_k = 1,\ \sigma_\epsilon = 1.3. \tag{4.26}$$

however different flows yield different ideal constant values. With the k transport equation included, the system of equations is once again closed.

The standard $k-\epsilon$ model is only applicable for turbulent, i.e. 'high' Re, flows (Launder and Spalding, 1974). In regions where this is not the case, such as on wall boundaries where the no-slip condition results in molecular viscosity having a significant impact, the models capability is compromised due to an over-prediction of the turbulent viscosity here (Wilcox, 2006). To correct for this, 'wall-functions' are applied at all wall boundaries. These functions ensure that the 'log-law' of the wall[1] is enforced and, as such, the full k and ϵ transport equations are not actually solved; the velocity profiles are instead calculated based on further modelling assumptions (Kalitzin et al., 2005) .

Figure 4.1 shows various predicted solutions for flow near a wall-boundary. The turbulence model used in this figure is not actually the $k-\epsilon$ model, but the figure illustrates the

[1]So-called due to the velocity profile being almost universally a function of log for flows near solid wall boundaries.

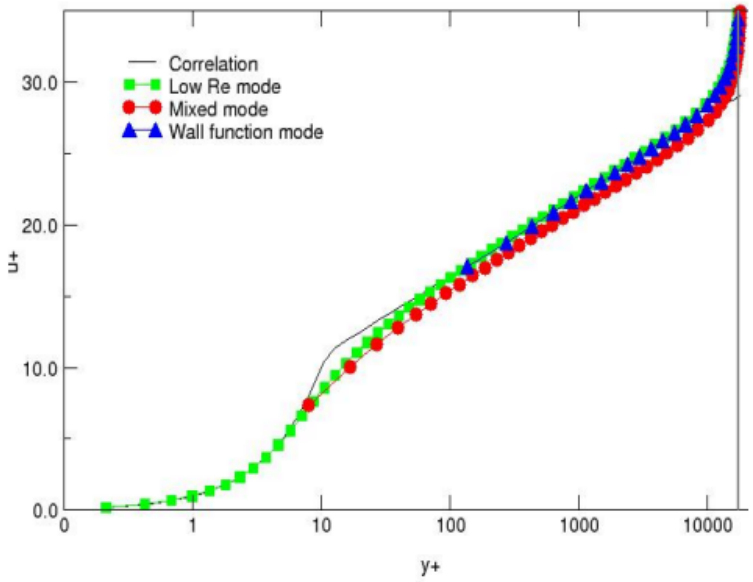

Figure 4.1: Various near-wall modelling approaches (coloured markers) aiming to recreate the theoretical log-law profile (black line) (Menter et al., 2003).

important features when modelling near a wall boundary. The axes are labelled as U^+ and y^+, which represent a non-dimensional velocity parallel to the wall boundary and non-dimensional distance perpendicular to the wall boundary, respectively. The log-law of the wall is highlighted by the black line, which is well reproduced by this model, the green markers, all the way to the wall ($y^+ = 0$). When wall-functions are turned on for this model, solutions are obtained only as far down as $y^+ = 100$, below which point all CVs take their velocity values from the specified wall function and not from the solutions of the NS and turbulence model equations.

It is worth noting that the $k - \epsilon$ model is, arguably, the most popular turbulence model of the past 40 years, despite this shortcoming (Wilcox, 2006). However, this shortcoming is often not encountered during indoor air applications, as the wall boundaries are seen as insignificant compared to the free shear motions within the air space that the $k - \epsilon$ model is capable of capturing. This is led to the model being one of the most popular, if not the most, when modelling indoor air flows (Zhai et al., 2007).

$k - \omega$ Model

As shown previously, the second transport equation does not necessarily have to solve for the length-scale $\hat{L}$ explicitly. Solving for k as well means that $\hat{L}$ can be obtained as long as the second variable is of the form $k^a \hat{L}^b$, as ϵ is in equation (4.23). Another popular

choice of second variable is the specific dissipation rate ω, where:

$$\omega = \frac{\epsilon}{C_\mu k} \qquad \Longrightarrow \ \mu_t = \frac{\rho k}{\omega} \tag{4.27}$$

with corresponding transport equation

$$\frac{\partial(\rho\omega)}{\partial t} + \frac{\partial\left(\rho\bar{U}_j\omega\right)}{\partial x_j} = \frac{\partial}{\partial x_j}\left(\left(\mu + \frac{\mu_t}{\sigma_\omega}\right)\frac{\partial\omega}{\partial x_j}\right) + \frac{\omega}{k}\alpha\left(2\mu_t S_{ij}\frac{\partial\bar{U}_i}{\partial x_j}\right) + P_{\omega b} - \beta\rho\omega^2 \tag{4.28}$$

where

$$\alpha = \frac{4}{5}, \quad \beta = \frac{3}{40}, \quad \sigma_\omega = 2 \tag{4.29}$$

are constants (Wilcox, 1988). The buoyancy term, $P_{\omega b}$, has again been included for completeness. Additionally, when using the $k-\omega$ model the transport equation for k is modified so that $\sigma_k = 2$ and the dissipation term in equation (4.22) is changed from $(-\rho\epsilon)$ to $(-\beta^*\rho\omega k)$, where $\beta^* = 0.09$.

Baseline (BSL) Model

Although the $k-\epsilon$ model has a known shortcoming when attempting to reproduce the log-law of the wall, not all two-equation models suffer the same fate. One of the main advantages the $k-\omega$ model has over the $k-\epsilon$ model, is that the equations may be solved right up to a wall-boundary, as first shown by Saffman (1970), making wall-functions unnecessary (Wilcox, 2006). This leads to one of the $k-\omega$ model's main strengths: the prediction of strong gradients at the wall and separation flows. However, once away from the wall, the $k-\omega$ model shows a strong sensitivity to values in ω in the free stream (Menter et al., 2003). As a way of improving upon the $k-\epsilon$ and $k-\omega$ models, Menter (1994) formulated a combination of the two models that used the $k-\omega$ model at the wall, and the $k-\epsilon$ model once away from it, with a blending function. This model is known as the baseline (BSL) model. The original $k-\omega$ model equations for k and ω are multiplied by a blending function, F_1, and added to a transformed version of the $k-\epsilon$ model equations to yield:

$$\frac{\partial(\rho k)}{\partial t} + \frac{\partial(\rho\bar{U}_j k)}{\partial x_j} = \frac{\partial}{\partial x_j}\left(\left(\mu + \frac{\mu_t}{\sigma_{k3}}\right)\frac{\partial k}{\partial x_j}\right) + 2\mu_t S_{ij}\frac{\partial\bar{U}_i}{\partial x_j} + P_{kb} - \beta^{'}\rho k\omega \tag{4.30}$$

$$\frac{\partial(\rho\omega)}{\partial t} + \frac{\partial\left(\rho\bar{U}_j\omega\right)}{\partial x_j} = \frac{\partial}{\partial x_j}\left(\left(\mu + \frac{\mu_t}{\sigma_{\omega 3}}\right)\frac{\partial\omega}{\partial x_j}\right) + \frac{\omega}{k}\alpha_3\left(2\mu_t S_{ij}\frac{\partial\bar{U}_i}{\partial x_j}\right) + (1-F_1)\frac{2\rho}{\omega\sigma_{\omega 2}}\frac{\partial k}{\partial x_j}\frac{\partial\omega}{\partial x_j}P_{\omega b} - \beta_3\rho\omega^2 \tag{4.31}$$

for model parameters α_3, $\beta^{'}$, β_3, σ_{k3}, $\sigma_{\omega 2}$, $\sigma_{\omega 3}$. These parameters are themselves made up of the model parameters associated with the $k-\epsilon$ and $k-\omega$ models and take on different values according to the blending function F_1 (see Menter (1994) for details).

Shear-Stress Transport (SST) Model

The BSL model was also improved upon in Menter's (1994) study, by taking into account the transport of the turbulent shear-stresses in adverse pressure boundary layers. This model is known as the shear-stress transport (SST) model and differs from the BSL model in the way the eddy viscosity is calculated. Menter (1994) found that despite the BSL improvements over the other two-equation models it still failed to correctly capture the onset of flow separation, hence the proposal of this second model. The SST model enforces Bradshaws hypothesis, in which it is assumed that the shear stress may be linearly related to the turbulent kinetic energy, k (Peng and Eliasson, 2007). In employing Bradshaws hypothesis, the SST model typically shows superior performance in predicting adverse pressure gradients than most other models (Menter, 1994). The SST model differs from the BSL model in only one equation, namely the formulation of the eddy viscosity:

$$\mu_t = \frac{\rho k\, a_1}{\max(a_1\omega, S\,F_2)} \tag{4.32}$$

where $a_1 = 0.31$ is a model constant, F_2 another blending function and S the magnitude of the strain rate tensor S_{ij}. For details on the blending functions, see Menter (1994).

4.4.5 Reynolds-Stress Models

All the models so far have been based on the eddy-viscosity concept (4.14), which assumes that the Reynolds stresses may be related to the mean strain rate tensor S_{ij}. Instead of modelling the Reynolds stresses via this assumption, another approach is to solve transport equations for these stresses. These models are known as Reynolds-stress models (RSMs). While solving the extra equations will clearly increase computation time, solving for each stress individually means isotropy of the stresses is no longer assumed and hence more complex flows should benefit from the solving of these new transport equations:

$$\frac{\partial \rho \overline{U_i' U_j'}}{\partial t} + \frac{\partial (\bar{U}_k \rho \overline{U_i' U_j'})}{\partial x_k} - \frac{\partial}{\partial x_k}\left(\left(\mu + \frac{2C_s \rho k^2}{3\epsilon}\right)\frac{\partial \overline{U_i' U_j'}}{\partial x_k}\right) = -\rho \overline{U_i' U_k'}\frac{\partial \bar{U}_j}{\partial x_k} - \rho \overline{U_j' U_k'}\frac{\partial \bar{U}_i}{\partial x_k} - \frac{2\rho\epsilon\delta_{ij}}{3} + \phi_{ij} + P_{ij,b} \quad (4.33)$$

where C_s is a constant, $P_{ij,b}$ the buoyancy term and ϕ_{ij} is a pressure-strain correlation, which differs depending on which formulation of the model is used. The quasi-isotropic variant of the RSM model developed by Launder, Reece and Rodi (henceforth LRR-QI) is used here; details on the pressure-strain term can be found in Launder et al. (1975). As can be seen in (4.33), the dissipation rate ϵ still appears in the formulation and so the transport equation (4.25) is solved for it, only with revised constant values.

4.4.6 Large Eddy Simulations

So far, all models considered have used the RANS equations (4.12) for their formulation, solving mean and fluctuating parts of the flow variables. An alternative approach is to resolve all the length-scales up to a given threshold and model the rest. This method of resolving the larger length-scales of the flow results in an increased computational demand when compared to RANS turbulence models. This is the way in which large-eddy simulations (LES) are performed.

A filter-function G is applied to all variables to determine up to what point the variable is resolved, so for a variable Ω we denote the filtered part:

$$\bar{\Omega}(x) = \int_D \Omega(x') G(x; x') dx', \quad (4.34)$$

where Ω takes values in some fluid domain D. Applying the filter means there exists a resolvable part, $\bar{\Omega}$ and a part that is not to be resolved, but modelled:

$$\Omega' = \Omega - \bar{\Omega}. \quad (4.35)$$

Remembering that each variable takes on a value inside each CV, this provides an initial filtering operation:

$$\bar{\Omega}(x) = \frac{1}{V}\int_V \Omega(x')\, dx', \quad (4.36)$$

for control volume V. For the LES model used here, there is no further filtering so that G is effectively:

$$G(x;x') = \begin{cases} \frac{1}{V}, & x' \in V \\ 0, & \text{Otherwise.} \end{cases} \tag{4.37}$$

Much like the RANS equations were derived after considering each variable as a mean and fluctuating part, so the filtered NS equations can be obtained after considering each variable as a resolved and unresolved part:

$$\frac{\partial(\rho\bar{U}_i)}{\partial t} + \frac{\partial(\rho\bar{U}_i\bar{U}_j)}{\partial x_j} = -\frac{\partial\bar{p}}{\partial x_i} + \frac{\partial}{\partial x_j}\left(2\mu S_{ij}\right) - \frac{\partial(\rho\tau_{ij})}{\partial x_j}, \tag{4.38}$$

where

$$\tau_{ij} = \overline{U_iU_j} - \bar{U}_i\bar{U}_j, \tag{4.39}$$

are the subgrid-scale (SGS) stresses. This final term means that (4.38) is not closed and so a SGS model is used. An approach similar to that of the Boussinesq approximation is used, so that the SGS stresses τ_{ij} are related to the larger/resolved stresses S_{ij} by:

$$-\left(\tau_{ij} - \frac{\delta_{ij}}{3}\tau_{kk}\right) = \frac{2\mu_{sgs}S_{ij}}{\rho}, \tag{4.40}$$

where μ_{sgs} represents an eddy-viscosity only for the unresolved, small scales and is itself modelled according to the approach of Smagorinsky (1963):

$$\frac{\mu_{sgs}}{\rho} = (C_s h)^2 \left|S\right|, \tag{4.41}$$

where h is the unresolved length-scale (typically $\sqrt[3]{V}$), $|S|$ is the magnitude of the mean strain rate tensor S_{ij} and C_s is the Smagorinsky constant:

$$C_s = \frac{1}{\pi}\left(\frac{2}{3C_k}\right)^{3/4}. \tag{4.42}$$

$C_k \approx 1.5$ is the Kolmogorov constant, closing the filtered NS-equations. The value of this constant is based on the idea that the turbulence is isotropic once the length-scale is small enough (Lilly, 1967).

4.4.6.1 Direct Eddy Simulation (DES)

Since there is often a significant difference in computational cost between using RANS and LES models, there are also models that aim to transition between the two, much like the way the BSL and SST models do for the $k-\epsilon$ and $k-\omega$ models, to reduce the computational cost whilst still resolving the larger length-scales.

Direct eddy simulations (DES) propose the use of a RANS model in attached and less-complex flow regions, switching to an LES approach for more complex regions, such as regions of separation. The DES model used in CFX is only available with the SST model as the RANS component, as it is the most capable RANS model at predicting flow separation. This switch is achieved by changing the length-scale, $\hat{L}$, used when calculating the turbulent dissipation rate ϵ to the local mesh size Δ:

$$\epsilon = \frac{k^{\frac{3}{2}}}{\hat{L}} \mapsto \frac{k^{\frac{3}{2}}}{C_{DES}\Delta} \tag{4.43}$$

where Δ is the largest length of a particular CV, C_{DES} a constant and

$$\hat{L} = \frac{\sqrt{k}}{\beta^*\omega}. \tag{4.44}$$

This change in length-scale is integrated into the SST model by modifying the ϵ term in the k transport equation, so that:

$$\epsilon = \beta^* k\omega \mapsto F_{DES}(\beta^* k\omega) \tag{4.45}$$

where

$$F_{DES} = \max\left(\frac{\hat{L}}{C_{DES}\Delta}, 1\right). \tag{4.46}$$

Setting $C_{DES} = 0.61$ acts as a limiter, to help ensure the RANS and LES parts are used in the appropriate regions of the domain (Strelets, 2001).

4.4.6.2 Scale Adaptive Simulation

A similar approach to that of DES is the scale-adaptive simulation (SAS), also combining elements of RANS and LES modelling. However, whereas DES uses the grid spacing of the mesh as a control over the length-scale, SAS modelling includes a second length-scale, the

von-Karman length-scale, $\hat{L}_{vk}$, to increase the range of resolvable turbulent length-scales. This means that for regions experiencing strongly time-dependent flow the model used isbased on an LES approach, whereas for relatively steady regions the RANS approach is adopted. The RANS model used in the SAS formulation is usually the SST model. It differs from the standard SST model by the inclusion of an additional source term Q_{SAS} in the ω transport equation (4.28):

$$Q_{SAS} = \max\left[\rho\xi_2\kappa S^2\left(\frac{\hat{L}}{\hat{L}_{vk}}\right) - \frac{2\rho kC}{\sigma_\phi}\max\left(\frac{1}{\omega^2}\left(\frac{\partial\omega}{\partial x_j}\right)^2, \frac{1}{k^2}\left(\frac{\partial k}{\partial x_j}\right)^2\right), 0\right] \tag{4.47}$$

with model parameters $\xi_2 = 3.51, \sigma_\phi = 0.67, C = 2$. The length scales are defined as:

$$\hat{L} = \frac{\sqrt{k}}{\omega\sqrt[4]{C_\mu}} \qquad \hat{L}_{vk} = \frac{\kappa S}{|U''|} \tag{4.48}$$

where $\kappa = 0.41$ is the von-Karman constant and

$$|U''| = \sqrt{\sum_i\left(\frac{\partial^2 U_i}{\partial x_j^2}\right)}. \tag{4.49}$$

4.5 Finite Volume Method

There are three main approaches to solving the NS equations over a given domain: the finite difference method (FDM), the finite element method (FEM) and the finite volume method (FVM). The three approaches differ in their discretising of the NS equations within a domain, and approximations to derivatives and fluxes, though these are not discussed any further in this study. The FVM is often used in industrial applications, such as CFD codes, due to its stability and computational efficiency (Eymard et al., 2000) and is the approach used by CFX.

As already mentioned, when using the FVM the governing equations are solved in CVs in the domain concerned. To create these CVs, the domain is first discretised into a mesh, combined of many cells. The centroids of these cells are then connected by a series of shape functions to obtain the CVs. The discretisation and consequent size of the cells, and CVs, directly impacts on the accuracy of which it is possible to capture the domain's true size and shape. The concept is displayed in Figure 4.2. The following section outlines

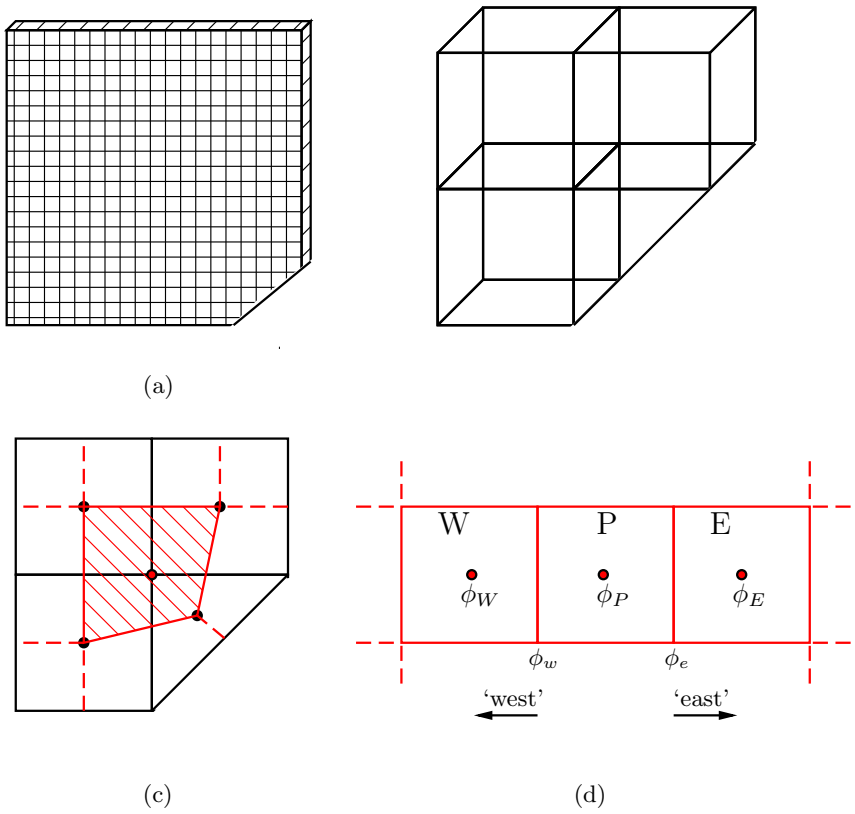

Figure 4.2: (a) Typical geometry discretised into a mesh; (b) Closeup of just a small number of mesh elements; (c) Sketch of same cells, now in 2D, with control volume shaded; (d) Series of (regular) control volumes, with labelling used for discretisation theory.

some of this in more detail for a series of one-dimensional CVs, for simplicity, though two and three dimensions are very similar.

Consider the general transport equation for scalar ϕ:

$$\frac{\partial(\rho\phi)}{\partial t} + \frac{\partial(\rho U_j \phi)}{\partial x_j} - \frac{\partial}{\partial x_j}\left(\Gamma\left(\frac{\partial \phi}{\partial x_j}\right)\right) = 0 \tag{4.50}$$

with diffusivity Γ. By using the divergence theorem, the integral of equation 4.50 over a CV becomes:

$$\underbrace{\frac{d}{dt}\int_V \rho\phi \, dV}_{\text{Transient}} + \underbrace{\int_S \rho U_j \phi \, dn_j}_{\text{Advection}} - \underbrace{\int_S \Gamma\left(\frac{\partial \phi}{\partial x_j}\right) dn_j}_{\text{Diffusion}} = 0 \tag{4.51}$$

where n_j is the outward surface vector, V the CV volume and S its area. It has been assumed that the volumes do not change in time (so that the time derivative can be moved outside the integral). At this stage, equation 4.51 is still in conservative form and is exact,

no approximations have been made.

4.5.1 Discretising the Governing Equations

The integrals of equation 4.51 need to be discretised in order to be solved numerically. Each of these terms is approximated using a different discretisation scheme. These are now considered in turn, for the schemes used in this study.

4.5.1.1 Transient Term

The transient term is discretised using the second-order backward Euler scheme, chosen for its increased accuracy over the first-order scheme:

$$\frac{d}{dt}\int_V \rho\phi \, dV = \rho V \left(\frac{3\phi^t - 4\phi^{t-1} + \phi^{t-2}}{2\Delta t} \right), \tag{4.52}$$

where, the superscripts denote the time level, the subscripts denote the spatial position (see Figure 4.2) and Δt is the timestep size. This discretisation scheme is implicit, meaning that the discretised form of equation 4.51 is solved using values of ϕ at the current time step. This means solving for ϕ is not a simple 'time-marching' procedure, i.e. $\phi^{t+1} = f(\phi^t)$, and solutions are obtained by simultaneously solving systems of linear equations.

4.5.1.2 Advection Term

Various schemes can be used for the discretisation of the advection term, three of which are now described that are relevant to this study. The advection term is calculated at the 'face' between two CVs. When evaluating variables at these faces, it is common to talk about the faces to the 'west' and 'east' of a CV (see Figure 4.2), a terminology which is used here. For simplicity, considering only the advection term at the west face of P:

$$\int_S \rho U_j \phi \, dn_j = \rho U_w \Delta n_w \phi_w \tag{4.53}$$

where subscript w denotes values are taken at the west face, and Δn represents the outward surface vector, though can represent a distance, vector or surface depending upon dimension. A similar equation is obtained at the east face. The manner in which ϕ_w is obtained is dependent upon the discretisation scheme used.

Upwind Scheme

The upwind scheme (UWS) simply assumes that the values at the face are taken from the upwind CV value, that is, the node in the direction opposing the flow. If a flow is assumed from west to east:

$$\phi_w = \phi_W. \tag{4.54}$$

For a flow from east to west,

$$\phi_w = \phi_P. \tag{4.55}$$

This first-order scheme is known to be very stable, but is not very capable of capturing sharp gradients (Anderson, 1995). It is not directly used in this study, but it is the 'worst case scenario' of one of the high resolution scheme to follow (see equation 4.57).

Central Difference Scheme

The central difference scheme (CDS) uses information from the CVs both up and downwind of the face, and is an average of these values:

$$\phi_w = \frac{1}{2}(\phi_W + \phi_P). \tag{4.56}$$

The CDS is second-order accurate, but is generally considered to be less stable than the UWS. It is unbounded in the form stated above, meaning that simulations using the scheme can 'blow up', leading to non-convergence. A bounded version of the CDS does exist, which reverts back to the UWS if stability criteria are not met (ANSYS, Inc., 2012c), though the standard, unbounded version is used in this study.

High Resolution Scheme

The high resolution scheme (HRS) is a combination of both the UWS and the CDS. A blending parameter, β, is used so that a value of 0 restores the UWS and a value of 1 restores the CDS:

$$\phi_w = \phi_W + \beta \left(\frac{\phi_P - \phi_W}{2} \right) \tag{4.57}$$

A value of β is calculated to be as close to one as possible, so as to aim for second-order accuracy, but is subject to criteria such that the stability of the simulation is not

compromised. The HRS scheme contains the advantages of both the previous schemes, whilst minimising the disadvantages.

4.5.1.3 Diffusion Term

The diffusion term, again considering only the west face, is discretised as:

$$\int_S \Gamma \left(\frac{\partial \phi}{\partial x_j} \right) dn_j = \Gamma \Delta n_w \frac{(\phi_P - \phi_W)}{\Delta x_w} \tag{4.58}$$

where Δx_w is the distance between CVs P and W. This means that the diffusion terms are always discretised using the CDS in CFX.

4.5.2 Moving Mesh

When evaluating the integrals of equation (4.51) it was assumed that the CV dimensions were not changing in time. However, the CFD models developed in this study require the use of a moving mesh to describe the movement of the cylinder (see Chapters 5 and 6), and hence the CVs are no longer stationary. This means that the time derivative of the transient term can no longer be pulled outside the integration and Leibniz's rule must be enforced:

$$\frac{d}{dt} \int_{V(t)} \phi \, dV = \int_V \frac{\partial \phi}{\partial t} \, dV + \int_S \phi Z_j \, dn_j \tag{4.59}$$

where it has been assumed that the CV boundary is moving with velocity Z_j. This yields a slightly modified advection term so that the equation being integrated is now:

$$\frac{d}{dt} \int_V \rho \phi \, dV + \int_S \rho (U_j - Z_j) \phi \, dn_j - \int_S \Gamma \left(\frac{\partial \phi}{\partial x_j} \right) dn_j = 0 \tag{4.60}$$

The discretisation of this equation follows the same format as just outlined for equation (4.51).

4.6 Sources of Error

By using a model to represent a real flow, sources of error are inherent and unavoidable. However, many of the errors encountered when modelling can be minimised so that the model solution still bears a close resemblance to the real counterpart. Acknowledging the sources of these errors allows for improvement in the relevant areas of the model.

4.6.1 Modelling Error

The most obvious source of error arises due to the difference between the flow that is to be modelled and the subsequent mathematical model built. This is most easily understood if the geometry of the model is scrutinised and compared with the real flow. For example, the walls of most CFD models are assumed to be perfectly smooth, whereas in reality microscopic details in a material's surface suggest otherwise. Here, the CFD models are assumed to be isothermal, whereas in reality the water used in the water-bath experiments no doubt had small local temperature differences ($< 1°$C) that cannot be estimated with any real accuracy. Differences of this nature are deemed to be insignificant and their impact on the overall solution is assumed to be small. Having experimental validation data for CFD models allows for confirmation that any assumptions made are justified. The modelling error is reduced in this study by knowing certain initial and boundary conditions with a high level of accuracy, such as translation frequency, amplitude, and the water-bath/domain dimensions.

It is not just the differences in the physical properties of model and real flow which comprise the modelling errors. The size of the cells in the mesh of the numerical model may also be classed as modelling error even though their size impacts upon the numerical calcuations. There is a considerable size difference between the diameter/length of a typical pathogen ($O(10^{-6})$ m) and the smallest cells of the mesh cells ($O(10^{-4})$ m), meaning that tracking individual pathogens is beyond the scope of this study.

The NS equations are known to be a good representation of most fluid flows, particularly those that are laminar. However, once turbulent flows are considered there are various ways in which its effects can be modelled; the choice of turbulence model directly relates to the modelling error. In order to reduce this error, in this study, a number of turbulence models are tested to see which is most adequate as a representation of the turbulent properties of the flow (see Section 5.3.5).

4.6.2 Numerical Error

Discretisation

Discretisation error arises due to the flow being modelled as a system of equations, which are discretised in finite differences of time and space. This, in turn, relates to the choice of step size in time, Δt, and space, Δx, and the choice of discretisation scheme for all

derivatives in the NS equations. This means that there is, in general, a difference between the exact solutions of the equations solved and the numerical solution obtained.

The Taylor series expansions used when discretising the gradient terms to finite differences are dependent on Δx and Δt. The choice of discretisation scheme (UWS, CDS, HRS, etc) directly impacts on the importance of the size of these step sizes. For example, the CDS errors may be seen by looking at the Taylor series below:

$$f(x+\Delta x) = f(x) + \Delta x f'(x) + \frac{(\Delta x)^2 f^{(2)})(x)}{2!} + \frac{(\Delta x)^3 f^{(3)}(x)}{3!} + ... \quad (4.61)$$

$$f(x-\Delta x) = f(x) - \Delta x f'(x) + \frac{(\Delta x)^2 f^{(2)}(x)}{2!} - \frac{(\Delta x)^3 f^{(3)}(x)}{3!} + ... \quad (4.62)$$

$$f(x+\Delta x) - f(x-\Delta x) = 2\left(\Delta x f'(x) + \frac{(\Delta x)^3 f^{(3)}(x)}{3!} + \frac{(\Delta x)^5 f^{(5)}(x)}{5!} + ...\right) \quad (4.63)$$

$$\underbrace{\frac{f(x+\Delta x) - f(x-\Delta x)}{2(\Delta x)}}_{\text{CDS discretisation of } f'(x)} = f'(x) + \underbrace{\frac{(\Delta x)^2 f^{(3)}(x)}{3!} + O(\Delta x^4)}_{\text{Error}} \quad (4.64)$$

Equation (4.64) shows how by representing the derivative using the central difference scheme, the error terms are of order $(\Delta x)^2$ and higher, indicating the scheme is second-order accurate. As $\Delta x \to 0$ the derivative is recovered, but since the numerical models have a finite mesh spacing it is clear that the error term of order $(\Delta x)^2$ will always be there.

Since Δx is small $\implies (\Delta x)^2 < \Delta x$, higher order discretisation schemes ought to yield a higher degree of accuracy by reducing the size of the error term. However, in doing so the schemes often become more unstable and oscillatory behaviour is sometimes introduced at sharp gradients (Gao et al., 2012). Further, Godunov's theorem (Godunov, 1999) states that only first order schemes are monotonicity preserving, avoiding the spurious oscillations that can appear with higher order schemes. This would imply that first order schemes should be used for discretisation. However, first-order schemes are associated with numerical diffusion and an inability to capture sharp gradients (Versteeg and Malalasekera, 1995). Since the prediction of strong gradients is necessary to capture the complex flow structures that are associated with the eddy shedding from cylinders, second-order schemes are preferred for this study. The choice of discretisation scheme relating to specific simulations is discussed in Section 5.3.2

Convergence

The discretised NS equations are solved by means of an iterative procedure. Once the discretised form of the NS equations is obtained, they make up a system that can be described in matrix form as:

$$A\phi = \boldsymbol{b} \tag{4.65}$$

where A is the matrix of coefficients that correspond with the terms yielded from the discretisation of the NS equations, $\boldsymbol{\phi}$ is the unknown solution vector and $\boldsymbol{b}$ comprises the source/sink terms. The iterative procedure starts with an initial solution $\boldsymbol{\phi}^n$ with the aim of improving upon this solution by applying a correction $\boldsymbol{\phi}^{'}$, so that $\boldsymbol{\phi}^{n+1} = \boldsymbol{\phi}^n + \boldsymbol{\phi}^{'}$ where:

$$A\boldsymbol{\phi}^{'} = \boldsymbol{R}^n \tag{4.66}$$

and

$$\boldsymbol{R}^n = \boldsymbol{b} - A\boldsymbol{\phi}^n \tag{4.67}$$

is the residual, i.e. the difference between the calculated and actual solutions to (4.65), and the superscripts again indicate the time level and not a power. This procedure is repeated until the residual is less than a specified value. Therefore, the error relating to the convergence of the solution can be controlled by specifying a particular value for $\boldsymbol{R}^n$. For this study, a series of tests were performed that investigated the effect on the residual size to a typical simulation, to determine a suitable residual size (see Section 5.3.2).

The matrix A is solved using an "Incomplete Lower Upper factorization technique" (ANSYS, Inc., 2012c). This direct approach involves factorising the matrix of coefficients A into a lower-triangular and upper-triangular matrix, L and U respectively:

$$\begin{array}{ccc} A & = & L \qquad\qquad\qquad\qquad U \end{array} \tag{4.68}$$

$$\begin{pmatrix} a_{1,1} & a_{1,2} & a_{1,3} & a_{1,4} \\ a_{2,1} & a_{2,2} & a_{2,3} & a_{2,4} \\ a_{3,1} & a_{3,2} & a_{3,2} & a_{3,4} \\ a_{4,1} & a_{4,2} & a_{4,3} & a_{4,4} \end{pmatrix} = \begin{pmatrix} l_{1,1} & & & \\ l_{2,1} & l_{2,2} & & \\ l_{3,1} & l_{3,2} & l_{3,3} & \\ l_{4,1} & l_{4,2} & l_{4,3} & l_{4,4} \end{pmatrix} \begin{pmatrix} u_{1,2} & u_{1,3} & u_{1,3} & u_{1,4} \\ & u_{2,2} & u_{2,3} & u_{2,4} \\ & & u_{3,3} & u_{3,4} \\ & & & u_{4,4} \end{pmatrix}$$

where it is understood that the blank matrix entries are equal to 0, giving:

$$LU\boldsymbol{\phi} = \boldsymbol{b}. \tag{4.69}$$

If two of the matrices in equation 4.69 are combined to give a new system of equations:

$$U\boldsymbol{\phi} = \boldsymbol{\Phi}, \tag{4.70}$$

where $\boldsymbol{\Phi}$ is an unknown vector, there are now two systems of linear equations, those of equation 4.70 and:

$$L\boldsymbol{\Phi} = \boldsymbol{b}. \tag{4.71}$$

Both of these systems of equations are easily solvable due to the sparsity and structure of L and U. First, $L\boldsymbol{\Phi} = \boldsymbol{b}$ is solved for $\boldsymbol{\Phi}$. Due to the first row of L having only one term, $l_{1,1}$, the first term of $\boldsymbol{\Phi}$ is obtained with virtually no calculation, as $\boldsymbol{b}$ is made of known terms:

$$l_{1,1}\Phi_1 = b_1 \tag{4.72}$$

$$\Phi_1 = \frac{b_1}{l_{1,1}}. \tag{4.73}$$

Knowing Φ_1, Φ_2 is easily obtained from the second row:

$$l_{2,1}\Phi_1 + l_{2,2}\Phi_2 = b_2 \tag{4.74}$$

$$\Phi_2 = \frac{b_2 - l_{2,1}\Phi_1}{l_{2,2}} \tag{4.75}$$

This procedure is simply repeated through every line of the system of equations 4.71 until $\boldsymbol{\Phi}$ is obtained. The same procedure is then repeated for $U\boldsymbol{\phi} = \boldsymbol{\Phi}$ to obtain the solution variable of interest, $\boldsymbol{\phi}$. This is the general technique used for solving the discretised equations 4.65 for all the simulations in this study.

The solving of equation 4.65 is performed at every timestep until either the specified value of $\boldsymbol{R}^n$ is reached or a specified number of iterations has been performed. A schematic of the whole solver process is shown in Figure 4.3.

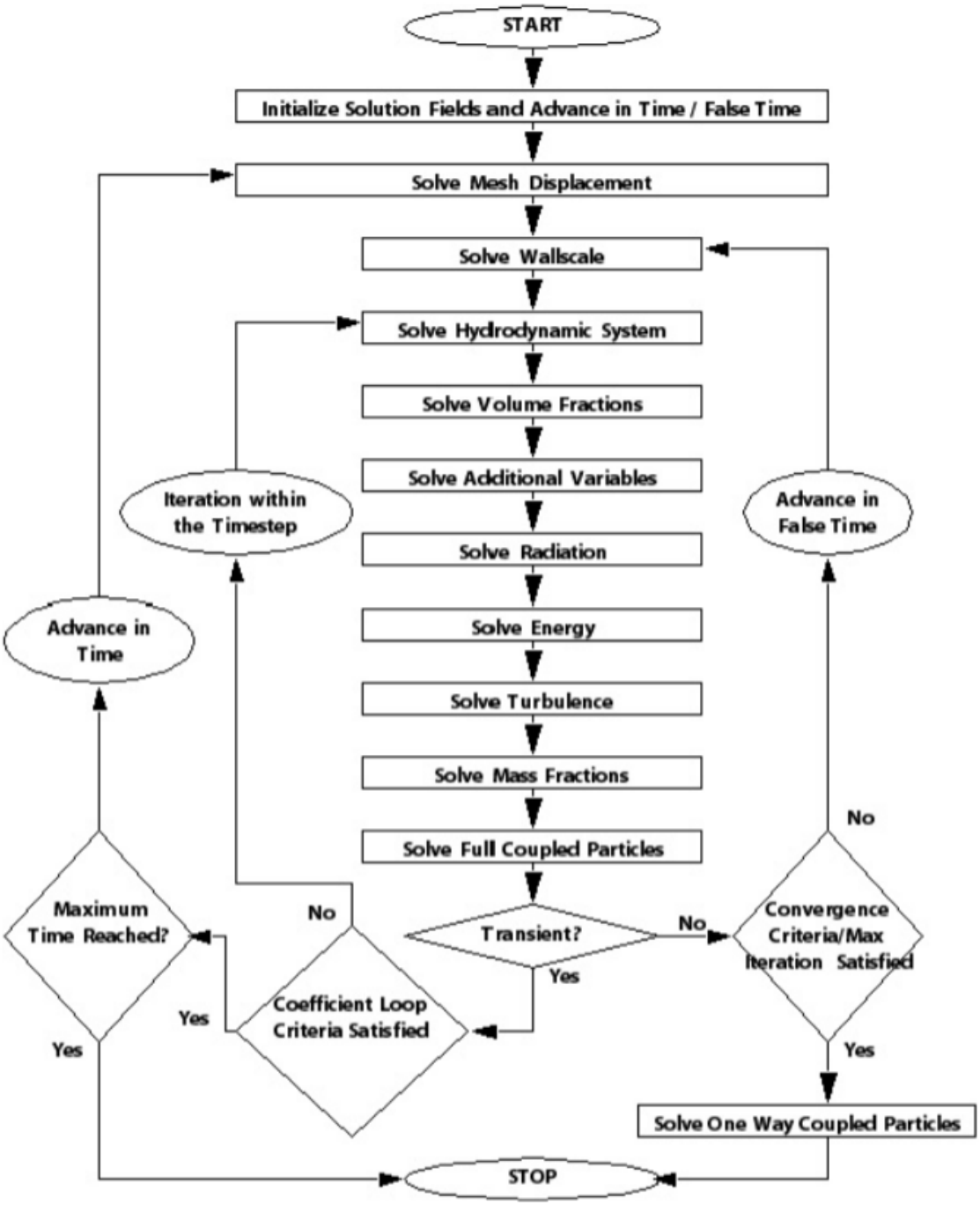

Figure 4.3: Flow chart of the procedures involved for a CFX simulation (ANSYS, Inc., 2012c).

4.7 Summary

The commercial software CFX is used for the vast majority of simulations carried out in this study. To understand how this software is capable of giving numerical data that is relatable to the water-bath experiments of Chapter 3, the underlying theory of this software was presented.

The Navier-Stokes equations that so accurately describe fluid flow were first presented in compressible form, then in the incompressible form in which they are applied to, and solved for, the flows here. Solving the NS equations for turbulent flows requires obtaining solutions on many length-scales, including the very small. This often implies large computational demand and so turbulence models are used to counteract this.

The most common form of turbulence modelling employs the RANS approach, whereby the flow variables are made to consist of a mean value and fluctuating part. The RANS approach is the basis of many of the most popular turbulence models. The theory behind the RANS models that are used in this study were then presented. The alternate approach involving LES, and the models which are based on elements of its theory, were then described.

The NS and turbulence model equations were all presented in exact and conservative form. As there is no general analytical solution for these equations, they are not solvable in the forms presented up to this point. The finite volume method is used by CFX to solve a system of linear equations that are close approximations of the NS and turbulence model equations. The way in which these equations are discretised from their exact form is a very important part of the CFD approach. The individual terms of a generic scalar transport equation in one-dimension is used to highlight this process, with it being understood that the equivalent in three-dimensions is very similar, only containing more terms.

By discretising and approximating the exact equations, error is introduced. The various sources of error relating to the converting of a physical model to a numerical model, as well as those relating to the numerical model itself, were discussed. This included the importance of the residual, the term which relates the difference between the exact and calculated solutions to the system of equations 4.65.

Chapter 5

2D CFD Modelling of Water-Bath Experiments

Contents

This chapter evaluates the potential to model the transport of a scalar due to a moving cylinder in a channel using a two-dimensional CFD model. It is also used to determine mesh, turbulence models and solver settings for the three-dimensional models to follow.

5.1 Introduction

The water-bath experiments, presented in Chapter 3, were conducted to obtain data that, once scaled, allows the prediction of contaminant transport under kinematically similar conditions at a larger geometric scale, representative of a person moving down a corridor. This is the first of two simulation chapters that aim to examine whether CFD simulations can capture and predict the same parameters found in Chapter 3. As CFD models are more easily adapted than water-baths, if the CFD models can be shown to produce similar flows, then more advanced and realistic CFD models can be built with confidence to provide understanding of more complex environments.

A 2D representation of the experiments is considered first. Since there are fewer cells in the 2D mesh than the 3D equivalent, there are fewer equations to solve. Hence, 2D simulations require less computational resources than their 3D counterparts, making them ideal for preliminary tests.

As highlighted in Section 2.3.4.2, the wake produced by fluid flowing past a circular cylinder is made up of a series of vortices, for flows satisfying $Re \geq 47$[1]. These vortices are known to enhance mixing and mass transfer within the wake (Cohen and Director, 1975) and are therefore highly relevant for the flows considered here. However, capturing these vortices in a CFD simulation with sufficient resolution, both spatially and temporally, is not trivial. Therefore, it is important that any CFD simulation that can be compared to the water-bath experiments also captures the vortex-shedding process sufficiently. Capturing data relating to the shedding of vortices is more easily achieved when using a stationary cylinder, compared to a moving cylinder. The flow past a 2D stationary circular cylinder is therefore considered first, before considering the flow caused by a translating 2D circular cylinder. It should be noted that the stationary setup is not intended to be truly representative of the water-bath experiments, rather it is necessary to ensure that the flow around a cylinder is captured sufficiently for subsequent models. It can be seen as the first step in the construction of a model that allows for the predicting of fluid flows due to a translating cylinder.

The geometry and mesh for all the 2D simulations were constructed in such a way that

[1]At such a low Re the flow is not turbulent, however as the Re increases the flow transitions into being turbulent. The value at which the flow is considered turbulent is problem dependent but is usually taken to be $Re \approx 2 \times 10^3$.

they could be used for both stationary and moving cases. This means that the preliminary tests and simulations performed with a stationary cylinder are directly comparable to those using a moving cylinder.

5.2 Geometry and Mesh

There are three different planes to consider when choosing a two-dimensional representation of the water-bath, (x, y), (y, z) and (x, z), where x corresponds to the direction of translation, y, the width of the water-bath, and z the height of the water-bath. As the translation and dye transport takes place in the x direction, this dimension is clearly the one of most importance, reducing the choice of plane to two possibilities, (x, y) and (x, z). Although the experimental images were captured by looking at the water-bath in the (x, z) plane, it is the (x, y) representation which makes a better choice for a 2D CFD model. Figure 5.1 shows how the two 2D geometries are interpreted once the relevant third dimension is considered. Despite looking like the images obtained from the experimental photographs, the (x, z) geometry (Figure 5.1a) does not interpret as a cylinder when the y direction is considered. Instead, the geometry represents a channel with a wall, or blockage, that spans its width. However, the (x, y) geometry (Figure 5.1b) does represent a cylinder in a channel, albeit of infinite height. Since the cylinder shape is maintained

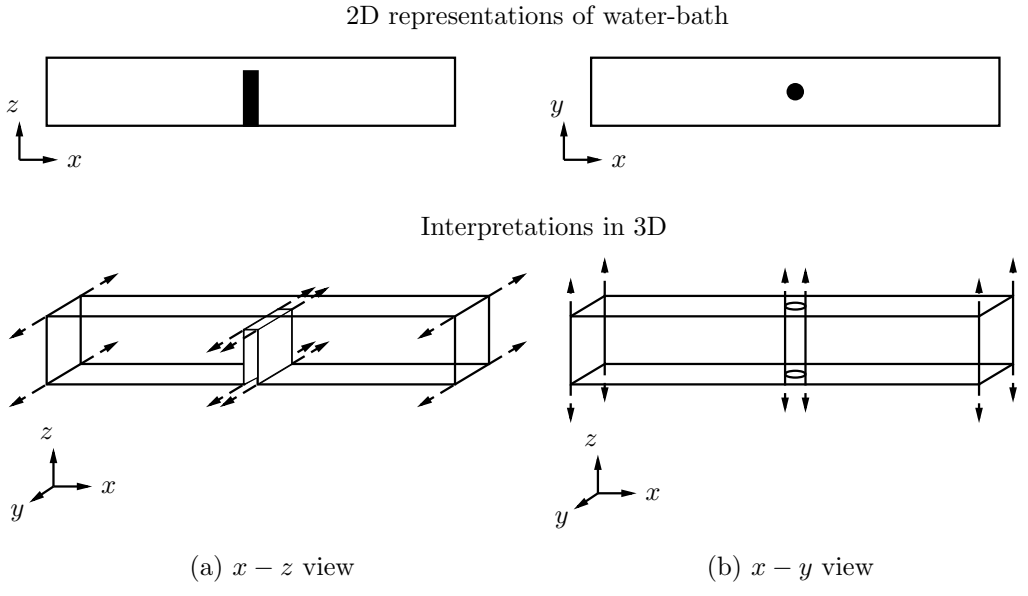

(a) $x - z$ view (b) $x - y$ view

Figure 5.1: Two different 2D representations of the water-bath geometry and how they are interpreted in 3D for geometries in the: (a) $x - z$ plane; (b) $x - y$ plane. Arrowed lines indicate direction of infinite extension.

in this geometry, the vortices that are shed from the cylinder can be modelled. As the wake of the cylinder and its interaction with the flow field can be captured, the geometry is a closer representation of the water-bath than that offered by the (x, z) plane. The geometry corresponding to the (x, y) view is therefore used for the 2D simulations.

5.2.1 2D Representation of Water-Bath Geometry

The dimensions of the 2D geometry used for the CFD simulations agree with those of the physical water-bath in the areas that are deemed important. This means that the width of the corridor, W, and the diameter of the cylinder, d, agree with those of the physical water-bath apparatus, but the length of the geometry differs as the end tanks are not included in the CFD simulations. The exclusion of the end-tanks is considered to not be significant as the experimental data is obtained in the central 1 m corridor section of the water-bath.

The CFD model has been purposefully constructed to be longer than the water-bath to account for the movement of, what will be termed, the 'region of translation'. The region of translation is defined to be the 100 x 98 mm area surrounding the cylinder outlined in Figure 5.2. The significance of this part of the geometry follows in Section 5.2.3.

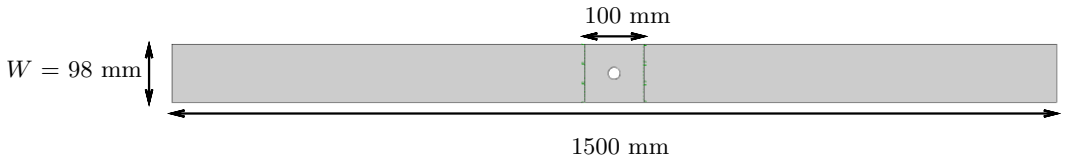

Figure 5.2: Plan view of the 2D geometry used. The central 100 x 98 mm region around the cylinder's starting location is the region of translation.

N.B. Since the simulations were performed using ANSYS CFX, the simulations could not be performed in two-dimensions in the true meaning of the phrase, i.e. the NS equations are only solved in the x and y directions. CFX only allows the solving of the full 3D NS equations and so the geometry needs to possess a height, or value of z. The height itself is not of importance, rather it is important to ensure that there is only one cell division in this direction so that the simulations are nominally 2D. Therefore, although the geometry is made to be 1 mm thick, this is of no significance as the mesh created from this geometry is only one cell deep.

5.2.2 Mesh for Stationary Cylinder Simulations

The meshes are created from the geometry using ANSYS Meshing. The mesh is designed such that all of the cells are hexahedral, with the majority being cubes or cuboids. The reduction in numerical diffusion and memory usage, when compared to using the popular alternative tetrahedral cells, means hexahedral cells should be used when possible (Anderson, 1995). However, one of the main difficulties when meshing a geometry with a curved surface is the transition from the curved cells adjacent to the boundary to the straight-edged cuboidal cells that are most sought after. The gradual switch from these curved cells to the cuboidal cells takes place in the region of translation, so that the the rest of the domain comprises cells of a more regular hexahedral shape. The additional importance of this for the moving mesh simulations is described in Section 5.2.3 that follows. Carefully prescribing the number of divisions along key edges of the geometry resulted in a mesh as seen in Figure 5.3a, with higher levels of refinement close to the cylinder (see Figure 5.3b).

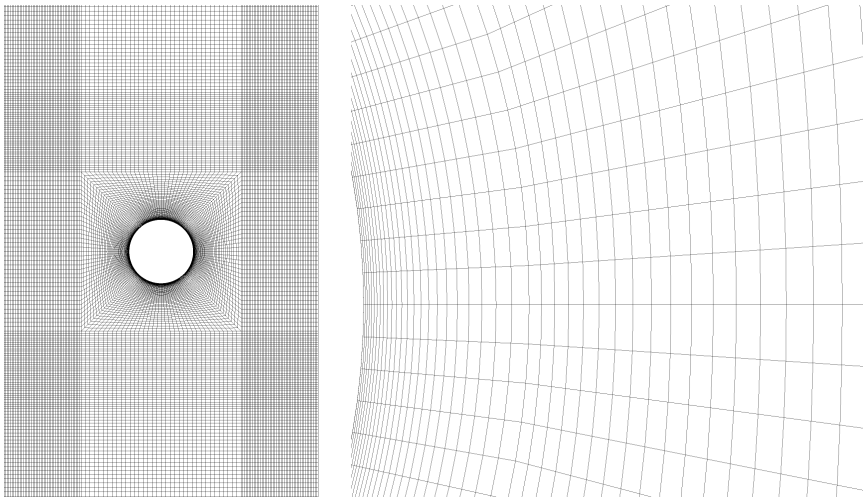

(a) (b)

Figure 5.3: (a) Central section of the mesh used for 2D simulations; (b) Exploded view of (a) showing cells near the cylinder wall.

5.2.3 Moving Mesh Considerations

For the stationary cylinder simulations the region of translation is of no special importance, this part of the domain is stationary like all the rest. However, for the translating cylinder simulations, the movement is implemented by applying a velocity to this entire region. Early attempts were made that only applied motion to the walls of the cylinder but the

fine cell-structure at the surface of the cylinder, necessary to accurately predict the vortex shedding, was lost. By applying the same motion to all cells surrounding the cylinder for a considerable distance, the structure of the cells surrounding the cylinder is not disturbed.

When the region of translation is at the extents of its motion (see Figure 5.4), the mesh to one side of it is fully compressed, while the other is fully extended. The creation of this region of compression is why the geometry had to be extended beyond the 1 m amplitude of translation. A value of 1.5 m was chosen as it was found to be sufficiently long enough that it prevented the mesh from becoming so distorted that simulations failed to complete.

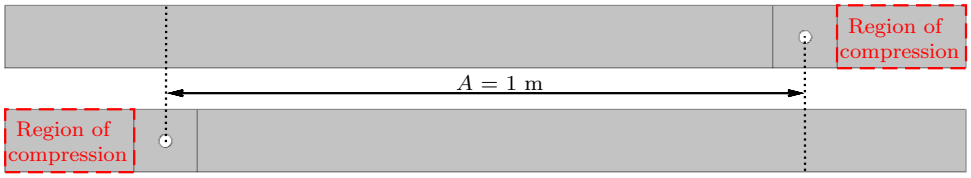

Figure 5.4: Geometry at the extents of translation. Regions of maximum compression indicated. The mesh corresponding to the geometry when in this state of maximum compression and expansion is presented later in Figure 5.12.

5.2.3.1 Alternative Approaches

Other approaches were investigated that could have potentially been used to model the effects of a cylinder translating in a channel. One approach explored involved the use of a stationary geometry and translating wall boundaries and fluid. This is essentially the same scenario as a translating cylinder in a stationary fluid, only from a different frame of reference. However, it was decided that implementing a moving geometry and mesh was important to the study in order to explore the capabilities of the CFD model when capturing the flow around a moving cylinder. Due to limited resources, this alternative approach was not tested and so a comparison between these two modelling approaches is beyond the scope of this study. A sliding mesh approach was also tested, whereby a much smaller section of the mesh slides against a predominantly stationary geometry, though this was not successful due to difficulties encountered in aligning the necessary interfaces.

An altogether different approach was tried, but rejected based on limitations of its implementation within the software. The immersed boundary method (IBM) approach allows for the boundary of a solid object to pass through the fluid domain and mesh.

Using this approach, the entire channel could be modelled using regular hexahedral elements, with no complications incurred at the cylinder boundary. Instead, the cylinder is implemented as a solid object and has cells of its own, which overlap those of the fluid domain. The effects of the solid, on the fluid, are then calculated based on the theory of Peskin (1972). However, the IBM approach implemented in CFX does not allow for any additional variables to be implemented. As the implementation of an additional scalar is very important to this work, this approach was quickly dismissed in the early stages of this study. Furthermore, as the approach does not consider the wall boundary conditions, there are potential limitations around reliably capturing the flow close to the wall.

As an alternative to the hexahedral mesh, a tetrahedral mesh was tested in a series of trial simulations carried out using ANSYS Fluent. However, it was found that the tetrahedral cells undergoing compression were distorted to a much greater degree than the hexahedral cells, often resulting in cells of such insufficient quality that the simulation could not finish. This may be able to provide an alternative approach to the meshing, however the restriction to tetrahedral cells it seen as a drawback.

5.3 Stationary Model Simulations

5.3.1 Boundary Conditions

All simulations in this section used the boundary conditions set out here, unless stated otherwise. For the stationary cylinder scenario, only the 20 mm cylinder is modelled to allow comparison with the data of Kanaris et al. (2011), who conducted CFD simulations similar to those outlined here at $Re = 300$. Here, the length scale used to calculate Re is taken as the cylinder diameter, d.

For these first cases, the cylinder is stationary and a unidirectional flow is imposed by creating an inlet and outlet as seen in Figure 5.5. All walls are constrained by the no-slip

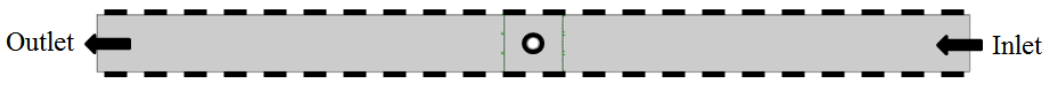

Figure 5.5: Boundary conditions for 2D stationary cylinder simulations. Dashed, black lines represent walls, inlet and outlet marked with arrows. The face presented, and the equivalent parallel face 'underneath', are defined as symmetry planes.

boundary condition, i.e. $U_i = 0$. The 'top' and 'bottom' planes of the geometry are modelled as symmetry planes. To aid in establishing the effects of the walls on the flow velocity, a parabolic velocity-profile, typically associated with flow in a channel, is applied at the inlet:

$$U_x = U_c \left(1 - \left(\frac{x - \frac{W}{2}}{\frac{W}{2}} \right)^2 \right) \tag{5.1}$$

$$U_y = 0 \tag{5.2}$$

where U_c is the centreline velocity at the inlet and $W = 98$ mm is the width of the channel. The outlet is specified as a pressure outlet and set to 0 Pa, relative to the inlet.

The fluid properties are set to those of water at 25°C, a temperature comparable to that of the laboratory where the experiments were carried out, with corresponding viscosity $\mu = 8.899 \times 10^{-4}$ kg m^{-1} s^{-1} and density $\rho = 997$ kg m^{-3}. Using U_c as the representative velocity when calculating the Reynolds number, $U_c = 0.014$ m s^{-1} leads to $Re = 314$. Here, the length scale used to calculate Re is taken as the cylinder diameter, d. However, as the flow progresses down the pipe the blockage ratio of the cylinder comes into effect which alters the velocity profile. The peak velocity $2d$ upstream of the cylinder is $U_x \approx 0.0124$ m s^{-1}, giving $Re \approx 278$. So although the value of Re clearly depends on where the velocity scale is chosen, $U_c = 0.014$ yields a value of $Re \approx 300$, meaning a comparison with the data of Kanaris et al. (2011) is worthwhile.

5.3.2 Solver Settings

All simulations were conducted using a transient approach, taking into account unsteady motions. Each simulation was set to run for 250 s using time-steps, $\Delta t = 0.025$ s. This time frame allowed those models that are capable of predicting the vortex-shedding phenomena to reach a stage where the shedding frequency is regular. The second-order backward Euler method was employed for the time discretisation in all simulations.

Data collection started after 150 seconds of flow and continued for 100 seconds. At $Re \approx 300$ this led to the flow properties being calculated over approximately 12 successive shedding cycles. Looking at the literature, it can be seen that the number of cycles over which the flow is averaged varies from study to study with no definitive value agreed

upon, however, the value of 12 used here is in agreement with the values used by other authors when investigating flows around circular cylinders (Kravchenko and Moin, 2000; Parnaudeau et al., 2008; Rosetti et al., 2012).

To determine the moment at which the solution is deemed to have converged, a short study was undertaken to see the impact of changing the residual associated with the solution of the (mass) continuity equation, i.e. equation (4.3).

To see what impact the changes in residual had on the solution, values of four properties relevant to the flow around a cylinder were calculated; Strouhal number, St; lift coefficient, C_L; drag coefficient, C_D; and base pressure coefficient, C_{pb}:

$$C_D = \frac{2F_L}{dU_c^2}, \quad C_L = \frac{2F_D}{dU_c^2}, \quad St = \frac{fd}{U_c}, \quad C_{pb} = \frac{2(p_b - p_\infty)}{\rho U_c^2}. \tag{5.3}$$

Here, F_L is the lift force per unit length, F_D the drag force per unit length, U_c the centreline velocity, d the cylinder diameter, f the vortex shedding frequency, p_b the pressure at the rear stagnation point and p_∞ the free-stream pressure.

Two monitoring points, P_{St} and P_{pb}, were positioned 'behind' the cylinder, relative to the flow direction, at (-0.04 m, 0.015 m) and (-0.01 m, 0 m) respectively, giving the necessary pressure data to calculate St and C_{pb} (see Figure 5.6). The forces F_L and F_D used in the calculation of C_D and C_L were calculated from the walls of the cylinder. The components of the resultant force acting on a surface are readily available in the post-processing software used, CFDPost, calculated by integrating the pressure over the entire surface. The lift force, F_L, is defined to be the component of force that acts perpendicular to the free-stream velocity, U_c. Using the coordinate system shown in Figure 5.6 this equates to the y component of the force acting on the cylinder surface. The drag force, F_D, is the component of force acting parallel to U_c but in the opposite direction, equating to the force acting on the cylinder in the x direction. The mean value of the drag coefficient, $\bar{C}_D$, and the root mean square (rms) value of the lift coefficient, C_L', are used for comparisons with the literature.

Kanaris et al. (2011) provide values for $\bar{C}_D, C_L', St$ and C_{pb} at a blockage ratio of $\beta = d/W = 0.2$. This value of β coincides with the experimental results for $d = 0.02$ m which possess a blockage ratio of $\beta = 0.204$. The SST model was employed for these tests as its performance for predicting separated flows is well known (Wilcox, 2006). The prediction

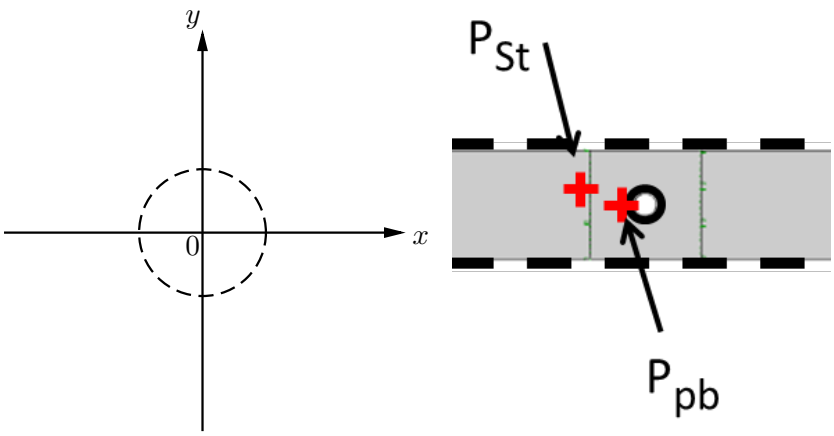

(a) (b)

Figure 5.6: (a) 2D coordinates system used. Both x and y origins are located at the cylinder's centre. (b) Positions of the two monitoring points, P_{St} and P_{pb}, located at (-0.04, 0.015) and (-0.01, 0), used for monitoring pressure values to calculate St and C_{pb}, respectively.

of flow separation is important as it directly relates to the vortex-shedding associated with flows around cylinders, in turn affecting the values of F_L, F_D, f and p_b.

The results can be seen in Table 5.1. As the target residual is changed there is almost no variation in the four flow properties across the first four orders of magnitude, $\bar{C}_D$ and C'_L show no change while St and C_{pb} vary by 0.5 % and 0.1 %, respectively. The solutions obtained with convergence criteria smaller than this appear to then show a small change in flow properties. Although the solution obtained with a residual of 10^{-4} is still dependent on the convergence criteria, this value is chosen to be used throughout this study, for both 2D and 3D simulations. Despite this dependency not being ideal, attempts made to employ a smaller convergence criteria of 10^{-5} resulted in impractical run times once fully 3D simulations were performed, and so a value of 10^{-4} was chosen for consistency. As the rate of eddy shedding is believed to be of importance to the mixing and mass transport in

Table 5.1: Flow properties at $Re = 300$ for varying convergence criteria.

Residual	$\bar{C}_D$	C'_L	St	C_{pb}	Run time (hrs)
10^{-1}	1.138	0.345	0.188	0.863	6
10^{-2}	1.138	0.345	0.188	0.864	6
10^{-3}	1.138	0.345	0.188	0.864	6
10^{-4}	1.138	0.345	0.189	0.864	12
10^{-5}	1.113	0.274	0.193	0.827	13
10^{-6}	1.113	0.274	0.193	0.826	21

the simulations in this study, choosing the residual to be 10^{-4} means there is only a very small difference in St value (0.5 %), and hence rate of eddy shedding, when compared to solutions of a higher degree of accuracy.

5.3.3 Mesh Independence

The mesh previously shown in Figure 5.3 is representative of the mesh used for all 2D simulations. To test the mesh dependence, seven meshes with the same basic structure but with different numbers of cells were created. Essentially this resulted in a sequential refinement of the meshes. The adequacy of the seven meshes was determined by looking at values of the same four properties investigated when looking at a suitable residual size. Calculated parameters for the seven simulations are given in Table 5.2.

No. Cells	Re	$\bar{C}_D$	C'_L	St	C_{pb}	Shedding Cycles	Run Time (hrs)
6,432	300	1.054	0.254	0.166	0.708	12	2
14,472	300	1.101	0.324	0.178	0.799	12	4
25,728	300	1.120	0.337	0.184	0.834	12	7
40,200	300	1.131	0.341	0.187	0.852	12	10
57,888	300	1.138	0.345	0.189	0.864	12	15
78,792	300	1.144	0.348	0.190	0.873	12	20
102,912	300	1.146	0.346	0.191	0.876	12	26
Kanaris et al	300	1.236	0.562	0.202	1.049	150	n/a

Table 5.2: Calculated flow properties from simulations performed on successively refined 2D meshes, with flow velocity $U_c = 0.014$ m s^{-1} using the SST model. Data from Kanaris et al. (2011) is provided for comparison.

It can be seen that the difference between successive values of the four variables of interest decreases as the mesh is refined. This is to be expected as it was shown in equation (4.64) that in the limit of $\Delta x \to 0$ the exact solution to the PDEs being solved is recovered. Although the exact solution of the PDEs is unknown, and hence so are the four variables of interest here, once the solution variables are changing by a small order of magnitude between successively refined meshes the solution may be judged mesh-independent. The difference between the values of the solution variables obtained from the two largest meshes would indicate that the 78,792 cell mesh be used as the values are only changing by $O(10^{-3})$. However, taking the run-time data into account it was decided that the 57,888 cell mesh offered a better compromise between solution accuracy and computational cost. The 57,888 cell mesh is, therefore, used throughout for all 2D simulations.

The values in Table 5.2 agree in order of magnitude with those obtained by Kanaris et al. (2011) but there is clearly room for improvement, hence the need for other turbulence models to be tested. Although the values reported by Kanaris et al. (2011) are not validated with experimental data, they are in good agreement with other numerical studies at comparable Re giving some confidence that the mesh is capable of providing a solution that others have deemed valid.

5.3.3.1 Quantifying Mesh Quality

The quality of the mesh, or rather the cells that constitute it, can be determined by investigating the value of certain key parameters. In this case the relevant parameters can be found in the ANSYS meshing program. There are a number of different parameters referring to cell quality but three of the most relevant are presented here: cell orthogonality, cell skewness and maximum corner angle. These represent a measure of how close the cells are to regular and, hence, 'ideal' cells. Details on the calculation of the metrics can be found in ANSYS, Inc. (2012d). Both skewness and orthogonality take on values between 0 and 1, where 1 is the best for orthogonality and the worst for skewness.

Looking at the values for the three parameters in Table 5.3, the 'average cell' clearly displays almost 'perfect' qualities. This is not surprising as the vast majority of the domain is made up of hexahedral cells with all corner angles equal to 90°. The cells that take on parameter values furthest from the ideals are those in the corners of the region of translation, a substantial distance from the cylinder boundary, as seen in Figure 5.7. This is worth noting as it gives confidence that the cells that determine the vortex-shedding, i.e. those on the cylinder boundary, are of a reasonable quality.

Table 5.3: Cell quality for 57,888 cell mesh used for 2D simulations.

	Orthogonality	Skewness	Max. Corner Angle (°)
Minimum	0.712	1.306×10^{-10}	90
Maximum	1	0.500	134.350
Average	0.995	0.001	91.289

Only the SST model has been used, so far, to perform the mesh dependency check. The six other turbulence models presented in Chapter 4.1 are now considered for the same boundary conditions and mesh described.

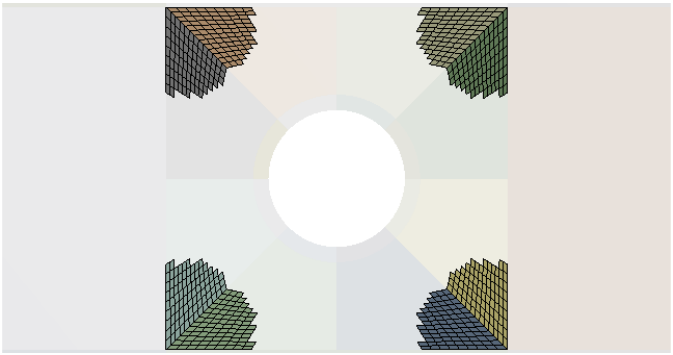

Figure 5.7: Cells highlighted are those with an orthogonality value less than 0.84, which coincides with cells of skewness greater than 0.35 and maximum corner angle greater than 120°.

5.3.4 Turbulence Model Discretisation Schemes

To make a fair comparison between the different turbulence models, it was necessary to keep the rest of the CFD model, such as boundary conditions and fluid properties, as consistent as possible. That being said, one of the most important aspects of the numerical model, the discretisation of the advection term in the NS equations, was altered depending on the turbulence model used. As previously mentioned in Section 4.5.1, the discretisation scheme impacts on the stability and the amount of numerical diffusion seen in a CFD model. Upwind schemes (UWS) are generally favoured over the central-difference schemes (CDS) due to their increased stability, albeit at the cost of increased numerical diffusion for sharp gradients. However, Breuer (1998) found that CFD models using the LES turbulence model produced much better solutions when the CDS was used, as opposed to an UWS. This was found to be true even when the formal order of the UWS was higher than that of the CDS. Because of this, the CDS is used for the models that include elements of LES modelling: SAS, DES and LES; and the high-resolution scheme (HRS) is used for the rest: $k-\epsilon$, $k-\omega$, SST, QI-RSM.

5.3.5 Low Reynolds Number Results

The first set of simulations were carried out to examine the performance of the turbulence models at $Re = 300$, allowing comparison with the data of Kanaris et al. (2011). The cases are summarised in Table 5.4.

Results obtained from the seven turbulence models considered, for the flow properties of concern, are summarised in Table 5.5. Although three of the turbulence models show values of the four flow properties in reasonable agreement with the literature and the previously

Turb. Model	Advection	U_c (m s^{-1})	Re	Δt (s)	Flow Time (s) (s)	Run Time (hrs)
SST	HRS	0.014	300	0.025	250	15
$k-\epsilon$	HRS	0.014	300	0.025	250	13
$k-\omega$	HRS	0.014	300	0.025	250	14
QI-RSM	HRS	-	-	-	-	-
SAS	CDS	0.014	300	0.025	200	17
DES	CDS	0.014	300	0.025	250	16
LES	CDS	0.014	300	0.025	250	14

Table 5.4: Summary of 2D cases. Advection schemes: HRS - high resolution scheme; CDS - central difference scheme.

considered SST model, it is clear that two ($k-\epsilon$ and QI-RSM) failed to capture the flow properties to a sufficient level of accuracy. The $k-\epsilon$ model clearly shows flow properties that are in not in agreement with the others and the QI-RSM model failed to yield a solution. The remaining models all yield values comparable to those of Kanaris et al. (2011), with the DES and LES models performing best.

Table 5.5: Flow properties for various turbulence models using the 57,888 cell mesh with a flow velocity of $U_c = 0.014$ m s^{-1}. Data from Kanaris et al. (2011) is provided for comparison.

Turb. Model	Re	$\bar{C}_D$	C'_L	St	C_{pb}
SST	300	1.138	0.345	0.189	0.864
Kanaris et al	300	1.236	0.562	0.202	1.049
$k-\epsilon$	300	0.785	5.27×10^{-6}	N/A	0.222
$k-\omega$	300	1.150	0.286	0.163	0.744
QI-RSM	300	-	-	-	-
DES	300	1.218	0.536	0.195	1.007
SAS	300	1.201	0.445	0.197	0.959
LES	300	1.234	0.593	0.209	1.087

There are several ways to visualise the turbulent eddies (vortices) in CFD solution data, but only two are used here. The two chosen are the vorticity, $\boldsymbol{\omega}_u$, and the swirling strength, λ_{ci}, where:

$$\boldsymbol{\omega}_u = \nabla \times \mathbf{U} \tag{5.4}$$

and λ_{ci} is the imaginary part of the two complex eigenvalues of $\nabla \boldsymbol{U}$ (Adrian and Balachandar, 1999). For the 2D simulations, only the vorticity is used to visualise the wake. Values of λ_{ci} are used to visualise the solutions of the 3D simulations in Chapter 6. Contour plots of $\boldsymbol{\omega}_u$ are presented in Figure 5.8. Of the six turbulence models that yielded

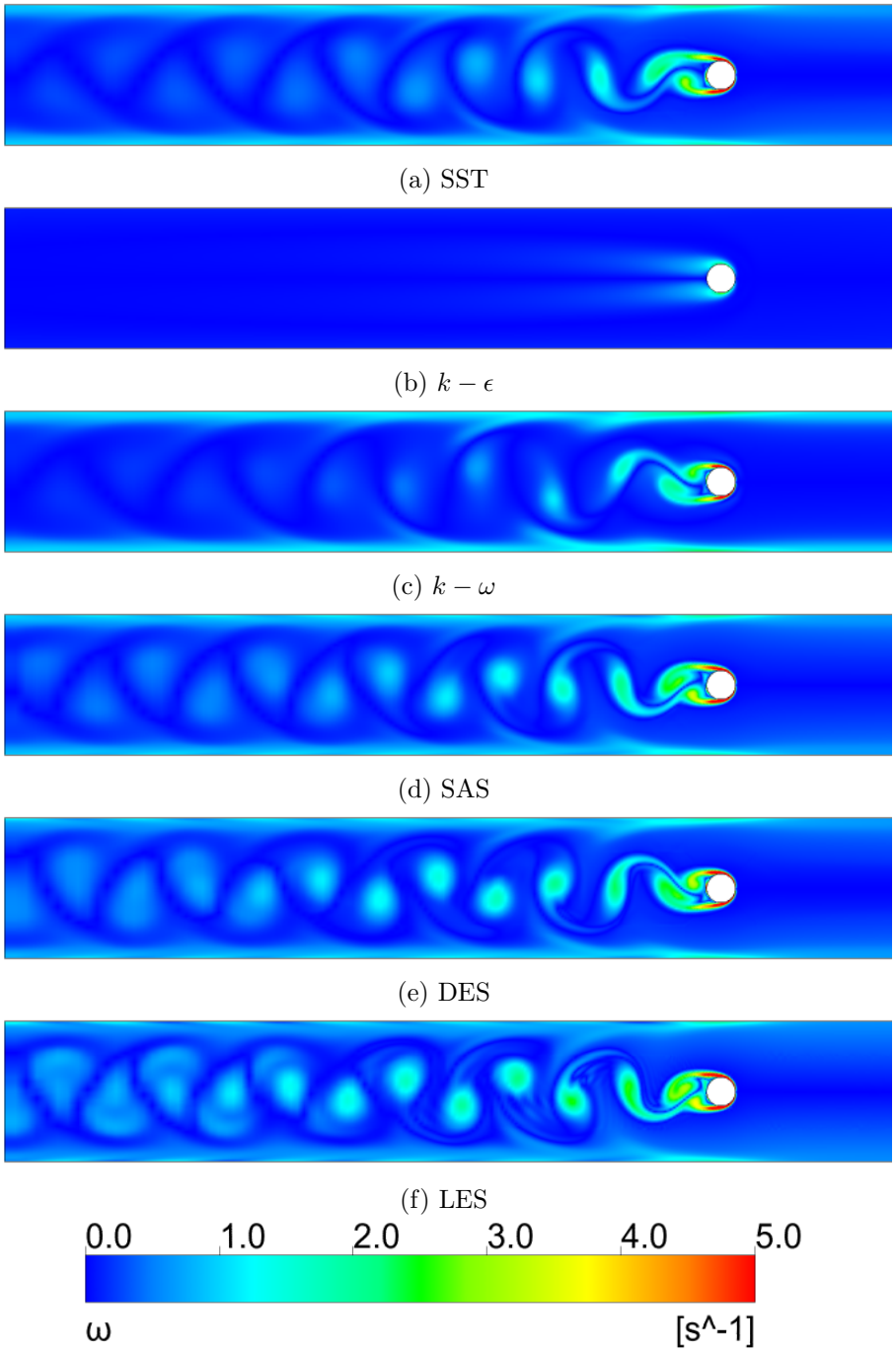

Figure 5.8: Contour plots of vorticity, $\boldsymbol{\omega}_u$, obtained for $Re = 300$ on the downstream half of the domain at $t = 250$ s, in the top symmetry plane of the geometry, for: (a) SST; (b) $k-\epsilon$; (c) $k-\omega$; (d) SAS; (e) DES; (f) LES.

a solution, five show patterns of vorticity that one would expect to find in the wake of a circular cylinder. The (approximately) circular regions of high vorticity are typical of vortices in a wake. However, Figure 5.8b, which corresponds to the solution data provided by the $k-\epsilon$ model, clearly shows no signs of distinct vortices.

Each turbulence model that is able to predict the onset of vortex shedding shows a different wake pattern. The vorticity contour plots of Figure 5.8 highlight the differences in turbulence and eddy-viscosity prediction. Comparing the $k-\omega$ and SST models (Figures 5.8c and 5.8a), the influence of Bradshaw's hypothesis can be seen as an increase in vorticity in the wake (and reduction of eddy-viscosity) of the SST model. Comparing the LES model (Figure 5.8f), which has no such assumption, to the SST model, it can also be seen that the LES model exhibits a more turbulent wake where the vorticity dissipates less downstream, a sign of a lower eddy-viscosity.

As mentioned in Section 2.3.4.2, the vortex-shedding phenomena seen in the wake of a circular cylinder is formed by the roll up of shear layers, after the onset of an instability at $Re \approx 47$. Therefore, in order for a CFD model to capture the vortex-shedding and subsequent vortices, it is necessary to first capture this instability. By investigating values of the wall shear stress, τ_w (see Figure 5.9), it is clear that the $k-\epsilon$ model is not able to capture the instability in the shear layers (Figure 5.9b) in the same way that the other turbulence models can. This is evidenced by symmetric values of τ_w around the cylinder for a significant period of time (100 s).

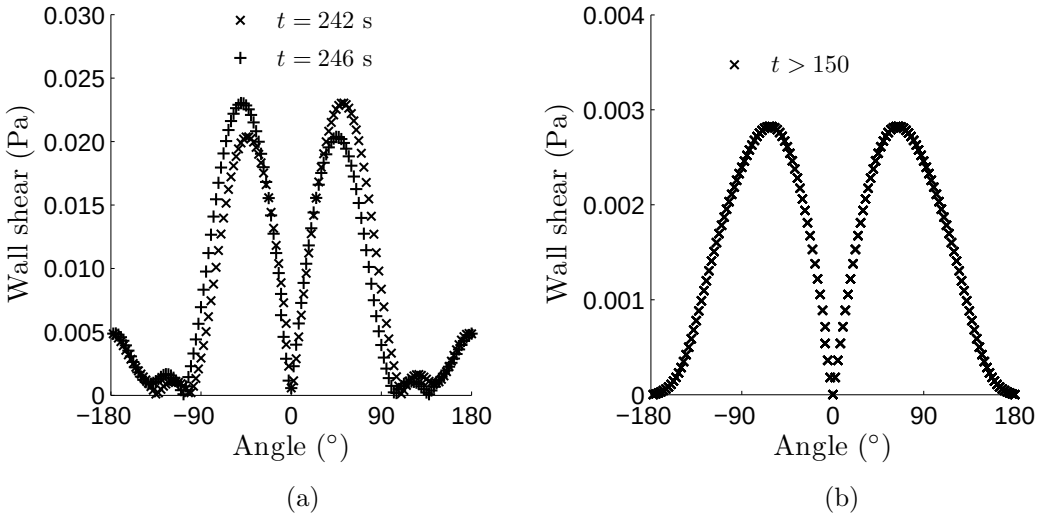

Figure 5.9: Wall shear stress, τ_w, plots for: (a) SST model at times $t = 242$ and 246 s; (b) $k-\epsilon$ model for $t > 150$ s. Angles are measured from the stagnation point at the front of the cylinder.

It is worth noting that the $k-\epsilon$ model is designed for modelling fully turbulent flows and so it is not surprising it has not performed well here. These initial simulations were undertaken to see which models were capable of capturing the changes in the flow properties when the cylinder is confined to a channel. To compare with the literature

this meant comparing to data obtained at $Re \approx 300$, which is low compared to the flows of interest and clearly not in a turbulent regime. For this reason, a second series of simulations were carried out at a much higher, and turbulent, Re.

5.3.6 High Reynolds Number Results

Table 5.6 presents an overview of the cases considered in this section.

Turb. Model	Advection	U_c (m s^{-1})	Re	Δt (s)	Flow Time (s)	Run Time (hrs)
SST	HRS	1.87	42,000	0.0001	1	22
$k-\epsilon$	HRS	1.87	42,000	0.0001	1	18
$k-\omega$	HRS	1.87	42,000	0.0001	1	22
QI-RSM	HRS	-	-	-	-	-
SAS	CDS	1.87	42,000	0.0001	1	24
DES	CDS	1.87	42,000	0.0001	1	22
LES	CDS	1.87	42,000	0.0001	1	20

Table 5.6: Summary of cases. Advection schemes: HRS - high resolution scheme; CDS - central difference scheme.

These simulations were carried out at $U_c = 1.87$ m s^{-1}, equating to $Re \approx 42,000$, in an 'unbounded' domain. The term unbounded in this case is taken to mean that the width of the domain is not imposing on the flow, which is taken to mean $\beta < 0.06$ (West and Apelt, 1982). As before, the value of Re may be taken to be slightly lower than this value depending upon where the velocity scale reading is chosen from, but the flow is now undoubtedly turbulent and the value of Re is comparable to that of the full-scale scenario, assuming a walking speed of $O(1)$ m s^{-1} and shoulder width = 0.5 m. Flow properties obtained from the results of the seven turbulence models tested under these conditions are presented in Table 5.7

Modelling in a pseudo two-dimensional way (i.e. the geometry is only one cell deep) means three dimensional effects are not properly captured. Mittal and Balachandar (1995) found that the forces on a cylinder are over-predicted in the two-dimensional case, when compared to the three-dimensional counterpart, due to the lack of resolvable length-scales in the spanwise direction. This is reflected in the values of $\bar{C}_D$ and $C_L^{'}$ when compared with the literature. Norberg (2003) compiled the data from many studies relating to flow around circular cylinders and provides values for $C_L^{'}$ over a large range of Re, as shown in Figure 5.10a. Similar data for $\bar{C}_D$ is shown in Figure 5.10b, as found in Roshko (1961).

Table 5.7: Flow properties for various turbulence models using the 57,888 cell mesh with a flow velocity of $U_c = 1.87$ m s^{-1}.

Model	Re	$\bar{C}_D$	C'_L	St	C_{pb}
SST	42,000	1.031	0.759	0.238	1.256
$k-\epsilon$	42,000	0.275	0.005	0.301	0.240
$k-\omega$	42,000	0.899	0.659	0.246	1.109
QI-RSM	42,000	-	-	-	-
DES	42,000	1.330	1.094	0.259	1.930
SAS	42,000	1.291	1.100	0.243	1.871
LES	42,000	1.626	1.402	0.204	2.063

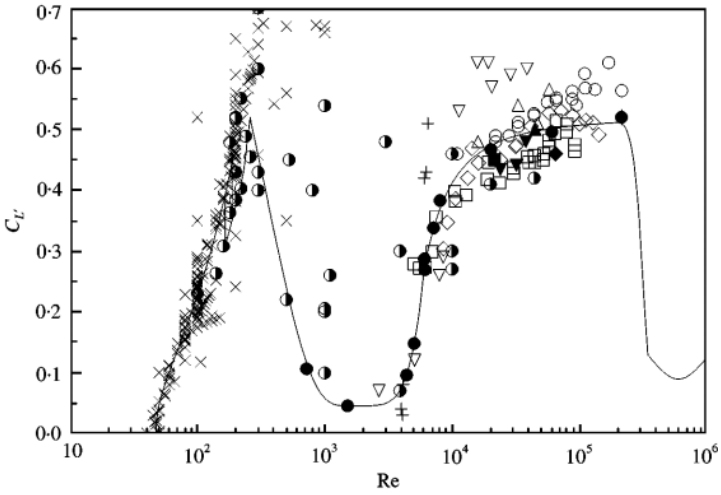

(a)

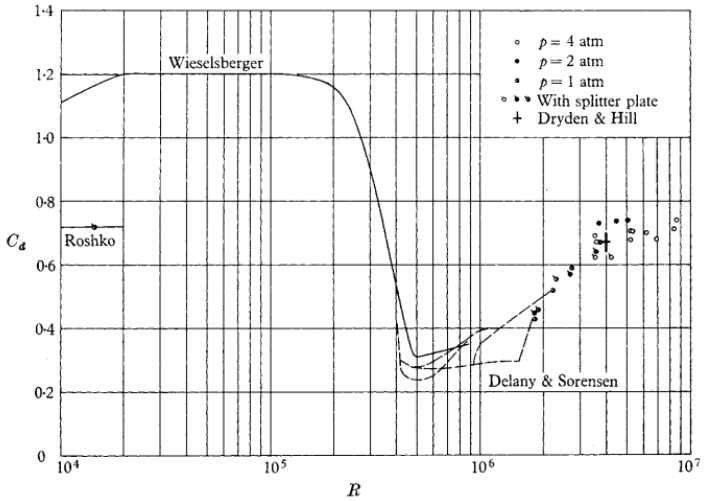

(b)

Figure 5.10: (a) C'_L as a function of Re, as found in Norberg (2003); (b) $\bar{C}_D$ as a function of Re, as found in Roshko (1961).

It can be seen that for $Re \sim O(10^4)$ previous experiments have shown $\bar{C}_D \approx 1.2$ and $0.4 < C'_L < 0.6$. Comparing these values with those in Table 5.1, the majority of the 2D results do indeed appear to slightly over-predict the values of C'_L and $\bar{C}_D$.

5.4 Moving Model Simulations

5.4.1 Boundary Conditions

So far, the flow has been determined by the inlet and outlet conditions at opposing ends of the domain. These boundary conditions were implemented to test model parameters and turbulence models. To make the 2D model a closer representation of the water-bath experiments, the inlet and outlet conditions are changed to walls, rendering the fluid in an initial state of quiescence, and the cylinder is now given a time-dependent velocity profile. This means that all background flow is removed and any fluid motion is down to the movement of the cylinder.

In the water-bath experiments, the cylinder's motion was determined by the linear actuator. The direction of motion was determined by the rotation of actuator's belt and reversed once one of the contacts at the end of the tank was depressed. To simulate this motion in CFX requires the use of CFX expression language (CEL), allowing a higher degree of user-input than standard. An algorithm, henceforth *Alg*-1, prescribing the displacement of the cylinder was developed that was able to replicate this motion:

```
t = <time>
w = <translation frequency>
A = <translation amplitude>
w1 = 1/w
t1 = w1/2
t2 = w1/4
t3 = mod(int(t2 + (t/2))/t1,2)
t4 = mod((t/t1) + 1,2) - 1
disp = (-1)^(t3)*(t4*A)
```

where `mod` is the modular function, and `int` refers to the integer part of (sometimes referred to as the 'floor function'). Qualitative information about the output of *Alg*-1 can be seen in Figure 5.11.

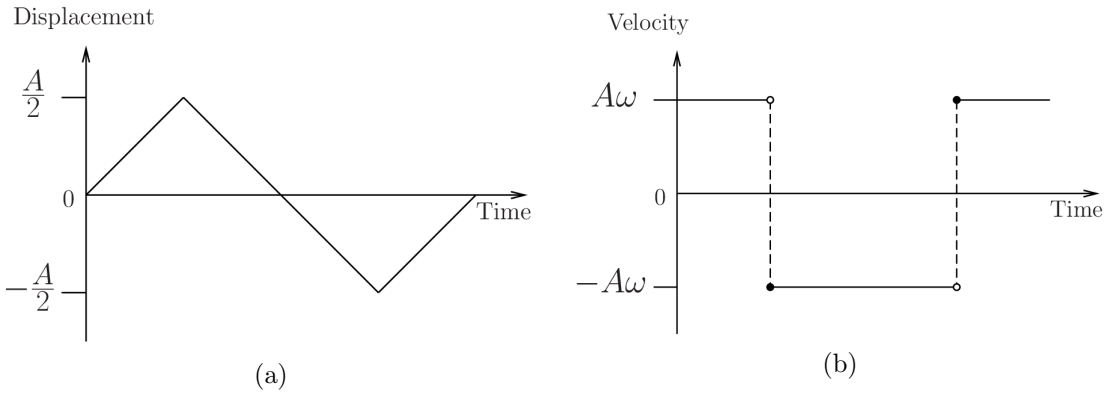

Figure 5.11: (a) Sketch of displacement versus time as calculated by CEL; (b) Corresponding velocity versus time plot.

The value of `disp`, as output from *Alg*-1, is applied to the wall boundaries of the cylinder and the mesh elements surrounding it. Applying this displacement to only a subset of the domain means that, before any other modifications, there will be overlapping elements. The CVs calculated from these overlapping elements leads to invalid elements, making any simulations impossible. Therefore, the mesh that is not subject to the displacement criteria of *Alg*-1is set to an 'unspecified' setting, which allows the interior nodes to be displaced but keeps all exterior walls fixed. Doing so means the mesh is constantly contracting and expanding, altering the properties of the mesh over time. The extent to which the mesh is distorted can be seen in Figure 5.12.

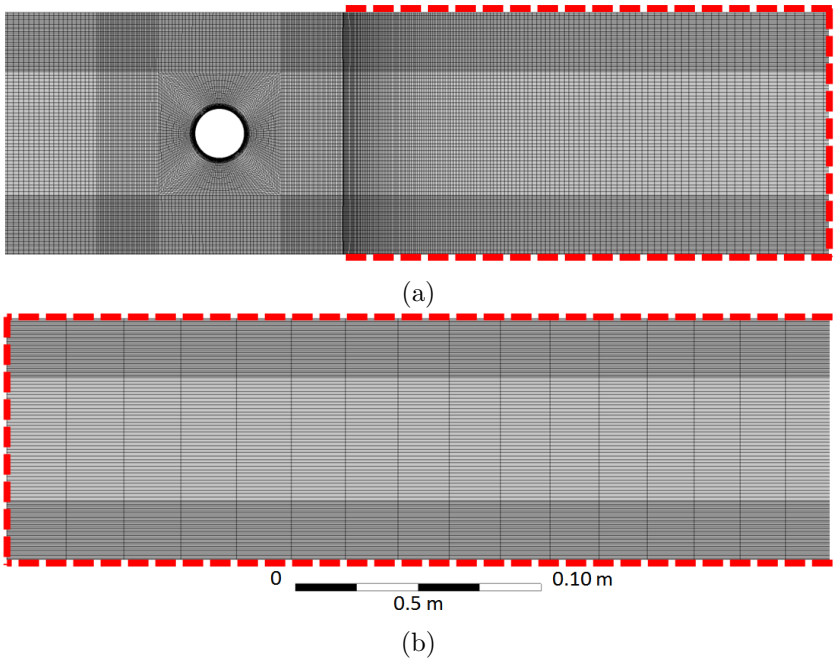

Figure 5.12: Mesh depicted at (a) maximum compression; (b) maximum extension. Region of compression/extension indicated by the dotted red line, as previously seen in Figure 5.4.

To determine the influence of the mesh compression upon the resulting flow, a simulation using the stationary cylinder approach was carried out using the mesh at maximum distortion/expansion. The change in flow properties, when compared to the cylinder being centrally located, can be seen in Table 5.8.

Cylinder Position	Model	Re	$\bar{C}_D$	C'_L	St	C_{pb}
Central	SST	300	1.138	0.345	0.189	0.864
Max. Compression	SST	300	1.171	0.310	0.194	0.857
Change (%)	-	-	+ 2.9	- 10.1	+ 2.6	- 0.8

Table 5.8: Comparison between flow properties calculated from compressed and uncompressed meshes.

The lift force shows the largest variation at $\approx 10\%$, however could be down to the entrance length (the length of the channel before the velocity profile is fully developed or, in this case, the distance up to the cylinder) being much shorter for the mesh at maximum compression. This could lead to a slightly different velocity profile as the flow has had less time to develop to a steady state.

Comparing the U_x profiles across the channel at the stagnation point, the two cases show very similar values (see Figure 5.13a). However, the compressed mesh shows slightly higher pressure along the channel (see Figure 5.13b), leading to differences in forces calculated on the cylinder walls and, subsequently, lift and drag coefficients. However, the main property of interest, as regards the transport of a scalar ϕ, is the value of St and not $\bar{C}_D$

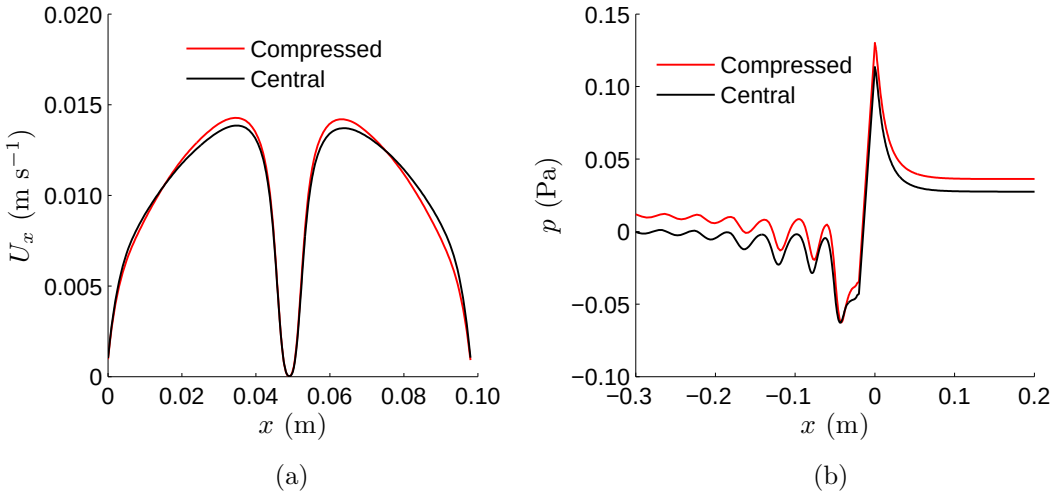

Figure 5.13: (a) U_x profiles across the tank at the stagnation point; (b) p profile along the centreline, where $x = 0$ is the stagnation point.

or C_L'. The value of St varies only very slightly between the two solutions, providing some confidence that the vortex-shedding is being captured sufficiently throughout the entire domain, when the cylinder is in motion.

Upon application of *Alg*-1to the cylinder walls and surrounding mesh, every cell in the domain changes size after every time-step. Changing the cell size has no impact on the solution obtained in any CVs constructed from only interior cells, as this is effectively just changing the volume of fluid contained within the CV; the boundary conditions of the flow are unaltered from the point of view of these cells. However, this is not the case once a CV is constructed from a cell with a wall boundary. By default, wall velocities are defined to be relative to the "*Mesh Motion*". This means that upon application of the no-slip (zero-velocity) condition to any cell on the domain boundary, any sides of the CV associated with the wall condition are subject to $U_i - Z_i = 0$, where Z_i is the velocity of the cell/mesh. This would be representative of the water-bath model walls moving with velocity Z_i, which obviously they do not. To correct for this, the wall velocity conditions are modified to be calculated relative to the "*Boundary Frame*", restoring the standard no-slip condition $U_i = 0$. The difference between solutions obtained from these two approaches is shown in Figure 5.14.

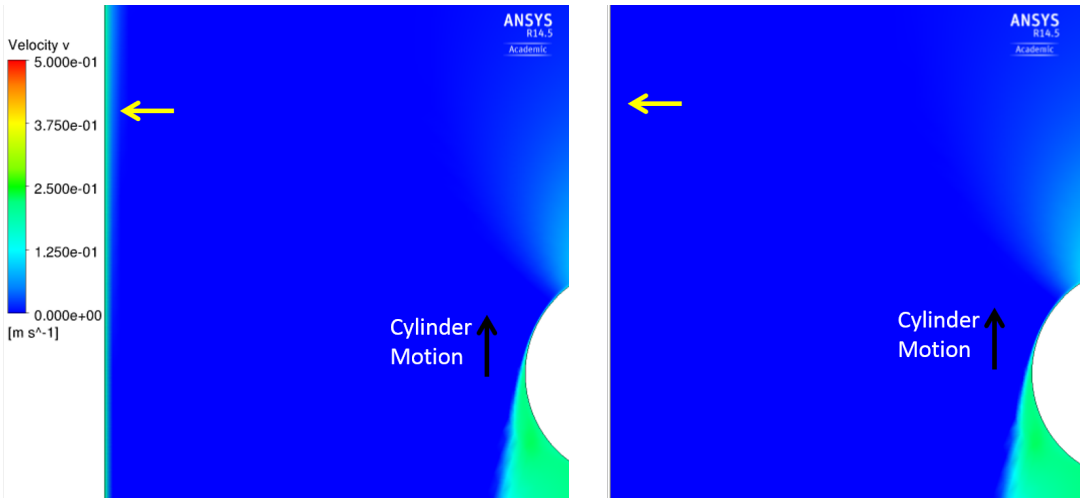

(a) (b)

Figure 5.14: Contours of U_x after 1 s of motion with (a) default wall boundary conditions; (b) $U_i = 0$ condition imposed. Note the velocity change on the left-hand side wall (change from green to blue), indicated by the yellow arrow.

The dye solution used in the experiments was found to have a negligible density difference when compared with water (see Section 3.2.2). This effectively means that it acts as a

passive tracer; it is implemented as such in the CFD model. Over the time scales concerned diffusive effects were also assumed to be negligible and so the scalar implemented here is modelled to reflect this. Typically, the generic scalar transport equation 4.50 is used to describe the motion of a scalar, however, due to the (assumed) negligible diffusion effects of the dye, the diffusion term is not included in the transport equation solved for the scalar. A scalar, ϕ, is set to be constant, with initial value $\phi_0 = 1$, in an area spanning the width of the tank and 50 mm in either direction of the cylinder's centre. This is the same initial condition applied to the dye solution in the water-bath model (see Figure 5.15).

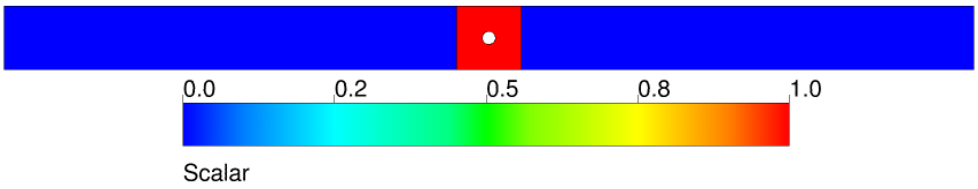

Figure 5.15: Initial ϕ value and location.

The 2D translating cylinder cases all used the same cylinder diameter and translation frequency, $d = 20$ mm and $\omega = 0.200$ s^{-1}. This value was chosen as the water-bath data obtained for the same d and ω was one of the readings least affected by fluctuations, giving confidence in the solution when comparing to the CFD model. Additional combinations of d and ω are considered in the 3D models in Chapter 6.

5.4.2 Changes to Solver Settings

The majority of the solver settings are kept the same as those or the stationary cylinder simulations with the only notable exception being that the timestep size, Δt, and total run time are different. The flow time is changed to 60 s, which corresponds to $\omega t = 12$, which is less than ωt^* for $d = 20$ mm and $\omega = 0.200$ s^{-1}. By running simulations for a period of time that equates to a value of $\omega t \leq \omega t^*$, it reduces the likelihood that if the CFD model does over predict the rate of transport slightly, the scalar should still be in the central 1 m section of the geometry, meaning post processing is unaffected.

The value of Δt is altered depending on the turbulence model in use. For LES modelling, the value of Δt is often chosen such that the Courant-Friedrichs-Lewy (CFL) condition:

$$\frac{|U_i|\Delta t}{h} = CFL \leq 1 \tag{5.5}$$

is adhered to for all cells, where h is a length-scale of the cell ($h = \Delta x$ in the case of a

unidirectional flow). Ensuring this criteria is met means that a parcel of fluid can never 'pass through' a cell in a given time-step, in which case it would go unresolved. The value of 1 may be relaxed (increased) for implicit schemes, like those used in CFX, though at the cost of reduced accuracy.

For a stationary cylinder, adaptive time-stepping may be used, whereby Δt is chosen to satisfy equation 5.5. However, for the moving mesh considered here, the cells that undergo compression can result in very small cells, requiring $\Delta t \sim O(10^{-5})$ s to meet the CFL condition. For this reason, fixed values for Δt were enforced, such that $\Delta t = 0.01$ s when using the SST model and $\Delta t = 0.0025$ s for the other three. A value of $\Delta t = 0.0025$ s was tested when using the SST model, but was found to produce no noticeable change when compared to the solution obtained using $\Delta t = 0.01$ s. A value of $\Delta t = 0.01$ s was kept to keep computational costs down.

5.4.3 Results for Translating Cylinder at $Re = 4,000$

Table 5.9 presents an overview of the translating cylinder cases considered in this section.

Turb. Model	Advection	ω (s^{-1})	Re	Δt (s)	Flow Time s	Run Time (hrs)
SST	HRS	0.2	4,000	0.01	60	20
SAS	CDS/HRS	0.2	4,000	0.0025	60	24
DES	CDS/HRS	0.2	4,000	0.0025	60	46
LES	CDS/HRS	0.2	4,000	0.0025	60	36

Table 5.9: 2D translating cylinder cases. Note that CDS/HRS refers to the use of two advection schemes. The first in relation to the advection term of the NS equations and the second in relation to any gradients in the turbulence model transport equations.

The previous section used the four properties $\bar{C}_D$, C_L', St and C_{pb} to compare the solutions of the different turbulence models. This is straight forward to do for a stationary cylinder, but more complex once the cylinder is moving. For cases involving a moving cylinder, differences in properties relating to the transport of the scalar, ϕ, are investigated. At first glance, contours of ϕ may look qualitatively similar for the four turbulence models tested (see Figure 5.16) however differences between their solutions can be determined.

The transport of the dye in the water-bath experiments was characterised by the profiles of dye concentration, C, across the tank and the corresponding centre of mass, $\bar{X}$. Recalling

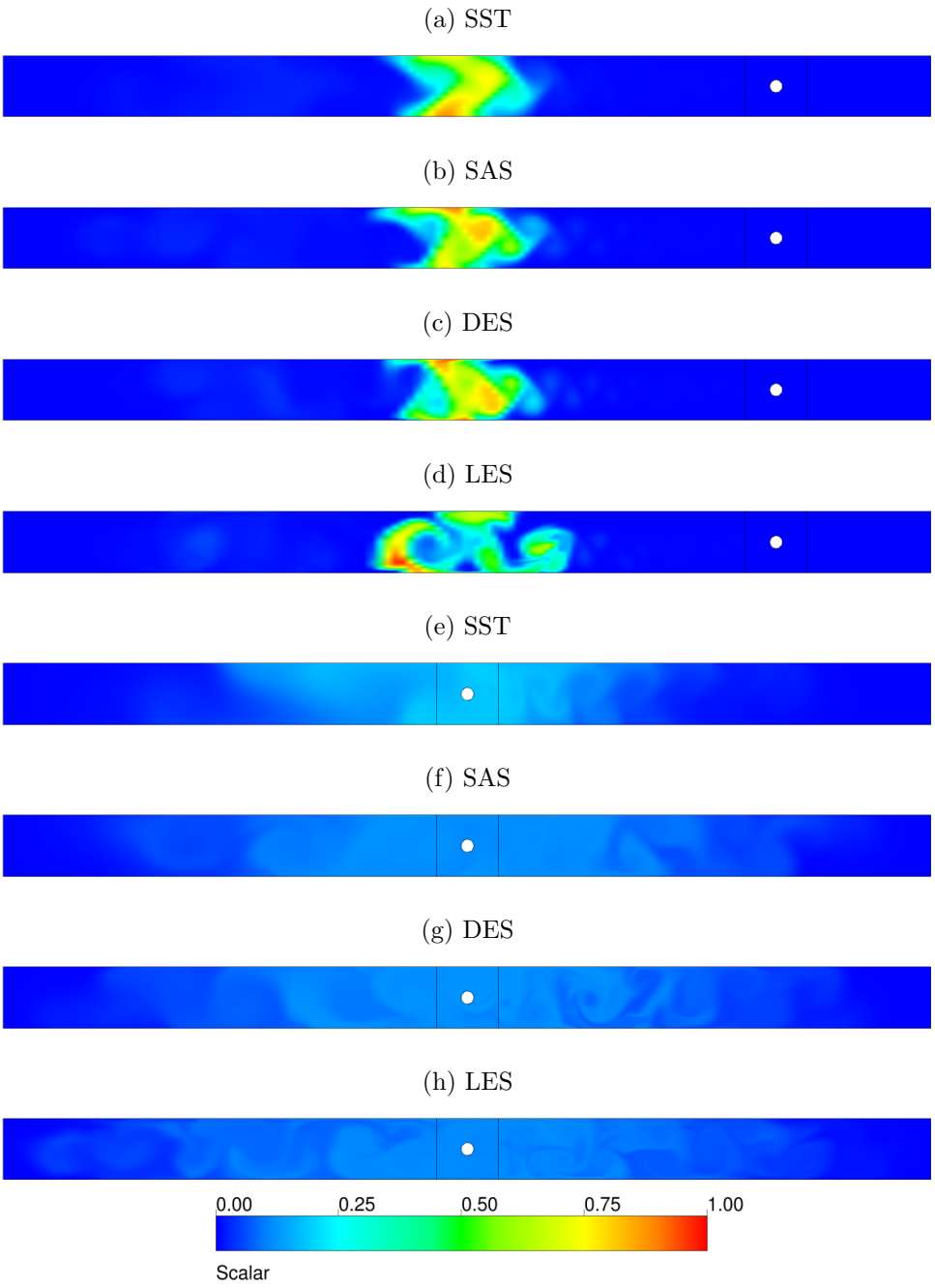

Figure 5.16: (a)-(d) ϕ contours after 7.5 s for the four turbulence models; (e)-(h) ϕ contours after 60.0 s.

equation 3.25, the centre of mass of a scalar ϕ may be defined similarly as:

$$\bar{X}_\phi = \frac{\sum_i x_i \phi^i}{\sum_i \phi^i} \tag{5.6}$$

where ϕ^i is the sum of the dye masses that have x-coordinate x_i for a given time-step.

Calculating this centre of mass is not a trivial matter as the values of x_i for the CVs around the cylinder are not regular. Recalling Figure 5.3, it can be seen that due to the radius of curvature of the cylinder, the x and y-coordinates are not subject to a regular grid spacing. To analyse the solution data, it is therefore necessary to interpolate on to a regular grid first.

The solution data is interpolated onto a 1500 $\times$ 98 grid in MATLAB. As the solution domain is 1.5 m $\times$ 0.098 m, this leads to the data being interpolated onto a grid of regular 0.001 m $\times$ 0.001 m cells. The smallest cell in the domain is $O(10^{-9})$ m^2 in area, meaning that there is to be a small loss of data during the interpolation. However, tests were performed on interpolation grids of various sizes, with no noticeable effect on the data for grids with a resolution finer than 1500 $\times$ 98 cells. For this reason, the 1500 $\times$ 98 grid is used throughout. Figure 5.17 shows that the interpolated solution data is almost indistinguishable from the raw solution data using the 1500 $\times$ 98 grid. The only discernible difference being the area occupied by the cylinder, where a condition is imposed during the interpolation such that all cells occupying the same space as the cylinder are set to possess a scalar value of zero (see Figure 5.17). Once the solution data is interpolated onto the regular grid, values of x_i are easily obtained and $\bar{X}_\phi$ is calculable.

For comparison with the water-bath experimental data, properties relating to the transport of ϕ are only calculated on the relevant 1 m central section of the channel, i.e. 0.5 m either side of the cylinder's initial position. As was performed on the water-bath data for dye concentration C, profiles of ϕ are investigated first as a time series and then rescaled by $\sqrt{\omega t}$.

Solutions from the CFD simulations have the benefit of being obtained at clearly defined moments in time. The solutions were output every 0.5 s for all simulations, so a comparison can be made at different values of ωt. The y-averaged ϕ profiles across the length of the water-bath are presented in Figures 5.18 for all four turbulence models at five different ωt values. By averaging in y, values of ϕ are seen to only vary with x, making them comparable with the water-bath model results. Looking at the ϕ profiles for any one value of ωt, it is clear that transport properties relating to ϕ are turbulence model dependent. All four models show identical profiles at $\omega t = 0$, showing that all simulations start from the same initial conditions. After this moment, the SST, SAS and DES models all show qualitatively similar profiles, although the SAS and DES models exhibit a slightly faster

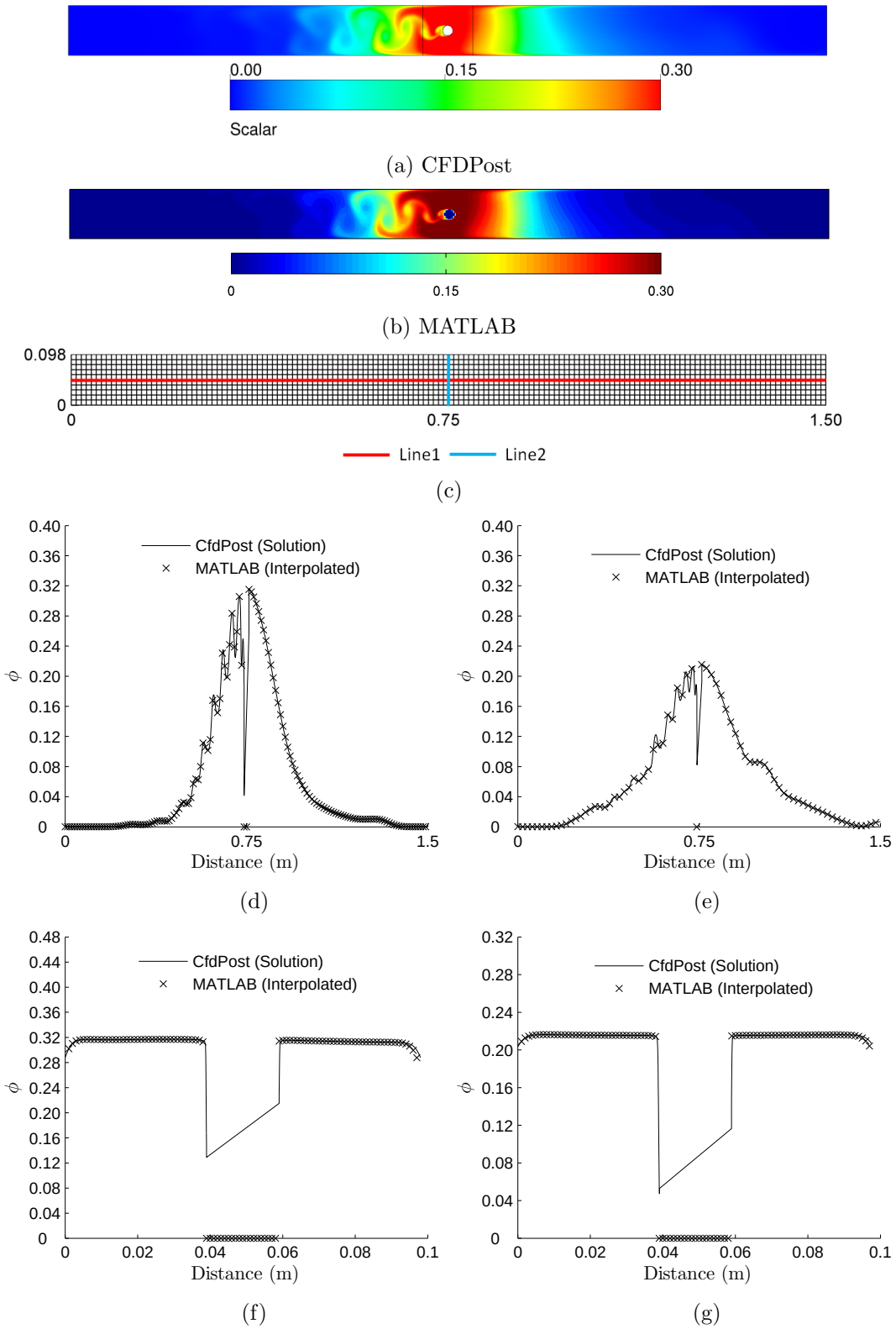

Figure 5.17: Comparisons between raw solution data for ϕ, as calculated in CFDPost, and interpolated solution data, as calculated in MATLAB. (a) ϕ contour from CFDPost; (b) ϕ contour from MATLAB; (c) Example of interpolation grid (150 $\times$ 10); ϕ profiles plotted along (d) Line1 after 30 s; (e) Line1 after 60 s; (f) Line2 after 30 s; (g) Line2 after 60 s.

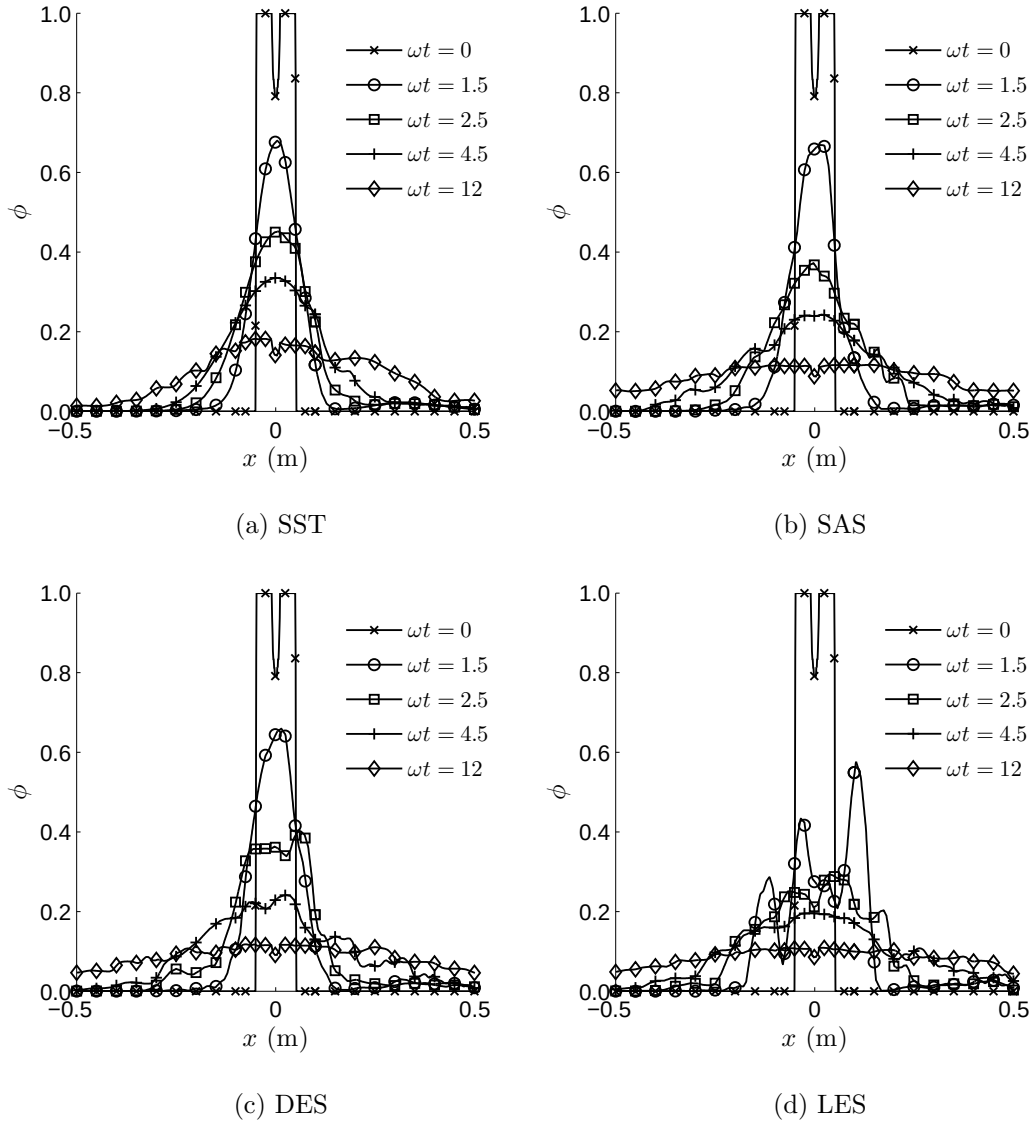

(a) SST (b) SAS

(c) DES (d) LES

Figure 5.18: ϕ profiles at $\omega t = [0, 1.5, 2.5, 4.5, 12]$ when using the (a) SST model; (b) SAS model; (c) DES model; (d) LES model.

rate of spread. This is most notable when looking at the $\omega t = 12$ result, where the SST model shows ϕ only just having reached the ends of the tank, whereas the DES and SAS models give a larger ϕ value at $x = \pm 0.5$ m. The LES model shows slightly different behaviour to the other models from $\omega t = 1.5$ onwards. The other three turbulence models show that the ϕ region predominantly stays near $x = 0$, while the LES model shows a much more sporadic profile.

Rescaling these profiles by $\sqrt{\omega t}$, as was done previously, yields plots comparable with those seen in Chapter 3 with very similar trends observed. These rescaled profiles are presented in Figure 5.19.

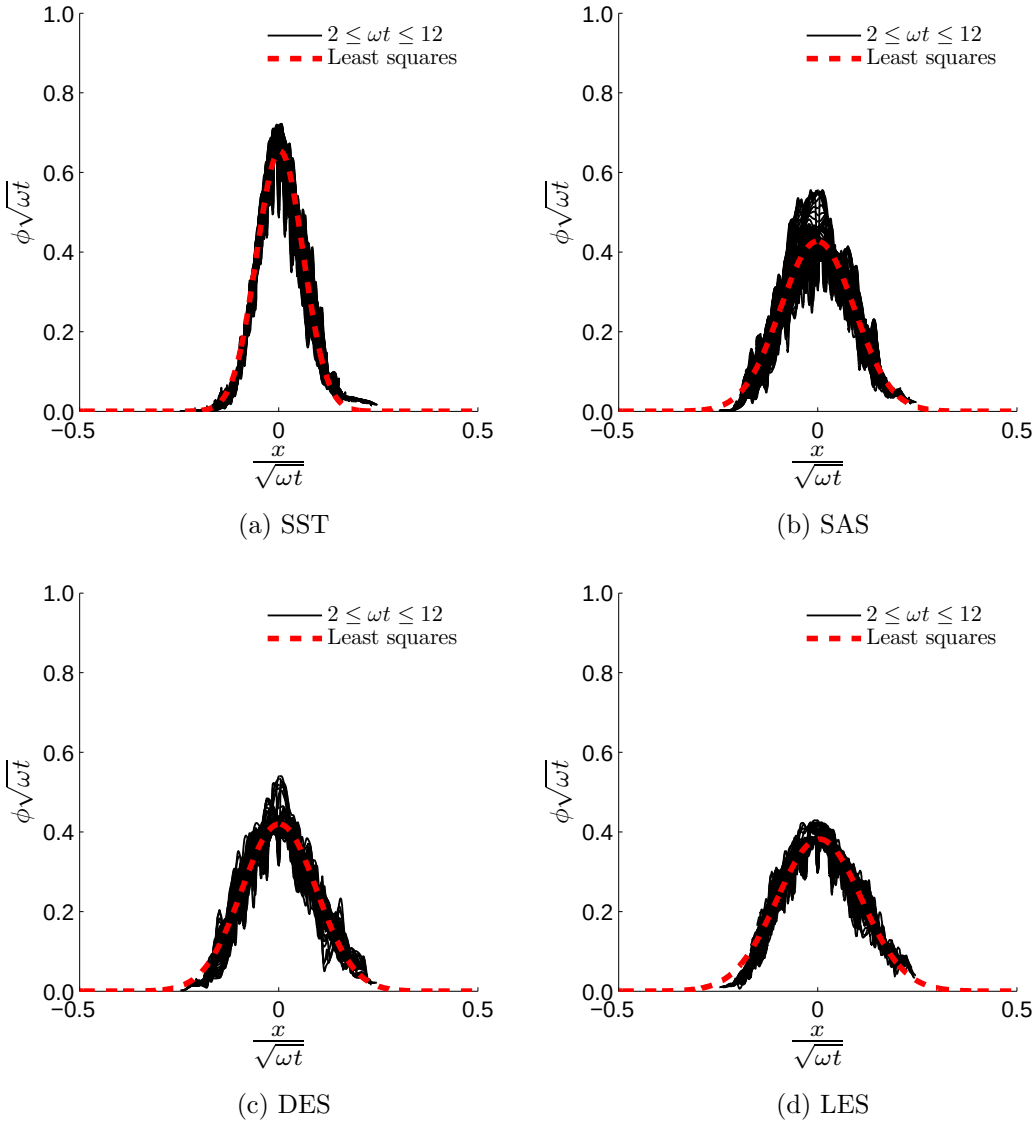

(a) SST (b) SAS

(c) DES (d) LES

Figure 5.19: ϕ profiles for $2 \leq \omega t \leq 12$ after rescaling by $\sqrt{\omega t}$ using the (a) SST model; (b) SAS model; (c) DES model; (d) LES model. The least-squares plot is provided by fitting equation 5.7 to the solution data.

The dashed red lines were obtained by fitting the function:

$$G(x) = \frac{c_2}{\sqrt{c_1}} e^{\left(\frac{-x^2}{c_1}\right)} \tag{5.7}$$

to the solution data, where c_1, c_2 are constants. The SAS and DES models show the most scatter in the data, while the SST and LES models show the rescaling collapses the data well. The SAS, DES and LES models all show profiles with a peak ≈ 0.4, while the SST model shows a peak ≈ 0.65. To see which of these models best captures the profiles obtained from the experimental data, the least-squares fit of the rescaled profiles of each

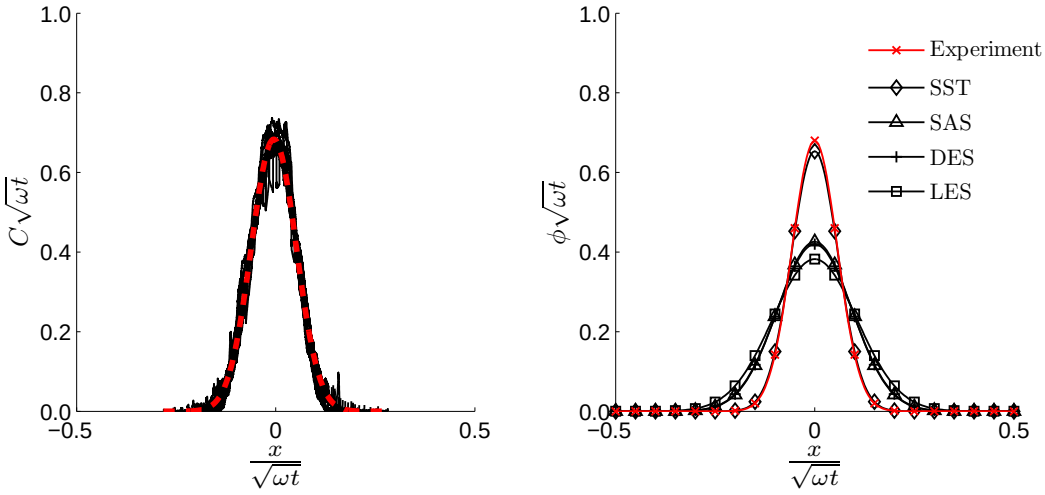

(a) (b)

Figure 5.20: (a) Experimental C profiles for $d = 20$ mm and $\omega = 0.200$ s^{-1}. The dashed red line represents equation 5.7 fitted in a least-squares sense; (b) Comparison between least-squares fitted ϕ profiles for different turbulence models and corresponding least squares fitted C profile for $d = 20$ mm and $\omega = 0.200$ s^{-1}.

turbulence model and the experimental data at $d = 20$ mm and $\omega = 0.200$ s^{-1} are now compared.

Figure 5.20 brings together the least-squares fitted profiles from Figure 5.19 with the equivalent water-bath data.

The SST model clearly outperforms the other three models, replicating the trends found in the experiments almost perfectly, while the others all appear to be too dispersive, predicting that the scalar reaches the ends of the tanks too quickly. Moreover, despite no goodness of fit test being performed, it can clearly be seen in Figure 5.20b that the averaged ϕ values of the SST model are the closest match to the averaged C values of the water-bath model. This trend is repeated when comparing values of $\bar{X}$ with values of $\bar{X}_\phi$ (see Figure 5.21). This is to be expected as the water-bath data shows good agreement with the fitted function $G(x)$ (see Figure 5.20a), while the SST model shows good agreement to the same $G(x)$ (see Figure 5.20b). The other three models all still show a $\sqrt{t}$ dependence, as indicated by the linear portion of the plots in Figure 5.21b, despite the weaker agreement when compared to the experimental data.

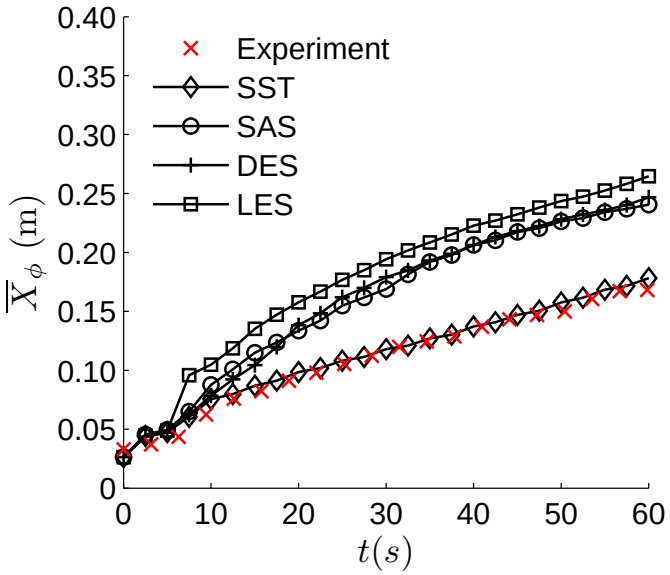

(a)

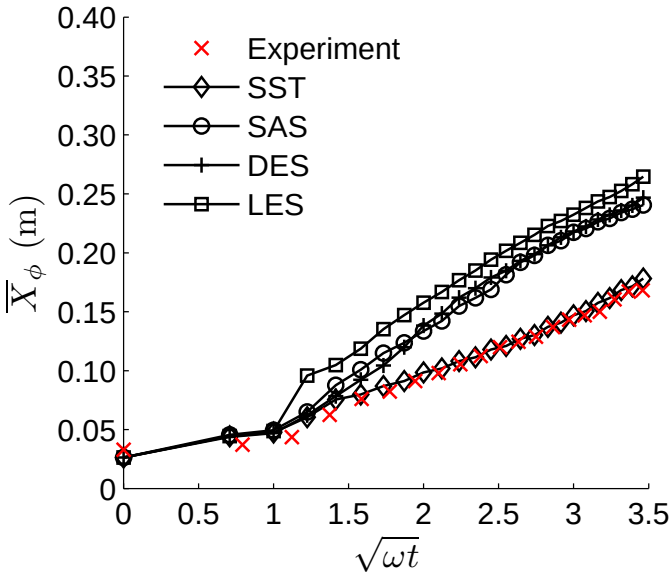

(b)

Figure 5.21: $\bar{X}_\phi$ plotted as a function of (a) time; and (b) $\sqrt{\omega t}$, for the four turbulence models considered, compared against experimental values of $\bar{X}$ for $d = 20$ mm and $\omega = 0.200$ s^{-1}.

5.4.4 Discussion

Of the turbulence models tested, the SST model shows better performance than the others at predicting scalar transport for the boundary conditions as outlined previously. It is postulated that the SST model's performance advantage lies within its eddy-viscosity prediction, through the application of Bradshaw's hypothesis. At this stage, it appears as though the SST model has a clear advantage over the other turbulence models in its ability to capture transient scalar transport when modelling the problem in 2D. However,

it needs to be stated that there is one key limitation to the CFD study thus far: the simulations have all been performed using a pseudo-two-dimensional geometry, i.e. one cell thick. This means there is no allowing for variations in the z direction. This is of particular significance here, not only because the water-bath experiments were (obviously) conducted using a three-dimensional cylinder, but it is known that the wake of a cylinder loses its two-dimensional nature for $Re \geq 189$ (Henderson and Barkley, 1996).

It is perhaps surprising that the SST model outperforms the other three LES-based models here, when LES is often considered superior to RANS models due to the additional length-scales it is capable of resolving. However, the LES-based models are not constrained by the assumption of an isotropic eddy viscosity for all length-scales (see Chapter 4), and so one would expect to see an improvement once a true 3D geometry is considered, where the true three-dimensionality of turbulence can be captured. It has been shown in previous studies that 2D simulations using LES to investigate the flow around a circular cylinder perform poorly (Breuer, 1998). Although it has already been highlighted that 2D simulations are known to over-predict lift and drag forces, the significance of a 2D geometry, here, will be seen in the next chapter.

5.5 Summary

The flow around a stationary 2D cylinder was investigated in a channel and the free-stream. The channel flow was conducted with $\beta = 0.2$, comparable with that of the 20 mm cylinder in the water bath, albeit at a much lower Re than those considered here. For this reason, simulations were conducted at $\beta = 0.02$ (where the flow may be considered 'unbounded') at $Re = 42,000$, which is clearly turbulent. Both these models were tested for seven different turbulence models and compared with the literature.

The stationary cylinder models considered here are clearly not physically comparable to water-bath model experiments, due to the lack of movement. However, the data provided by the testing of different turbulence models is invaluable as it rules out those models which are clearly not capable of predicting realistic flow features. The four turbulence models that showed values most consistent with those in the literature - SST, DES, SAS and LES - were then used in simulations more comparable to the water-bath experiments, with a translatory motion and scalar source.

Next, changes from the stationary cylinder study were outlined, with attention drawn to those that implemented the cylinder's motion. Once this motion was applied to the cylinder, the resulting mesh was shown to deform, but this deformation was shown to be able to produce flow properties in relatively good agreement with those obtained when the cylinder was centrally located. Changes to the default boundary conditions applied at the walls were shown, and the manner in which a scalar, ϕ, was introduced to the flow was also described.

The transport of ϕ in an initially quiescent water-filled channel was investigated using a series of pseudo-2D CFD simulations. The four chosen turbulence models were tested and their abilities at capturing profiles of ϕ (averaged across the channel) and the centre of mass, $\bar{X}_\phi$, of the corresponding distribution were evaluated. The numerical data was compared to experimental data obtained from an experiment performed under a comparable set of boundary conditions, as seen in Chapter 3. All models performed acceptably and showed similar trends to experiments, i.e. a $\sqrt{t}$ dependence was replicated and the C profiles showed a collapse of the data upon rescaling by $\sqrt{\omega t}$, however the SST turbulence model performed considerably better than the other three tested.

Chapter 6

3D CFD Modelling

Contents

This chapter considers CFD simulations that use a three-dimensional representation of the water-bath. The structure of this chapter follows a similar format to the previous chapter. First, the geometry and associated mesh is presented. The settings that differ to those of the 2D simulations are discussed, those that remain the same are omitted. Only results from the four best performing turbulence models - SST, DES, SAS, LES - are presented, from both stationary and moving models. The results from nine d and ω combinations are compared to the experimental data seen in Chapter 3.

6.1 Introduction

The 2D CFD simulations presented in Chapter 5 showed that when the SST turbulence model was employed, the transport of a scalar, ϕ, compared well with the experimental data of Chapter 3. The other three, LES-based, turbulence models compared less well with the experimental data.

LES-based models aim to resolve the larger length scales of the flow (see Chapter 4). When considering turbulent flows, the turbulent length-scales are usually three-dimensional and so modelling in two-dimensions reduces the ability of the turbulence model to resolve the correct length-scales. For the CFD simulations carried out in Chapter 5, the SST model suffers less from being applied in 2D as RANS models are based on averaging assumptions (see Chapter 4) and the flow and mixing is predominantly in the directions considered (x and y - see Figure 5.1).

A 3D representation of the simulations seen in Chapter 5 is now considered, allowing data to be captured in the z direction. This means that boundary layer effects on the bottom of the model are now considered which will have an effect on vortex creation in the z direction and consequently the transport of the scalar ϕ. By introducing the third dimension to the simulations, it is expected that the LES-based simulations will yield results with properties closer to those of the literature and water-bath model data. Since the flow induced by the translating cylinder is primarily in the x direction, the 3D simulations are not expected to change the findings relating to the SST model significantly.

6.2 Geometry and Mesh

For the 2D simulations, it was necessary to determine which pair of dimensions to consider for the model. This is no longer case and so the geometry used in this chapter is more easily recognisable as being representative of the physical water-bath. There are, however, subtle differences between the two which are highlighted in this Chapter.

6.2.1 3D Water-Bath Geometry

The 3D geometry used is an extrusion of the 2D geometry already seen, meaning that the 2D and 3D geometries agree in all dimensions except for the height, z. The geometry was extruded to agree with the height of the water level used in the experiments,

H_{water} = 136 mm (see Figure 6.1). This extrusion means that the cylinder spans the entire geometry from top to bottom, henceforth termed an 'infinite' cylinder, which is not in strict accordance with the water-bath set-up where there are end-effects. However, this approach is deemed to have minimal impact on results and enables post processing of the results to be simplified.

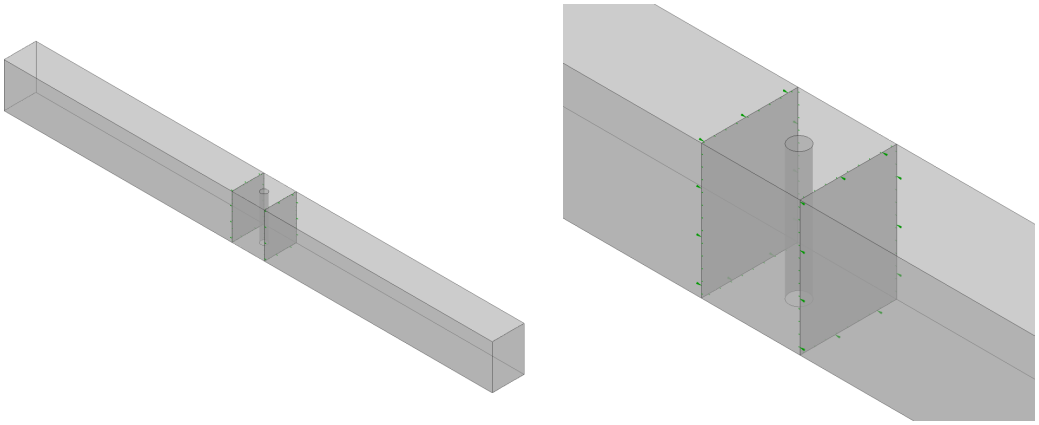

Figure 6.1: 3D geometry used. Upon closer inspection of the translating region the cylinder can be seen to span the entire geometry in the z-direction.

The post processing is performed in MATLAB, having first output all the information relating to CV location and ϕ value from CFDPost into a series of comma-separated variable (.csv) files. These .csv files are averaged through the cells layers (z-direction), a process which is made simpler if all the cell layers are the same, i.e. the geometry contains an infinite cylinder. The lack of agreement between CFD model and water-bath model above the height of the cylinder (the 26 mm, in the z direction, between the top of the cylinder and the water level) is discussed in detail in Section 7.4.3.1.

6.2.2 Mesh for 3D Simulations

To create a mesh for the 3D simulations, a natural starting point is an extruded version of the 57,888-cell mesh used for the 2D simulations. Doing this means that the 3D mesh resembles a series of layers; each one, essentially the mesh used in the 2D simulations. The number of layers/z divisions allowable is partly determined by the software used (in this case ANSYS Meshing). If the aspect ratio of the cells breaks a certain threshold during mesh creation, the mesh is not created as it is deemed to be of insufficient quality for a simulation. For the 57,888-cell mesh, this forced the number of divisions to result in a mesh with a minimum of $\approx$ 3.5m cells. The first series of simulations carried out using this mesh took around a week of computation to complete. This time frame was considered

to be far too long to carry out all the planned simulations, which meant trying one of the coarser meshes as the base for extrusion. The 25,728-cell mesh was eventually chosen as the base mesh for extrusion (see Figure 6.2), the number of divisions in the z direction chosen determined by a series of simulations using a stationary cylinder setup, similar to that presented in Section 5.3.

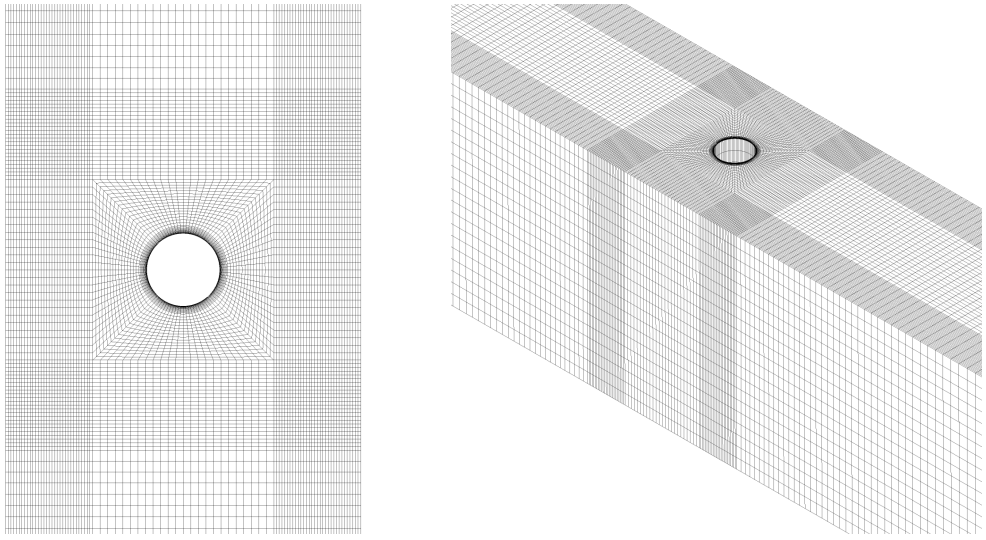

(a) (b)

Figure 6.2: (a) Plan view, of the section close to the cylinder, of the 3D mesh used; (b) Isometric view of the same mesh, showing the z divisions.

6.3 Stationary Model Simulations

6.3.1 Boundary Conditions

The 3D stationary model simulations were carried out using boundary conditions very similar to those used for the 2D version. That is, an inlet and outlet were set up at opposite ends of the domain to create a predominantly unidirectional flow (see Figure 6.3). The inlet was set so that incoming fluid contained a velocity of $U_{in} = 0.2$ m s^{-1}. The side-walls of the geometry were also set to possess the no-slip condition, as was the case for the 2D simulations. Since the 2D geometry was only one cell thick, the top and bottom faces had to be modelled as symmetry planes, or else there was no flow to consider. Now that there are to be a number of z divisions, the top and bottom planes can be modelled in a way that closer reflects the conditions of the physical water-bath.

Since the water-bath is open-topped, the water may be considered to possess a

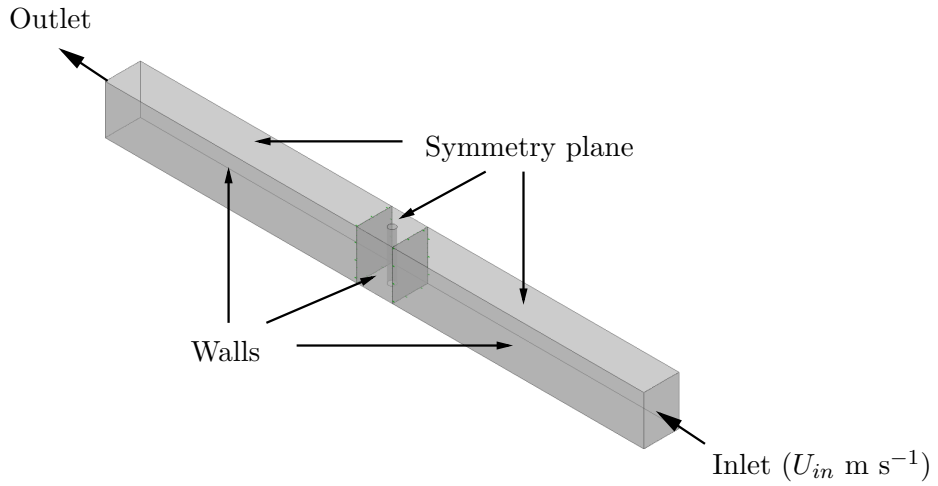

Figure 6.3: 3D geometry with boundary conditions labelled. The underside and farside faces, not labelled, are also wall conditions.

'free-surface'. That is, the water is free to move against the air above and not constrained by anything other than the arm supporting the cylinder. In contrast, the CFD model is clearly bounded above. The water-bath experiments were performed at translation frequencies that prevented sloshing in the tank and as such the height of the water surface varied by only a few millimetres. For this reason, the added complexity of modelling a free-surface, together with increased computational demand, was deemed not worthwhile and so the symmetry condition used in the 2D simulations remains. However, on the opposing 'bottom' surface, a wall boundary condition is now introduced, replacing the symmetry condition used in the 2D simulations and making the 3D model a closer representation of the physical water-bath than the 2D model.

6.3.2 Determining Number of Spanwise Mesh Divisions

To ensure that the number of divisions in the z direction was suitable, four different meshes were tested, with the same appearance as the 25,728-cell 2D mesh in the xy-plane, of 20, 30 60 and 100 z divisions. These meshes were tested using both the SST and LES turbulence models (see Table 6.1). These two models were chosen as they represent the most basic and advanced, in terms of resolving and modelling the length scales of the flow, of the four turbulence models considered here.

Simulations were set up using the boundary conditions set out in the previous section, for a total flow time of 10 seconds. The SST model simulations were set to run using

Turb. Model	z-divisions	Cells ($\times 10^6$)	Re	$\bar{C}_D$	C'_L	St	C_{pb}	Cpu Run Time (hrs)
SST	20	0.5	4,000	1.605	0.708	0.241	2.463	44
SST	30	0.8	4,000	1.594	0.772	0.239	2.180	78
SST	60	1.5	4,000	1.602	0.788	0.237	1.961	156
SST	100	2.6	4,000	1.484	0.408	0.230	1.789	296
LES	20	0.5	4,000	1.420	0.441	0.249	1.790	136
LES	30	0.7	4,000	1.314	0.106	0.247	1.779	192
LES	60	1.5	4,000	1.307	0.111	0.250	1.704	304
LES	100	2.6	4,000	1.271	0.078	0.255	1.543	544

Table 6.1: Flow properties using SST and LES turbulence models for meshes with different numbers of z divisions.

$\Delta t = 0.01$ s, while the LES model simulations used $\Delta t = 0.0025$ s. Table 6.1 shows the data obtained for the flow variables of interest for the different meshes and turbulence models.

One of the most striking features in the data is the change in the value of C'_L over the different meshes, particularly for the simulations employing the LES turbulence model. To determine if these changes, and other flow properties, are tending towards expected values as the mesh is refined, values from literature are needed. However, having searched for values in the literature to compare to, none were found at a comparable Re and β. This means, instead, it is necessary to compare these values to data obtained from studies performed at similar Re in an unconfined channel ($\beta < 0.05$). Therefore, comparing like-for-like values is not sensible, as the flows are not the same. Instead, these figures are used as guidelines, to make sure that the flow properties are sensible and of the right order of magnitude.

Norberg (2003) reported values of C'_L for cylinders at $Re \sim O(10^3)$ showing a sharp change in value around $Re \approx 4,000 - 5,000$, ranging from ≈ 0.05 to ≈ 0.15 (recall Figure 5.10a). This shows that C'_L is particularly sensitive to Re at the value tested here, which is in agreement with the values reported in Table 6.1.

The values of $\bar{C}_D$ reported by Wieselberger (1922) are slightly smaller than those found here (recall Figure 5.10b). However, Richter and Naudascher (1976) found increased values of St, $\bar{C}_D$ and C'_L for flows around cylinders in a channel, when compared to their counterpart values in an unbounded domain. This is also in agreement with the

values of St and C'_L found in Table 6.1. So although there is no ideal case to compare to, the values for the four flow properties reported in Table 6.1 are in agreement with the trends reported in the aforementioned literature. That is, values of C'_L are known to vary over an order of magnitude for small changes in Re between $Re \approx 4,000$ and $5,000$, and values of C'_L, $\bar{C}_D$ and St are known to be greater for cylinders in a channel.

When there is a velocity imposed on the fluid within the domain, as is the case for the simulations with a stationary cylinder, the transport of mass or any other scalar is predicted by the flow velocity. For the moving cylinder cases, where there is no background flow, the transport of a scalar is predicted by the vortices that are shed from the cylinder. Therefore, arguably the most important aspect of the moving cylinder simulations, to follow, is capturing the vortex-shedding with sufficient temporal and spatial resolution to predict the transport of a scalar ϕ. Since the rate of vortex-shedding is characterised by the non-dimensional shedding frequency St, this is considered to be the flow property of most importance. The coarsest of the meshes tested shows a value of St similar to that of the value obtained for the finest mesh, as indicated by only a 4.5% difference between St values using the SST model and a 2.4% difference for the LES model.

Comparing the total CPU run times for all simulations, the coarsest mesh shows an 84% saving on total CPU run time when using the SST model, and a 75% saving when using the LES model. Taking into account the small differences between values of St and large differences in CPU run time, the coarsest mesh of those presented, corresponding to 20 z divisions and 514,560 cells, is used for the moving-mesh simulations that follow. Despite the large difference in cell count between the coarsest and finest meshes, the differences between their prediction of the transport of a scalar is shown to be small (see Section 7.4.3).

6.3.3 Solver Settings

The timestep sizes used in the 2D stationary simulations were kept for the 3D stationary simulations. The simulation using the SST model used $\Delta t = 0.01$ s and the remaining simulations used $\Delta t = 0.0025$ s. The simulations were set to run until a flow time of 10 s was reached.

The solution was deemed to have converged, at each timestep, when the rms residuals

corresponding to the solutions of the velocity, mass and scalar transport equations reached a value less than 1×10^{-4}. One method of determining whether the solutions obtained using rms residuals of this size are close to the actual solutions of the relevant equations is to analyse the mass imbalance, to determine if the discretised version of the continuity equation (equation 4.3) is being solved adequately. The total mass of fluid is calculated at each timestep and the total imbalance is reported at the end of a simulation. Small imbalances correspond to obtained solutions in close agreement with actual solutions. For the solutions obtained using the specified boundary conditions, timestep sizes and convergence criteria, an overall mass imbalance of less than 0.01% was obtained for all turbulence models, confirming that the values of the rms residual and Δt are suitable.

6.3.4 Results

Simulations were carried out at $Re = 4,000$ for the SST, SAS, DES and LES turbulence models, as shown in Table 6.2.

Turb. Model	Advection	ω (s^{-1})	Re	Δt (s)	Flow Time (s)	Cpu Run Time (hrs)
SST	HRS	0.200	4,000	0.01	20	24
SAS	CDS/HRS	0.200	4,000	0.0025	20	36
DES	CDS/HRS	0.200	4,000	0.0025	20	32
LES	CDS/HRS	0.200	4,000	0.0025	20	40

Table 6.2: 3D stationary model properties for the four simulations presented in this section.

Due to the imposed flow, and the system not being closed, a scalar is not used to quantify turbulence model performance. Instead, values of the four flow properties previously used to investigate the flows involving the 2D stationary model are compared. Values of $\bar{C}_D$, C'_L, St and C_{pb} are presented in Table 6.3.

Turb. Model	Re	$\bar{C}_D$	C'_L	St	C_{pb}
SST	4,000	1.605	0.708	0.241	2.463
SAS	4,000	1.593	0.678	0.229	2.185
DES	4,000	1.584	0.629	0.227	1.939
LES	4,000	1.420	0.441	0.249	1.790

Table 6.3: Flow properties using SST and LES turbulence models for meshes with different numbers of z divisions.

The values of the four flow properties are in reasonable agreement with one another. As was pointed out in Section 6.3.2, values of C'_L are particularly sensitive to changes in Reynolds number at $Re \approx 4,000$, which could be one reason why these values are seen to vary. The lift coefficient, C'_L, is calculated from the lift force, which in turn is calculated by integrating the pressure field on the cylinder surface, it is also not surprising that values of C_{pb} and $\bar{C}_D$ are found to differ. Values of Strouhal number, St, are relatively consistent across the four turbulence models, indicating that the rate at which vortices are shed from the cylinder is similar for all four simulations.

Table 6.3 quantifies how the flow properties differ, but does little to aid the reader in visualising how each of the turbulence models represents the wake of a circular cylinder. Figures 6.4 and 6.5 show how the vortices in the wake are initially formed and later transported downstream. The figures use two approaches to visualise the core structure within the wake, after 0.75 and 10 seconds, respectively. The horizontal plane is coloured by vorticity, $\boldsymbol{\omega}_u$, while the grey cylindrical structures are surfaces of constant swirling strength, $\lambda_{ci} = 6$ s^{-1}. After 0.75 seconds, all four turbulence models show very similar predictions. Although the vortices are at slightly different stages in development, as indicated by differences in elongation in the x direction, the most notable difference in vortex structure is at the bottom, where the interaction with the bottom wall retards the vortex formation in different amounts. The SST and LES models show very little influence, whereas the DES and SAS models seem to show the no-slip condition having much more influence on the shape of the vortex.

Figure 6.5 shows how the predicted wake structure is strongly influenced by the choice of turbulence model, once the flow has reached the state of regular vortex shedding. Results from the SST model (see Figure 6.5a) still clearly show a well-defined wake structure. The vortices still bear close resemblance to when they were shed from the cylinder, even after 2 or 3 shedding cycles. By contrast, it is difficult to see any clearly defined structures in the wake predicted by the LES model (see Figure 6.5d). By resolving the larger length-scales within the flow, the LES model shows that turbulence is present in the majority of the fluid behind the cylinder. The SAS and DES models (see Figures 6.5b and 6.5c) show wake structure detail between that predicted by the SST and LES models, which is to be expected due to the blending functions they use between these two models. Despite the differences in wake structure, Figure 6.6 shows that the predicted velocity fields are

similar between the four turbulence models.

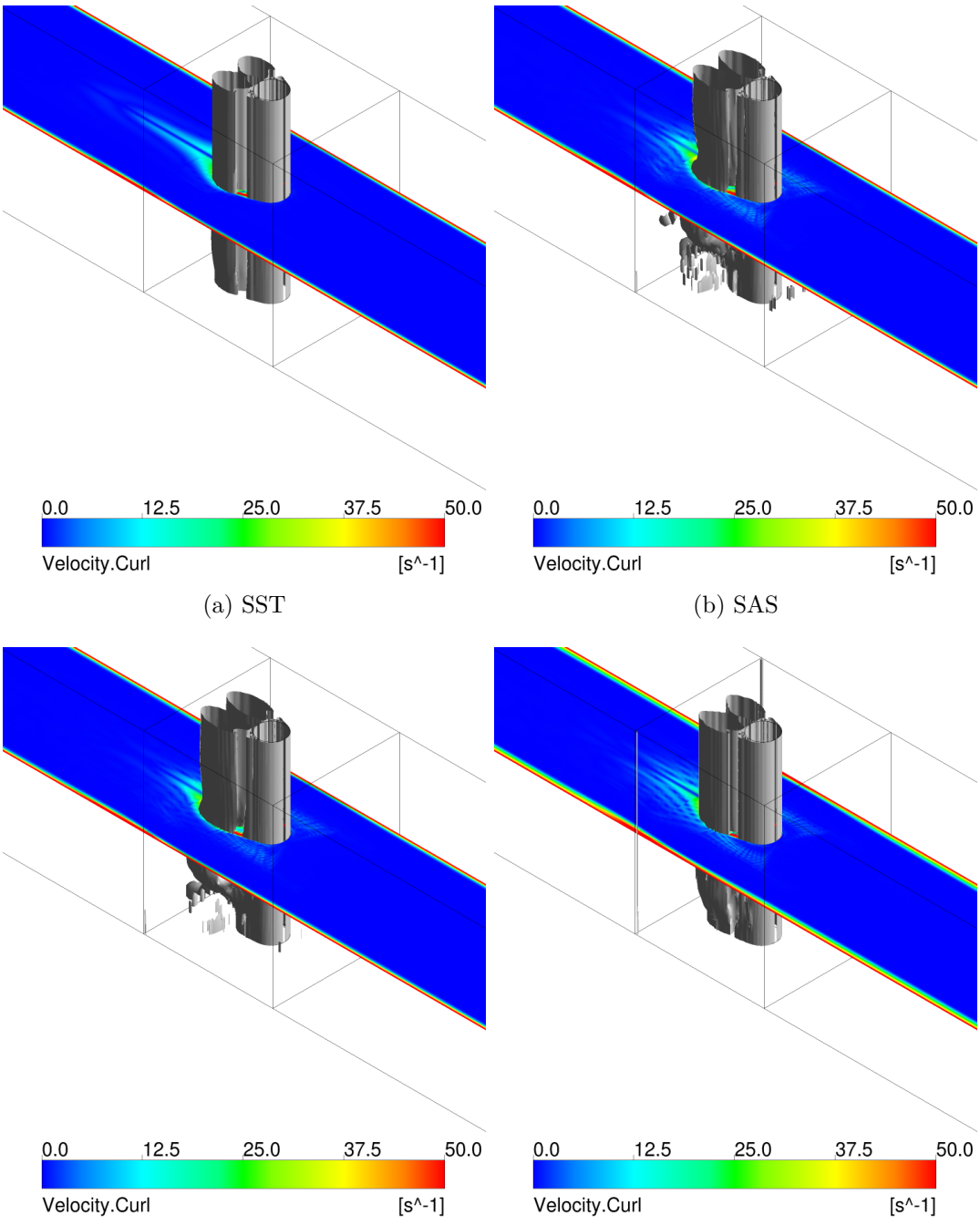

(a) SST (b) SAS

(c) DES (d) LES

Figure 6.4: Vortices illustrated for the four different turbulence models. Flow from right to left. Plane coloured by vorticity, $\boldsymbol{\omega}_u$, vortex cores (in grey) depicted for $\lambda_{ci} = 6$ s^{-1}. Images captured after 0.75 seconds of flow time when using: (a) SST; (b) SAS; (c) DES; (d) LES.

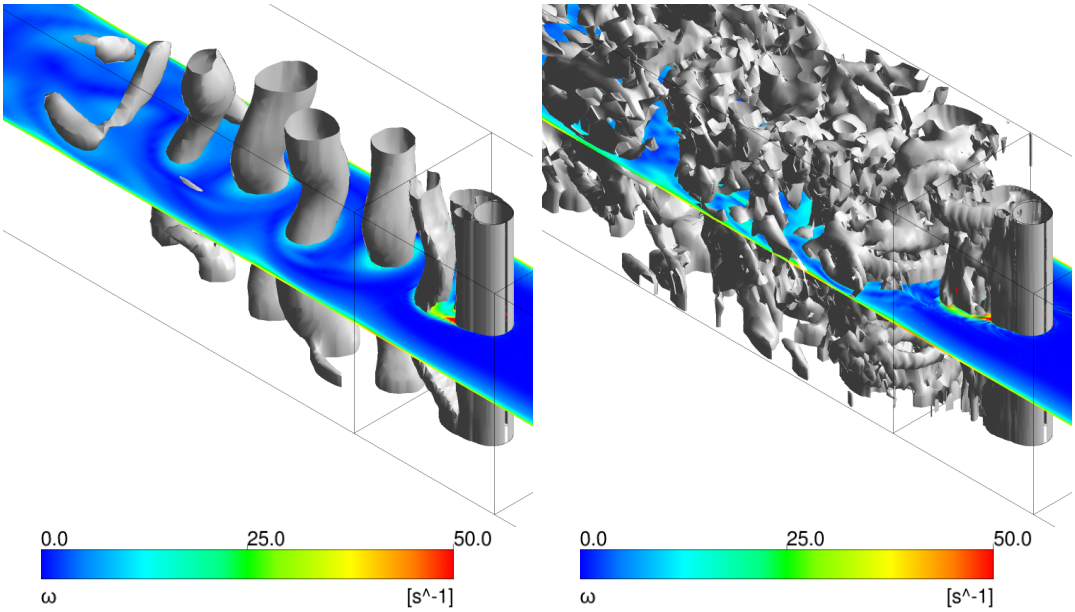

(a) SST

(b) SAS

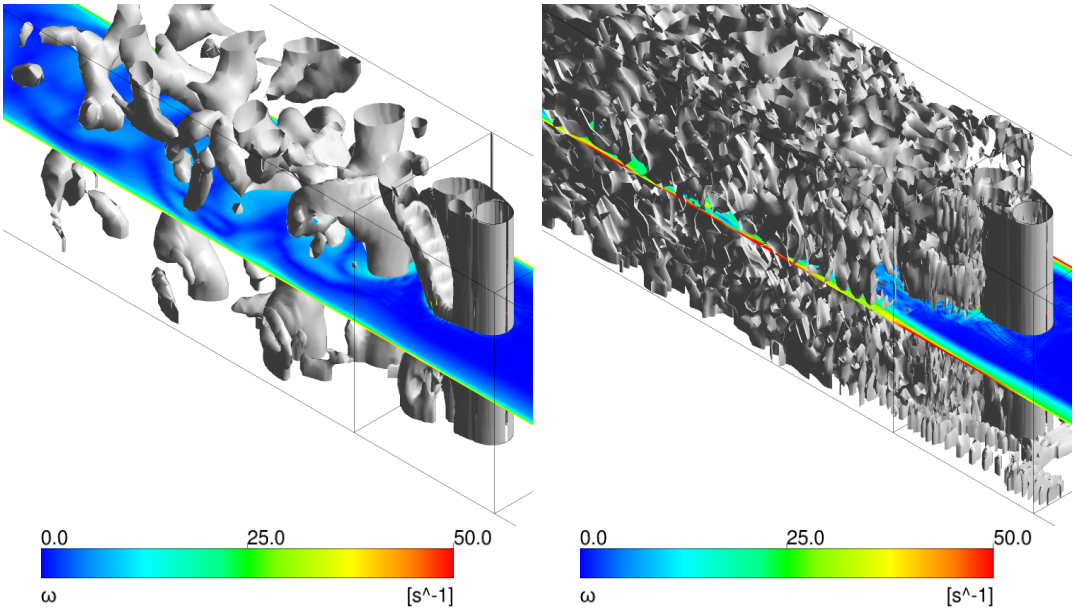

(c) DES

(d) LES

Figure 6.5: Vortices illustrated for the four different turbulence models after 10 seconds. Flow from right to left. Plane coloured by vorticity, $\boldsymbol{\omega}_u$, vortex cores (in grey) depicted for $\lambda_{ci} = 6$ s^{-1}when using: (a) SST; (b) SAS; (c) DES; (d) LES.

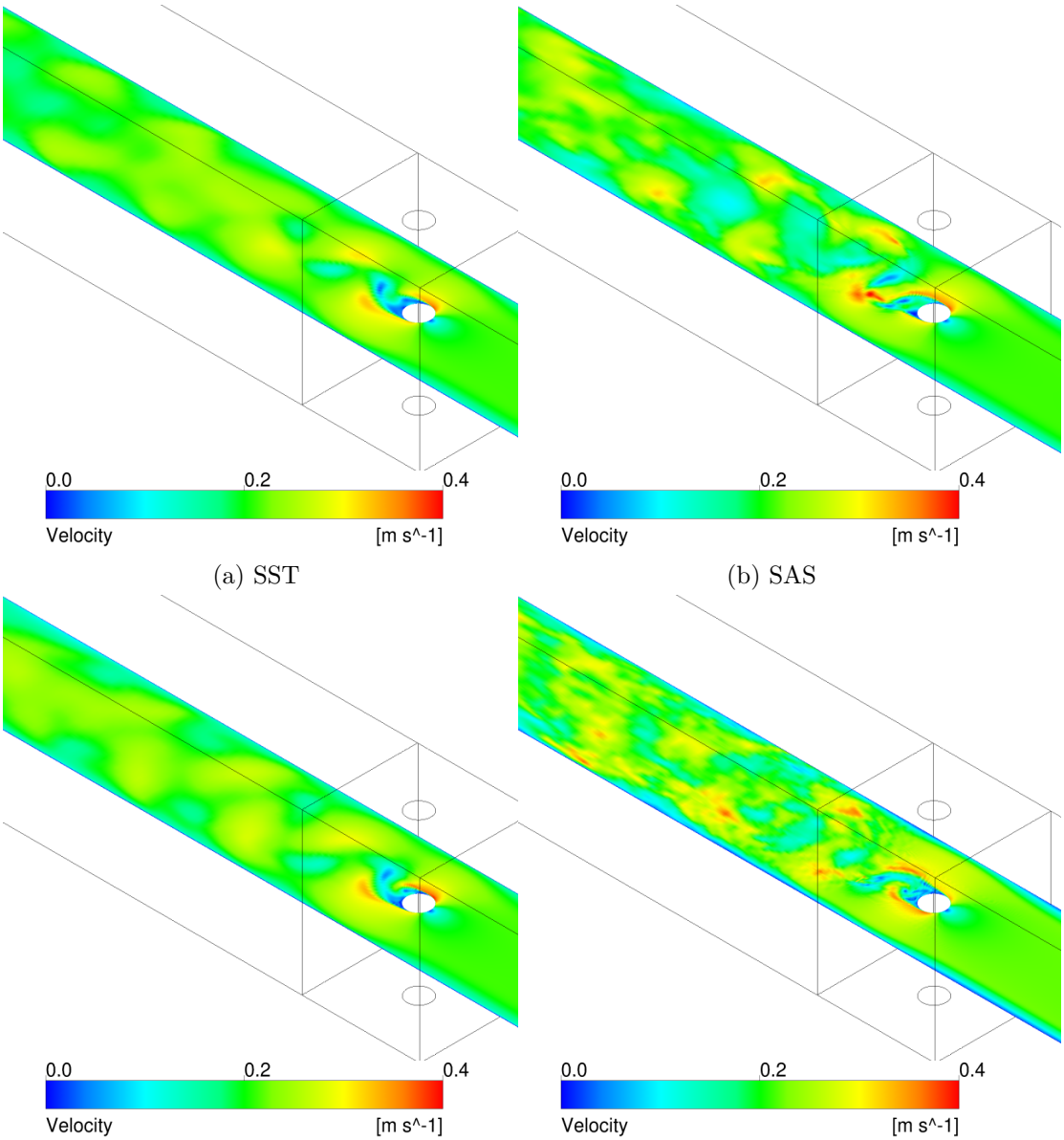

(a) SST (b) SAS

(c) DES (d) LES

Figure 6.6: Vortices illustrated for the four different turbulence models after 10 seconds. Flow from right to left. Plane coloured by local velocity magnitude: (a) SST; (b) SAS; (c) DES; (d) LES.

These four simulations highlight the differences, and similarities, between three-dimensional solutions when using different turbulence models. It is interesting to note that the finer detail relating to small turbulent structures is clearly not captured when using the SST model. However, the SST model is the model that has so far given results relating to scalar transport in closest agreement with the experimental data, during the 2D moving cylinder simulations.

6.4 Moving Model Simulations

The stationary model simulations showed that the 514,560 cell mesh, corresponding to 20 z divisions, is capable of capturing the three-dimensional elements of turbulence in the wake of a circular cylinder. Additionally, all the models gave values of St in reasonable agreement with one another and, more importantly, slightly above the expected value of St in the free-steam. This is in agreement with the findings of Richter and Naudascher (1976). Knowing that this mesh is capable of predicting reasonable rates of vortex shedding in 3D, simulations are now considered with a moving cylinder.

6.4.1 Boundary Conditions

The motion applied by Alg-1 for the 2D simulations is again used for the 3D simulations. No additions or alterations are made to the algorithm as it does not prescribe explicit instructions for x, y and z components, but on named sections of the geometry, the names of which are consistent between 2D and 3D geometries for this very reason. The inlet and outlet conditions used for the stationary simulations were replaced with wall boundary conditions. All other boundary conditions were the same as those applied for the simulations using a stationary geometry in the previous section and the same four turbulence models were tested.

The increase in resolution in the z direction not only increases the computational resource requirement to solve for the extra terms in the NS equations, but also increases the resources required to resolve the equations determining cylinder and mesh motion. For the 2D simulations, matching up the interface between the region of translation and the rest of the domain occurred on only one layer of cells, thus lining up the interfaces was trivial. The 3D mesh is made up of 20 layers and so 40 separate interfaces need to be matched up (two per layer - one on either side of the region of translation). Despite the

meshes of each layer having identical x and y coordinates, the first simulations carried out showed variations between the meshes of each layer. These variations propagated over time to eventually cause the elements at the interface to become so distorted that errors arose in the simulations. To stop this from occurring, the rms residual for the solution of the diffusion equation solved to determine the mesh displacement was reduced from the default 1×10^{-3}, to 1×10^{-5}. The maximum number of iterations allowed to reach this more stringent target was increased from 5 to 10. These alterations made sure that the interfaces between the cells were well resolved and the cylinder motion was implemented without destroying the quality of the mesh, though this resulted in increased computation time.

6.4.2 Changes to Solver Settings

The size of the timesteps, Δt, were kept the same as those used for the stationary geometry simulations, but the total flow time was increased to 60 seconds, the same flow time used for the 2D moving geometry simulations, corresponding to $\omega t = 12$. Convergence criteria and discretisation schemes remain the same as those mentioned in Section 6.3.

6.4.3 Results

Simulations using a moving domain were carried out for the four turbulence models as shown in Table 6.4.

Turb. Model	Advection	ω (s^{-1})	Re	Δt (s)	Flow Time (s)	Cpu Run Time (hrs)
SST	HRS	0.200	4,000	0.01	60	252
SAS	CDS/HRS	0.200	4,000	0.0025	60	840
DES	CDS/HRS	0.200	4,000	0.0025	60	800
LES	CDS/HRS	0.200	4,000	0.0025	60	772

Table 6.4: Properties for 3D moving geometry simulations presented in this section.

Once again, the SST model simulation required much less time to complete than the LES-based model simulations. The transport properties of a scalar ϕ were, used to evaluate the adequacy of each turbulence model, but an overview of the wake structures produced by the models is presented first.

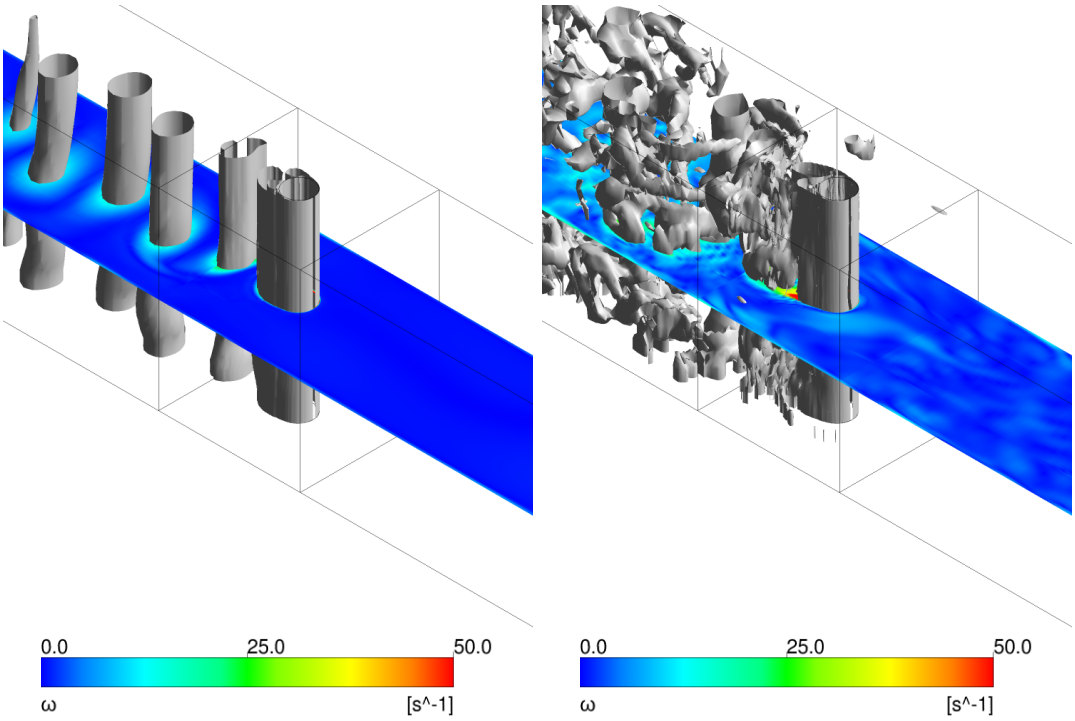

(a) SST (b) SAS

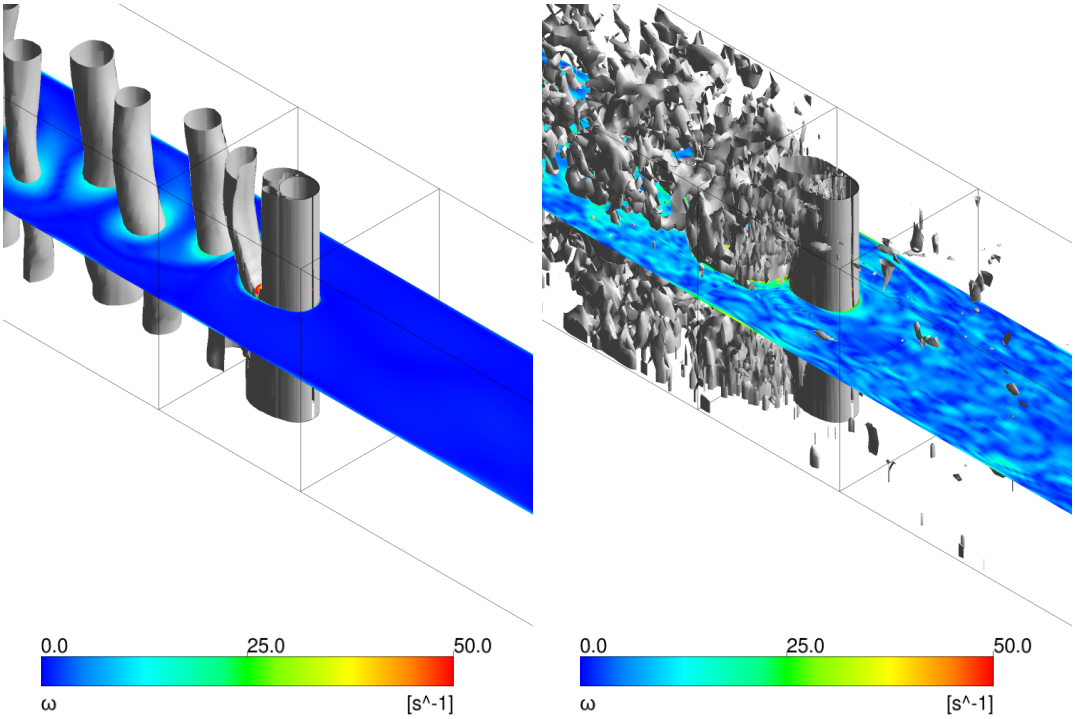

(c) DES (d) LES

Figure 6.7: Wake illustrated for the four different turbulence models after 60 seconds. The cylinder is in the process of moving left to right. Plane coloured by vorticity, $\boldsymbol{\omega}_u$, vortex cores (in grey) depicted for $\lambda_{ci} = 6$ s^{-1}when using: (a) SST; (b) SAS; (c) DES; (d) LES.

Figure 6.7 shows planes coloured by $\boldsymbol{\omega}_u$ and surfaces of $\lambda_{ic} = 6\ \mathrm{s}^{-1}$ obtained after 60 seconds of flow time for the four turbulence models. Comparing these four plots with those of Figure 6.5, which were obtained using the stationary model after 10 seconds, allows for some interesting observations.

After 60 seconds, the cylinder has translated back and forth at least once. The LES and SAS models show some evidence of this, as the vorticity is non-zero upstream of the cylinder. However, the SST and DES models do not show the same signs, indicating zero vorticity in the flow upstream of the cylinder. Zero vorticity is indicative of no 'turbulence' in the fluid, possibly suggesting that the SST and DES models are more dissipative when modelling the turbulence of the system, or that the SAS and LES models are not calculating the decay of the turbulence quickly enough.

The rate at which turbulence decay is calculated is clearly turbulence model specific and related to the calculated eddy-viscosity. By changing turbulence model parameters, the rate of decay could have been matched between the various models so that each turbulence model was producing the same (or a similar) rate of decay at a particular time, making it possible to compare each turbulence model's performance when starting from a similar turbulent flow. However, performing a turbulence model parameter sensitivity investigation like this is beyond the scope of this study.

Looking at the structure of each vortex, the models can again be separated into two groups. The SST and DES models show the vortices as coherent, cylindrical structures with no evidence of varying length-scales often associated with turbulent flows. In contrast, the SAS and LES models show some evidence of the same structures, but more evidence of the kinds of (seemingly) random, smaller-scale, structures and length-scales associated with turbulent flows. It is interesting to note that the DES model shows characteristics very similar to those of just the SST model, and no sign of the smaller scale structures resolved by the LES model. This was not the case for the stationary geometry simulations.

Compared to the 2D simulations, the addition of data in the z direction makes the interpolation stage more difficult. The wake of a finite cylinder is three-dimensional, meaning that the solutions in a plane of constant z are not necessarily the same for any two z values. This is evident from the wakes shown in Figures 6.4 and 6.5. The vortices clearly take on different properties for different z values. Rather than analyse each xy

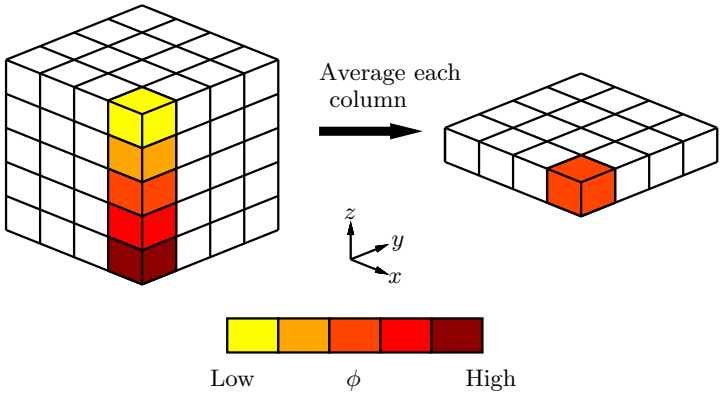

Figure 6.8: Sketch of how 2D data is obtained from 3D data for a sample block of cells.

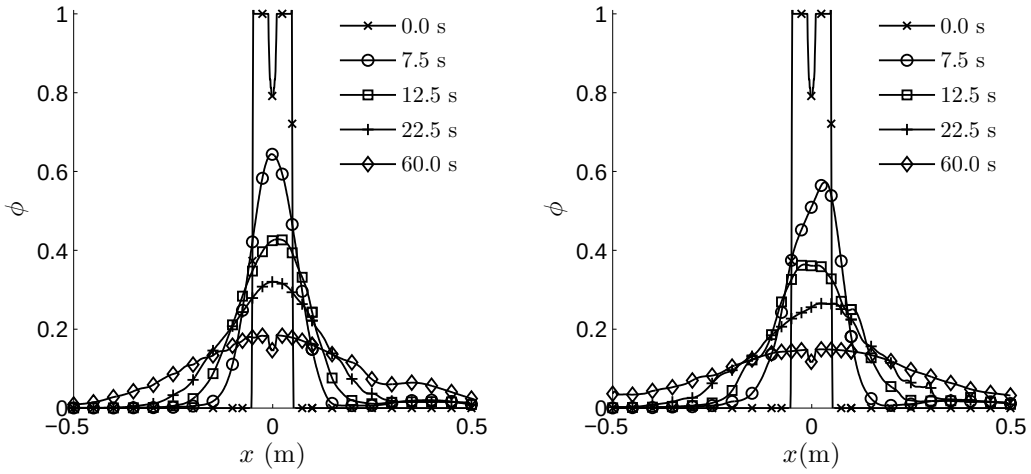

(a) SST

(b) SAS

(c) DES

(d) LES

Figure 6.9: Profiles of ϕ, averaged through y and z, at $t = [0, 7.5, 12.5, 22.5, 60]$ s when using the (a) SST model; (b) SAS model; (c) DES model; (d) LES model.

plane for all 20 values of z of each set of solution data, the solution is averaged through the z direction instead, resulting in solution data occupying a single plane. Following this, the analysis follows the same procedure as was carried out for the 2D data (see Figure 6.8).

The y and z-averaged ϕ profiles are presented in Figure 6.9. The profiles show a similar behaviour to those found for the 2D simulations, in that they all appear to obey a Gaussian distribution, however the profiles are much more similar now. The peaks and shape of each profile are very similar across all four turbulence models. Most notably, the readings at $\omega t = 12$ are now consistent and the sporadic profiles of the LES model are gone. If not well-studied, one could easily mistake any of the plots as being a repeat of another.

Performing a rescaling of the axes of these profile plots by $\sqrt{\omega t}$ again shows how similar the performance of the turbulence is for the 3D models (see Figure 6.10). The peaks of the LES-based models are now higher than those of the 2D moving cylinder simulations, resulting in profiles that are closer in shape to those of the experimental data. The SST model shows very little deviation from the 2D profile.

Figure 6.10e shows how the turbulence model profiles compare to the experimental data. As was seen in for the 2D simulations, the SST model appears to match the experimental data better than the LES-based turbulence models, however the latter are now closer, although the improvement for these latter models was to be expected. As mentioned in the introduction to this chapter (Section 6.1), the resolved length scales of the turbulence are able to be better captured in 3D and are not suppressed by the lack of resolution in the z direction, as was the case for 2D simulations.

Centre of mass, $\bar{X}_\phi$, plots are shown in Figure 6.11. Each of the four models is able to reproduce the $\sqrt{t}$ dependency observed in the experiments, as indicated by the, approximately, linear trend above $\omega t \approx 1.5$ in Figure 6.11b. All the CFD models slightly over-predict $\bar{X}_\phi$ when compared to the experimental data, though to differing degrees.

Although the SST model shows closest agreement to the experimental data, all four models show similar predictions. The DES model shows very similar $\bar{X}_\phi$ data to the SST model. Having seen that the two wakes were very similar in structure (see Figure 6.7) this is not surprising. The LES and SAS models over-predict values of $\bar{X}_\phi$ the most, but still show the correct trend.

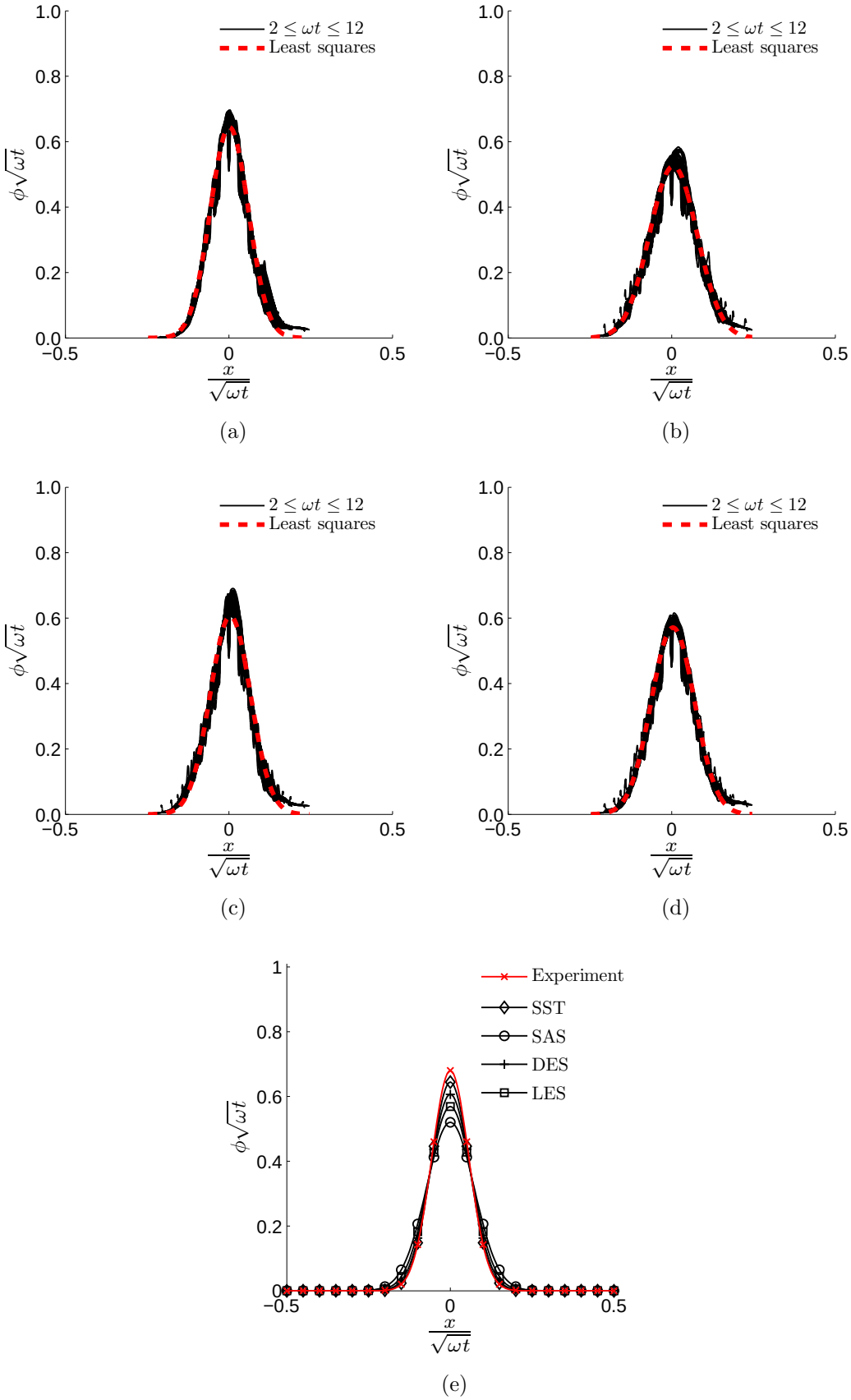

Figure 6.10: Profiles of ϕ, averaged through y and z, for $2 \leq \omega t \leq 12$ (or, $10 \leq t \leq 60$ s) after rescaling by $\sqrt{\omega t}$ using the (a) SST model; (b) SAS model; (c) DES model; (d) LES model. (e) Least squares fitted ϕ profiles for different turbulence models, compared with corresponding least squares fitted C profile for $d = 20$ mm and $\omega = 0.200$ s^{-1}.

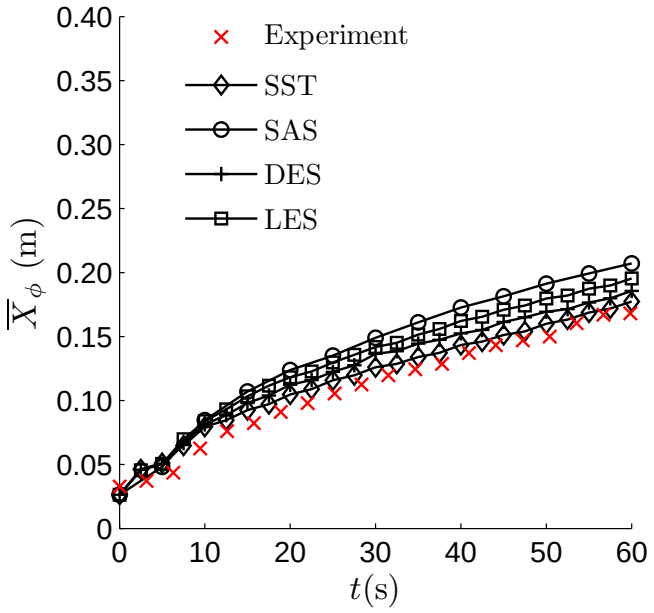

(a)

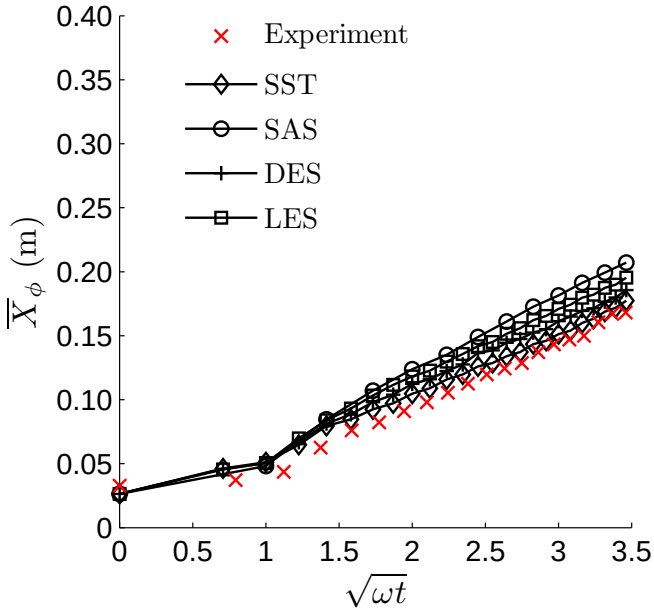

(b)

Figure 6.11: $\bar{X}_\phi$ plotted as a function of (a) time; and (b) $\sqrt{\omega t}$, for the four turbulence models considered, compared against experimental values of $\bar{X}$ for $d = 20$ mm and $\omega = 0.200$ s^{-1}.

Values of $\bar{X}_\phi$ give an indication of the bulk transport experienced by ϕ, but not of ϕ values at specific times and locations. Due to the line of sight averaging assumption made during the calculation of the dye concentrations in the experiments, extracting concentration data at a single point in the water-bath is not possible. However, the average concentration along a plane spanning the water-bath is calculable. This data is also easily obtainable from the CFD solution data.

Three planes were created to monitor the average ϕ value over time. The planes were created spanning the geometry in the $y-z$ plane at the cylinder's starting location and two additional locations located 0.15 and 0.30 m away (see Figure 6.12). The corresponding experimental data was calculated by averaging the pixels at the locations corresponding to $x = 0, 0.15$ and 0.3 m in the y-direction. Since the dye concentrations are already assumed averaged through the water-bath, this corresponds to an an average concentration in a plane.

Figure 6.12b shows how the average ϕ values in the three planes compare with the equivalent normalised C values, where the initial concentration C_0 is used as the normalising variable to make sure ϕ and C are comparable on a [0,1] scale. It can now be seen that the turbulence models do not predict the same rate of spread of ϕ, something that could not be determined by just looking at $\bar{X}_\phi$ data (see Figure 6.11).

Looking at the central plane, Plane 1, the SST model again performs the best in terms of predicting the transport of ϕ, with the worst model predictions provided by the SAS model. However, for the plane furthest from the centre, Plane 3, the SAS model provides the best comparison with the experimental data. This goes to show that there is no clear cut best model when looking at these plots relating to specific contaminant values at specific times, however, all the turbulence models show reasonable agreement between themselves and the experimental data.

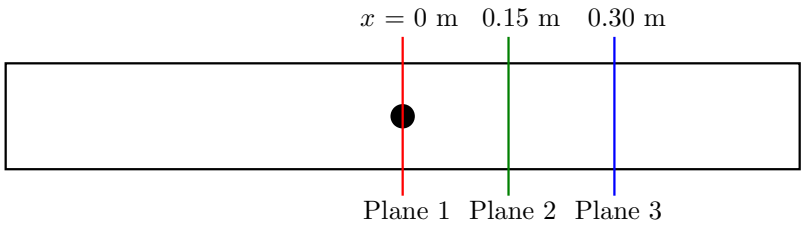

(a)

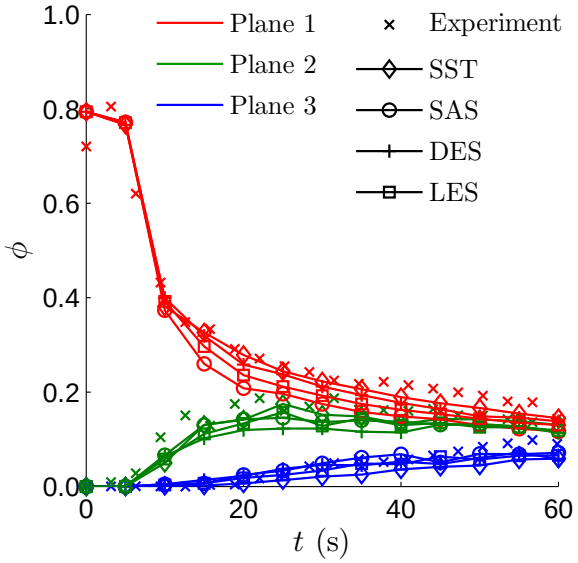

(b)

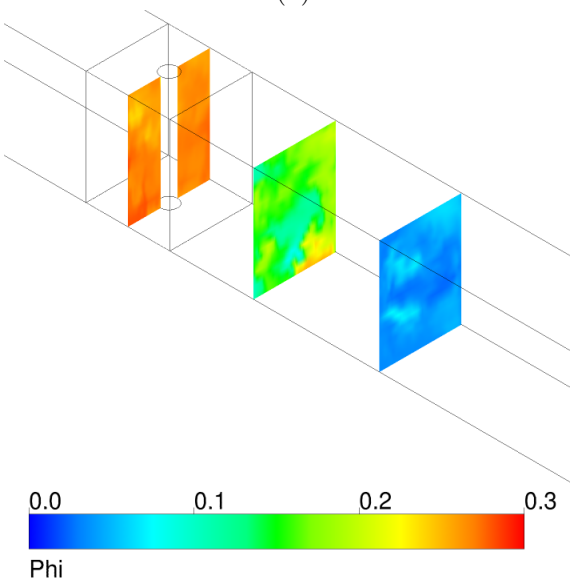

(c)

Figure 6.12: (a) Locations of Planes 1, 2 and 3, at $x = 0$ m, 0.15 m and 0.30 m, respectively; (b) Comparison between average ϕ values and average, normalised dye concentrations on Planes 1, 2 and 3. Line colours and markers determined by the combination of Plane colour and source of data; (c) Planes 1, 2 and 3 (left to right) coloured by ϕ value when using the LES turbulence model. Image taken after 25 s.

6.4.4 Influence of Cylinder Diameter and Translation Frequency

So far, only one d and ω combination has been examined with the CFD model ($d = 0.02$ m, $\omega = 0.200\ \mathrm{s}^{-1}$). More combinations are now tested, however only one turbulence model is used for these additional cases. The SST model is chosen for these further simulations as it has been the most consistently well performing in the prediction of scalar transport and offers a large ($\approx 70\%$) reduction in computing time required per simulation, when compared to the other three turbulence models.

Of the 33 combinations of d and ω tested during the water-bath experiments, eight were chosen for CFD simulation here, the details of which are presented in Table 6.5. The eight combinations chosen span the smallest and largest cylinder sizes and translation frequencies, and a large range of Re values. Since an additional four cylinder diameters were tested (d = 10, 33.5, 40 and 50 mm), four different geometries and meshes had to be constructed. These were created in a very similar manner to the previous geometries and meshes presented in this chapter and so bear a close resemblance, as can be seen in Figure 6.13.

Turb. Model	d (m)	ω (s^{-1})	Re	Δt (s)	Flow Time (s)	Cpu Run Time (hrs)
SST	0.0100	0.201	2,010	0.01	30	222
SST	0.0100	0.287	2,970	0.01	30	294
SST	0.0200	0.054	1,086	0.01	30	192
SST	0.0335	0.132	4,405	0.01	30	198
SST	0.0335	0.205	6,878	0.01	30	210
SST	0.0400	0.071	2,840	0.01	30	181
SST	0.0400	0.192	7,680	0.01	30	120
SST	0.0500	0.201	10,035	0.01	30	150

Table 6.5: Properties for 3D moving geometry simulations for the various d and ω combinations presented in this section.

In the previous section, all simulations were carried out over 60 s of flow time. For the SST model this meant a cpu run time of 252 hours and a simulation run time of 63 hours. Although this may seem a short duration compare to some numerical simulations[1], to reduce the computational demand for the eight simulations presented in this section, the flow time was halved to 30 s. This time is still sufficient to compare the CFD model to the experimental data. All other settings remain the same as those presented in Section

[1]Parkinson et al. (2014), for example, required a cpu run time of $\approx 100,000$ hours for their direct numerical simulations.

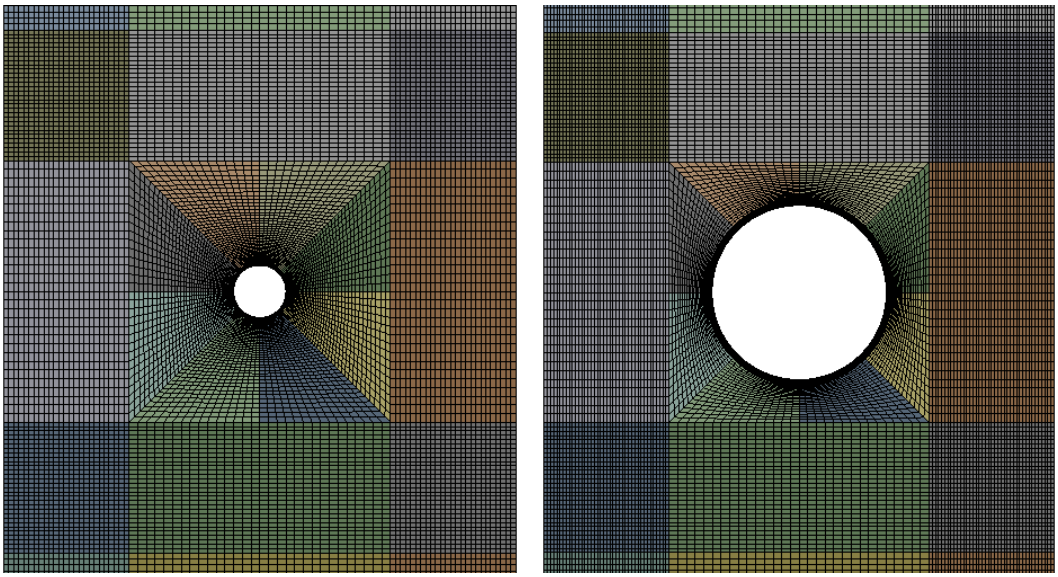

(a) 10 mm

(b) 33.5 mm

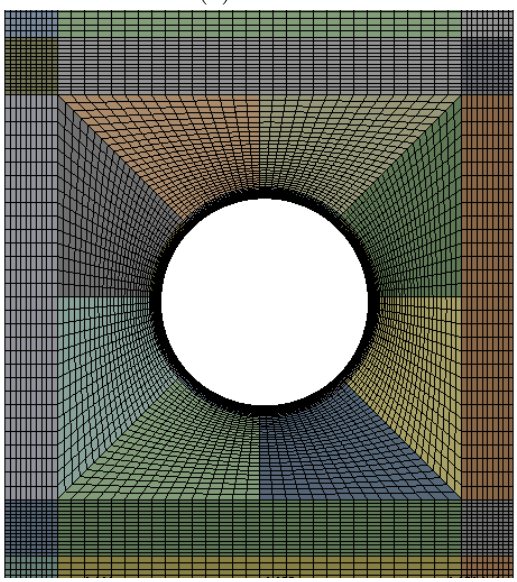

(c) 40 mm

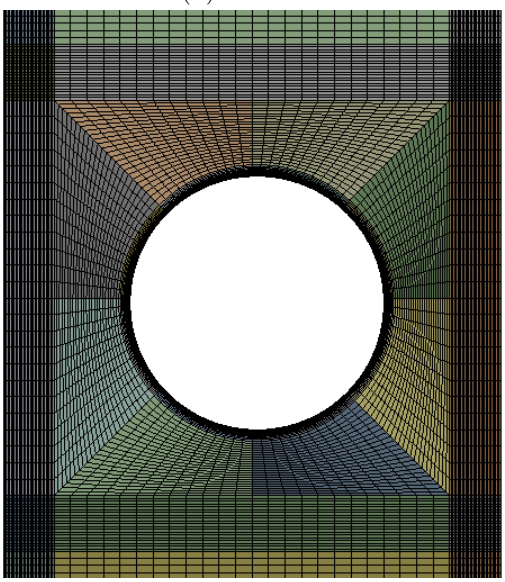

(d) 50 mm

Figure 6.13: Plan view, and close up, of the additional four meshes used in this section: (a) $d = 10$ mm; (b) $d = 33.5$ mm; (c) $d = 40$ mm; (d) $d = 50$ mm.

6.4.1. Values of $\bar{X}_\phi$ and ϕ on the three planes are again used to assess the capability of the CFD model. Figures 6.14 - 6.16 show plots of the centre of mass, $\bar{X}$, and the average ϕ value obtained in Planes 1-3 for all eight d and ω combinations in Table 6.5.

It is apparent that although $\bar{X}$ is a useful metric for measuring the overall competence of the CFD model, by reducing a three-dimensional data set to just one value, it is not able to demonstrate some of the differences between the experimental and CFD models that are seen in the plots that show average ϕ values in a plane.

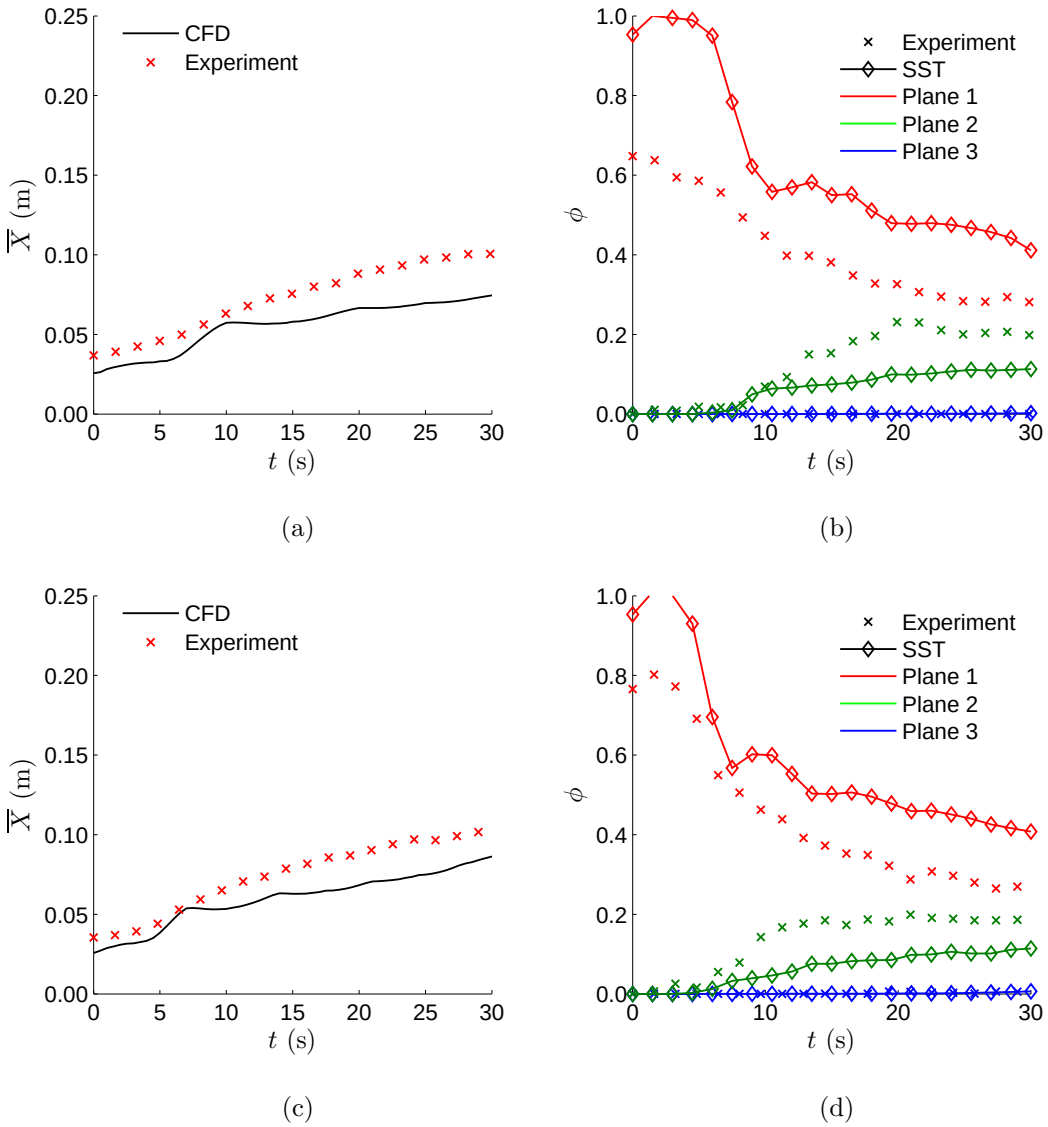

Figure 6.14: Comparison between experiments and CFD for $\bar{X}$ and average ϕ values on Planes 1, 2 and 3, for: (a)-(b) $d = 10$ mm and $\omega = 0.201$ s^{-1}; (c)-(d) $d = 10$ mm and $\omega = 0.287$ s^{-1}.

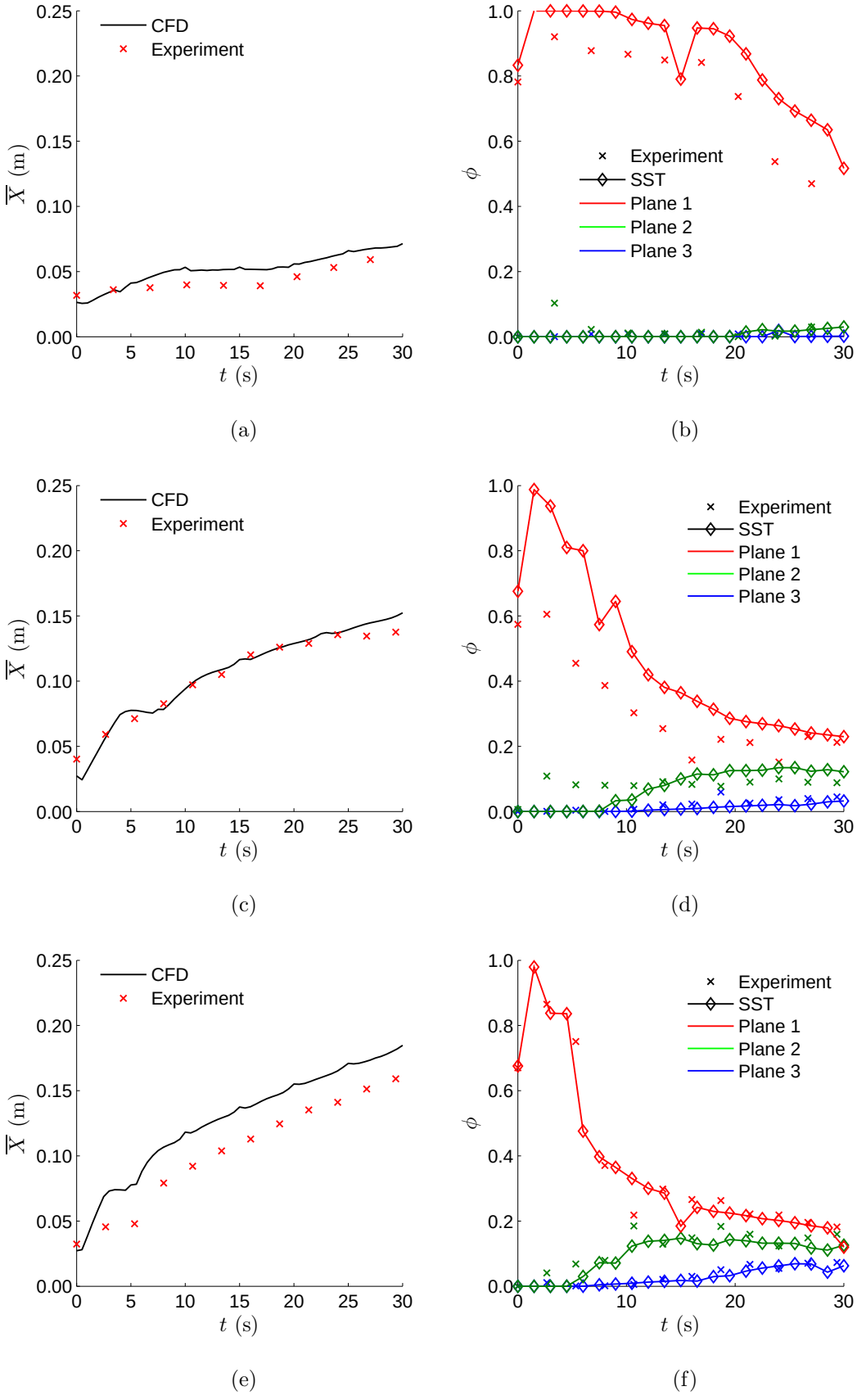

Figure 6.15: Comparison between experiments and CFD for $\bar{X}$ and average ϕ values on Planes 1, 2 and 3, for: (a)-(b) $d = 20$ mm and $\omega = 0.054$ s^{-1}; (c)-(d) $d = 33.5$ mm and $\omega = 0.132$ s^{-1}; (e)-(f) $d = 33.5$ mm and $\omega = 0.205$ s^{-1}.

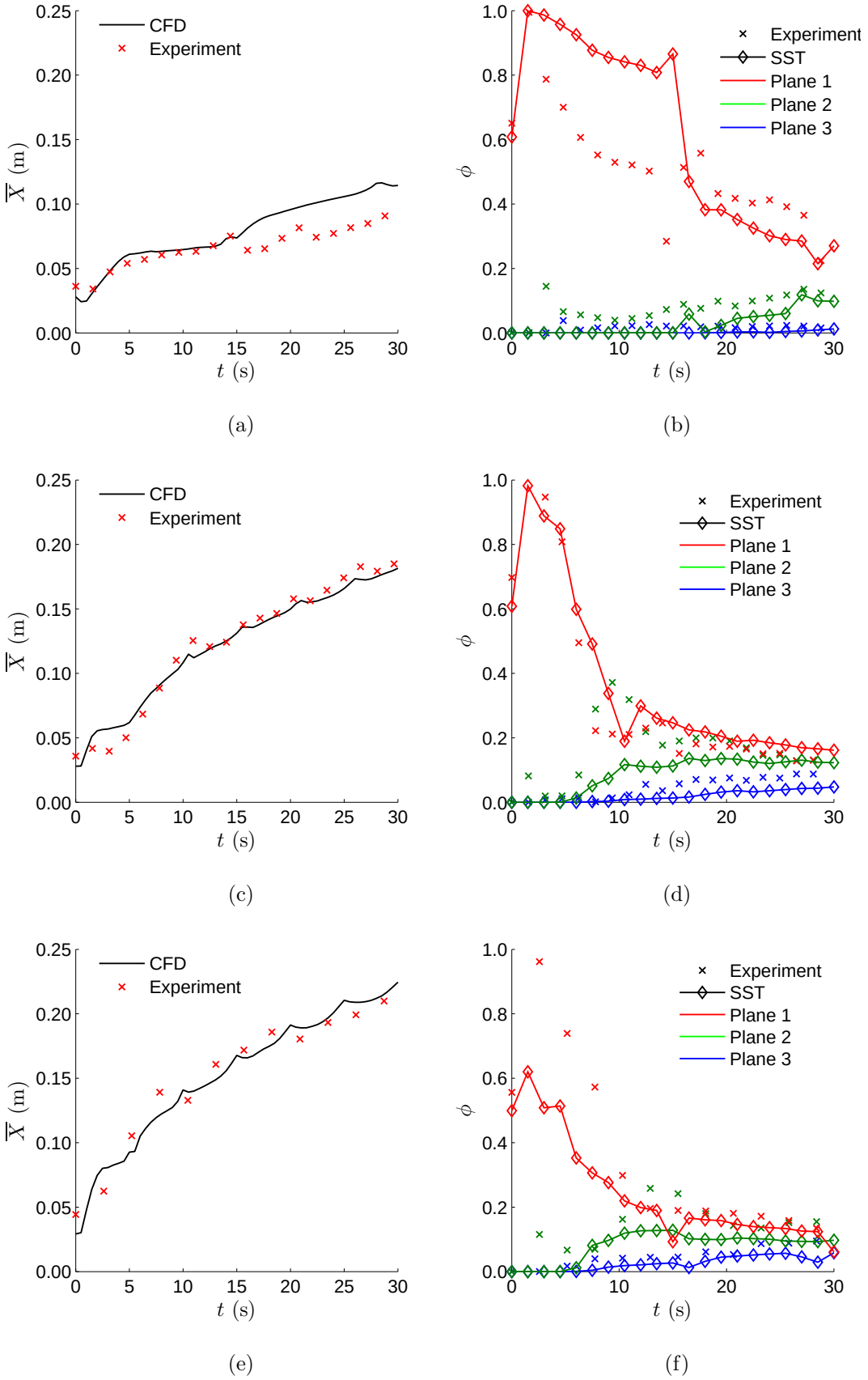

Figure 6.16: Comparison between experiments and CFD for $\bar{X}$ and average ϕ values on Planes 1, 2 and 3, for: (a)-(b) $d = 40$ mm and $\omega = 0.071$ s^{-1}; (c)-(d) $d = 40$ mm and $\omega = 0.192$ s^{-1}; (e)-(f) $d = 50$ mm and $\omega = 0.201$ s^{-1}.

The SST model appears to show good qualitative agreement with the experimental data for all cases tested and good quantitative agreement for many of them (see, for example, Figures 6.15c, 6.16c and 6.16e). The values of $\bar{X}$, on the whole, show excellent agreement with the experimental data. The largest cylinder diameters (d = 33.5, 40 and 50 mm) show the strongest agreement between the two sets of data. The slightly less favourable agreement for the smaller sized cylinders (d = 10 and 20 mm) could possibly be showing a weakness in the CFD model's predictions for lower Re values, although this is only postulation and needs further investigation.

Looking at the average ϕ values in the three planes, more can be learned about where the CFD model agrees with the experimental data. Values of ϕ in Plane 1 start close to the initial concentration at release then decline steadily over time, for all cases. For Planes 2 and 3, ϕ necessarily starts at zero, due to the imposed initial conditions, then experiences a shift to a non-zero value at some time and increases from there onwards. These same trends are seen in the experimental data, with the two data sets showing good agreement a lot of the time.

Agreement between CFD and experiment is not as strong during the first 5-10 seconds, where the CFD model over-predicts the average ϕ value for most cases. This is probably down to the localised flow effects that were experienced during the lock-gate removal when performing the experiments, as has been discussed previously. As this procedure is not repeated in the CFD experiments, the initial 'cube' of ϕ remains relatively undisturbed until the cylinder has made one traverse of the channel.

Overall, the CFD predictions are in line with experimental results and equation 3.13 in that the transport of a scalar ϕ is highly dependent upon the cylinder diameter, d, and cylinder velocity, U. This is apparent in both the $\bar{X}$ and ϕ plots where the scalar is seen to stay closer to its initial location for the slower moving cylinders and narrower cylinders. Figures 6.15a and 6.15b show how one of the smaller diameter cylinders (d = 20 mm) travelling at a low velocity (U = 0.054 m s^{-1}) results in ϕ not reaching Planes 2 and 3 until $\approx$ 20 s after the start of the simulation (this trend is also apparent in the experimental data). Conversely, Figures 6.16e and 6.16f show how a faster moving (U = 0.201 m s^{-1}) and larger diameter cylinder (d = 50 mm) result in Planes 2 and 3 seeing non-zero ϕ values after $\approx$ 6 s, resulting in a much quicker transportation and dispersion of the scalar.

6.4.5 Discussion

The 3D simulations carried out for $d = 20$ mm and $\omega = 0.200$ s^{-1} show a similar pattern to those of the 2D simulations. The SST model shows the best all round performance at predicting the transport of a scalar, ϕ, when compared to the LES-based models. However, the difference between the solutions obtained from the four turbulence models is now much smaller. The increased performance of the other three models was expected as the increase in z, and number of z divisions, allows the turbulent length scales to be better resolved.

The CFD model is able to capture the transport of ϕ with reasonable precision for the majority of d and ω combinations tested here, when employing the SST turbulence model. However, quantifying a residual or difference between the two solutions is not possible with the raw data as the data points for $\bar{X}$ are provided at different time intervals. The CFD simulations were set to output the data every 0.5 s, whereas the Δt value calculated for each experiment varied, with none a multiple of 0.5 s. Any comparison would therefore involve interpolating at least one of the solutions, which introduces further error in itself. Moreover, even if it were possible to extract both data sets at the same Δt values, the experimental data is subject to error itself, meaning any difference between the two solutions does not make for an easy error calculation. Therefore, comparisons between the two models are made by eye from the plots in Figures 6.14-6.16, which show that, for the most part the trends between the two approaches do agree, i.e., both show $\approx \sqrt{t}$ dependence for $\bar{X}$, and the ϕ values on Planes 1-3 show similar trends.

Although it is not possible to conclude that the SST model is the most suitable turbulence model for any d and ω combination, the others having only being tested on one, it can be stated that it does provide solutions in qualitatively good agreement with the experimental data across a range of conditions. Further, the SST model results are seen to agree quantitatively with the experiments for a number of cases, showing that CFD models are capable of capturing the flow features relevant to the transport of a scalar due to a translating cylinder.

All the simulations in this chapter considered the geometry at the model-scale, allowing comparison with the experimental data. The implications of these findings to full-scale simulations, and the impact this could have on a contaminant release in a hospital corridor, are presented in Chapter 7.

6.5 Summary

The CFD model presented in the previous chapter was modified to accommodate a 3D geometry that better represents the water-bath used in the experiments. The height of the CFD geometry was made to coincide with the water-level, $H_{water} = 136$ mm. The number of z divisions required for sufficient resolution of the turbulent length scales was determined by a mesh-dependency study, undertaken on both the SST and LES models, although the decision on which mesh to use was made taking computational expense into consideration. Although the agreement was not perfect, the values of St, $\bar{C}_D$ and C_{pb} obtained were deemed acceptable.

Simulations were set up using the 3D geometry, under almost identical conditions to the 2D simulations, with the major exception being that the 'bottom' of the geometry was changed from a symmetry condition to a no-slip wall. The transport of the same scalar, ϕ, was calculated using the same method as before, with the only slight change being that values for ϕ were averaged through z first. Profiles of ϕ and values of $\bar{X}_\phi$ were compared to the experimental data, with the SST model again showing the best performance.

The SST model was then tested on a further eight d and ω combinations, by comparing values of $\bar{X}_\phi$ with experimental data. The results showed that the CFD model is able to offer good prediction of scalar transport compared to the experimental data over a range of d, ω and Re combinations, when using the SST turbulence model. Agreement between the average ϕ values obtained on three planes and similar data from the experiments was not as strong as that of the $\bar{X}$ data, but the profiles were still qualitatively similar.

Chapter 7

Modelling Infection Risk

Contents

The findings from the experimental and CFD studies are now used to investigate contaminant transport in a full-scale corridor. The scaling principles applied to the water-bath model, to ensure that the approach is suitable for use in this study, are investigated using two CFD models. Two additional scenarios are also considered that are closer to a real corridor situation than the water-bath set up. A simplified breathing model is coupled with the theoretical contaminant transport model to look at the infection risk of people walking along a corridor with an airborne contaminant present. The chapter concludes by investigating the various limitations of all the models used in this study.

7.1 Full-Scale Contaminant Transport Predictions

All modelling in this study has, so far, been conducted on scales relevant to the water-bath described in Chapter 3, a 1:15 scale representation of a corridor. Before any information at the full-scale can be extracted from the 1:15 scale modelling approaches, first it is necessary to make sure that predictions made at the full-scale are meaningful. Only then can predictions be made about the infection risk associated with airborne pathogen transmission with any real confidence.

7.1.1 Length and Time Scales Revisited

Although both the water-bath modelling and CFD approaches are based on reliable theory and principles, and results have already shown good agreement between the two at 1:15 scale, checks are now made to ensure that the flows of equal Re yield similar solutions once length and time scale factors are taken into account. As no full-scale experimental data was obtained during the study, results are instead compared between two CFD simulations. Using a scaling feature in the geometry creation software ANSYS Modeler, a full scale geometry is created by applying a scaling factor of 15 to the original water-bath sized model, so that the two geometry structures are identical.

	Model 1	Ratio	Model 2
Cylinder diameter - d (m)	0.0335	1:15	0.5
Translation amplitude - A (m)	1	1:15	15
Translation frequency - ω (s^{-1})	0.294	1:0.077	0.0226
Linear speed - U (m s^{-1})	0.294	1:1.15	0.339
Fluid	Water	-	Air
Reynolds number - Re_{CFX}	11,046	1:1	11,046
Time scale - d/U (s)	0.114	1:13	1.480

Table 7.1: CFD properties relating to simulations carried out at (water-bath) model-scale and full-scale.

Two CFD simulations were conducted, one on each of the aforementioned geometries, the properties of which are outlined in Table 7.1. The two models are henceforth referred to as Model 1 and Model 2, where the former relates to the 1:15 scale water-bath model and the latter to the full-scale. The values of $d = 0.0335$ and $\omega = 0.294$ s^{-1}, used in Model 1, were chosen as they yield the largest Re value tested during the water-bath experiments using a cylinder with aspect ratio similar to a person ($\approx 3.3 : 1$). The corresponding values

for Model 2 were obtained by applying length and time-scale ratios. The transport of the scalar ϕ was investigated in a similar manner to that already seen for the moving cylinder CFD simulations.

With a factor of 1:15 between the lengths of the two geometries, it can be seen that if the Reynolds numbers are to be equivalent, the simulations need to be executed at different values of ω, and hence U. It is worth noting that the Re values here are calculated based on the default fluid viscosity and density values given in CFX, hence the increase in value compared to that given in Table 3.2, and denoted Re_{CFX}. Although this leads to Re_{CFX} being approximately 11% greater than the value of Re calculated for the water-bath model experiment, this is not expected to be significant as the simulations could just as easily be performed at another value of Re_{CFX} in the same subcritical flow regime.

If a relevant time scale is taken to be d/U, then the model-scale simulation data needs to be interpreted as occurring 13 times quicker. Therefore, to determine if these two simulations obey the suggested scaling principles mentioned in Section 3.1.1, plots relating to distance and time need to take these two ratios (1:15 and 1:13) into account. Differences in A and U are calculated using these two ratios (see Table 7.1). This can be done in one of two ways: either by simply multiplying time and distance values, or rescaling both sets of data to common non-dimensional parameters.

Values of $\bar{X}$ from the Models 1 and 2 are shown in Figure 7.1, where the model-scale data

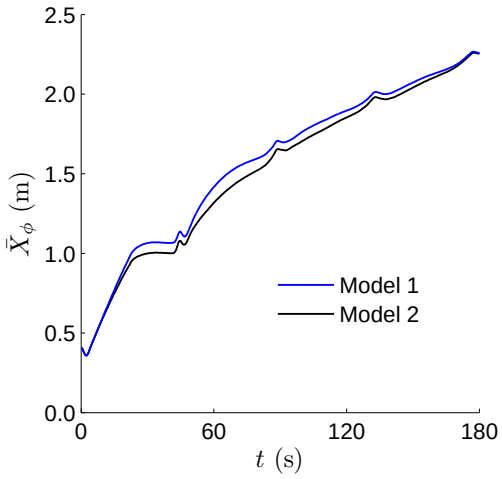

Figure 7.1: $\bar{X}_\phi$ plots comparing Model 1 scaled up in length (1:15) and time (1:13) against Model 2 at equivalent Re_{CFX}.

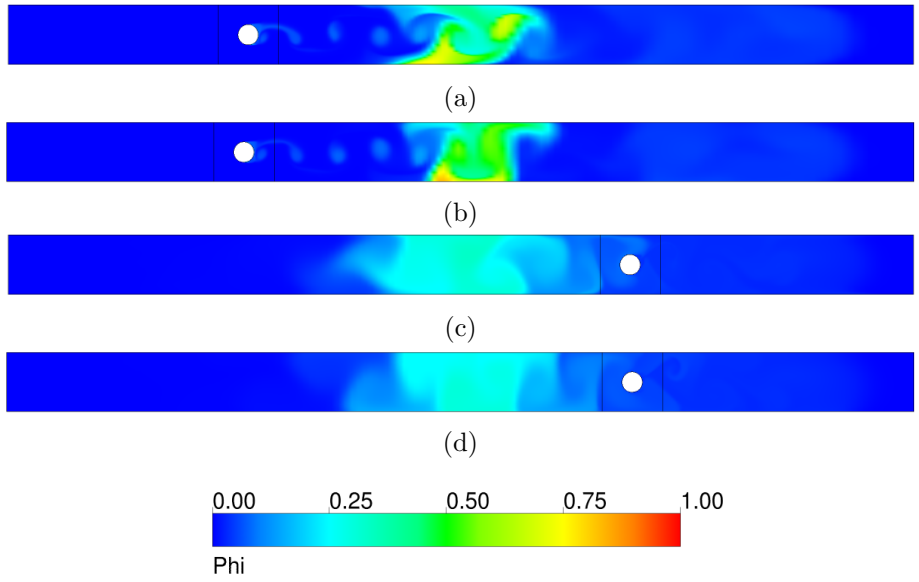

Figure 7.2: Contours of ϕ at the symmetry plane at the top of the corridor for: (a) Model 1 after 4.60 s; (b) Model 2 after 60 s; (c) Model 1 after 9.25 s; (d) Model 2 after 120 s.

is simply multiplied by 13 on the time axis and by 15 on the distance axis. The figure confirms that applying the scaling principles, and obtaining values like those presented in Table 7.1, yields solutions that are in very good agreement with one another. Figure 7.2 shows the ϕ distribution at two different time values for the two different models at the same location. Although the exact 1:13 ratio of times is not quite met, as the data output values do not precisely match this ratio, the time values are very close in value. The two sets of contours show that models 1 and 2 show good agreement between one another.

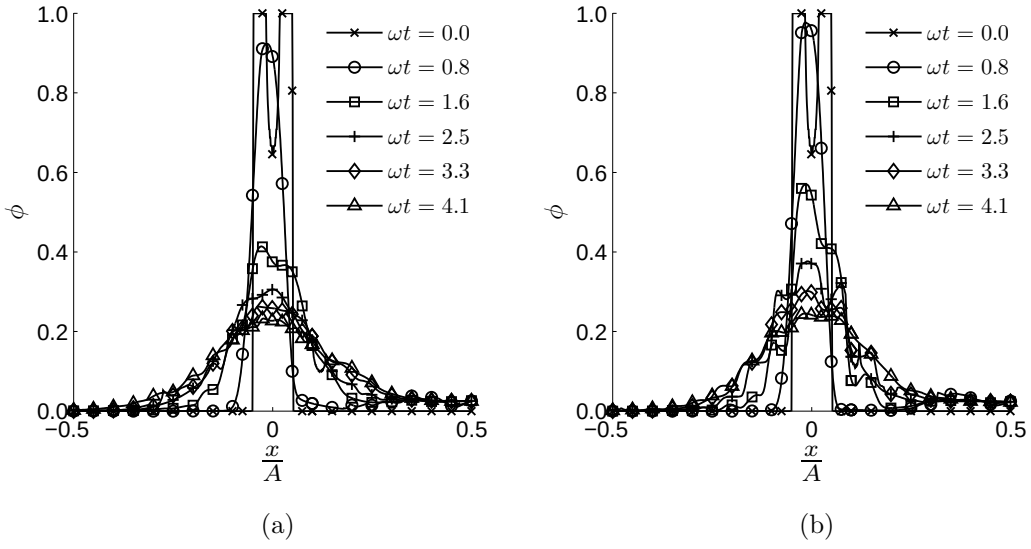

Figure 7.3: Profiles of ϕ at indicated ωt values for: (a) Model 1; (b) Model 2.

Profiles of ϕ at various values of ωt are shown in Figures 7.3a and 7.3b. The non-dimensional parameter ωt acts as the time rescaling, and the x axis is rescaled by the amplitude of translation, A, to make the two plots comparable using non-dimensional distances and times. Again, the figures show that the two simulations are very similar, with only slight disagreement on peak ϕ values for some of the ωt readings, most notably $\omega t = 1.6$ and $\omega t = 2.5$.

The images presented in Figures 7.1 - 7.3 show that the two models yield similar flows, once time and length scales are accounted for or the data is non-dimensionalised in the same way. That is, the results from Model 1 predict a virtually identical flow field over time when compared to Model 2. This is as we would hope, but it is very valuable to have this validated as it gives confidence that the water-bath modelling approach is capable of providing data that may be interpreted at the full-scale. With this confidence established, CFD models are now constructed at the full-scale and compared against theory based on the water-bath model findings of Chapter 3.

7.1.2 Imposed Unidirectional Flow

So far, all applications of equation 3.12, which was used to describe the evolution of the dye concentrations over time, have been limited to an initially quiescent flow. As mentioned in Section 2.2.2, ventilation is used in buildings as a means of mitigating airborne contaminants. Therefore, the effects of peoples movements on the transport of an airborne contaminant are now considered in a ventilated space.

7.1.2.1 Six Air Changes per Hour

The distribution of a contaminant C, or ϕ, is now considered where the corridor is experiencing a background flow. There is no specific experimental data available for validation of flows under these conditions and so only the previously validated theoretical and CFD models are considered here.

A unidirectional flow is imposed by implementing a constant velocity U_{in} m s^{-1} at one end of the corridor, resulting in a volumetric flow rate $Q = U_{in}A_r$, where A_r is the cross sectional area of the corridor. If the cylinder were not in place and the no slip condition not applied at the walls, a simple plug flow could be assumed, i.e. the fluid in the corridor is now subject to a displacement tU_{in} m over t seconds. Building upon the original

theoretical model, equation 3.12, it is postulated that this movement may be applied to the contaminant region by letting the centre of mass of the dye region, μ, be a function of time and move as if a plug flow were acting upon it:

$$C(x,t) = \frac{m}{\sqrt{4\pi D_t t}} e^{\left(-\frac{(x-U_{in}t)^2}{4D_t t}\right)}. \tag{7.1}$$

For a comparable CFD model, the 3D geometry, with $d = 20$ mm, is scaled using a factor of 1:15, resulting in a corridor with dimensions $22.5 \times 1.47 \times 2.04$ m (see Figure 7.4).

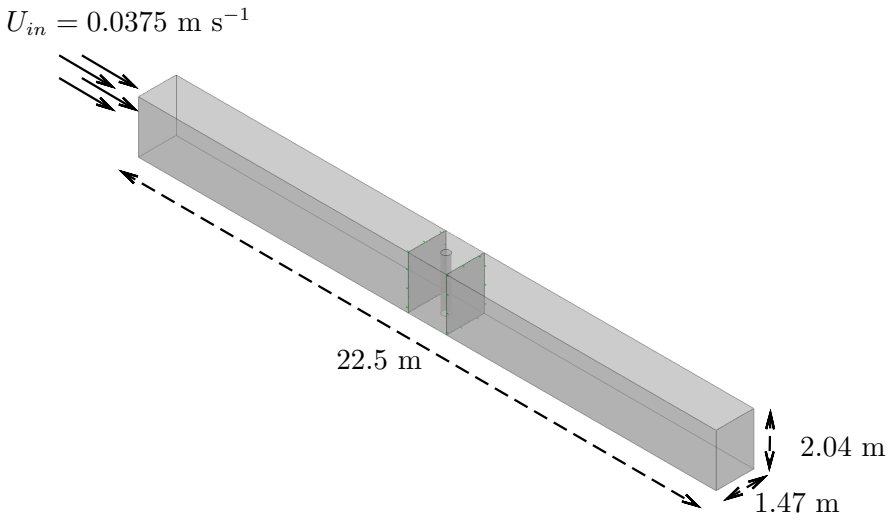

Figure 7.4: Dimensions of geometry once scaled up by a factor of 1:15. A constant velocity, U_{in}, is added to the flow entering one end of the corridor.

The cylinder is scaled up to possess a diameter $d = 0.3$ m and made to translate back and forth with an amplitude of $A = 15$ m at $\omega = 0.0667$ s^{-1}, corresponding to a velocity of 1 ms^{-1}. Using equation 3.24, this leads to a value of $D_t = 0.0294$ m^2 s^{-1}. Since D_t increases linearly with d, A and ω (see equation 3.24) any changes in the length of corridor, width of person or walking speed will have a direct impact upon the turbulent diffusion coefficient used in equation 7.1.

A unidirectional flow is imposed through one end of the corridor, of cross sectional area A_r, at a velocity U_{in}, yielding a volumetric flow rate $Q = U_{in}A_r$. It was highlighted in Section 2.2.2.1 that the ventilation guidelines for a general ward in a UK hospital is 6 ACH (Department of Health, 2007). As there is no explicit guidance for corridors, this value is implemented here to represent a suitable ventilation flow rate. To implement 6

ACH in the geometry described, a unidirectional flow of $U_{in} = 0.0375$ m s^{-1} is used:

$$V = 67.473 \text{ m}^3 \qquad A = 3.00 \text{ m}^2$$
$$Q = \frac{V \times 6}{3600} \text{ m}^3\text{s}^{-1} \qquad U_{in} = \frac{Q}{A_r} = 0.0375 \text{ m s}^{-1}.$$

This kind of flow is a best-case scenario in terms of contaminant removal as the air exchange efficiency is greatest for plug-flow, or displacement ventilation, when compared to fully-mixed systems (Chartier et al., 2009). Therefore, the findings of these models are likely to overestimate the contaminant removal and underestimate the transport of the contaminant against the flow.

A summary of details relating to the CFD simulation is presented in Table 7.2.

Turb. Model	Advection	ω (s^{-1})	Re_{CFX}	U_{in} (m s^{-1})	Δt (s)	Flow Time (s)
SST	HR	0.0667	19,426	0.0375	0.025	300

Table 7.2: Properties for the CFD simulation with a translating cylinder in a unidirectional flow.

Contours of ϕ over five ωt values are presented in Figure 7.5. By looking at Figures 7.5a - 7.5e, it is clear that the bulk transport of the scalar, ϕ, is predominantly determined by the imposed flow rate at the inlet (left hand side). It is only by looking at Figure 7.5f that it can be seen that despite the vast majority of the scalar being transported with the ventilation, a small proportion is able to be transported upstream due to the translation of the cylinder.

Figure 7.6 shows a comparison between the profiles obtained from the CFD solution using properties set out in Table 7.2 and those generated by equation 7.1, for the same five values of ωt presented in Figure 7.5. For equation 7.1, the D_t parameter was obtained using equation 3.24 and a value of $m = 1.5$ was used for the initial 'mass'. This value corresponds to the area under the curve for the initial ϕ distribution in the CFD simulations, which is a value of 1 across a 1.5 m section of the corridor. However, as was highlighted in Chapter 3, the initial conditions of the theoretical model do not quite agree with those implemented in the CFD model. The theoretical model necessarily starts as an infinitely long spike at $t = 0$. This is apparent in Figure 7.6, where the agreement between the two models is the weakest at the first value of ωt. After this first value, the agreement of the two models improves over time to the point where $\omega t = 12.7$ and the two sets of data almost overlap.

7.1.2.2 Two Air Changes per Hour

The volumetric flow rate imposed in the previous example assumes the corridor is ventilated at the recommended guideline value for a general ward, which here it is assumed is applicable to hospital corridors. It is also implicitly assumed that this ventilation system is well maintained and operating at full capacity. A scenario is now considered where the same unidirectional flow is implemented only at a much lower flow rate, 2 ACH. This could be relevant to corridors that have poorly maintained HVAC systems.

The corridor dimensions are the same as in the previous example (see Figure 7.4) so the inlet velocity necessary for 2 ACH is $U_{in} = 0.0125$ m s^{-1}. A CFD simulation was

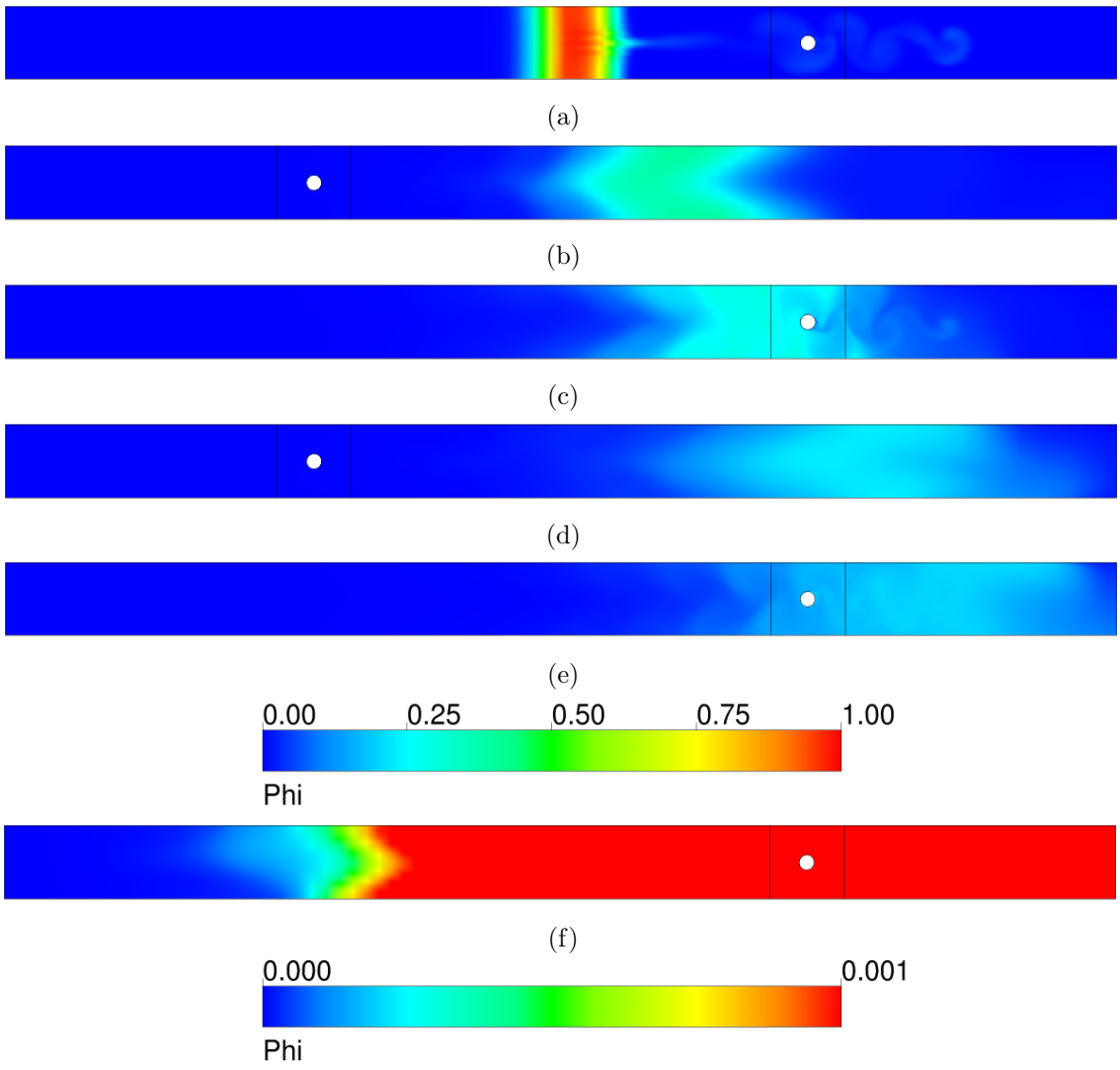

Figure 7.5: Contours of ϕ on a $x-y$ plane at $z = 1$ m with $U_{in} = 0.0375$ m s^{-1} (6 ACH) for: (a) $\omega t = 0.7$; (b) $\omega t = 3.7$; (c) $\omega t = 6.7$; (d) $\omega t = 9.7$; (e) $\omega t = 12.7$; (f) $\omega t = 12.7$, with alternative ϕ range;

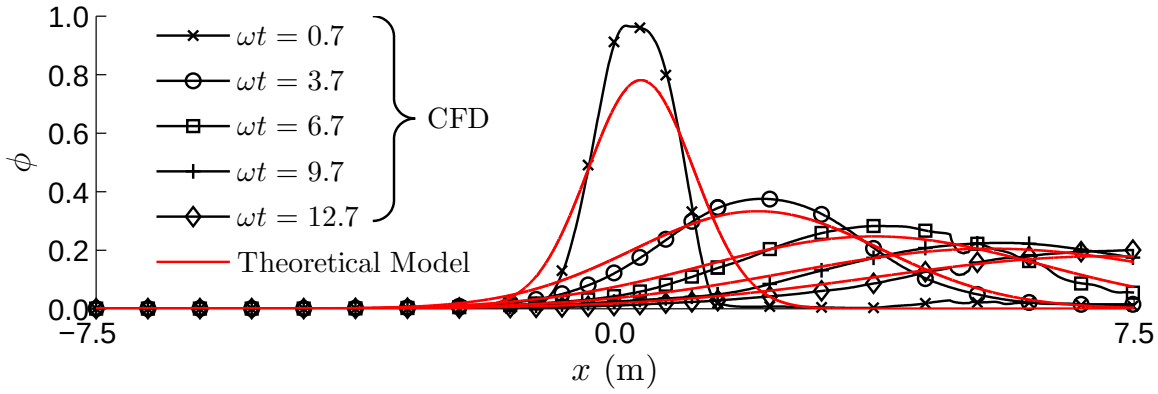

Figure 7.6: Comparison between CFD (black lines) and equation 7.1 (red lines) for $d = 0.3$ m, $\omega = 0.0667$ s^{-1} and $U = 0.0375$ m s^{-1} (6 ACH) at values of ωt as indicated.

carried out using this updated value of U_{in}, though all remaining properties regarding the simulation are identical to those presented in Table 7.2. For the theoretical calculations, equation 7.1 was again used.

Contours of ϕ are presented in Figure 7.7 for the 2 ACH simulation. As one would expect, the same overall trends are found as for the 6 ACH case only ϕ is not as quickly displaced in the direction of the ventilation (to the right). This leads to ϕ being carried further upstream, against the direction of the ventilation flow, for all time. Looking at Figure 7.7f, when $\omega t = 12.7$, small values of ϕ are detected almost at the ends of the corridor.

Figure 7.8 shows a comparison between the ϕ profiles obtained from the CFD solution and those generated by equation 7.1, for the same five ωt values in Figure 7.7. The solutions of equation 7.1 were obtained using the same values of D_t and m as used for the 6 ACH case. The agreement between theory and CFD is seen to be as good, if not better, than that seen in Figure 7.6 and the profiles show the same trends as those seen in Figure 7.7. That is, the main ϕ region remains more centrally located and larger ϕ values are obtained closer to the upstream end of the corridor.

Despite there being no experimental data to compare with, the agreement between the two different models, theoretical and CFD, gives confidence that both modelling approaches are valid for the unidirectional flows considered here. In terms of a real scenario, these two simulations show that even in the presence of a ventilation a person's wake may be able to transport an airborne contaminant against the main direction of the ventilation flow, even at flow rates consistent with current healthcare building recommendations.

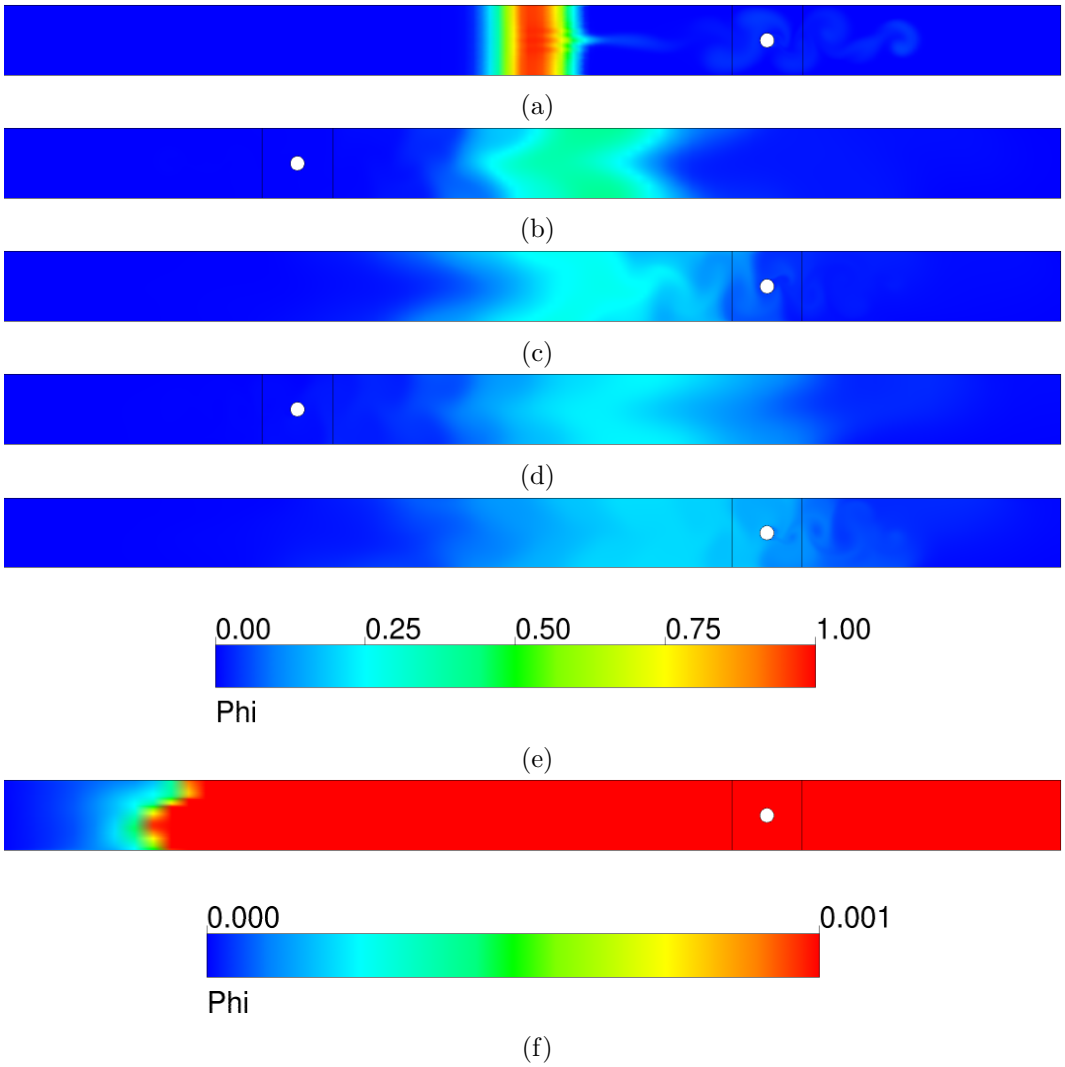

Figure 7.7: Contours of ϕ on a $x-y$ plane at $z = 1$ m with $U_{in} = 0.0125$ m s^{-1} (2 ACH) for: (a) $\omega t = 0.7$; (b) $\omega t = 3.7$; (c) $\omega t = 6.7$; (d) $\omega t = 9.7$; (e) $\omega t = 12.7$; (f) $\omega t = 12.7$, with alternative ϕ range;

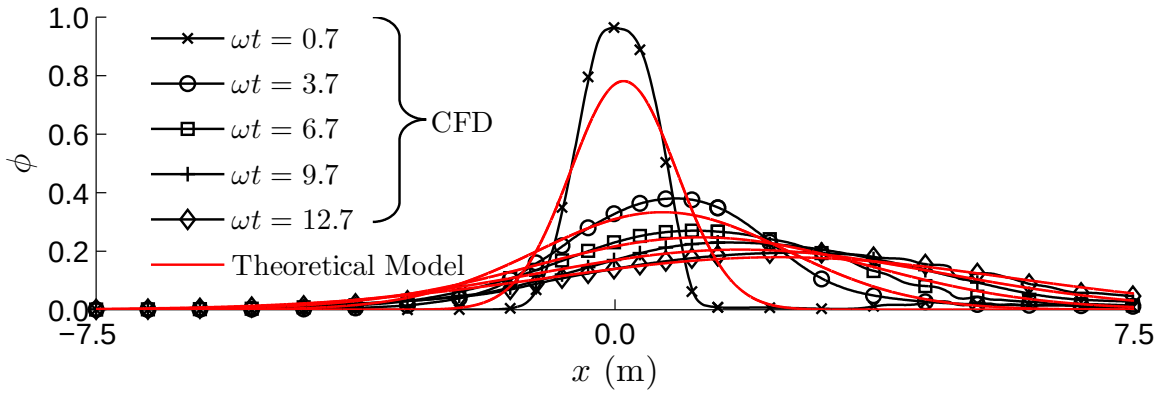

Figure 7.8: Comparison between CFD (black lines) and equation 7.1 (red lines) for $d = 0.3$ m, $\omega = 0.0667$ s^{-1} and $U = 0.0125$ m s^{-1} (2 ACH) at values of ωt as indicated.

7.1.3 Between Two Rooms

All the CFD simulations, so far, have considered flows involving a corridor, whose shape has not changed, with an initially centrally located contaminant region. A situation is now considered where the geometry takes on two additional alcoves (see Figure 7.9). This scenario is only investigated using a CFD model as there is no equivalent theoretical model to compare with.

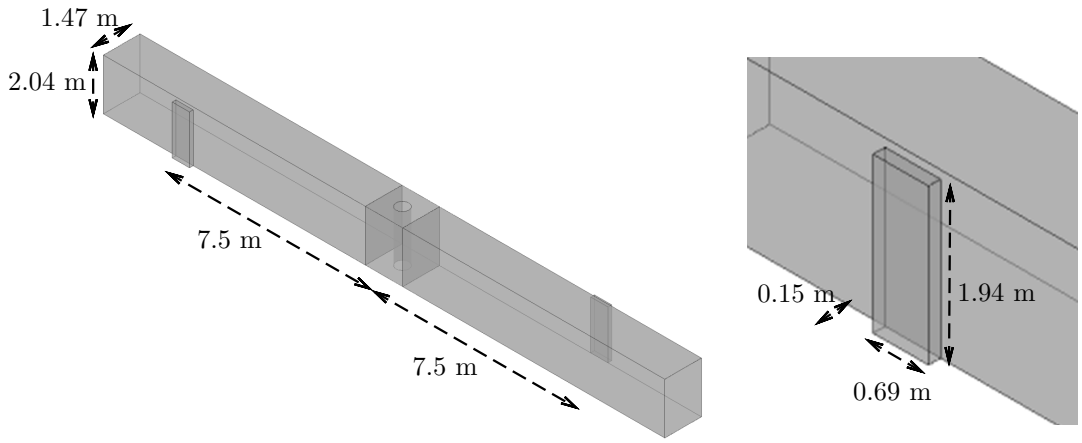

Figure 7.9: Geometry used to investigate the transport of ϕ between two alcoves/rooms.

A scalar is released from one alcove, representing a doorway into a room, and its value monitored at another alcove on the opposite side of the corridor, 15 m away. Each alcove possess a volume of 0.2 m^3, one of which initially possesses a value of $\phi = 1$ (see Figure 7.10). The alcoves are located so that the centre of the cylinder lines up with the centre of the alcove when the cylinder is at its maximum amplitude of translation. The simulation is carried out at full-scale, but the base cylinder diameter is $d = 0.0335$ m, which once upscaled yields $d_f = 0.5$ m (i.e. the cylinder diameter is still approximately one third of the corridor width). The translation frequency of $\omega = 0.0667$ s^{-1} is interpreted as a linear velocity of $U = 1$ m s^{-1} (which is appropriate for a person walking). The ends of the corridor are once again modelled as walls, not an inlet and outlet. A summary of the simulation properties is presented in Table 7.3.

Turb. Model	Advection	ω (s^{-1})	Re_{CFX}	Δt (s)	Flow Time (s)
SST	HR	0.0667	32,377	0.025	300

Table 7.3: Properties for the CFD simulation with a translating cylinder in a unidirectional flow.

The initial distribution of ϕ is shown in Figure 7.10. There is no imposed flow for this simulation and so all scalar transport from this point is dictated by the flow created by the translating cylinder, as it was for the majority of the results in Chapters 5 and 6.

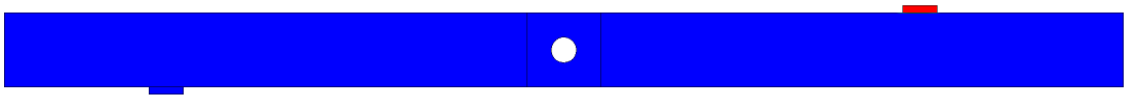

Figure 7.10: Initial conditions of $\phi = 1$ in one alcove at $\omega t = 0$, presented in plan view at a height of $z = 1$ m above the floor.

Figure 7.11 shows the evolution of ϕ over a period of 5 minutes, corresponding to $\omega t = 20$. The legend has been chosen to show values of ϕ up to 0.01, corresponding to 1 % of the initial value. Visualising the contours at these ϕ values, it can be seen that ϕ is transported to the other side of the corridor as soon as $\omega t = 10$.

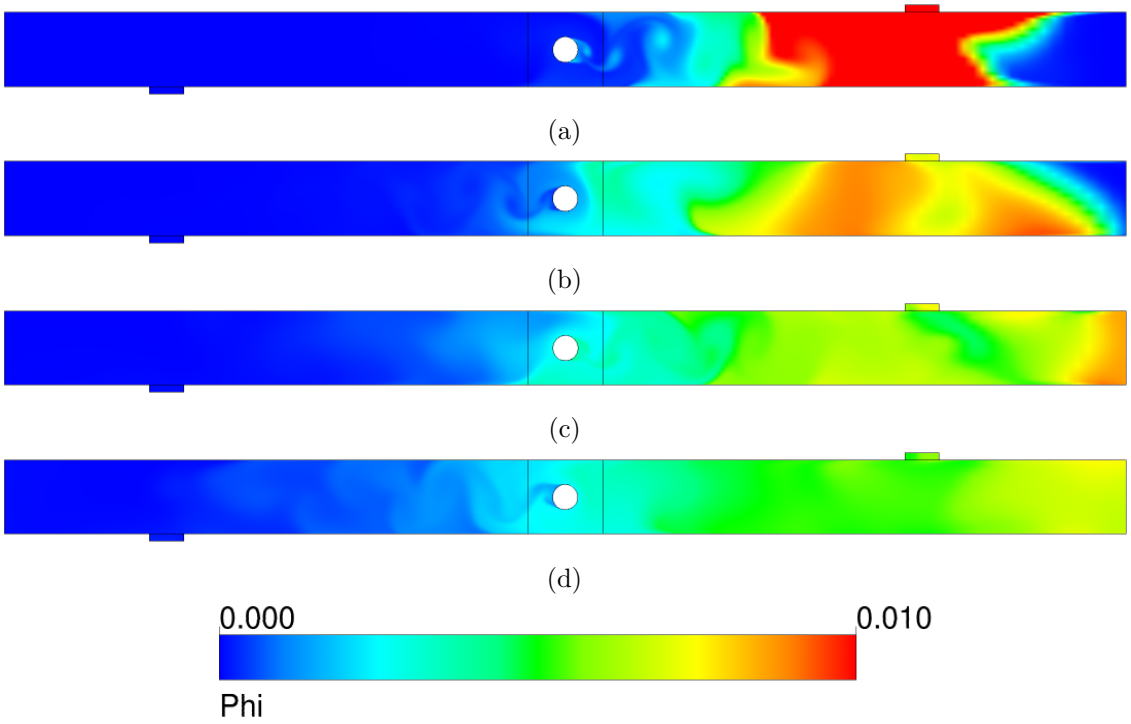

Figure 7.11: Contours of ϕ in $x - y$ plane located at $z = 1$ m after: (a) $\omega t = 5$; (b) $\omega t = 10$; (c) $\omega t = 15$; (d) $\omega t = 20$.

To see how ϕ is transported from its initial location to the other 'door', the normalised, cumulative ϕ value in each door is now plotted. For referencing, the door that initially housed ϕ at $\omega t = 0$ is henceforth *door*1 (upper right in Figure 7.11). The other door is henceforth *door*2. Assuming ϕ is representative of a concentration, the total 'mass' of ϕ is taken to be the initial value of ϕ integrated over the volume of *door*1 (0.2 m^3). The

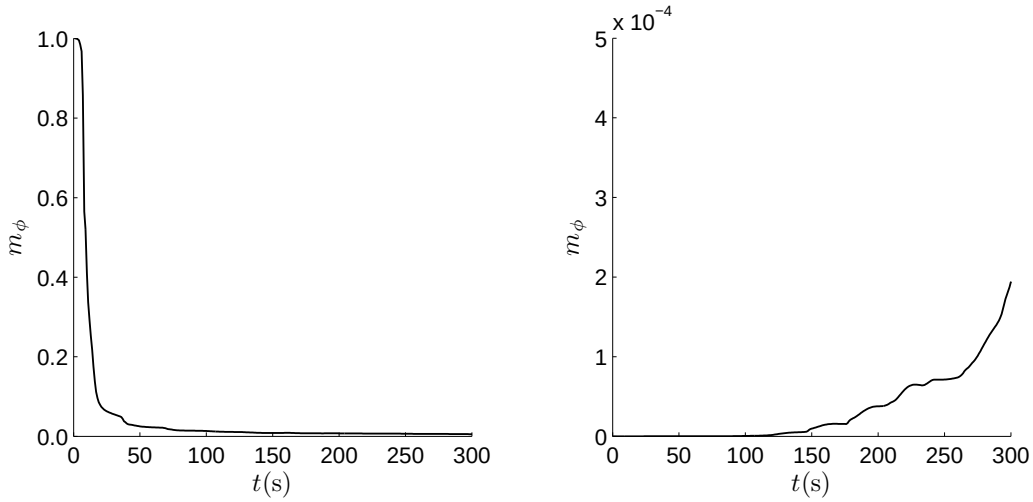

(a) (b)

Figure 7.12: Values of m_ϕ over time at (a) *door*1; (b) *door*2.

variable m_ϕ is now introduced as the normalised 'mass' of ϕ, so that $m_\phi = 1$ for all time.

Figure 7.12 shows how the values of m_ϕ in *door*1 and *door*2 change over time. Looking at *door*1, the door of release, Figure 7.12a shows how quickly ϕ is removed from its initial location. After 50 seconds, more than 95 % of m_ϕ has been transported into the corridor. Now looking at *door*2, it can be seen that it takes around 100 seconds (or ≈ 6.67 traverses) for m_ϕ to be detected. From this point on, the mass steadily increases. The scale on the plot in Figure 7.12b only goes up to 0.05 % of the total value of m_ϕ, which could be interpreted as a very small amount. However, it needs to be reiterated that when dealing with airborne contaminants and pathogens, small doses can still result in an infection.

7.2 Implications of Full-Scale Predictions

The modelling up to this stage has involved tracking the movement of a scalar. For the water-bath experiments, this scalar was the dye concentration, C. For the CFD simulations, the user variable ϕ was implemented as a scalar. From here on, these scalars are now thought of in the context of airborne disease transmission and to be representative of a dose of some airborne infection.

7.2.1 Infection Risk

Recall the proposed theoretical model for the prediction of the evolution of the dye concentration in the experiments, equation 3.12:

$$C(x,t) = \frac{m}{\sqrt{4\pi Dt}} e^{\left(-\frac{x^2}{4Dt}\right)}. \qquad \text{(3.12 revisited)}$$

This equation is now used to estimate the infection risk experienced by people walking along a corridor that has a contaminant release located in it, using a dose-response approach (see Section 2.3.3.2).

In order to estimate the dose that a person is exposed to, a model of a breathing cycle is introduced. By combining equations 3.12 with the location and volume of discrete breaths, an estimate of the inhaled infectious material can be obtained. To implement a breathing model, it is first necessary to outline related properties. The two breathing properties used here are: tidal volume, the volume of air inhaled during a typical breath; and respiratory frequency, how often the person breathes.

The values used for for tidal volume, T_v, and respiratory frequency, R_f, need to be relevant to the scenario being modelled. A volume of $T_v = 0.5 \times 10^{-3}$ m^3 is often used for a person breathing at rest (Barrett et al., 2012). Likewise, the respiratory frequency for a resting human is found to range from $R_f = 12 - 20$ (Barrett et al., 2012). However, since the theoretical model here considers a person walking along a corridor, these values are subject to change. Dalton (2013) reported mean values of $T_v = 1.1 \times 10^{-3}$ m^3 and $R_f = 23$ for a set of 12 participants walking at 3.5 mph (≈ 1.56 m s^{-1}). Although these values are clearly subject to change depending on a host of factors, they are assumed to be representative of a person walking at a medium pace along a corridor.

The inhalation and exhalation cycle is represented as a sinusoidal function for the volumetric flow rate:

$$Q = \begin{cases} \dfrac{N_B T_v \sin\left(\dfrac{2\pi}{T_b}\left(t + \dfrac{A}{2U}\right)\right)}{4.7746}, & \text{per inhalation} \\ 0, & \text{per exhalation} \end{cases} \qquad (7.2)$$

where N_B is the number of breaths taken whilst walking at U m s^{-1} along a corridor of length A m, and each breath takes T_b seconds. The factor of 4.7746 was back calculated to ensure that each breath (sine wave) corresponds to a total of T_v m^{-3} being inhaled and the first breath starts at $t = 0$ s. The model presented here assumes that the infectious dose is only dependent on what is inhaled. Each inhalation is represented by a sine wave and each exhalation is simply a pause in the flow rate (see Figure 7.13). The displacement of air due to exhalation, which may influence the local concentration of pathogens, is not considered.

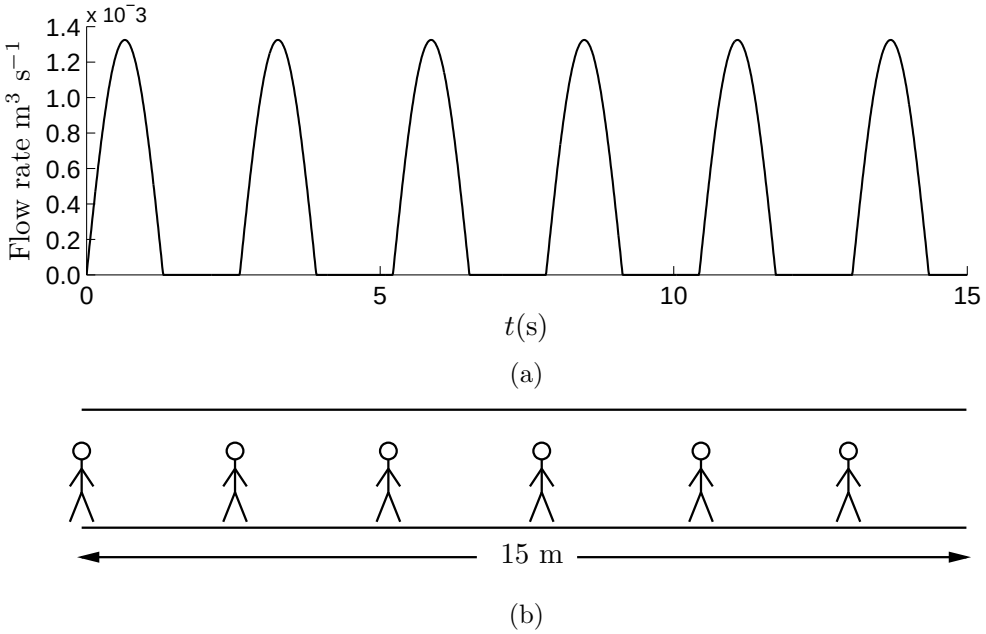

Figure 7.13: Sinusoidal breathing pattern for $T_v = 1.1 \times 10^{-3}$ m^3, $R_f = 23$, and $U = 1$ m s^{-1}. (a) Volumetric flow rate; (b) Locations of a person in the corridor when they start to inhale.

Equation 7.2 is evaluated over time steps of $\Delta t = 0.01$ s, at locations dictated by the distance travelled, which is calculated using the elapsed time t and walking velocity U. The amount of infectious material inhaled is then assumed to be:

$$m_{\text{in}} = \Delta t \Delta Q \Delta C, \tag{7.3}$$

where ΔQ and ΔC are the values of Q and C obtained from equations 7.2 and 3.12 over time Δt, respectively. Any infectious material inhaled is not removed from the space and is available for subsequent inhalation. Although this is not in strict accordance with a real situation, determining what is retained by the body and what is exhaled is beyond the scope of this study.

To quantify infection, the mass of inhaled material, m, is not appropriate. Instead, m is now replaced with q, a number corresponding to the amount of infectious material. To put q into context, an initial value q^0 can be considered as the number of infectious doses released into the space at $t = 0$, for example through a breath, cough or sneeze. This initial value is used in place of m in equation 3.12. A value of $q^0 = 10{,}000$ is used as this yields $\approx O(1)$ doses inhaled for the simulations to follow. However, this number is in effect arbitrary as a value of $q^0 = 1$ could just as easily have been chosen, and the number of q inhaled would be $\approx O(10^{-4})$.

7.2.1.1 One Pass Risk

Figure 7.14 compares two different scenarios using the breathing profile of equation 7.2. The first (Figure 7.14a), models the number of inhaled doses based on an initial release and evolution according to equation 3.12, where D is calculated for a person of shoulder width $d_f = 0.5$ m walking at U m s^{-1} along a 15 m corridor, for 15 seconds. The second (Figure 7.14b), models the number of inhaled doses using the same breathing profile only assuming that the same number of doses are homogeneously mixed in the entire corridor. These types of well-mixed models are common, particularly when using the Wells-Riley approach. The well-mixed model yields a total inhalation of $q = 1.47$, whereas the model taking into account the distribution through equation 3.12 yields a total inhalation of $q = 1.16$ (a reduction of $\approx 25\%$). Although these two values are not massively different,

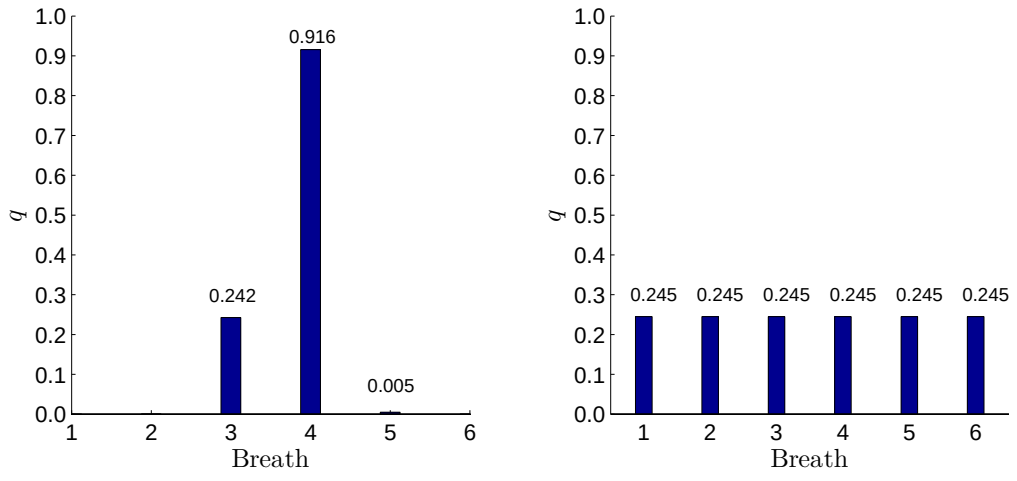

Figure 7.14: Number of doses inhaled per breath assuming: (a) q distribution obeying equation 3.12; (b) homogeneously mixed q distribution.

the values between the individual breaths are, as can be seen in Figure 7.14. The fourth breath in the first scenario yields an inhalation of $q = 0.916$, almost four times that of the amount inhaled in the well-mixed model, $q = 0.245$.

The amount of infectious material inhaled that leads to infection depends on the pathogen and the body's immune system. Taking four doses, over time, at a quarter of the size of one large dose does not necessarily result in the same chance of infection, though it is assumed it does here. For example, if a particular person's immune system is infected (the reponse) upon the inhalation of 10 microbes (the dose), inhaling 1 microbe every hour for 10 hours may not result in infection, despite being the same total dose, as their immune system is able to cope with the threat of just one microbe at a time. With this in mind, if the q^0 were changed to 20,000, the fourth breath of the first scenario would yield a value of $q = 1.84$, and hence infection, yet the individual doses from the well-mixed approach would never exceed $q = 1$. Depending on the pathogen, its airborne survival rate and the body's response, despite the cumulative dose being larger the person may not be expected to get infected in this well-mixed scenario.

7.2.1.2 Multi Pass Risk

The same models are now considered over 150 seconds so that the inhaled doses of 10 people can be calculated, where it is assumed that as soon as one person reaches the end of the corridor another person immediately starts a journey along it. (It does not actually matter which end the person is assumed to start from as the release is assumed to be central and the Gaussian distribution is symmetrical about the release.) Figure 7.15 shows the cumulative q dose using the two different approaches.

The most striking feature of Figure 7.15 is that the first person to pass through the contaminated region receives the lowest cumulative dose in the first scenario (see Figure 7.15a). The values of q calculated using equations 3.12 and 7.2 are dependent upon the locations of inhalation and so for the values of A and U used here, the timing of the breaths avoid most of the contaminated region. For all other persons other than the first, the two models show very similar expected total doses.

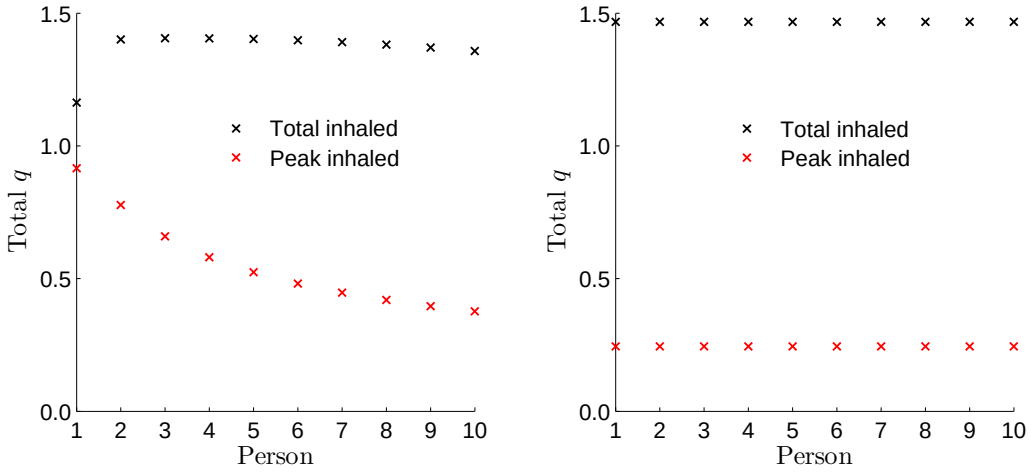

Figure 7.15: Total q inhalation for 10 people walking along a 15 m corridor at $U = 1$ m s^{-1} assuming a: (a) q distribution obeying equation 3.12; (b) homogeneously mixed q distribution.

7.2.1.3 Background Flow Risk

The single and multi pass cases both used equation 3.12 to model the dispersal of the airborne contaminant. The same procedure is repeated only with a unidirectional flow imposed in the corridor using equation 7.1. The ventilation is assumed to be operating at 6 ACH and so a value of $U_{in} = 0.0375$ m s^{-1} is used. All other aspects of the modelling procedure are the same as those described for the single and multi pass cases.

Figure 7.16a shows the calculated number of doses, q, inhaled per breath for a person walking at $U = 1$ m s^{-1}. Compared to the previous one pass case with no background ventilation, the third breath now contains a lower dose while the fourth and fifth breaths contain larger doses. The peak dose, inhaled during the fourth breath, is also increased compared to the case without ventilation.

Looking at the ventilated multi pass scenario, Figure 7.16b shows that the peak inhaled dose increases for the first three occupants of the corridor, and remains the same for the others. The total inhaled does is increased for the first four occupants, the same for the fifth, and reduced for the remaining five.

These changes in inhaled doses should not be interpreted as showing that ventilation increases peak inhalation dosage for those passing through a corridor soon after the release of a contaminant, but rather that ventilating a space does not necessarily lead to a reduced

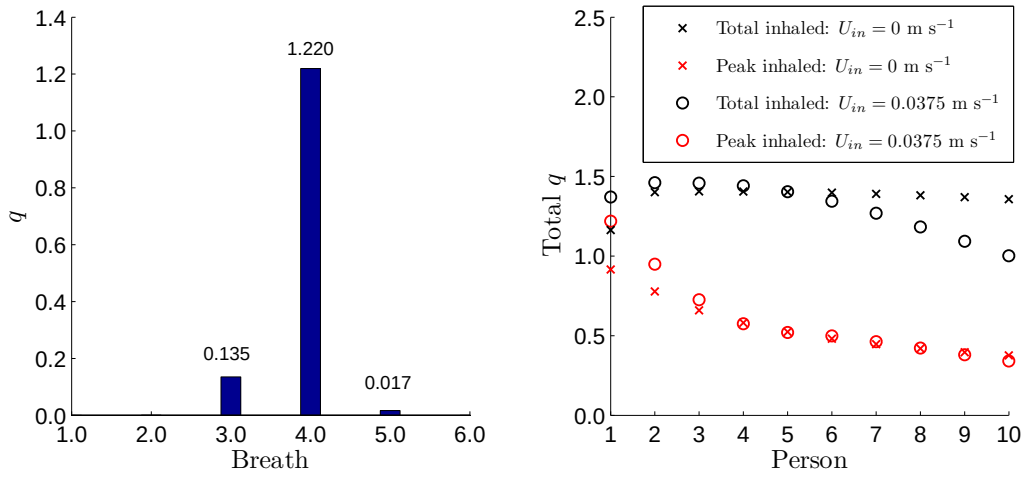

(a) (b)

Figure 7.16: Assuming a q distribution obeying equation 7.1 for 6 ACH, $U = 1$ m s^{-1}, $T_v = 1.1 \times 10^{-3}$ m^3 and $R_f = 23$: (a) Number of doses inhaled per breath by a person walking through the corridor at the moment of release; (b) Comparison between total q inhalation for 10 successive people walking along the corridor with and without ventilation.

infection risk for everyone within the space. This example shows that ventilation with a corridor may reduce infection risk in the long term, $O(10^2)$ s, but in the short term, $O(10^1)$ s, the effects of ventilation are not able to remove the contaminant from the space and only relocate it to another potential point of inhalation.

7.2.1.4 Stochastic Risk

To get a more generalised impression of what a typical person might get exposed to, a Monte-Carlo simulation was performed to look at the total q dose to the first person walking along the corridor shortly after an initial release. Values of walking velocity and respiratory frequency were set to vary randomly (using MATLAB's *rand* function) between $0.5 \leq U \leq 1.5$ m s^{-1} and $19 < R_f < 27$, respectively. The tidal frequency was set to be constant for all simulations at $T_v = 1.1 \times 10^{-3}$ m^3. A total of 1,000 simulations were performed (see Figure 7.17).

It was found that the largest total q values (> 3) corresponded to low walking speeds ($U < 0.6$ m s^{-1}) and high breathing rates ($R_f > 25$). This is not surprising as this corresponds to a scenario where a person is taking the most frequent breaths and is in the contaminated space the longest. The converse was also true; the lowest inhaled doses corresponded to those larger velocities ($U > 1.4$ m s^{-1}) and lower breathing rates

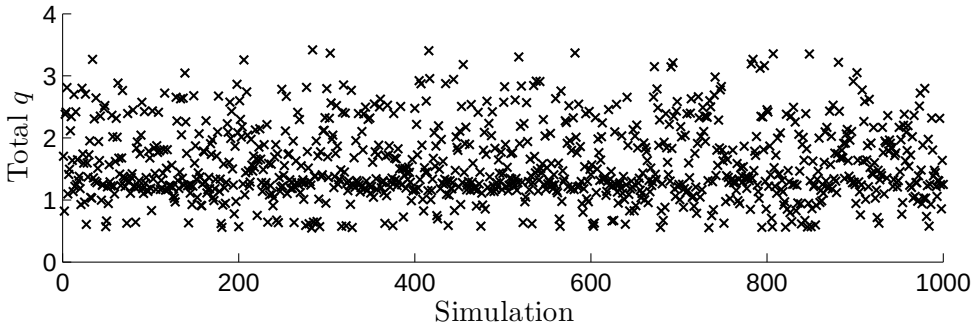

Figure 7.17: Total q inhalation for 1,000 simulations of one person walking along a 15 m corridor at $0.5 \leq U \leq 1.5$ m s^{-1} breathing at a rate of $19 < R_f < 27$ assuming a q distribution obeying equation 3.12 after an initial release of $q^0 = 10,000$ at time $t = 0$.

($R_f < 21$). These findings are in line with intuition.

In the first case presented with this model, it was predicted that a value of $q = 0.92$ could be inhaled in a single breath, based on the specified conditions. This value could in fact be orders of magnitude higher depending on the state of the initial release. Figure 7.18 shows how equation 3.12 models the initial release of q^0. From time $t = 0$ (Figure 7.18a), q starts off as an infinitely thin slice. For all subsequent times the contaminated region then spreads out, though it is assumed to always be well mixed in the y and z directions, obeying the Gaussian distribution until it reaches the corridor ends (Figure 7.18b). However, if the initial distribution were say a or sneeze, the initial volume would not necessarily be well mixed in the y and z directions. If a cube of, say, 0.5 m^3 were assumed to house the initial release of $q^0 = 10,000$ (Figure 7.18c), a single breath at this concentration could yield an inhalation of $q = 88$. The previous examples highlight why a well-mixed model cannot be simply assumed for all airborne disease models and why spatial variations in contaminant concentration are important to consider.

7.2.1.5 Quantum of Infection Values

The previous discussions all involved the parameter q, where it was understood that q is the dose of infectious material required to cause an infection. This bears close resemblance to the quanta used in equation 2.7. The main difference between the two parameters is that the inhalation of one quantum of infection is assumed to infect $1 - 1/e$ or $\approx 63\%$ of susceptibles (Beggs et al., 2003), whereas the inhalation of q used in this study is assumed to be the dose required to guarantee infection of a susceptible. Although the two parameters are clearly defined differently, values of quanta found in the literature

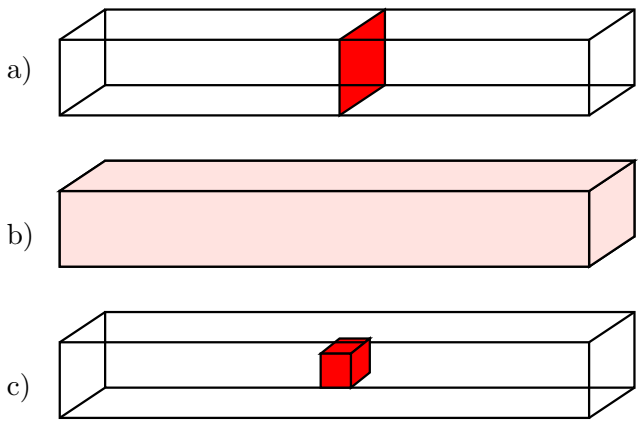

Figure 7.18: (a) Initial contaminant distribution for all models using equation 3.12; (b) Point up to which the model is applicable, when the contaminant has reached the ends of the corridor; (c) More realistic and likely initial contaminant distribution.

are used to compare to the values of q used and obtained in this study.

All the infection risk examples in this study have assumed an initial q^0 value larger than the quanta values usually considered. Noakes and Sleigh (2009) and Beggs et al. (2003) quote several other studies' values of quanta generation, which show that the calculated generated quanta per hour is typically $O(10^1 - 10^2)$, though there are cases that yield quanta generation rates of up to $O(10^3 - 10^4)$ per hour. Therefore, dealing with an initial release of $O(10^4)$ for a quantum like parameter is possibly a little unrealistic, as even the most contagious outbreaks yield quanta values of this order of magnitude after an hour of generation, or more. However, the scenario that assumes a contaminant release from a 0.5 m^3 initial volume does not require a large initial q^0 value ($10,000/88 \approx 114$) to lead to a person inhaling $q = O(1)$, and hence becoming infected. Further, outbreaks of airborne infections have occurred in healthcare buildings (Gustafson et al., 1982; Bloch et al., 1985) and schools (Riley et al., 1978; Phillips et al., 2004), so even if back calculated quanta values show a low generation and infection rate, the outbreak still happened. As the infectious dose per cough/exhale/sneeze/etc. is not known, quanta values can only be calculated a posteriori if ventilation rates and the number of infections are known. Therefore, it is difficult to conclusively determine whether a value of $q^0 = 10,000$ is an unlikely, or impossible, value for an initial release.

7.3 Summary

Checks were made to ensure that the water-bath modelling carried out in this study was able to represent the full-scale scenario of a person moving along a corridor. By applying scaling factors in length (1:15) and time (1:13) to two CFD simulations it was shown that the water-bath model approach is applicable for use in this study. Satisfied that the theoretical and CFD models can be scaled up to full-scale, two examples of scalar transport were investigated. The first example looked at a translating cylinder in a corridor with an imposed unidirectional flow, representative of a ventilated corridor. Despite the ventilation, it was shown that some contaminant could still be transported 'upstream' against the direction of the background flow. The second example looked at how a scalar can be transported between two opposite ends of a corridor by the wake of a translating cylinder. This suggests that in the presence of weak or no ventilation, the wake of a person is able to transport an airborne contaminant the length of a corridor.

The theoretical model derived from the water-bath model experiment results was interpreted at the full-scale to investigate infection risk in three different ways. First, the risk associated with the individual inhalations of a single person walking along a corridor containing a contaminant distribution obeying equation 3.12 was investigated. This simple scenario showed that contaminant transport models that assume a uniform concentration distribution are not able to distinguish the risk associated with individual breaths, as opposed to those that take into account spatial and temporal differences. This scenario was then extended to look at the risks associated with 10 people walking along the same corridor, one after the other. The well-mixed model failed to distinguish between the infection risks of the individuals, when compared to a model incorporating equation 3.12. To determine the people most likely at risk of infection in a corridor containing an airborne contaminant, a Monte-Carlo simulation was performed with varying velocities and respiratory frequencies. The model predicted that the people most at risk are those walking slowest through the space and breathing most frequently.

7.4 Limitations of Modelling Approaches

A model does not aim to capture the full extent of a system, situation or process. Through simplifying assumptions it aims to capture the features that remain important to the

original problem, yet eases the calculations necessary to make predictions using it. These assumptions influence model predictions and place limits on its application. These limits and influences are discussed here for the various models used throughout this study.

7.4.1 Experimental Model

Model geometry

A circular cylinder is clearly not a perfect representation of a human. The choice of cylinder was made based on it offering qualitatively similar wake properties to those of a human mannequin (Mattsson et al., 1997), and being much simpler to construct for the CFD model.It also removes the complications and difficulties associated with different shaped people. It was felt that the considerable added complexity of 'human shaped' objects was not necessary and would add too much uncertainty. Providing a comprehensive understanding of a simple object moving was seen to be a more beneficial step before considering additional complexity of human shape and movement. For a real person walking, the ensuing wake is determined by the airflow around the head, limbs and torso. The shape and movements of the limbs combined with the gap between the legs all combine to give a wake that is different from that of a cylinder (Edge et al., 2005; Mazumdar et al., 2011). Due to the additional limb movement, it is likely that a human wake exhibits greater local turbulence than that of a comparatively sized cylinder. This, in turn, suggests that the mixing exhibited by the translating cylinder may under represent the mixing induced by a person in a similar scenario.

The water-bath model was constructed such that the base was solid and the top open. Consequently, once filled with water, the water-bath model operated with a free-surface representing the upper surface boundary. This approach was chosen so that the linear actuator could operate from above the water-bath. Although it is possible to fit a solid ceiling (restoring the no-slip condition that is present on a real corridor ceiling) and a linear actuator to the underside of a water-bath, as was done by Tang et al. (2013), this was not feasible with resources available for this study.

The physical dimensions and properties of the water-bath limited the choice of translation frequencies to prevent sloshing, however the maximum value of Re tested in the water-bath (11,320) is still feasible for a person walking down a corridor. Moreover, as highlighted earlier, it has been pointed out by Zdravkovich (1997) that flows satisfying

$1,000 < Re < 40,000$ are classified in the same (subcritical) flow regime and consequently produce similar turbulent flows. Hence, although there was a limit put on ω by potential sloshing in the water-bath, if Re values were able to be tested up to $Re \approx 40,000$ (more in line with the Re of a person walking at an average walking speed), it is unlikely that they would significantly alter the findings of this study.

Regular translation frequency, ω

The linear actuator used was made to reverse its motion dependent upon the activation of two metal contacts. This meant that the frequency of translation was regular, consistent and predictable. This constant forwards and backwards motion is probably not encountered all too often in hospital corridors, where the traffic is likely irregular and erratic. However, to be able to determine the likely distribution of an airborne contaminant as a result of a random population moving along more realistic paths in a hospital (most likely modelled as a stochastic process), first the underlying mechanisms need to be obtained in simple scenarios, as was done here.

The CFD and theoretical models allow for predictions of contaminant transport based on a single traverse of a corridor. This could allow for models to be built that could predict the contaminant transport expected in a network of corridors, that typically comprise a hospital or healthcare building. So although the frequencies used in the model do not represent typical human movements, modelling in such a way is a necessary step if more realistic, stochastic models are to be constructed.

Only one point of view

All the experimental images were captured from one location, side-on to the water-bath and approximately 3 m from away. This means that the majority of the vortices responsible for the mixing are not captured in the images. Attempts were made to capture images from above the water-bath, but a combination of a low ceiling height with the refraction and reflection at the water-surface meant that these images were not suitable to quantify the dye concentration. Data from this view point would have been beneficial as it could have helped determine if the assumption of constant dye concentration through the width of the water-bath was correct. However, judging by eye, the dye region appeared well mixed through the water-bath for the bulk of the dye region and so the lack of data from this view point is assumed to not be too big a loss. Although subtle changes in physiology of the eye between different people will lead to differences in judging whether the region

was well mixed or not, without a top-down view of the tank judging by eye was deemed sufficient.

Camera parallax

The camera was positioned 3 m away from the water-bath and aligned with the cylinder's initial position in the centre. As the observable length of the water bath was 1 m, the ends of the water bath made an angle θ of:

$$\theta = \arctan\left(\frac{0.5}{3}\right) \approx 9.5^{\circ}. \tag{7.4}$$

Therefore, the lightrays leaving the water-bath and entering the camera lens make an angle of $0 < \theta < 9.5^{\circ}$, relative to an imaginary line drawn between the centre of the water-bath and the camera (see Figure 7.19). Throughout the image analysis in this study, the dye concentration was assumed to be line of sight averaged and constant through the water-bath's width. Taking the effects of the camera parallax into effect, this is not strictly true. However, this assumption is applicable for dye regions nearest the cylinder's initial location ($\theta \approx 0^{\circ}$) and less so for the dye near the ends of the water bath ($\theta \approx 9.5^{\circ}$).

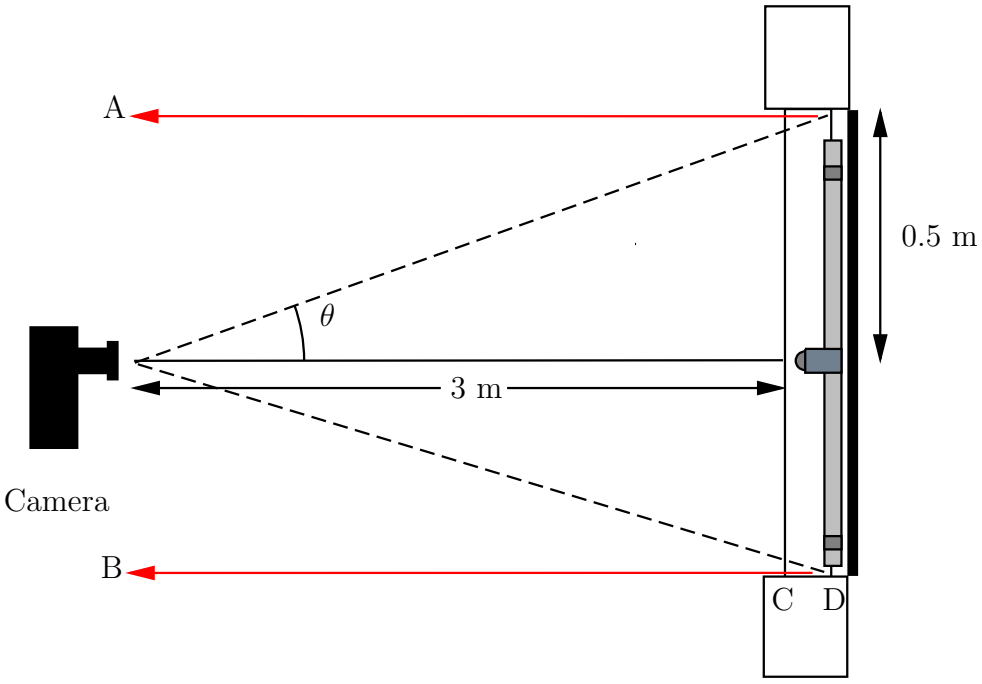

Figure 7.19: Camera parallax effects. The light from anywhere except the centre of the water-bath reaches the lens of the camera at a non-orthogonal angle, θ. The red lines indicate the path of the lightrays that should be observed. Locations A and B are camera locations that would remove parallax effects from the ends of the water-bath, while locations D and C correspond to the start and ends of a ray of light entering and existing the water-bath.

As the water-bath is 0.098 m wide, this is the distance that the light is *assumed* to pass through the dyed region, along a path that runs perpendicular from the backlight to the position of the camera. Taking one end of the water-bath as an example, for the ends of the water-bath this means that light is assumed to travel from D to C to B (see Figure 7.19). Due to parallax effects, light from the ends of the water-bath actually travels a distance of:

$$x = \frac{0.098 \text{ m}}{\cos(9.5^\circ)} = 0.099 \text{ m (3 dp)} \tag{7.5}$$

through the water-bath and at an angle θ to the camera, a difference of approximately 1%. The change in light intensity for light travelling through the water-bath, and its contents, from D to the camera obeys the Beer-Lambert law (Splinter and Hooper, 2006):

$$\frac{L_{cam}}{L_D} = e^{-fW} \tag{7.6}$$

where L is the light intensity, f is the dye absorbency, W is the width of the water-bath, and subscripts *cam* and D refer to the positions of the camera and location D, respectively. For weak concentrations, f may be assumed to be linear (Cendedese and Dalziel, 1998), so that the difference between the observed and actual light intensities for light having passed through the water-bath, L'_C and L_C respectively, is:

$$100 \times \left(\frac{L_C - L'_C}{L_C} \right) = 100 \times \left(\frac{e^{-0.098} - e^{-0.099}}{e^{-0.098}} \right) = 0.099\%. \tag{7.7}$$

A change in light intensity of this magnitude is not significant as a change in one shade of grey on the calibration curves (see Figure 3.5b) corresponds to a $\approx 0.39\%$ (1 in 256) change in light intensity.

To reduce the parallax effect, cameras could have been positioned in the same plane as the original camera at either ends of the water bath (locations A and B in Figure 7.19) so that multiple images could be compared, or the images could have been taken from further away to reduce the angle θ. Available resources prevented the use of three (or more) cameras while space in the laboratory made an increase in the distance between camera and water-bath not practical.

Model assumed to be isothermal

It was highlighted earlier that it is very difficult to match the necessary non-dimensional

parameters when taking thermal effects into account for water-bath models (see Section 3.1.1.1), consequently the models here are assumed isothermal.

The heat generated by the human thermal plume inevitably leads to buoyancy forces, which are not included. The relative importance of these buoyancy forces is determined from the Richardson number, Ri:

$$Ri = \frac{Gr}{Re^2} \tag{7.8}$$

where Gr is the Grashof number. Edge et al. (2005) calculated $Gr = 3.05 \times 10^8$ for a human, which gave $Ri = 0.109$, indicating that convection dominates the flow. Consequently, it is likely the that inclusion of thermal effects would not significantly change the results presented here, though they could be included in any of the presented CFD models.

7.4.2 Theoretical Model

One of the key simplifying assumptions in the image analysis method is that the dye concentration, C, is constant across the width of the tank for any pixel. This assumption greatly simplifies working as it removes the need to capture additional data relating to the dye profiles across the width of the water-bath. However, while the central mass of dye appears to be uniformly mixed across the tank for all time, nearer the edges of the cloud there typically exists wisps/strands of dye that are not. With the images obtained from the experiments, there is no way of distinguishing which regions of dye do, or do not, span the width of the water-bath. This is one reason why the mass conversation plots (see Figures 3.11 and 3.12) are subject to fluctuations. Further, this condition places a restriction on the initial conditions to those that were used here, namely that at the start of each experiment the dye is initially mixed to homogeneity in a region that spans the water-bath. Early attempts were made to quantify the concentrations of dye in similar experiments only with the dye initially introduced to the water-bath via a pipette. Doing so meant that the assumption of constant concentration across the width of the water-bath was severely violated, leading to erroneous mass conservation plots and data that did not represent the true distribution of the dye.

7.4.3 CFD Model

Run times.

One of the main limitations placed on all CFD simulations is the availability of computational resources. Here, the CFD simulations were carried out on the HPC facilities at the University of Leeds; more specifically, on the Advanced Research Computing (ARC) facility ARC2. This cluster is made up over 3,000 2.6 GHz processor cores, 6,000 GB of memory and 170 TB of storage space. However, the fair use policy employed on this system means only a fraction of these resources are available for any one user. A request for an increase in resources leads typically leads to a longer wait time. This means that to run a job on the optimum number of cores is not a trivial task.

Each simulation was set to run on a number of cores such that:

$$\frac{\text{Mesh size}}{\text{Number of cores}} \approx 100,000 \text{ to } 300,000, \tag{7.9}$$

though sometimes the number of cores requested was reduced so that a job would fit in the submission queue; it being better to have a job start immediately with slightly non-optimal resources than the job not starting for a significant number of hours/days.

The values in equation 7.9 are based on the author's own prior experience of CFX's parallel[1] performance in relation to mesh size. The majority of 3D simulations used the 514,560 cell mesh and were executed on 4 cores, which is in accordance with equation 7.9. Although this number of cores may not have necessarily been the optimum, it is expected to not be far from it.

Ideally, to assess the performance of each turbulence model, 3D CFD simulations would have been carried out for each experimental case. Based on the values given in Table 6.4, the 3D simulations took $\approx 0.7 - 3.5$ hours of processing time per 1 second of flow time, depending on turbulence model. If each experimental case were to be tested on just the four turbulences used for 60 seconds of flow time, which does not even guarantee reaching ωt^* for all cases, approximately 22,000 hours (909 days or 2.5 years) of computing time would be needed. The available resources could not possibly accommodate this over the time frame of this study, hence the small number of d and ω combinations modelled using CFD.

[1]Parallel in this case referring to the use of more than one processor core.

The convergence criteria of each CFD simulation affects both the accuracy of the solution and the overall run time. Ideally, the residual should be set as small as the solver will allow, 1×10^{-16} for 'double precision' mode in CFX, but practicality means this value is not used as the convergence criteria here. Table 5.1 showed how varying the convergence criteria by six orders of magnitude changed flow properties and the run time for the 2D simulations.

Boundary conditions

In a further effort to minimise the run time of CFD simulations, certain aspects of the flow need to be simplified. For the CFD models used in this study, one such simplifying assumption was the enforcing of a symmetry condition on the upper surface of the geometry, at the water's surface, H_{water} (see Figure 3.1). A more realistic approach to modelling the water-bath experiments would have been to make the geometry the same height as the water-bath, H_{tank}, and to model the interior as a combination of both water and air (as it was in reality). It was decided that modelling using only water and applying a symmetry condition was a valid approach, as long as the water level did not deviate too much from H_{water}, which it did not for all the experiments conducted here. However, while testing some of the larger diameter cylinders ($d = 40$ and 50 mm) in the water-bath, at speeds close to the actuators maximum (0.3 m s^{-1}), sloshing was noticed. These cases were not photographed or analysed because of the sloshing, but if they were to have been included, the symmetry condition applied in the CFD model would no longer be a valid assumption. The CFD model could also have easily had a wall boundary condition on the upper surface of the geometry, to be a closer representatation of a real corridor ceiling. However, a symmetry condition was chosen to keep the numerical model a closer representation of the physical water-bath.

The water-bath model was assumed to be isothermal. Heat effects were not taken into consideration based on the principles outlined in Section 7.4.1. Nevertheless, the flows resulting from the water-bath experiments were subject to some temperature conditions, obeying thermodynamic laws like everything else. The CFD simulations, however, *were* modelled isothermally, the energy equation was not solved and there was no change in fluid properties due to temperature. Although the temperature difference is likely to be insignificant here, where changes are assumed to be $O(1)$°C, the CFD model may have to revised to take thermal effects into account depending on any future applications.

Turb. Model	Advection	Mesh size ($\times 10^6$ cells)	ω (s^{-1})	Δt (s)	Flow Time (s)	CPU run time (hrs)
LES	CDS/HRS	0.5	0.2	0.0025	20	224
LES	CDS/HRS	3.5	0.2	0.0025	20	1,980

Table 7.4: Properties for the two CFD simulations using two different meshes.

Mesh size

The 514,560 cell mesh used for the 3D simulations was shown to still be slightly influential on the results, yet it was used as it offered similar rates of vortex-shedding to the finer meshes at a greatly reduced computational cost (see Table 6.1). A comparison between a solution obtained on this mesh and a much finer mesh, comprising 3.5×10^6 cells, is now presented.

The LES model has been chosen for this comparison as it is the one that is most reliant on mesh size. As the mesh size acts as a filter for resolvable length-scales (see Chapter 4), using two different sized meshes means that this turbulence model is more likely to show differences between solutions. Both simulations were set up to be identical in every way, except for the mesh they used. The settings chosen were the same as those presented in Section 6.4. The settings for the two simulations is presented in Table 7.4.

Figure 7.20 shows that the difference in solutions between the two meshes is small, when

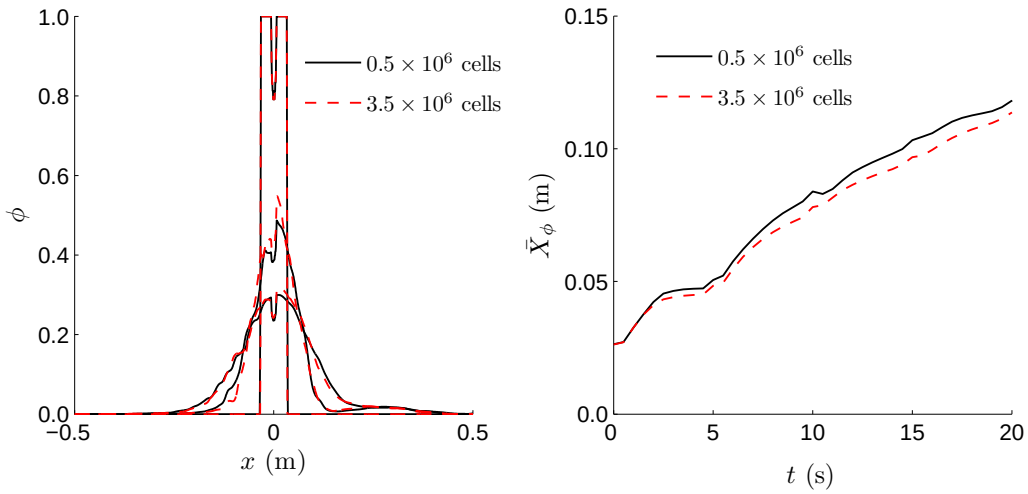

(a) (b)

Figure 7.20: (a) Profiles of ϕ for two different sized meshes at $t = 0, 10$ and 20 seconds. (b) Plots of $\bar{X}_\phi$ for $0 \leq t \leq 20$ ($\omega t = 4$).

comparing the transport properties of a scalar ϕ. The three profiles of ϕ shown in Figure 7.20a are hard to distinguish between, except at the peak of the reading at $\omega t = 2$. Plots of $\bar{X}_\phi$ reveal a slight difference between the two solutions, but the trends are still very much the same. By the end of the 20 seconds of simulation, the values of $\bar{X}_\phi$ are only separated by $\approx 3\%$. These plots reinforce the point made earlier in Chapter 6 that although properties relating to pressure may not agree between the mesh used and the finer meshes tested, the vortex shedding and subsequent scalar transport are very similar.

7.4.3.1 Finite Versus Infinite Cylinder

The CFD models aim to capture the important flow characteristics regarding scalar transport due to a translating cylinder in a channel. As the data from the water-bath experiments was used for comparison, the geometry of the CFD model closely resembled that of the water-bath. However, it must be stressed that it was not created to be an exact replica of the water-bath geometry, many simplifying assumptions were put in place: such as the symmetry condition and isothermal assumption. Arguably the most obvious difference between the two geometries is the difference between cylinder heights, H_{cyl}. So far, the CFD model has used an 'infinite' cylinder, with $H_{cyl} = H_{water} = 136$ mm. The implications from this assumption are now presented by comparing results to those offered by a CFD model created with a finite cylinder, with $H_{cyl} = 110$ mm, which represents a scenario more in line with people walking along a corridor (as most people's heads do not touch the ceiling).

The geometry used for the finite cylinder simulations is shown in Figure 7.21. The metal arm supporting the cylinder is not included as it was designed to have a very slender and aerodynamic profile, to impose a small influence on the fluid, and it is still assumed to

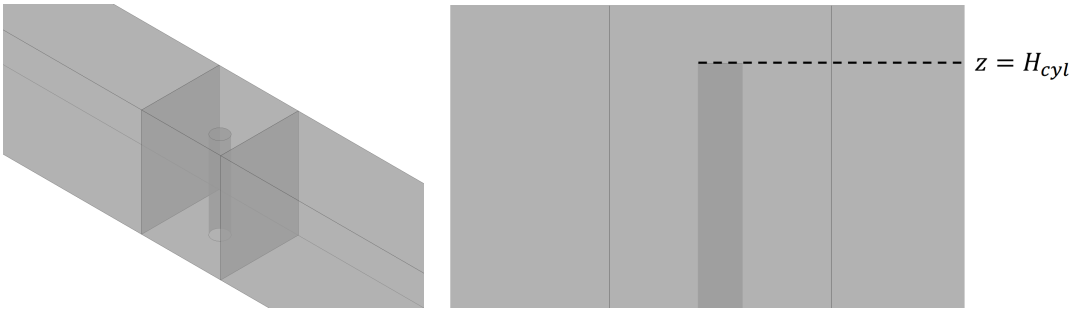

Figure 7.21: (a) Geometry used for simulations with a finite cylinder. (b) Close up view of the side of the geometry, clearly showing the gap between the cylinder and the top.

have such.

The mesh created for the finite cylinder geometry is no longer consistent between mesh layers. However, there are two distinct sections that do have identical x and y components. One for the mesh layers up to the height of the cylinder, $z \leq H_{cyl}$, and one above, $z > H_{cyl}$ (see Figure 7.22). The solutions obtained using the finite cylinder mesh used the same averaging 'through z' procedure described previously (see Section 6.4), only it was performed in two stages. Each mesh layer was first interpreted onto a 1,500 $\times$ 98 grid, as described in Section 5.4.3. Once the solution on each layer was interpreted onto this regular grid, they were then averaged through z, sidestepping the problem of non-constant (x, y) coordinates for all layers.

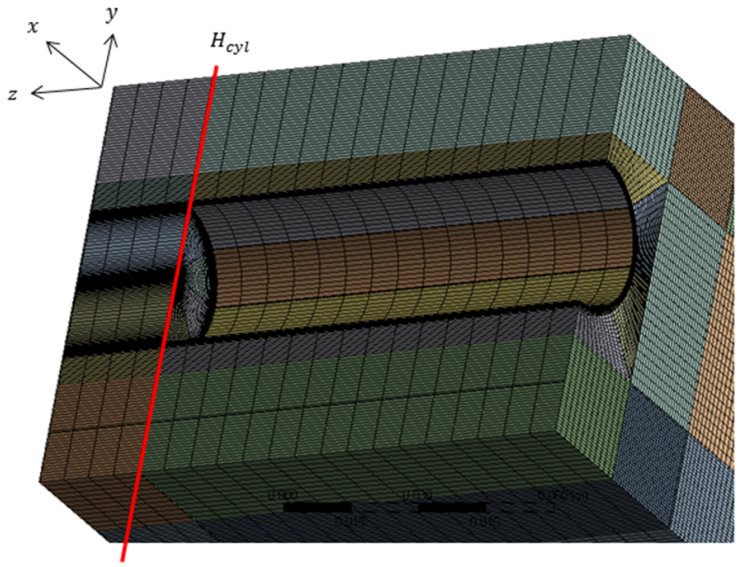

Figure 7.22: Slice through the mesh used for the finite cylinder simulations. Note the difference in mesh layers between those with $z \leq H_{cyl}$, and those with, $z > H_{cyl}$.

Results

Four different d and ω combinations were tested to investigate the difference between the finite and infinite cylinder. To be able to investigate the influence of the cylinder height on the transport of the scalar ϕ, the finite cylinder simulations were set up with boundary and initial conditions identical to their infinite cylinder counterparts (see Section 6.4.4), with the only difference being the geometry/mesh. An overview of the simulations is presented in Table 7.5.

Figure 7.23 shows how the centre of mass of the scalar, $\bar{X}_\phi$, differ between the four finite cylinder simulations and the infinite cylinder versions. All four plots show significant

Turb. Model	Advection scheme	d (m)	ω (s^{-1})	Δt (s)	Flow Time (s)
SST	HRS	0.01	0.200	0.01	30
SST	HRS	0.02	0.054	0.01	30
SST	HRS	0.02	0.200	0.01	30
SST	HRS	0.0335	0.132	0.01	30

Table 7.5: Properties for the four CFD simulations using finite cylinder geometries and meshes.

differences between the pairs of solutions. The shape of the two plots is comparable in each case. All four cases show reasonable agreement between the pairs of models for a short period ($< \omega t \approx 1$), but in all cases the finite cylinder eventually appears to over predict the rate of transport of ϕ.

Looking at the average ϕ values on Planes 1, 2 and 3 (see Section 6.4.3), Figures 7.24 and 7.25 show that despite differences in bulk transport, both approaches are still able offer similar predictions. The shape of the planar averages is very similar between finite and infinite cylinder predictions, as is the point at which the scalar becomes non-zero for Planes 2 and 3.

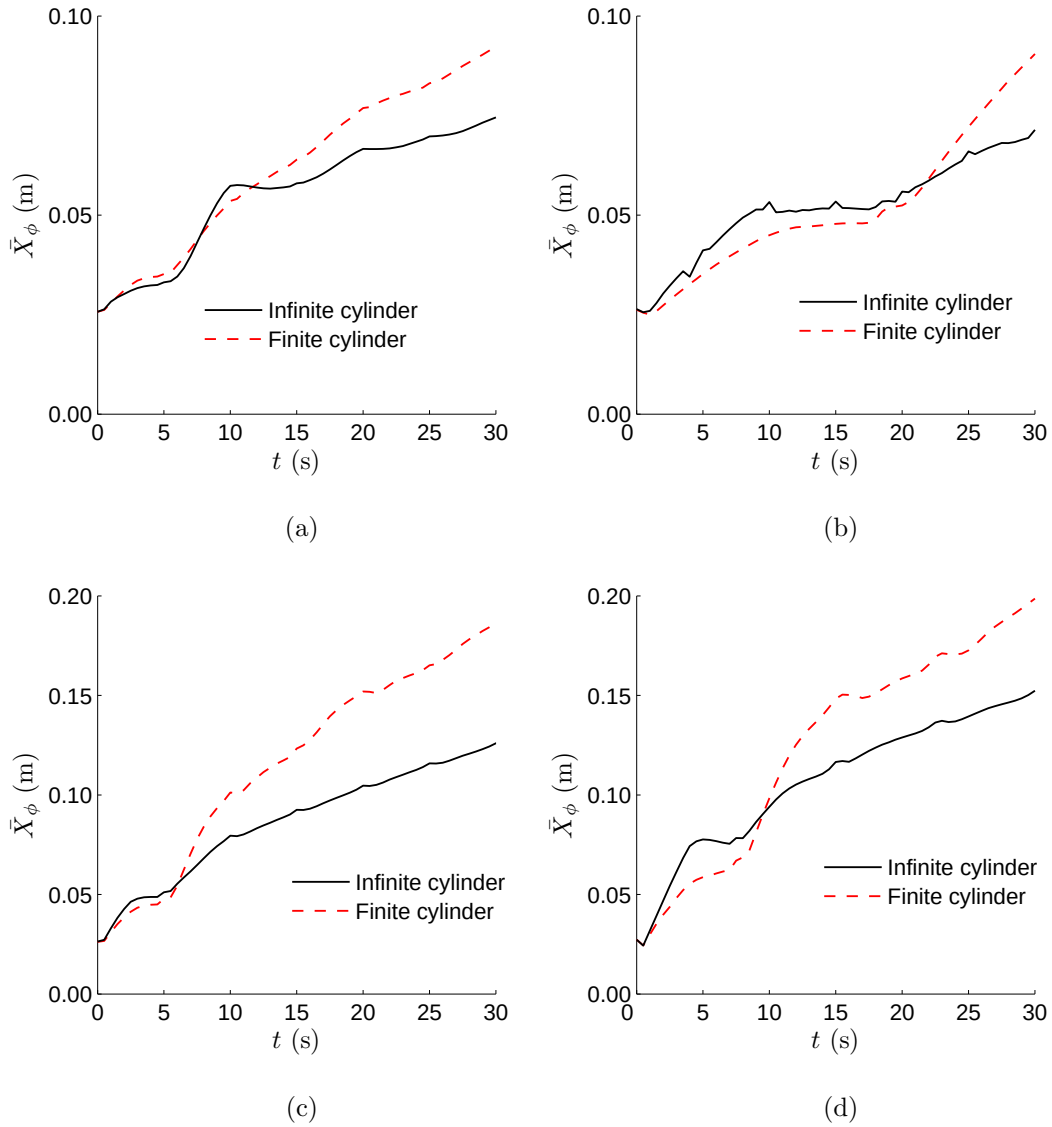

Figure 7.23: Plots of $\bar{X}_\phi$ over time using the finite cylinder geometry for: (a) $d = 0.01$ m, $\omega = 0.200$ s^{-1}; (b) $d = 0.02$ m, $\omega = 0.054$ s^{-1}; (c) $d = 0.02$ m, $\omega = 0.200$ s^{-1}; (d) $d = 0.0335$ m, $\omega = 0.132$ s^{-1}.

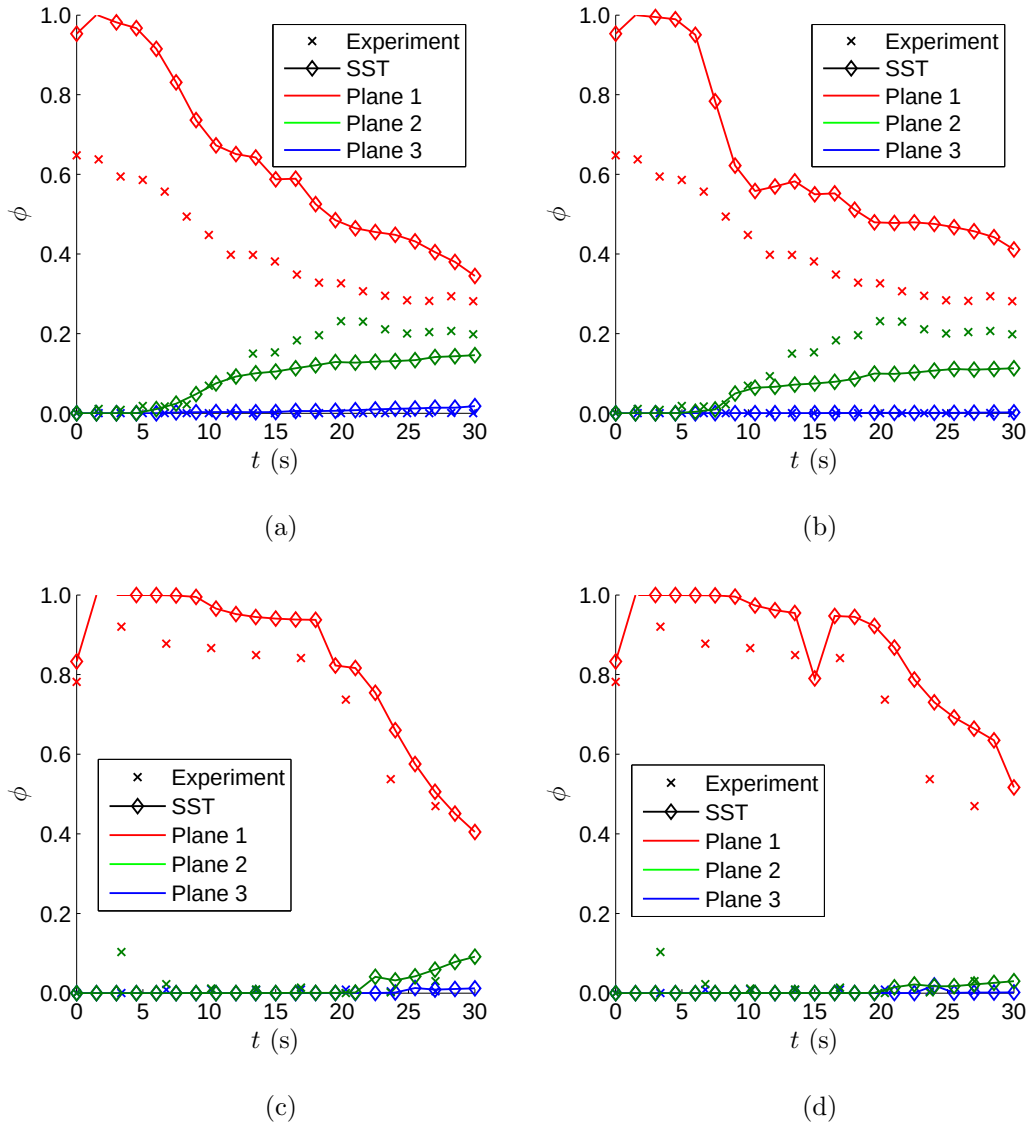

Figure 7.24: Comparison between average ϕ values from CFD simulations and average, normalised dye concentrations on Planes 1, 2 and 3. Line colours and markers determined by the combination of Plane colour and source of data. (a) $d = 0.01$ m, $\omega = 0.200$ s^{-1} - finite cylinder (b) $d = 0.01$ m, $\omega = 0.200$ s^{-1} - infinite cylinder (c) $d = 0.02$ m, $\omega = 0.054$ s^{-1} - finite cylinder (d) $d = 0.02$ m, $\omega = 0.054$ s^{-1} - infinite cylinder.

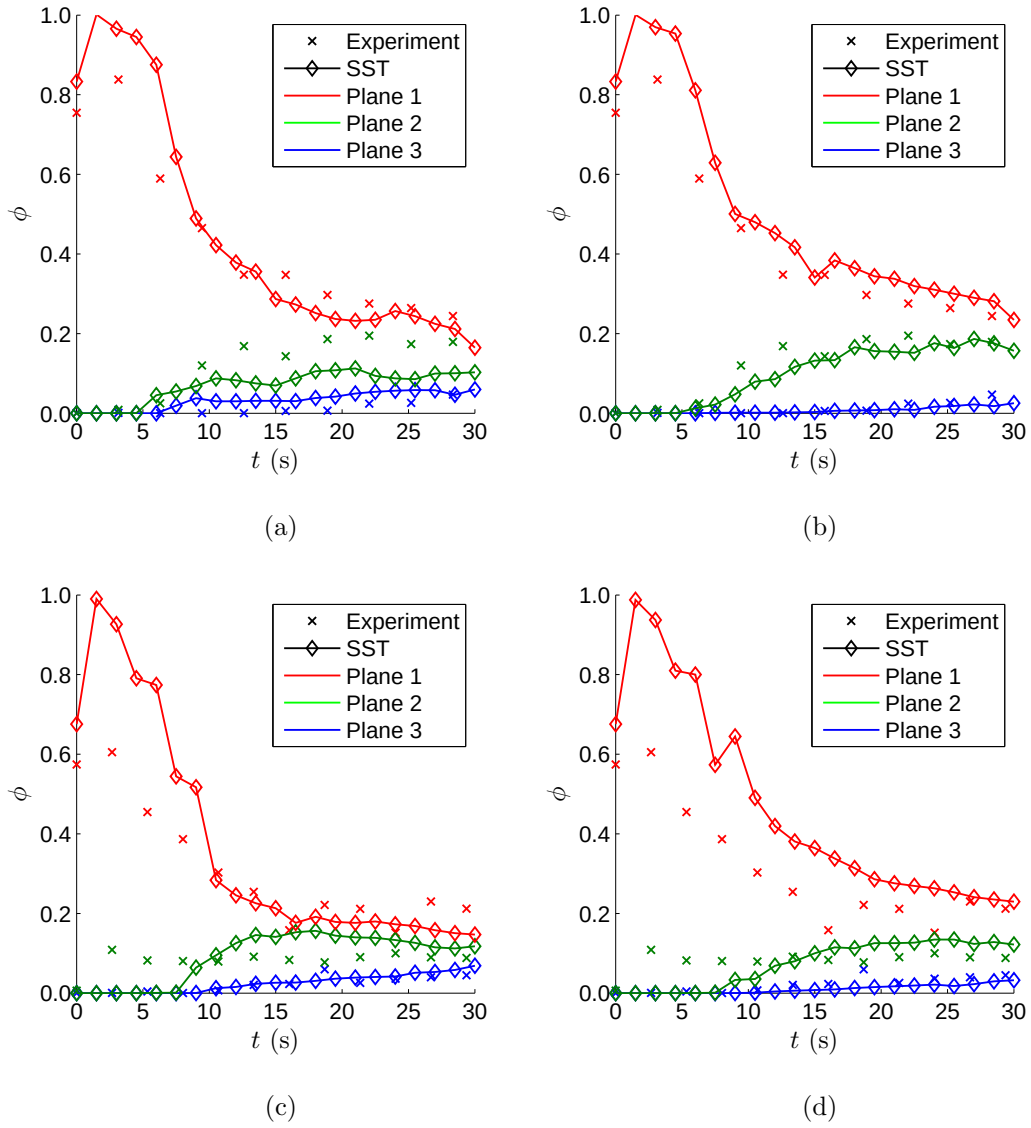

Figure 7.25: Comparison between average ϕ values from CFD simulations and average, normalised dye concentrations on Planes 1, 2 and 3. Line colours and markers determined by the combination of Plane colour and source of data. (a) $d = 0.02$ m, $\omega = 0.200$ s^{-1} - finite cylinder (b) $d = 0.02$ m, $\omega = 0.200$ s^{-1} - infinite cylinder (c) $d = 0.0335$ m, $\omega = 0.132$ s^{-1} - finite cylinder (d) $d = 0.0335$ m, $\omega = 0.132$ s^{-1} - infinite cylinder.

Chapter 8

Conclusions and Further Work

Contents

This final chapter brings together the findings of the previous chapters and relates them back to the aims and objectives set out at the beginning of the study. Conclusions are drawn based on the findings of the individual chapters. An overview of the implications from all modelling approaches is presented, highlighting the significance of the study as a whole. To end, a range of topics that could be considered as future work, or extensions of this study, are presented.

8.1 Conclusions

This study investigated the effects of a translating cylinder on the dispersion of a passive scalar by employing physical, theoretical and numerical models. Although of interest in their own right, these models were developed to investigate the infection risk of people located in a hospital corridor and the influence of human movement. Both numerical and theoretical models were validated against the experimental data, ensuring that predictions in this study are meaningful. These models were applied to various scenarios at the full-scale to highlight differences in infection risk depending upon a person's location and duration within a hospital corridor containing the release of an airborne contaminant.

The key findings of this study are presented based on the chapter in which the information was presented. It is also highlighted which objective the key finding relates to, based on the aims and objectives presented in Section 1.5.

Water-Bath Modelling

- An image-analysis technique was developed, based on a previous method developed by Cenedese and Dalziel (1998), which allowed for the quantification of dye concentrations in time and space when using non-homogeneous light sources. The square cell-based averaging method applied by previous authors was adapted to take into account more arbitrary shapes of non-homogeneity using a Gaussian low-pass filter. This was shown to be an accurate technique to track the dye. [Objective 2i].

- The water-bath modelling approach is shown to be capable of providing quantitative, not just qualitative, data relating to contaminant transport. To the author's knowledge, this is the first time that the method has been used to obtain quantitative data when using a moving body. Particularly noteworthy is that even with a portion of the geometry and contaminant hidden, by applying simple estimation techniques, the concentration of the fluid that is occluded can be calculated accurately. [Objective 2ii].

- Two theoretical models are proposed to model the mixing/dispersion of a scalar in a channel. These models show that the dominant factors responsible for the mixing of a scalar in a channel, by a circular cylinder, are the cylinder diameter, translation

amplitude and translation frequency. Specifically, the transport of such a scalar was found to depend upon the square root of the product of the cylinder diameter, translation amplitude, translation frequency and elapsed time. [Objective 2iii].

2D CFD Modelling of Water-Bath Experiments

- A two-dimensional CFD model, with a geometry bearing close resemblance to the water-bath used in the experiments, was able to identify which turbulence models were suitable for the three-dimensional CFD models to follow. The results from the Shear Stress Transport (SST) model showed a performance in excellent agreement with the experimental data and was proposed as the most suitable. [Objectives 3i & 3ii].

- The dynamic meshing method employed during the moving model simulations was shown to create meshes capable of capturing the eddy shedding and subsequent complex features often produced by flows around circular cylinders. Despite constantly changing, the meshes allowed for the prediction of scalar transport in good agreement with experimental data. [Objective 3i]

3D CFD Modelling

- A three-dimensional CFD model, with a geometry bearing close resemblance to the water-bath used in the experiments, was found to be capable of simulating the transport of a passive scalar, ϕ, in agreement with comparable data for the transport of food dye in a water-bath. Although previous studies have used CFD to show similar qualitative patterns and trends to water-bath experiments, to the author's knowledge this is the first time that a quantitative comparison has been made between the two, when concerning contaminant concentrations in a hospital corridor. The work demonstrates that CFD can be reliably used to predict the transport of a scalar due to a moving body in a channel. [Objective 3i].

- For the cylinder diameter and translation frequency combination investigated using four turbulence models, $d = 20$ mm and $\omega = 0.2\ \mathrm{s}^{-1}$, the SST model offered results in closest agreement with the experimental data and at $\approx 70\%$ reduced computational cost when compared to SAS, DES and LES models. [Objective 3ii].

- The SST model was able to offer good predictions for the transport of a passive scalar under the influence of a translating cylinder across eight d and ω combinations (see

table 6.5), when compared to the experimental data. It is recommended that the SST models should be chosen for CFD models that investigate moving cylindrical bodies in a channel. [Objective 3ii].

- Despite being the most commonly used in industrial applications, including indoor airflows, the $k-\epsilon$ model is shown to be inferior to the SST, SAS, DES and LES turbulence models, for the flows modelled in this study. It is concluded that the $k-\epsilon$ model is not suitable for investigations that are concerned with the accurate prediction of eddy-shedding or similar wake features produced from the flow around a cylindrical body in a channel. [Objective 3ii].

Modelling Infection Risk

- The time-scale (1:13) and length-scale (1:15) relations applied in this study, when considering changes in viscosity and density of the fluid, were shown to be correct when applied to the CFD simulations. As a result, the water-bath model data and resulting theoretical models can be interpreted at different length-scales with a high degree of confidence.

- By applying a one-way 'plug flow' to a simulated corridor, it was found that a contaminant is quickly removed from a corridor space. However, the wake of a cylinder is still capable of transporting contaminant against the direction of the flow. The flow rate used was representative of a ventilation rate of 6 ACH, but the ensuing flow is likely to be much more uniform than the kinds of flows experienced in a real corridor. That is to say, the 'ventilation' applied here in this study is probably removing a contaminant faster than a real ventilation system is likely to, yet still some contaminant is transported upstream. [Objective 4i].

- When a scalar is initially located at the end of the translation stroke, it is still able to be transported to the opposite end of the stroke quickly. Although for the CFD simulation presented the scalar was present at the other end of the corridor in small concentrations, if the scalar were to be interpreted as a concentration of a highly infectious disease, such as TB or measles, small concentrations may still be enough for infection. [Objective 4i].

- By interpreting the scalar concentration as quanta of an infectious disease and using a simplified breathing model it was shown that assuming a well-mixed contaminant

concentration in a space can both over and under predict a person's infection risk when compared to a model that takes into account temporal and spatial variations, like the models presented in this study. [Objective 4ii].

8.2 Implications of Results

This study has demonstrated that it is possible to quantify the effect of a moving body on the dispersion of a contaminant in a water-bath. It has also demonstrated that CFD models, particularly those employing the SST turbulence model, are able to predict the transport of a scalar due to a moving body in good agreement with experiments.

The water-bath results showed that a contaminant can be quickly transported beyond the ends of a corridor. In the case of the larger cylinders, this occurred as soon as 4 or 5 traverses of the water-bath had been completed. It is clear from the results that an increase in speed and cylinder diameter transported the contaminant faster.

With changes in time and length-scale acknowledged, CFD simulations showed that the water-bath model results can be representative of full-scale flows for people moving in a corridor. Interpreting model solutions at the full-scale, it is probable that human wakes are able to transport an airborne contaminant a significant distance down a hospital corridor, even in the presence of a ventilation system exhibiting 6 ACH.

Current guidelines for UK hospitals recommend 6 ACH for general wards (Department of Health, 2007). There is no specific rate recommended for corridors and it is likely that many are ventilated below 6 ACH. The research presented in this study has shown that ventilating at 6 ACH may be insufficient to eliminate the contribution from human movement on the transport of an airborne contaminant in a ventilated corridor. This, in turn, suggests that any calculations made in quantifying the infection risk of a person in a ventilated space need to consider people's movements, if an accurate value is to be sought. This may be particularly important in areas of hospitals where the risk or consequence of airborne infection is high.

8.3 Further Work

Every aspect of this study was conducted thoroughly based on the techniques and time available. Nevertheless, certain areas of the study would benefit through the implementation of additional or alternative methods.

The cylinders used in the water-bath experiments are clearly not able to capture the intricate details of limb shape or movement. Introducing these features to the cylinder, or modelling with a figurine, would clearly make the water-bath experiments a better geometrical representation of a person walking in a corridor[1]. This figurine could also be heated to model the thermal plume of a person, adding buoyancy effects to the model. Although it is difficult to achieve the balance of the various non-dimensional parameters when conducting water-bath experiments with elements of heat transfer (Chen, 2009), should the correct balance of parameters be found, implementing a heating element to the cylinders is not too difficult a task. Thermal plume effects are likely to be dominated

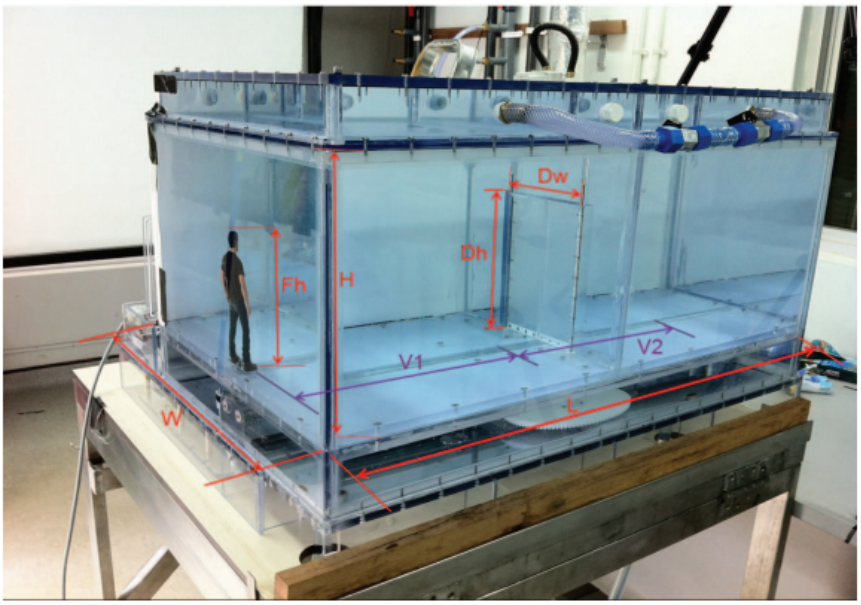

Figure 1.2b: Experimental apparatus used by Tang et al. (2013) with actuator situated underneath the fully enclosed water-bath, allowing for image capture from above (repeated from page 12).

[1]Water-bath experiments were actually carried out that used a figurine in place of the cylinder. Although similar dye transport behaviour was observed, quantifying the dye concentration in these experiments was not possible due to the lack of calibration data for this setup with a raised water level, necessary to accommodate the figure's increased height when compared to the cylinders. Consequently this data is not analysed and is not presented in the study.

by the wake of the figurine, however modelling them would help determine whether the human thermal plume increases or decreases the mixing of an airborne contaminant.

The initial dye region was well mixed throughout the water-bath so that the assumption of a constant dye concentration was applicable. If the dye was released as a point source, this would help determine how a cough or sneeze is mixed soon after its release. Some early experiments were conducted with an initial release closer to a point source, introduced through a pipette, though were not suitable for quantification as the side on images could not take account of the dye spreading across the tank. However, quantifying a point release could be achieved when partnered with image-capturing from above the water-bath. As highlighted in Section 7.4.1, efforts were made to capture images from above the water-bath but these were not consistent enough to obtain quantitative data on the food dye concentration. To capture images from above the water-bath would need to be redesigned to include a lid, to remove the water's free-surface. Additionally, the linear actuator would need to be relocated to the underside of the water-bath to leave the view from above free from obstruction. Tang et al. (2013) included these two changes to their water-bath, showing that the capabilities are in place to allow for image-capture from above (see Figure 1.2b). Image capture from above would also help determine at

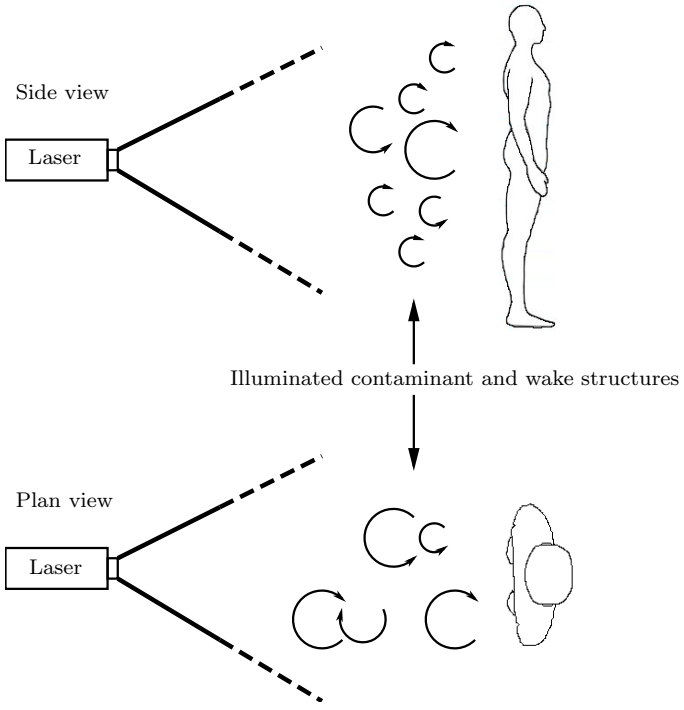

Figure 8.2: Potential experimental setup for laser and smoke experiment. By passing a mannequin or person through a gaseous visualising agent, illuminated by a laser 'sheet', information relating to the transport of a contaminant and wake structure could be obtained.

what times and locations the assumption of constant dye concentration across the width of the water-bath is suitable, further improving the accuracy and validity of the theoretical model put forward in this study.

With the aforementioned improvements to the experimental modelling procedure in place, the water-bath model would be an even closer representation of a full-scale scenario. To ensure that this is the case, full-scale validation data could be captured. Full-scale data could be obtained by releasing smoke, or a similar visualising tracer, in a corridor and subjecting it to either people walking or a mannequin passing through it. A laser focussed in one place could then be shone along the wake of the person, or mannequin, to identify the transport of the gas as well as the eddy structure of the wake (see Figure 8.2). Even if the degree to which this was quantifiable was not to the same high-quality standard as that of the water-bath and CFD modelling conducted here, it could provide a good approximation as to whether the rates of transport predicted in this study are likely or possible.

All these improvements could then be brought together in a more complete airborne contaminant transport model by taking into account real building layouts, which would benefit the design of any hospitals (or other corridor networks) in the future. Modelling a single corridor is a natural starting point, however this is only representative of a

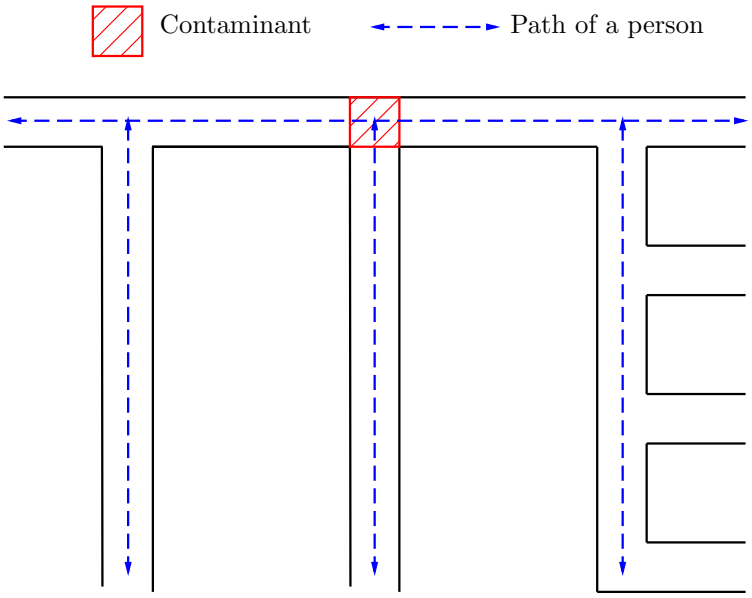

Figure 8.3: Sketch of a network of corridors that could be investigated, with an initial release indicated by the red-hatched square and human paths marked by the blue, dashed lines.

very small section of a hospital and not a ward or building. Although the findings are meaningful and have implications at the full-scale, they could be developed by looking at a network of corridors and traffic distributions that are much closer to a real healthcare building. During the early stages of the water-bath modelling, data was obtained that looked at the transport of the dye when initially located asymmetrically in the water-bath. This included testing when the dye was located at the very ends of the water bath. If asymmetric initial dye locations were investigated in the same detail as those presented here, a model could then be established which takes into account a network of corridors, such as that shown in Figure 8.3. Once turbulent diffusion coefficients, D_t, are obtained for cases with initially asymmetric contaminant locations, a zonal model could be created which takes into account the concentrations in other corridors. This model could then be adapted to take into account a less regular pattern of translation or movement. This could be performed by adjusting the linear actuator's controls by hand, but a more repeatable and thorough method of adjusting the potentiometer could be achieved by implementing hardware controlling software, such as Simulink, where more realistic human traffic patterns could be applied and investigated.

Appendices

Appendix A

A selection of scripts that were used in this study are given on the attached CD. The CD by no means contains all the scripts used during this study, but a selected sample of some of the most important. Below is a brief description of what each of these scripts does. Files with no extension are bash scripts, .m extensions are read by MATLAB, .c by C, and .cse by CFDpost.

`Script name`	Description
`analysis.m`	An example of the kind of script used to analyse experimental images to obtain dye concentration values used in calculation of C and $\bar{X}$.
`breathing_profile.m`	M-file read by `infection_risk.m` to implement different breathing profiles based on equation 7.2.
`calibration.m`	Calibration script run prior to `analysis.m`. Relates light intensity to dye concentration, to obtain images like those seen in Figure 3.5.
`cfd_all_in_one.m`	Uses .csv files output from `csv_exporting` to obtain averaged ϕ profiles from CFD simulations, corresponding $\bar{X}_\phi$ values, and data necessary for making the contour plots. Only applicable for the 'infinite cylinder' cases.
`csv_exporting`	Parent script that creates a .cse file (used by CFDpost) to output the .csv files used for analysis of the CFD simulations, calling on `csvLoop` and `csvBaseFile.cse`.
`csvBaseFile.cse`	The .cse file adapted by `csv_exporting` that, once combined with the output of `csvLoop`, is used to obtain .csv files containing ϕ data from CFD simulations.

`csvLoop`	File amended, and looped over, by `csv_exporting`. The amended version is attached to the end of `csvBaseFile.cse`.
`cylinder_movement.c`	Early implementation of cylinder movement in Fluent using a user-defined function (UDF).
`finite_cylinder.m`	Same as `cfd_all_in_one.m`, only used for the finite cylinder cases.
`gauss_script.m`	Uses `gaussfit.m` to obtain values of least squares fitted variables to a data set using the `lsqcurvefit` MATLAB function.
`gaussfit.m`	Function fitted to experimental data by `gauss_script.m`.
`gaussian_cfd.m`	Parent m-file, employing `gauss_script.m`, to obtain properties relating to the fitting of equation 3.12 to experimental data stored in .csv format.
`infection_risk.m`	M-file used to calculate infection risk based on the simple scenario put forward in Section 7.2.
`mAtlab`	Example of a batch submission script for a MATLAB job.
`postrun3D.cse`	.cse file used to output .csv files that contain information relating to C_D, C_L, St and C_{pb}.
`strouhal.m`	MATLAB script used to read in .csv files holding pressure data - used to calculate values of C_D, C_L, St and C_{pb}.
`time_modulo.m`	Testing, and plotting, of modulo function used to implement necessary cylinder translation in CFX.

Bibliography

Abbey, H. (1952). An Examination Of The Reed-Frost Theory Of Epidemics. *Human Biology*, 24(32):201–233.

Adrian, R. J. and Balachandar, S. (1999). Mechanisms For Generating Coherent Packets Of Hairpin Vortices In Channel Flow. *Journal Of Fluid Mechanics*, 387:353–396.

Anderson, J. D. (1995). *Computational Fluid Dynamics: The Basics With Applications*. Mcgraw-Hill Higher Education.

ANSYS, Inc. (2012a). ANSYS CFX. *ANSYS®Academic Research, Release 14.5*.

ANSYS, Inc. (2012b). ANSYS Fluent. *ANSYS®Academic Research, Release 14.5*.

ANSYS, Inc. (2012c). Help System: ANSYS CFX-Solver Theory Guide. *ANSYS® Academic Research, Release 14.5*.

ANSYS, Inc. (2012d). Help System: ANSYS Meshing User's Guide. *ANSYS® Academic Research, Release 14.5*.

Armstrong, T. W. and Haas, C. N. (2007). A Quantitative Microbial Risk Assessment Model For Legionnaires' Disease: Animal Model Selection And Dose-Response Modeling. *Risk Analysis*, 27(6):1581–1596.

ASHRAE (2013). ASHRAE Standard 170-2013: Ventialtion Of Health Care Facilities.

Bachelor, G. K. (1967). *An Introduction To Fluid Dynamics*. Cambridge University Press.

Bain, R., Cronk, R., Hossain, R., Bonjour, S., Onda, K., wright, J., Yang, H., Slaymaker, T., Hunter, P., Prüss-Ustün, A., and Bartram, J. (2014). Global Assessment Of Exposure To Faecal Contamination Through Drinking Water Based On A Systematic Review. *Tropical Medicine And International Health*, 19(8):917–927.

Barrett, K. E., Barman, S. M., Boitano, S., and Brooks, H. L. (2012). *Ganong's Review Of Medical Physiology*. McGraw Hill, 24th edition.

Beggs, C. B. (2003). The Airborne Transmission Of Infection In Hospital Buildings: Fact Or Fiction. *Indoor and Built Environment*, 12:9–18.

Beggs, C. B., Kerr, L. G., Noakes, C. J., Hathway, E. A., and Sleigh, P. A. (2008). The Ventilation Of Multiple-Bed Hospital Wards: Review And Analysis. *American Journal Of Infection Control*, 36:250–259.

Beggs, C. B., Noakes, C. J., Shepherd, S. J., Kerr, K. G., Sleigh, P. A., and Banfield, K. (2006). The Influence Of Nurse Cohorting On Hand Hygiene Effectiveness. *American Journal Of Infection Control*, 34(10):621–626.

Beggs, C. B., Noakes, C. J., Sleigh, P. A., Fletcher, L. A., and Siddiqi, K. (2003). The Transmission Of Tuberculosis In Confined Spaces: An Analytical Review Of Alternative Epidemiological Models. *International Journal Of Tuberculosis And Lung Disease*, 7(11):1015–1026.

Bjorn, E. and Nielsen, P. V. (2002). Dispersal Of Exhaled Air And Personal Exposure In Displacement. *Indoor Air*, 12:147–164.

Blachere, F. M., Lindsley, W. G., Pearce, T. A., Anderson, S. E., Fisher, M., Khakoo, R., Meade, B. J., Lander, O., Davis, S., Thelis, R. E., Celik, I., Chen, B. T., and Beezhold, D. H. (2009). Measurement Of Airborne Influenza Virus In A Hospital Emergency Department. *Clinical Infectious Diseases*, 48(4):438–440.

Bloch, A. B., Orenstein, W. A., Ewing, W. M., Spain, W. H., Mallison, G. F., Herrmann, K. L., and Hinman, A. R. (1985). Measles Outbreak In A Pediatric Practice: Airborne Transmission In An Office Setting. *Pediatrics*, 75(4):676–683.

Bohne, J. E. and Cohen, B. S. (1985). Aerosol Resuspension From Fabric: Implications For Personal Monitoring In The Beryllium Industry. *American Industrial Hygiene Association Journal*, 46:73–79.

Boulic, R., Thalman, N., and Thalmann, D. (1990). A Global Human Walking Model With Real-Time Kinematic Personification. *The Visual Computer*, 6(6):344–358.

Bourouiba, L., Dehandschoewercker, E., and Bush, J. W. M. (2014). Violent Expiratory Events: On Coughing And Sneezing. *Journal Of Fluid Mechanics*, 745:537–563.

Boussinesq, J. (1887). Essai Sur La Théorie Des Eaux Courantes. *Mémoires Présentés Par Divers Savants À L'Académie Des Sciences XXIII, (1)*.

Brachman, P. S. (1970). Nosocomial Infection - Airborne Or Not? *Proceedings Of The International Conference On Nosocomial Infections. American Hospital Association*, pages 189–192.

Brauer, F. (2005). The Kermack-McKendrick Epidemic Model Revisited. *Mathematical Biosciences*, 198:119–131.

Braza, M., Perrin, R., and Hoarau, Y. (2006). Turbulence Properties In The Cylinder Wake At High Reynolds Numbers. *Journal of Fluids and Structures*, 22:757–771.

Breuer, M. (1998). Large Eddy Simulation Of The Subcritical Flow Past A Circular Cylinder: Numerical And Modeling Aspects. *International Journal For Numerical Methods In Fluids*, 28:1281–1302.

Brohus, H., Balling, K. D., and Jeppesen, D. (2006). Influence Of Movements On Contaminant Transport In An Operating Room. *Indoor Air*, 16:356–372.

Buttner, M. P., Cruz-Perez, P., Stetzenbach, L. D., Garrett, P. J., and Luedtke, A. E. (2002). Measurements Of Airborne Fungal Spore Dispersal From Three Types Of Flooring Materials. *Aerobiologia*, 18(1):1–11.

CD-adapco (2004). STAR CCM+. www.cd-adapco.com/products/star-ccm. Accessed: 23rd April 2015.

CDC (2005). Guidelines For Preventing Transmission Of Myobacterium Tuberculosis In Health-Care Settings, 2005. *Morbidity And Mortality Weekly Report*, 54:1–142.

Celik, B. and Beskok, A. (2009). Mixing Induced By A Transversely Oscillating Circular Cylinder In A Straight Channel. *Physics Of Fluids*, 21:073601.

Cendedese, C. and Dalziel, S. (1998). Concentration And Depth Fields Determined By The Light Transmitted Through A Dyed Solution. *Unpublished - though often cited.*

Cenedese, C. and Dalziel, S. (1998). Concentration And Depth Fields Determined By The Light Transmitted Through A Dyed Solution. *Proceedings of the 8th International Symposium On Flow Visualization.*

Centers for Disease Control (1988). Perspectives In Disease Prevention And Health Promotion Update: Universal Precautions For Prevention Of Transmission Of Human Immunodeficiency Virus, Hepatitis B Virus, And Other Bloodborne Pathogens In Health-Care Settings. *Morbidity And Mortality Weekly Report*, 37(24):377–388.

Centers for Disease Control (2007). 2007 Guidelines For Isolation Precautions: Preventing Transmission Of Infectious Agents In Healthcare Settings. *American Journal of Infection Control*, 35.

Centers for Disease Control (2014). CDC Estimates of Foodborne Illness in the United States. http://www.cdc.gov/foodborneburden/2011-foodborne-estimates.html. Accessed 29th July 2015.

cfd-online (2015). Codes. http://www.cfd-online.com/Wiki/Codes. Accessed 10th August 2015.

Chakrabarti, S. K. (1987). Hydrodynamics Of Offshore Structures. *WIT Press*.

Chao, C. H., Wan, M. P., Morawska, L., Johnson, G. R., Ristovski, Z. D., Hargreaves, M., Mengersen, K., Corbett, S., Li, Y., Xie, X., and Katoshevski, D. (2009). Characterization Of Expiration Air Jets And Droplet Size Distributions Immediately At The Mouth Opening. *Aerosol Science*, 40:122–133.

Chartier, J. A. Y., Pessoa-Silva, C. L., Jensen, P., Li, Y., and Seto, W. H. (2009). *Natural Ventilation For Infection Control In Health-Care Settings*. World Health Organization.

Chen, Q. (2009). Ventilation Performance Prediction For Buildings - A Method Overview And Recent Applications. *Building And Environment*, 44:848–858.

Choi, J. and Edwards, J. (2008). Large Eddy Simulation And Zonal Modeling Of Human-Induced Contaminant Transport. *Indoor Air*, 18:233–249.

Choi, J. I. and Edwards, J. R. (2012). Large Eddy Simulation Of Human-Induced Contaminant Transport In Room Compartments. *Indoor Air*, 22:77–87.

Chow, T. T., Lin, Z., and Bai, W. (2006). The Integrated Effect Of Medical Lamp Position And Diffuser Discharge Velocity On Ultra-Clean Ventilation Performance In An Operating Theatre. *Indoor And Built Environment*, 15:315–331.

Chow, T. T. and Yang, X. Y. (2005). Ventilation Performance In The Operating Theatre Against Airborne Infection: Numerical Study On An Ultra-Clean System. *Journal Of Hospital Infection*, 59:138–147.

Clay Mathematics Institute (2000). The Millenium Prize Problems Website. http://www.claymath.org/millennium-problems/millennium-prize-problems. Accessed 31st October 2014.

Cohen, L. S. and Director, M. N. (1975). Transport Processes In The Two-Dimensional Near Wake. *The American Institute of Aeronautics and Astronautics Journal*, 13(8):969–970.

Coia, J. E., Ritchie, L., Adisesh, A., Booth, C. M., Bradley, C., Bunyan, D., Carson, G., Fry, C., Hoffman, P., Jenkins, D., Phin, N., Taylor, B., Nguyen-Van-Tam, J. S., Zuckerman, M., and Healthcare Infection Society Working Group on Respiratory and Facial Protection (2011). Guidance On The Use Of Respiratory And Facial Protection Equipment. *PLoS ONE*, 6(6).

Craven, B. A. (2014). Design Of A High-Throughput Chemical Trace Detection Portal That Samples The Aerodynamic Wake Of A Walking Person. *Sensors*, 14(6):1852–1866.

Craven, B. A. and Settles, G. S. (2006). A Computational And Experimental Investigation Of The Human Thermal Plume. *Journal of Fluids Engineering*, 128:1251–1258.

Crowe, C. T., Troutt, T. R., and Chung, J. N. (1996). Numerical Models For Two-Phase Turbulent Flows. *Annual Review Of Fluid Mechanics*, 28:11–43.

Dai, L. and Jazar, R. N. (2012). *Nonlinear Approaches In Engineering Applications*.

Dalton, N. (2013). A Comparison Of Cardiovascular Responses During Walking And Jogging On The Treadmill With And Without Handrail Support. *Journal Of Exercise Physiology Online*, 16(1):64–71.

Darrigol, O. (2002). Between Hydrodynamics And Elasticity Theory: The First Five Births Of The Navier-Stokes Equation. *Archive For History Of Exact Sciences*, 56(2):95–150.

Deller, S., Mascher, F., Platzer, S., Reinthaler, F. F., and Marth, E. (2006). Effect Of Solar Radiation On Survival Of Indicator Bacteria In Bathing Waters. *Central European Journal For Public Health*, 14(3):133–137.

Department of Health (2001). The Epic Project: Developing National Evidence-Based Guidelines For Preventing Healthcare Associated Infections. Phase 1: Guidelines For Preventing Hospital-Acquired Infections. *Journal of Hospital Infection*, 47.

Department of Health (2007). Health Technical Memorandum 03-01: Specialised Ventilation For Healthcare Premises.

Department of Health (2014). epic3: National Evidence-Based Guidelines For Preventing Healthcare Associated Infections In NHS Hospitals In England. *Journal of Hospital Infection*, 86.

Department Of Health (2014). The Use Of Facemasks And Respirators During An Influenza Pandemic: Scientific Evidence Base Review.

Després, V. R., Huffman, J. A., Burrows, S. M., Hoose, C., Safatov, A. S., Buryak, G., Fröhlich-Nowoisky, J., Elbert, W., Andreae, M. O., Pöschl, U., and Jaenicke, R. (2012). Primary Biological Aerosol Particles In The Atmosphere: A Review. *Tellus B*, 64:1–58.

Duguid, J. P. (1946). The Size And The Duration Of Air-Carriage Of Respiratory Droplets And Droplet Nuclei. *Journal of Hygiene*, 44(6):471–479.

Eames, I., Shoaib, D., Klettner, C. A., and Taban, V. (2009). Movement Of Airborne Contaminants In A Hospital Isolation Room. *Journal Of The Royal Society Interface*, 6:S757–S766.

Edge, B., Paterson, E., and Settles, G. (2005). Computational Study Of The Wake And Contaminant Transport Of A Walking Human. *Journal Of Fluids Engineering*, 127:967–977.

Escombe, A. R., Oeser, C., Gilman, R. H., Navincopa, M., Ticona, E., Martinez, C., Caviedes, L., Sheen, P., Gonzalez, A., Noakes, C., Moore, D. A. J., Friedland, J. S., and Evans, C. A. (2007). The Detection Of Airborne Transmission Of Tuberculosis From HIV-Infected Patients, Using An In Vivo Air Sampling Model. *Clinical Infectious Diseases*, 44(10):1349–1357.

Eymard, R., Gallouët, T., and Herbin, R. (2000). Finite Volume Methods. *Handbook of Numerical Analysis*, 7:713–1020.

Fine, P. E. M. (1977). A Commentary On The Mechanical Analogue To The Reed-Frost Epidemic Model. *American Journal of Epidemiology*, 106(2):87–100.

Finlayson, E. U., Gadgil, A. J., Thatcher, T. L., and Sextro, R. G. (2004). Pollutant Dispersion In A Large Indoor Space: Part 2 - Computational Fluid Dynamics Predictions And Comparison With A Scale Model Experiment For Isothermal Flow. *Indoor Air*, 14.

Fischer, H. B., List, E. J., Koh, R. C. Y., Imberger, J., and Brooks, N. H. (1979). Mixing in Inland and Coastal Waters. *Academic Press*. Chapter 2.

Fletcher, L. A., Gaunt, L. F., Beggs, C. B., Shepherd, S. J., Sleigh, P. A., Noakes, C. J., and Kerr, K. G. (2007). Bactericidal Action Of Positive And Negative Ions In Air. *BMC Microbiology*, 7(32).

Gammack, D., Doering, C. R., and Kirschner, D. E. (2004). Macrophage Response To Myobacterium Tuberculosis Infection. *Journal Of Mathematical Biology*, 48:218–242.

Gao, N. P. and Niu, J. L. (2007). Modeling Particle Dispersion And Deposition In Indoor Environments. *Atmospheric Environment*, 41:3862–3876.

Gao, W., Li, H., Liu, Y., and Jian, Y. J. (2012). An Oscillation-Free High Order TVD/CBC-Based Upwind Scheme For Convection Discretization. *Numerical Algorithms*, 59:29–50.

Garcia, M., Chatterjee, A., Ruina, A., and Coleman, M. (1998). The Simplest Walking Model: Stability, Complexity, And Scaling. *ASME Journal Of Biomechanical Engineering*, 120:281–288.

Gilkeson, C. A., Camargo-Valero, M. A., Pickin, L. E., and Noakes, C. J. (2013). Measurement Of Ventilation And Airborne Infection Risk In Large Naturally Ventilated Hospital Wards. *Building And Environment*, 65:35–48.

Gladstone, C. and Woods, A. (2001). On Buoyancy-Driven Ventilation Of A Room With A Heated Floor. *Journal Of Fluid Mechanics*, 441:293–314.

Global Burden of Disease (2013). Global, Regional, And National Age-Sex Specific All-Cause And Cause-Specific Mortality For 240 Causes Of Death, 1990-2013: A Systematic Analysis For The Global Burden Of Disease. *The Lancet*, 385(9963):117–171.

Godunov, S. K. (1999). Reminiscences About Difference Schemes. *Journal Of Computational Physics*, 153:6–25.

Gopalakrishna, G., Choo, P., Leo, Y. S., Tay, B. K., Lim, Y. T., Khan, A. S., and Tan, C. C. (2004). SARS Transmission And Hospital Containment. *Emerging Infectious Diseases*, 10(3):395–400.

Gordon, S. B. and Read, R. C. (2002). Macrophage Defences Against Respiratory Tract Infections. *British Medical Bulletin*, 61(1):45–61.

Gostiaux, L. and Dauxois, T. (2007). Laboratory Experiments On The Generation Of Internal Tidal Beams Over Steep Slopes. *Physics Of Fluids*, 19:028102.

Grimsrud, D. T. (1980). An Intercomparison Of Tracer Gases Used For Air Infiltration Measurements. ASHRAE Annual Meeting, Los Angeles, CA.

Gupta, J. K., Lin, C. H., and Chen, Q. (2011). Transport Of Expiratory Droplets In An Aircraft Cabin. *Indoor Air*, 21:3–11.

Gustafson, T. L., Lavely, G. B., Brawner, E. R., Hutcheson, R. H., Wright, P. F., and Schaffner, W. (1982). An Outbreak Of Airborne Nosocomial Varicella. *Pediatrics*, 70(4):550–556.

Haas, C. N. (1983). Estimation Of Risk Due To Low Doses Of Microogranisms: A Comparison Of Alternative Methodologies. *American Journal Of Epidemiology*, 118(4):573–582.

Han, Z. Y., Weng, W. G., and Huang, Q. Y. (2013). Characterizations Of Particle Size Distribution Of The Droplets Exhaled By Sneeze. *Journal Of The Royal Society Interface*, 10(88).

Hathway, A., Papakonstantis, I., Konuah, A. B., and Brevis, W. (2014). Towards Understanding The Role Of Human Activity On Indoor Air Flows: A Case Study Of Door Motion Based On Both Field And Experimental Activities. *Indoor Air 2014 - 13th International Conference On Indoor Air Quality And Climate*, pages 435–442.

Health And Safety Executive (2008). Evaluating The Protection Afforded By Surgical Masks Against Influenza Bioaerosols.

Health Protection Agency (2008). Mandatory Surveillance Of Healthcare Associated Infections Report.

Health Protection Agency (2011). Surveillance Of Surgical Site Infections In NHS Hospitals in England.

Health Protection Agency (2012). Infection Control Precautions To Minimise Transmission Of Respiratory Tract Infections (RTIs) In The Healthcare Setting.

Heasman, M. A. and Reid, D. D. (1961). Theory And Observation In Family Epidemics Of The Common Cold. *British Journal Of Preventive And Social Medicine*, 15(1):12–16.

Heisenberg, W. (1927). Über Den Anschaulichen Inhalt Der Quantentheoretischen Kinematik Und Mechanik. *Zeitschrift Für Physik*, 43(3-4):172–198.

Henderson, R. D. and Barkley, D. (1996). Secondary Instability In The Wake Of A Circular Cylinder. *Physics Of Fluids*, 8(6).

Hunt, G. and Linden, P. (1999). The Fluid Mechanics Of Natural Ventilation - Displacement Ventilation By Buoyancy-Driven Flows Assisted By Wind. *Building And Environment*, 34:707–720.

Jennison, M. W. (1942). Atomizing Of Mouth And Nose Secretions Into the Air As Revealed By. In *Aerobiology* (ed. Moulton F. R.), pages 106–128. Washington, DC.

Kalitzin, G., Medic, G., Iaccarino, G., and Durbin, P. (2005). Near-Wall Behavior Of RANS Turbulence Models And Implications For Wall Functions. *Journal Of Computational Physics*, 204:265–291.

Kalliomäki, P., Sarrinen, P., Tang, J. W., and Koskela, H. (2014). Airflow Patterns Through A Single Hinged And A Sliding-Door In Hospital Isolation Room. *Proceedings of Indoor Air 2014*, HP0821.

Kanaris, N., Grigoriadis, D., and Kassinos, S. (2011). Three Dimensional Flow Around A Circular Cylinder Confined In A Plane Channel. *Physics Of Fluids*, 23(064106):1–14.

Kermack, W. O. and McKendrick, A. G. (1927). A Contribution To The Mathematical Theory Of Epidemics. *Proceedings of the Royal Society A: Mathematical, Physical and Engineering Sciences*, 115(772):700–721.

Kerr, K. G., Beggs, C. B., Dean, S. G., Thornton, J., Donnelly, J. K., Todd, N. J., Sleigh, P. A., Qureshi, A., and Taylor, C. C. (2006). Air Ionisation And Colonisation/Infection With Methicillin-Resistant Staphylococcus Aureus And Acinetobacter Species In An Intensive Care Unit. *Intensive Care Medicine*, 32(2):315–317.

Kim, T. and Flynn, M. (1991). Modelling A Worker's Exposure From A Hand-Held Source In A Uniform Freestream. *American Inudustrial Hygiene Association Journal*, 52:458–463.

Kolmogorov, A. N. (1942). Equations Of Turbulent Motion Of An Incompressible Fluid. *Izvestia Academy of Sciences, USSR; Physics*, 6(1:2):56–58.

Kowalski, W. (2009). Ultraviolet Germicidal Irradiation Handbook: UVGI For Air And Surface Disinfection. *Springer-Verlag Berlin Heidelberg, 1st Edition.*

Kowalski, W. J. and Bahnfleth, W. (1998). Airborne Respiratory Diseases And Mechanical Systems For Control Of Microbes. *HPAC Heating, Piping Air Conditioning*, 70(7):34–48.

Kravchenko, A. G. and Moin, P. (2000). Numerical Studies Of Flow Over A Circular Cylinder at ReD = 3900. *Physics of Fluids*, 12(2):403–417.

Lai, A. C. K. and Cheng, Y. C. (2007). Study Of Expiratory Droplet Dispersion And Transport Using A New Eulerian Modeling Approach. *Atmospheric Environment*, 41:7473–7484.

Lambrecht, B. N. (2006). Alveolar Macrophage In The Driver's Seat. *Immunity*, 24(4):366–368.

Launder, B. E., Reece, G. J., and Rodi, W. (1975). Progress In The Development Of A Reynolds-Stress Turbulence Closure. *Journal of Fluid Mechanics*, 68(3):537–566.

Launder, B. E. and Spalding, D. B. (1972). Lectures In Mathematical Models Of Turbulence. *Academic Press.*

Launder, B. E. and Spalding, D. B. (1974). The Numerical Computation Of Turbulent Flow. *Computer Methods In Applied Mechanics And Engineering*, 3:269–289.

Li, Y., Duan, S., Yu, I. T. S., and Wong, W. (2004). Multi-Zone Modeling Of Probable SARS Virus Transmission By Airflow Between Flats In Block E, Amoy Gardens. *Indoor Air*, 15:96–111.

Li, Y., Huang, X., Yu, I. T. S., Wong, T. W., and Qian, H. (2005). Role Of Air Distribution In SARS Transmission During The Largest Nosocomial Outbreak In Hong Kong. *Indoor Air*, 15:83–95.

Li, Y., Leung, G. M., Tang, J. W., Yang, X., Chao, C. Y. H., Lin, J. Z., Lu, J. W., Nielsen, P. V., Niu, J., Qian, H., Slrigh, A. C., Su, H. J. J., Sundell, J., Wong, T. W., and Yuen, P. L. (2007). Role Of Ventilation In Airborne Transmission Of Infectious Agents In The Built Environment - A Multidisciplinary Systematic Review. *Indoor Air*, 17:2–18.

Lide, D. R. (2001). CRC Handbook Of Chemsitry And Physics. *CRC*, 82nd Edition.

Lidwell, O. M., Lowbury, E. J. L., Whyte, W., Blowers, R., Stanley, S. J., and Lowe, D. (1983). Airborne Contamination Of Wounds In Joint Replacement Operations: The Relationship To Sepsis Rates. *Journal of Hospital Infection*, 4(2):111–131.

Lilly, D. K. (1967). The Representation Of Small-Scale Turbulence In Numerical Simulation Experiments. *IBM Scientific Computing Symposium On Environmental Sciences, IBM Form No 320-1951*, pages 195–210.

Linden, P. and Simpson, J. (1985). Buoyancy Driven Flow Through An Open Door. *Air Infiltration Review*, 6(4):4–5.

Lipsitch, M., Cohen, T., Cooper, B., Robins, J. M., Ma, S., James, L., Gopalakrishna, G., Chew, S. K., Tan, C. C., Samore, M. H., Fisman, D., and Murray, M. (2003). Transmission Dynamics And Control Of Sever Acute Respiratory Syndrome. *Science*, 300(5627):1966–1970.

Loomans, M. G. L. C., van Houdt, W., Lemaire, A. D., and Hensen, J. L. M. (2008). Performance Assessment Of An Operating Theatre Design Using CFD Simulation And Tracer Gas Measurements. *Indoor And Built Environment*, 17:299–312.

Luoma, M. and Batterman, S. A. (2001). Characterization Of Particulate Emissions From Occupant Activities In Offices. *Indoor Air*, 1(1):35–48.

Mackwood, P. R. and Bearman, P. W. (1997). Wave And Current Flows Around Circular Cylinders At Large Scale. *Health And Safety Executve - Offshore Technology Report.*

Mahfouz, F. M. and Badr, H. M. (2002). Mixed Convection From A Cylinder Oscillating Vertically In A Quiescent Fluid. *Heat And Mass Transfer*, 38:477–286.

Mattsson, M., Bjorn, E., Sandberg, M., and Nielsen, P. (1997). Simulating People Moving In Displacement Ventilated Rooms. *Proceedings of "Healthy Buildings '97"*. 5th International Conference on Healthy Buildings, Sep. 27 - Oct 3 1997, Washington DC, USA.

Mazumdar, S., Poussou, S., Lin, C., Isukapalli, S., Plesniak, M., and Chen, Q. (2011). Impact Of Scaling And Body Movement On Contaminant Transport In Airliner Cabins. *Atmospheric Environment*, 45(33):6019–6028.

Mcdonagh, A. and Byrne, M. A. (2014). The Influence Of Human Physical Activity And Contaminated Clothing Type On Particle Resuspension. *Journal Of Environmental Radioactivity*, 127:119–126.

Menter, F. R. (1992). Improved Two-Equation $k-\omega$ Turbulence Models for Aerodynamic Flows. *NASA Technical Memorandum 103975*.

Menter, F. R. (1994). Two-Equation Eddy-Viscosity Turbulence Models For Engineering Applications. *The American Institute of Aeronautics and Astronautics Journal*, 32(8):1598–1605.

Menter, F. R., Kuntz, M., and Langtry, R. (2003). Ten Years Of Industrial Experience With The SST Turbulence Model. *Turbulence, Heat and Mass Transfer 4*.

Menzies, D., Fanning, A., Yuan, L., FitzGerald, J. M., and The Canadian Collaborative Group In Nosocomial Transmission Of TB (2000). Hospital Vesntilation And Risk For Tuberculous Infection In Canadian Health Care Workers. *Annal Of Internal Medicine*, 133(10):779–789.

Mittal, R. and Balachandar, S. (1995). Effect Of Three-Dimensionality On The Lift And Drag Of Nominally Two-Dimensional Cylinders. *Physics Of Fluids*, 7(8):1841–1865.

Mochon, S. and McMahon, T. A. (1979). Ballistic Walking: An Improved Model. *Mathematical Biosciences*, 52:241–260.

Morawska, L. (2006). Droplet Fate In Indoor Environments, Or Can We Prevent The Spread Of Infection? *Indoor Air*, 16:335–347.

Morawska, L. and Salthammer, T. (2003). Indoor Environment: Airborne Particles And Settled Dust. *Wiley-VCH, 1st Edition*.

Munz, P., Hudea, I., and Smith?, J. I. R. J. (2009). When Zombies Attack!: Mathematical Modelling Of An Outbreak Of Zombie Infection. *Infectious Disease Modelling Research Progress*, 88.

National Audit Office (2000). The Management And Control Of Hospital Acquired Infection In Acute NHS Trusts In England.

National Research Council (2004). Learning From SARS: Preparing For The Next Disease Outbreak - Workshop Summary. *Washington, DC. The National Academic Press*.

Nazaroff, W. W., Nicas, M., and Miller, S. L. (1998). Framework For Evaluating Measures To Control Noscomial Tuberculosis Transmission. *Indoor Air*, 8(4):205–218.

Newman, S. P. (1985). Aerosol Deposition Considerations In Inhalation Therapy. *CHEST*, 88(2):152S–160S.

NewScientist (2003). Face Masks Are Best Protection Against SARS. http://www.newscientist.com/article/dn3692-face-masks-are-best-protection-against-sars.html. Accessed: 23rd April 2015.

Nguyen, N. T. and Wereley, S. T. (2006). *Fundamentals And Applications of Microfluidics, Second Edition (Integrated Microsystems)*. Artech Print on Demand.

Nicas, M. (1996). An Analytical Framework For Relating Dose, Risk, And Incidence: An Application To Occupational Tuberculosis Infection. *Risk Analysis*, 16(4):527–538.

Nightingale, F. (1863). Notes On Hospitals. *Longman, Green, Longman , Roberts, and Green*.

NIOSH (2015). Hierarchy Of Controls. http://www.cdc.gov/niosh/topics/hierarchy/. Accessed: 24th April 2015.

Noakes, C. J., Beggs, C. B., and Sleigh, P. A. (2004). Modelling the Performance Of Upper Room Ultraviolet Germicidal Irradiation Devices In Ventilated Rooms: Comparison of Analytical and CFD Methods. *Indoor and Built Environment*, 13:477–488.

Noakes, C. J. and Sleigh, P. A. (2009). Mathematical Models For Assessing The Role Of Airflow On The Risk Of Airborne Infection In Hospital Wards. *Journal Of The Royal Society Interface*, 6(6):S791–S800.

Noakes, C. J., Sleigh, P. A., and Khan, M. A. I. (2012). Appraising Healthcare Ventilation Design From Combined Infection Control and Energy Perspective. *HVAC&R Research*, 18(4):658–670.

Norberg, C. (2003). Fluctuating Lift On A Cylinder: Review And New Measurements. *Journal Of Fluids And Structures*, 17:57–96.

Oberdörster, G., Sharp, Z., Atudorei, V., Elder, A., Gelein, R., Kreyling, W., and Cox, C. (2004). Translocation Of Inhaled Ultrafine Particles To The Brain. *Inhalation Toxicology*, 16:437–445.

Office for National Statistics (2013). Deaths Involving MRSA: England and Wales, 2008 to 2012. *Statistical Bulletin*.

OpenFOAM (2011). www.openfoam.org. Accessed: 23rd April 2015.

Parkinson, S. D., Hill, J., Piggott, M. D., and Allison, P. A. (2014). Direct Numerical Simulations Of Particle-Laden Density Currents With Adaptive, Discontinuous Finite Elements. *Geoscientific Model Development Discussions*, 7(3):1945–1960.

Parnaudeau, P., Carlier, J., Heitz, D., and Lamballais, E. (2008). Experimental And Numerical Studies Of The Flow Over A Circular Cylinder At Reynolds Number 3900. *Physics of Fluids*, 20.

Peng, S. H. and Eliasson, P. (June 2007). Examination of the Shear Stress Transport Assumption with a Low-Reynolds Number k-omega Model for Aerodynamic Flows. *37th AIAA Fluid Dynamics Conference and Exhibit, Miami FL*.

Peskin, C. S. (1972). Flow Patterns Around Heart Valves: A Digital Computer Method For Solving The Equations Of Motion. *PhD Thesis, Albert Einstein College of Medicine*, page 211. Available from: http://www.umi.com/hp/Products/DisExpress.html, order no. 7230378.

Phillips, L., Carlile, J., and Smith, D. (2004). Epidemiology Of A Tuberculosis Outbreak In A Rural Missouri High School. *Pediatrics*, 113(6):514–519.

Poussou, S. (2008). Experimental Investigation Of Airborne Contaminant Transport By A Human Wake Moving In A Ventilated Aircraft Cabin. *Thesis from Purdue University, Indiana, USA*.

Poussou, S., Mazumdar, S., Plesniak, M., Sojka, P., and Chen, Q. (2010). Flow And Contaminant Transport In An Airliner Cabin Induced By A Moving Body: Model Experiments And CFD Predictions. *Atmospheric Environment*, 44(24):2830–2839.

Poussou, S. B. and Plesniak, M. W. (2012). Vortex Dynamics And Scalar Transport In The Wake Of A Bluff Body Driven Through A Steady Recirculating Flow. *Experiments In Fluids*, 53(3):747–763.

Poynton, C. A. (2003). *Digital Video And HDTV: Algorithms And Interfaces*. Morgan Kauffmann.

Prandtl, L. (1925). Bericht Über Untersuchungen Zur Ausgebildete Turbulenz. *Zeitschrift Für Angewandte Mathematik Und Mechanik*, 5:136–139.

Prandtl, L. (1945). Uber Ein Neues Formelsystem Fur Die Ausgebildete Turbulenz. *Nachrichten Der Akademie Der Wissenschaften Zu Göttingen, Mathematisch-Physikalische Klasse 1945*, pages 6–19.

Prüss-Ustün, A., Bartram, J., Clasen, T., Colford, J. M., Cumming, O., Curtis, V., Bonjour, S., Dangour, A. D., France, J. D., Fewtrell, L., Freeman, M. C., Gordon, B., Hunter, P. R., Johnston, R. B., Mathers, C., Mäusezahl, D., Medlicott, K., Neira, M., Stocks, M., Wolf, J., and Cairncross, S. (2014). Burden Of Disease From Inadequate Water, Sanitation And Hygiene In Low- And Middle-Income Settings: A Retrospective Analysis Of Data From 145 Countries. *Tropical Medicine And International Health*, 19(8):894–905.

Public Health England (2014a). Annual Epidemiological Commentary: Mandatory MRSA MSSA and E. Coli Bacteraemia And C. Difficile Infection Data, 2013/14.

Public Health England (2014b). Surveillance Of Surgical Site Infections In NHS Hospitals In England 2013/14.

Public Health England (2014). Tuberculosis In The UK: 2014 Report.

Qian, H., Li, Y., Nielsen, P. V., and Huang, X. (2009). Spatial Distribution Of Infection Risk Of SARS Transmission In A Hospital Ward. *Building And Environment*, 44:1651–1658.

Qian, J. and Ferro, A. R. (2008). Resuspension Of Dust Particles In A Chamber And Associated Environmental Factors. *Aerosol Science And Technology*, 42(7):566–578.

Remington, P. L., Hall, W. N., Davis, I. H., Herald, A., and Gun, R. A. (1985). Indoor Infection In A Modern Building. *Journal Of The American Medical Association*, 253(11):1574–1577.

Reynolds, O. (1883). An Experimental Investigation Of The Circumstances Which Determine Whether The Motion Of Water Shall Be Direct Or Sinuous, And Of The Law Of Resistance In Parallel Channels. *Transactions Of the Cambridge Philosophical Society*, 174:935–982.

Richmond-Bryant, J. (2009). Transport Of Exhaled Particulate Matter In Airborne Infection Isolation Rooms. *Building And Environment*, 44:44–55.

Richter, A. and Naudascher, E. (1976). Fluctuating Forces On A Rigid Circular Cylinder In Confined Flow. *Journal of Fluid Mechanics*, 78(3):561–576.

Riley, E. C., Murphy, G., and Riley, R. K. (1978). Airborne Spread Of Measles In A Suburban Elementary School. *American Journal Of Epidemiology*, 107(5):421–432.

Riley, R. L., Mills, C. C., Nyka, W., Weinstock, N., Storey, P. B., Sultan, L. U., Riley, M. C., and Wells, W. F. (1959). Aerial Dissemination Of Pulmonary Tuberculosis. *American Journal Of Epidemiology*, 70(2):185–196.

Riley, S., Fraser, C., Ghani, C. A. D. A. C., Abu-Raddad, L. J., Hedley, A. J., Lwung, G. M., Ho, L., Lam, T., Thach, T. Q., Chau, P., Chan, K., Lo, S., Leung, P., Tsang, T., Ho, W., Lee, K., Lau, E. M. C., Ferguson, N. M., and Anderson, R. M. (2003). Transmission Dynamics Of The Etiological Agent Of SARS In Hong Kong: Impact Of Public Health Interventions. *Science*, 300(5627):1961–1966.

Rosetti, G. F., Vaz, G., and Fujarra, A. L. C. (2012). URANS Calculations For Smooth Circular Cylinder Flow In A Wide Range Of Reynolds Numbers: Solution Verification And Validation. *Journal of Fluids Engineering*, 134:121103–1 – 121103–18.

Roshko, A. (1955). On The Wake And Drag Of Bluff Bodies. *Journal Of The Aeronautical Sciences*, 22(2):124–132.

Roshko, A. (1961). Experiments On The Flow Past A Circular Cylinder At Very High Reynolds Number. *Journal Of Fluid Mechanics*, 10(3):345–356.

Rubins, J. B. (2003). Alveolar Macrophages: Wielding The Double-Edged Sword Of Inflammation. *American Journal Of Respiratory And Critical Care Medicine*, 167:103–104.

Rudnick, S. N. and Milton, D. K. (2003). Rick Of Indoor Airborne Infection Transmission Estimated From Carbon Dioxide Concentration. *Indoor Air*, 13(3):237–245.

Rummel, A. C., v. Carmer, C. F., and Jirka, G. H. (2002). Mass Transport In Shallow Turbulent Wake Flow By Planar Concentration Analysis Technique. *Proceedings Of The 2002 International Conference On Hydraulic Measurements & Experimental Methods.*

Rydock, J. P. and Eian, P. K. (2004). Containment Testing Of Isolation Rooms. *Journal Of Hospital Infection*, 57(3):228–232.

Saffman, P. G. (1970). A Model For Inhomogeneous Turbulent Flow. *Proceedings Of The Royal Society Of London, Series A: Mathematical And Physical Sciences*, 317(1530):417–433.

Schenzle, D. (1982). Problems In Drawing Epidemiological Inferences By Fitting Epidemic Chain Models To Lumped Data. *Biometrics*, 38(3):843–847.

SD Association (2015). Speed Class. https://www.sdcard.org/developers/overview/speed_class/. Accessed: 28th April 2015.

Seinfeld, J. H. (1986). Atmospheric Chemistry And Physics Of Air Pollution. *John Wiley & Sons*, 1st ed.(p325).

Seinfeld, J. H. and Pandis, S. N. (1998). Atmospheric Chemistry And Physics: From Air Pollution To Climate Change. *John Wiley & Sons*, 1st ed.(p467).

Selwyn, S. (1991). Hospital Infection: The First 2500 Years. *Journal Of Hospital Infection*, 18:5–64.

Settles, G. (2006). Fluid Mechanics And Homeland Security. *Annual Review Of Fluid Mechanics*, 38:87–110.

Shah, N. H. and Gupta, J. (2013). SEIR Model And Simulation For Vector Borne Diseases. *Applied Mathematics*, 4:13–17.

Shiomori, T., Miyamoto, H., and Makishima, K. (2001). Significance Of Airborne Transmission Of Methicillin-Resistant Staphylococcus Aureus In An Otolaryngology - Head And Neck Surgery Unit. *Archives Of Otolaryngology - Head And Neck Surgery*, 127(6):644–648.

Sibille, Y. and Reynolds, H. Y. (1990). Macrophages And Polymorphonuclear Neutrphils In Lung Defense And Injury. *American Review Of Respiratory Diseases*, 142:471–501.

Smagorinsky, J. (1963). General Circulation Experiments With The Primitive Equations. *Monthly Weather Review*, 93:99–165.

Song, F., Zhao, B., Yang, X., Jiang, Y., Dobbs, V. G. G., and Sahm, M. (2008). A New Approach On Zonal Modeling Of Indoor Environment With Mechanical Ventilation. *Building and Environment*, 43:278–286.

Splinter, R. and Hooper, B. A. (2006). *An Introduction to Biomedical Optics*. CRC Press.

Stehle, J., Voirin, N., Barrat, A., Cattuto, C., v. colizza, Isella, L., Regis, C., Pinton, J. F., Khanafer, N., and den Broeck andP. Vanhems, W. V. (2011). Simulation Of An SEIR Infectious Disease Model On The Dynamic Contact Network Of Conference Attendees. *BMC Medicine*, 9(87).

Stewart, S. L., Grinshpun, S. A., Willeke, K., Terzieva, S., Ulevicius, V., and Donnelly, J. (1995). Effect Of Impact Stress On Microbial Recovery On An Agar Surface. *Applied Environmental Microbiology*, 61(4):1232–1239.

Stokes, G. G. (1851). On The Effect Of The Internal Friction Of Fluids On The Motion Of Pendulums. *Transactions Of the Cambridge Philosophical Society*, 9:8–106.

Strelets, M. (2001). Detached Eddy Simulation Of Massively Separated Flows. *AIAA Paper 2001-0879, 39th Aerospace Sciences Meeting and Exhibit.*

Strouhal, V. (1878). Uber Eine Besondere Art Der Tonerregung. *Annalen Der Physik Und Chemie*, 5(10):216–251.

Sze-To, G. N. and Chao, C. Y. H. (2010). Review And Comparison Between The Wells-Riley And Dose-Response Approaches To Risk Assessment Of Infectious Respiratory Diseases. *Indoor Air*, 20(1):2–16.

Sze-To, G. N., Wan, M. P., Chao, C. Y. H., Wei, F., Yu, S. C. T., and Kwan, J. K. C. (2008). A Methodology For Estimating Airborne Virus Exposures In Indoor Environments Using The Spatial Distribution Of Expiratory Aerosols And Virus Viability Characteristics. *Indoor Air*, 18:425–438.

Tang, J. W., Eames, I., Li, Y., Taha, Y. A., Wilson, P., Bellingan, G., Ward, K. N., and Breuer, J. (2005). Door-Opening Motion Can Potentially Lead To A Transient Breakdown In Negative-Pressure Isolation Conditions: The Importance Of Vorticity And Buoyancy Airlows. *Journal Of Hospital Infection*, 61:283–286.

Tang, J. W., Li, Y., Eames, I., Chan, P. K. S., and Ridgway, G. L. (2006). Factors Involved In The Aerosol Transmission Of Infection And Control Of Ventilation In Healthcare Premises. *Journal Of Hospital Infection*, 64:100–114.

Tang, J. W., Nicolle, A., Pantelic, J., Klettner, C. A., Su, R., Kalliomaki, P., Saarinen, P., Koskela, H., Reijula, K., Mustakallio, P., Cheong, D. K. W., Sekhar, C., and Tham, K. W. (2013). Different Types Of Door-Opening Motions As Contributing Factors To Containment Failures In Hospital Isolation Rooms. *PLoS ONE*, 8(6).

Tang, J. W., Nicolle, A. D. G., Pantelic, J., Jiang, M., Sekhr, C., Cheong, D. K. W., and Tham, K. W. (2011a). Qualitative Real-Time Schlieren And Shadowgraph Imaging Of Human Exhaled Airflows: An Aie To Aerosol Infection Control. *PLoS ONE*, 6(6).

Tang, J. W., Noakes, C. J., Nielsen, P. V., Eames, I., Nicolle, A., Li, Y., and Settles, G. S. (2011b). Observing And Quantifying Airflows In The Infection Control Of Aerosol- And Airborne-Transmitted Diseases: An Overview Of Approaches. *Journal Of Hospital Infection*, 77:213–222.

Taylor, G. I. (1935). Statistical Theory Of Turbulence. *Proceedings of the Royal Society of London. Series A, Mathematical and Physical Sciences*, 151(873):421–444.

Thatcher, T., Wilson, D. J., Wood, E. E., Craig, M. J., and Sextro, R. G. (2004). Pollutant Dispersion In A Large Indoor Space: Part 1 - Scaled Experiments Using A Water-Filled Model With Occupants And Furniture. *Indoor Air*, 14.

Turner, J. T., Popiel, C. O., and Robinson, D. I. (1993). Evolution Of An Improved Vortex Generator. *Flow Measuremnt And Instrumentation*, 4(4):249–258.

U. S. Environmental Protection Agency (1989). Report To Congress On Indoor Air Quality: Volume 2. *EPA/400/1-89/001C. Washington, DC.*

van Sommeren, D. D. J. A., Caulfield, C. P., and Woods, A. W. (2012). Turbulent Buoyant Convection From A Maintained Source Of Buoyancy In A Narrow Vertical Tank. *Journal of Fluid Mechanics*, 701:278–303.

Versteeg, H. K. and Malalasekera, W. (1995). An Introduction To Computational Fluid Dynamics: The Finite Volume Method. *Prentice Hall, 1st ed.*

Visser, M. D., McMahon, S. M., Merow, C., Dixon, P. M., Record, S., and Jongejans, E. (2015). Speeding Up Ecological And Evolutionary Computations In R; Essentials

Of High Performance Computing For Biologists. *PLOS Computational Biology*, pages 1–11.

Wang, J. and Chow, T. T. (2011). Numerical Investigation Of Influence Of Human Walking On Dispersion And Deposition Of Expiratory Droplets In Airborne Infection Isolation Room. *Building and Environment*, 46:1993–2002.

Weber, D. J., Rutala, W. A., Miller, M. B., Huslage, K., and Sickbert-Bennett, E. (2010). Role Of Hospital Surfaces In The Transmission Of Emerging Health Care-Associated Pathogens: Norovirus, Clostridium Difficile, And Acinetobacter Species. *American Journal Of Infection Control*, 38(5):25–33.

Wells, W. F. (1934). On Air-Borne Infection. Study II. Droplets And Droplet Nuclei. *American Journal Of Epidemiology*, 20(3):611–618.

Wells, W. F. (1955). *Airborne Contagion And Air Hygiene: An Ecological Study Of Droplet Infection*. Published For The Commonwealth Fund by Harvard University Press.

Wells, W. F. and Lurie, M. B. (1941). Experimental Air-Borne Disease. Quantitative Natural Respiratory Contaion Of Tuberculosis. *American Journal Of Epidemiology*, 34B(1):21–40.

West, G. S. and Apelt, C. J. (1982). The Effects Of Tunnel Blockage And Aspect Ratio On The Mean Flow Past A Circular Cylinder With Reynolds Numbers Between 10^4 And 10^5. *Journal Of Fluid Mechanics*, 114:361–377.

Whyte, W., Lidwell, O. M., Lowbury, E. J., and Blowers, R. (1983). Suggested Bacteriological Standards For Air In Ultraclean Operating Rooms. *Journal of Hospital Infection*, 4(2):133–139.

Wieselberger, C. (1922). New Data On The Laws Of Fluid Resistance. *NACA-TN-84*.

Wilcox, D. C. (1988). Multiscale Model For Turbulent Flows. *The American Institute of Aeronautics and Astronautics Journal*, 11(11):1311–1320.

Wilcox, D. C. (2006). Turbulence Modeling For CFD. *DCW Industries, Inc.*

Wilcox, D. C. and Alber, I. E. (1972). A Turbulence Model For High Speed. *Proceedings Of The 1972 Heat Transfer And Fluid Mechanics Institute, Stanford University Press*, pages 231–252.

Williamson, C. H. K. (1984). Sinusoidal Flow Relative To Circular Cylinders. *Journal Of Fluid Mechanics*, 155:141–174.

Williamson, C. H. K. and Roshko, A. (1988). Vortex Formation In The Wake Of An Oscillating Cylinder. *Journal Of Fluids And Structures*, 2:355–381.

Wilson, J. (2006). Infection Control In Clinical Practice. *Bailliere Tindall, 3rd Edition*, pages 45–46.

Wong, T. W., Lee, C. K., Tam, W., Lau, J. T. F., Yu, T. S., Lui, S. F., Chan, P. K. S., Li, Y., Bresee, J. S., Sung, J. J. Y., and Parashar, U. D. (2004). Cluster of SARS among Medical Students Exposed to Single Patient, Hong Kong. *Emerging Infectious Diseases*, 10(2):269–276.

World Health Organisation (2009). Natural Ventilation For Infection Control In Health-care Settings. *WHO Publication/Guidelines*.

World Health Organisation (2015). http://www.who.int/csr/sars/country/table2004_04_21/en/. Accessed: 23rd April 2015.

World Health Organization (2009). Advice On The Use Of Masks In The Community Setting In Influenza A (H1N1) Outbreaks. http://www.who.int/csr/resources/publications/Adviceusemaskscommunityrevised.pdf. Accessed: 22nd April 2015.

World Health Organization (2014). Vevtor-borne Diseases. http://www.who.int/mediacentre/factsheets/fs387/en/. Accessed 30th July 2015.

Xie, X., Li, Y., Chang, A., Ho, P., and W.H.Seto (2007). How Far Droplets Can Move In Indoor Environments - Revisiting The Wells Evaporation-Falling Curve. *Indoor Air*, 17:211–225.

Yan, W., Zhang, Y., Sun, Y., and Li, D. (2009). Experimental And CFD Study Of Unsteady Airborne Pollutant Transport Within An Aircraft Cabin Mock-Up. *Building And Environment*, 44:34–43.

Yeung, R. W. and Vaidhyanathan, M. (1993). Flow Past Oscillating Cylinders. *Journal Of Offshore Mechanics And Arctic Engineering*, 115(4):028102.

Yu, I. T. S., Wong, T. W., Chiu, Y. L., Lee, N., and Li, Y. (2005). Temporal-Spatial Analysis Of Severe Acute Respiratory Syndrome Among Hospital Inpatients. *Clinical Infectious Diseases*, 40:1237–1243.

Zdravkovich, M. M. (1997). Flow Around Circular Cylinders Volume 1: Fundamentals. *Oxford Univeristy Press*.

Zhai, Z. J., Zhang, Z., Zhang, W., and Chen, Q. (2007). Evaluation Of Various Turbulence Models In Predicting Airflow And Turbulence In Enclosed Environemnts By CFD: Part 1 - Summary Of Prevalent Turbulence Models. *HVAC & R Research*, 13(6):853–870.

Zhu, S., Kato, S., and Yang, J. H. (2005). Study On Transport Characteristics Of Saliva Droplets Produced By Coughing In A Calm Indoor Environment. *Building And Environment*, 41:1691–1702.

Zoon, W. A. C., Loomans, M. G. L. C., and Hensen, J. L. M. (2011). Testing The Effectiveness Of Operating Room Ventilation With Regard To Removal Of Airborne Bacteria. *Building And Environment*, 46:2570–2577.